



Tailored routes to metal-containing nanoparticles for hydrogenation reactions in solution : surface design for H₂ activation

Rémi F. André

► To cite this version:

Rémi F. André. Tailored routes to metal-containing nanoparticles for hydrogenation reactions in solution : surface design for H₂ activation. Material chemistry. Sorbonne Université, 2021. English. NNT : 2021SORUS190 . tel-04232631

HAL Id: tel-04232631

<https://theses.hal.science/tel-04232631>

Submitted on 9 Oct 2023

HAL is a multi-disciplinary open access archive for the deposit and dissemination of scientific research documents, whether they are published or not. The documents may come from teaching and research institutions in France or abroad, or from public or private research centers.

L'archive ouverte pluridisciplinaire **HAL**, est destinée au dépôt et à la diffusion de documents scientifiques de niveau recherche, publiés ou non, émanant des établissements d'enseignement et de recherche français ou étrangers, des laboratoires publics ou privés.

Sorbonne Université

Ecole doctorale 397, Physique et Chimie des Matériaux

Laboratoire de Chimie de la Matière Condensée de Paris (LCMCP)

**Tailored routes to metal-containing nanoparticles
for hydrogenation reactions in solution:
surface design for H₂ activation**

Par **Rémi F. ANDRÉ**

Thèse de doctorat de Chimie de Sorbonne Université

Dirigée par Dr. Sophie CARENCO

Présentée et soutenue publiquement le 7 Octobre 2021

Devant un jury composé de :

QUADRELLI Elsje Alessandra	Directrice de recherches – Université Lyon 1	Rapporteuse
HUC Vincent	Directeur de recherches – Université Paris Saclay	Rapporteur
GÓMEZ Montserrat	Professeur – Université Toulouse 3 – Paul Sabatier	Examinatrice
CARRIER Xavier	Professeur – Sorbonne Université	Examinateur
CARENCO Sophie	Chargée de recherches – Sorbonne Université	Directrice de thèse

Abstract

In this thesis work, the use of metal-containing nanoparticles such as carbides, oxides and phosphides is explored for colloidal catalysis. In an attempt to build a Frustrated Lewis Pair (FLP)-like catalytic system for H_2 activation, the synergy with a molecular Lewis base is assessed. In the bibliographic introduction, the stakes and the challenges of H_2 activation in solvent are presented, with an emphasis on the use of non-purely metallic catalysts for the hydrogenation of model compounds. In the first part, early transition metal carbides and hydrides are synthesized *via* solid-state metathesis. The influence of process parameters is explored to tune the phase speciation in the products. The most promising carbon-supported catalysts, Mo_2C/C and W_2C/C , are studied for gas phase and liquid phase hydrogenations of olefins. In the second part, cerium and indium oxides are obtained *via* hydrothermal pathways. The relevance of oxygen defects in CeO_{2-x} is established for H_2 gas phase activation and semi-hydrogenation of phenylacetylene in solvent. The last part is dedicated to the non-aqueous syntheses of molybdenum and tungsten oxides, and nickel carbide and phosphides. The syntheses mechanisms are studied by means of NMR for the organic species and XAS and XRD for the nature of the inorganic species. The catalytic activity of the unsupported nanoparticles is finally evaluated for the hydrogenation of nitrobenzene and phenylacetylene in various solvents.

Dans ces travaux de thèse, nous avons exploré différentes classes de nanoparticules métalliques telles que des carbures, des oxydes et des phosphures, pour des applications en catalyse colloïdale. Afin de construire un système catalytique de type « Paire de Lewis Frustrée », la synergie avec des bases de Lewis moléculaires a été étudiée. En introduction, les enjeux et les défis de l'activation de H_2 en solvant sont présentés, avec un focus sur les catalyseurs non purement métalliques pour l'hydrogénation de composés modèles. Dans la première partie, des carbures et des hydrides de métaux de début de transition ont été synthétisés par métathèse solide-solide. Nous avons exploré l'influence de différents paramètres de procédé sur la spéciation de phase des produits. Les catalyseurs supportés les plus prometteurs, Mo_2C/C et W_2C/C , ont été étudiées pour l'hydrogénation d'oléfines en phase gaz et en solvant. Dans la deuxième partie, des oxydes de cerium et d'indium ont été produits par voie hydrothermale. L'importance de défauts d'oxygène dans CeO_{2-x} pour l'activation de H_2 en phase gaz et pour la semi-hydrogénation du phénylacétylène a été établie. La dernière partie est dédiée à la synthèse solvothermale d'oxydes de molybdène et de tungstène, ainsi qu'à celle de carbure et de phosphures de nickel. Les mécanismes de synthèse ont été étudiés par RMN pour la partie organique et par XAS et DRX pour la partie inorganique. L'activité catalytique des nanoparticules non supportées a finalement été évaluée pour l'hydrogénation du nitrobenzène et du phénylacétylène dans plusieurs solvants.

Remerciements

Avant toute chose, je souhaiterais remercier chaleureusement ma directrice de thèse, Sophie Carencu, pour son encadrement au quotidien tout au long de ces trois années. Merci en premier lieu pour m'avoir recruté et fait confiance très rapidement. Etant donné le vaste champ d'études de ma thèse, tu m'as permis d'acquérir des connaissances dans de nombreux domaines et sur de nombreuses techniques de caractérisation, et je t'en sais gré ! Ce fut un plaisir de discuter sciences avec toi bien évidemment (nous ne mentionnerons pas l'effet nanoKirkendall ici), mais également de certaines de tes passions comme la musique ou la voile (j'ai notamment appris l'importance des deux safrans sur un voilier...). Ton sens de l'organisation et ton efficacité resteront pour moi un idéal, probablement jamais atteint. Malgré les hauts et les bas inévitables d'une thèse et les expériences qui ne marchent pas (c'est la vie !), tu as toujours fait preuve d'optimisme et de motivation pour la suite : je n'en retiendrai donc que le meilleur et je peux dès à présent dire que je fais partie de ces chanceux pour qui la thèse restera un bon souvenir, en large partie grâce à toi.

Je souhaiterais également remercier Florian d'Accrisio qui m'a formé lors de mon arrivée au LCMCP. Ta formation initiale était exactement ce qu'il fallait et le tout dans la bonne humeur. Tu m'as permis d'entrer très vite dans le monde fascinant des nanoparticules, malgré un bref contre-temps à base de KC_8 et de poubelle inflammable en début de parcours. Merci aussi à Léna Meyniel que j'ai encadrée en stage « Zoom » de mars à juillet 2020. Malgré les conditions plus qu'inhabituelles, tu as su rester motivée et travailler efficacement tout au long de ces mois. Partageant nos origines auvergnates, nous n'avons pu que bien nous entendre ! Bon vent pour la suite de ta thèse.

Merci aux instances qui ont rendu possible cette thèse : l'Europe pour le financement ERC Starting Grant « NanoFLP » (Grant N° 758480), le CNRS, mon employeur, et Sorbonne Université et l'Ecole Doctorale 397 « Physique et Chimie des Matériaux » pour l'accompagnement.

Merci aux membres du jury qui ont accepté de lire et juger mon travail de thèse : Dr. Elsje Alessandra Quadrelli de l'IRCELYON, Dr. Vincent Huc de l'ICMMO, Prof. Montserrat Gòmez du LHFA et Prof. Xavier Carrier du LRS.

Je voudrais remercier la direction du laboratoire, Florence Babonneau, Christian Bonhomme et François Ribot, ainsi que Corinne Chanéac pour l'animation de l'équipe Nano. Merci également à toute l'équipe administrative du LCMCP : Hélène Gervais,

Corinne Pozzo di Borgo, Diana Lesueur, Nora Abdoul-Aribi et Simon Dadoun. En plus de leur impressionnante efficacité au quotidien, leur bonne humeur et leur convivialité font du laboratoire un super lieu de travail. Un grand merci aussi à l'équipe technique avec Patrick Le Griel (MET, atelier), Isabelle Génois (MEB, XRF) et Mohamed Selmane (DRX) ainsi qu'à Capucine Sassoie pour son aide sur la cristallographie, David Portehault sur la diffraction électronique et François Ribot sur la RMN.

Une pensée particulière pour le bureau/labo du 5^{ème} avec qui j'ai travaillé tous les jours sur le projet NanoFLP : Antoine Pesesse, alias le leach king, Cyprien Poucin, Alexy Freitas, Alberto Palazzolo et Anthony Ropp. Je tiens toutefois à rappeler qu'à la course de qui aura activé le plus de CO₂ sur la durée du projet, mon chlorophytum est encore largement en tête ! Plus généralement, ce fut un plaisir de rencontrer tout le monde au LCMCP, de discuter sciences ou autres choses. Donc merci aux doctorants, notamment à la promo 2018-2021 (la meilleure bien évidemment), aux post-doctorants et aux permanents, présents ou passés.

Cette thèse a aussi été pour moi l'occasion d'enseigner, ce qui restera je pense pour longtemps une passion et dont j'espère pouvoir faire mon métier. Je voudrais donc remercier tous les enseignants concernés, le personnel de plate-forme et les étudiants qui n'ont fait que confirmer et développer mon intérêt.

J'ai eu la grande chance de pouvoir aller plusieurs fois réaliser des expériences sur différentes lignes de lumière du synchrotron SOLEIL où j'ai toujours eu bon accueil et je souhaiterais remercier Andrea Zitolo (SAMBA), Benedikt Lassalle-Kaiser (LUCIA), Jean-Jacques Gallet et Fabrice Bournel (TEMPO B) ainsi que Valérie Briois et Laurent Barthe (ROCK). Je dois également souligner toutes les contributions durant cette thèse : Laurent Delannoy du LRS et Helena Kaper du LSFC pour les tests catalytiques en phase gaz, Beatriz Roldan et ses collaborateurs du FHI pour les tests en électrocatalyse, Ovidiu Ersen, Corinne Ulhaq et Mounib Bahri de l'IPCMS pour les données HRTEM, Benoît Fleury de l'IPCM pour l'ATG-DSC et Antoine Miche du LRS pour l'XPS.

Pour finir sur une note plus personnelle, je souhaiterais remercier tous les amis que j'ai rencontrés ces dernières années. Merci à Vincent, alias Hervin, et à mes deux colocataires, Gaétan et Simon, qui m'ont stoïquement entendu me plaindre de mes expériences non reproductibles tout au long de cette thèse. Ce fut un plaisir de vous rencontrer et de partager votre quotidien. Enfin, surtout, je souhaiterais remercier de tout mon cœur ma famille et mes proches qui m'ont toujours encouragé dans mes choix et qui m'ont permis de devenir qui je suis aujourd'hui. J'en suis fier et c'est grâce à vous !

À ma famille,

Table of contents

Abstract.....	3
Remerciements	5
Table of contents.....	9
List of abbreviations	13
Résumé en Français.....	15
General introduction.....	27
<i>Chapter I – Literature review on metal-containing catalysts for hydrogenation in solvent</i>	31
1. Context of colloidal hydrogenation reactions.....	31
1.1. From conventional catalysts to catalysts with new compositions.....	31
1.1. Substrate molecules	32
1.2. Experimental setups for hydrogenation.....	35
2. Theoretical and experimental tools to study H₂ dissociation	37
2.1. Microscopic description	37
2.2. Experimental techniques for H ₂ activation characterization.....	45
2.2.1. Thermal technique.....	45
2.2.2. Vibrational spectroscopies	45
2.2.3. Direct probing of the hydrogen.....	47
2.2.3. Indirect probing <i>via</i> the metal center.....	47
2.2.4. Chemical reactivity.....	48
2.3. Reactions in solvent: where is the difference ?	48
2.3.1. Solubility of H ₂ in solvents	48
2.3.2. Reaction medium: impact on adsorption and solvation energies	51
3. Metal-containing catalysts for colloidal hydrogenation.....	52
3.1. Metal borides.....	53
3.2. Metal silicides.....	55

3.3. Metal phosphides.....	55
3.4. Metal carbides and nitrides	57
3.5. Metal oxides	60
3.6. Metal sulfides	63
4. Toward the “NanoFLP” system	66
4.1. Frustrated Lewis Pair catalysis	66
4.2. Boosting the surface reactivity of nanoparticles with ligands.....	68
4.3. Philosophy of work	70
5. Bibliography.....	71
Part 1: Solvent-free syntheses	81
<i>Chapter II – Solid-state metathesis of carbide and hydride nanoparticles</i>	<i>83</i>
1. Refractory compounds syntheses by solid-state metathesis	83
2. Solid-state metathesis and chemical trends with KC_8 and KC_4	85
2.1. Combustion reaction.....	85
2.2. Structural and morphological characterization.....	87
2.3. Determination of reaction temperature by thermodynamic considerations...	93
3. Study of the process parameters impact.....	99
4. Mechanism proposal.....	104
5. Reagent choice and potential products.....	111
6. Conclusion.....	115
7. Bibliography.....	116
<i>Chapter III – Catalysis with carbon-supported metal carbides</i>	<i>121</i>
1. Hydrogenation of butadiene	121
2. Liquid phase catalysis	125
2.1. Styrene dimerization.....	125
2.2. Phenylacetylene semi-hydrogenation	128
2.3. Conclusion on hydrogenation reactions in solvent.....	129
3. Bibliography.....	130

Part 2: Hydrothermal syntheses	133
<i>Chapter IV – Syntheses of defective cerium oxide nanoparticles for H₂ activation.....</i>	<i>135</i>
1. Tailored hydrothermal synthesis of defective cerium oxide catalyst.....	138
1.1. Cerium oxide nanorods	138
1.2. Toward Ce ^(III) rich cerium oxide and cerium hydroxide.....	141
2. Structural study of cerium hydroxide Ce(OH) ₃ aging.....	146
2.1. Structural characterization	146
2.2. Structural comparison with lanthanide hydroxides	157
2.3. Phase proposal	160
3. Post-synthesis treatments.....	162
3.1. Hydrothermal dehydration	162
3.2. Dry calcination in inert and reductive atmosphere	162
3.3. NAP-XPS: <i>in situ</i> measurements of thermal annealing.....	166
3.4. Summary of the syntheses and treatments of cerium-containing phases	170
4. Hydrogenation reactions by reduced cerium oxide.....	172
4.1. NAP-XPS of hydrogen activation by reduced cerium oxide in gas phase...	172
4.2. Liquid phase hydrogenation of styrene and phenylacetylene.....	175
4.3. Conclusion on the catalytic activity of cerium oxide.....	179
5. Bibliography.....	180
<i>Chapter V – Indium oxide catalysts for phenylacetylene hydrogenation</i>	<i>185</i>
1. Syntheses of indium oxide catalysts.....	186
1.1. Bismuth doped cubic indium oxide.....	186
1.2. Pristine and bismuth doped rhombohedral indium oxide.....	188
2. Hydrogenation reactions.....	191
3. Conclusion.....	193
4. Bibliography.....	194

Part 3: Solvothermal syntheses	195
<i>Chapter VI – Non-aqueous syntheses of molybdenum and tungsten oxides for hydrogenation reactions</i>	197
1. Non-aqueous metal oxide syntheses in high boiling point solvents.....	198
1.1. Tungsten oxide $W_{18}O_{49}$ nanowires.....	199
1.2. Molybdenum oxide nanoparticles.....	203
1.3. Conclusion on metal oxides syntheses.....	217
2. Hydrogenation reactions.....	218
3. Bibliography.....	220
<i>Chapter VII – Nickel-containing nanoparticles for hydrogenation in solvent</i>	223
1. Nickel carbide and phosphide syntheses.....	224
1.1. One-step nickel phosphide synthesis	224
1.2. Synthesis of nickel carbide Ni_3C and subsequent phosphidization.....	228
1.3. Carbide-free nickel(0) nanoparticle synthesis.....	239
2. Hydrogenation reactions.....	241
2.1. Nitrobenzene hydrogenation	241
2.2. Phenylacetylene hydrogenation.....	243
3. Conclusion.....	245
4. Bibliography.....	246
General conclusion and Perspectives.....	249
Appendix I – Experimental section.....	253
Appendix II – Thermodynamic calculations.....	261
Appendix III – Written and oral contributions	266

List of abbreviations

acac	Acetylacetonate
ac-b	Acetylene black
ATR	Attenuated Total Reflectance
BF	Bright Field
CUS	Coordinatively Unsaturated Site
DCM	Dichloromethane
DFT	Density Functional Theory
DMF	Dimethylformamide
DMSO	Dimethylsulfoxide
d.o.	Degree of Oxidation
DOS	Density Of States
DRIFTS	Diffuse Reflectance Infrared Fourier Transform Spectroscopy
EDX	Energy Dispersive X-Ray Spectroscopy
EELS	Electron Energy-Loss Spectroscopy
EXAFS	Extended X-Ray Fine Structure Spectroscopy
FAL	Furfuryl alcohol
FF	Furfural
FLP	Frustrated Lewis Pair
FTIR	Fourier Transform IR
GC-FID	Gas Chromatography – Flame Ionization Detector
GIC	Graphite Intercalation Compound
HAADF	High Angle Annular Dark Field
HCD	Heterolytic Cleavage of Hydrogen
5-HMF	5-hydroxymethylfurfural
HRTEM	High Resolution Transmission Electron Microscopy
HDC	Hydrodecarboxylation
HDN	Hydrodenitrogenation
HDO	Hydrodeoxygenation
HDS	Hydrodesulfurization
INS	Inelastic Neutron Scattering
IR	InfraRed spectroscopy
JCPDS	Joint Committee on Powder Diffraction Standards
MAS	Magic Angle Spinning
MCR-ALS	Multivariate Curve Resolution – Alternating Least Squares
2-MF	2-methylfuran
MOF	Metal-Organic Framework
MSSM	Modified Solid-State Metathesis

NAP-XPS	Near-Ambient Pressure XPS
NP	Nanoparticle
NMR	Nuclear Magnetic Resonance
OAc	Oleic acid
OAl	Oleyl alcohol
OAm	Oleylamine
ODE	1-octadecene
PXRD	Powder X-Ray Diffraction
r.t.	Room temperature
SAED	Selection Area Electron Diffraction
SAXS	Small Angle X-Ray Scattering
SEM	Scanning Electron Microscopy
SHS	Self-propagating High temperature Synthesis
SPO	Secondary Phosphine Oxide
SSM	Solid-State Metathesis
ss-NMR	Solid-state NMR
TEM	Transmission Electron Microscopy
THF	Tetrahydrofuran
TM	Transition Metal
TMC	Transition Metal Carbide
tmp	Tetramethylpiperidine
TOP	Trioctylphosphine
TPD	Temperature-Programmed Desorption
UHV	Ultra-High Vacuum
XANES	X-Ray Absorption Near Edge Spectroscopy
XAS	X-Ray Absorption Spectroscopy
XPS	X-Ray Photoelectron Spectroscopy
XRD	X-Ray Diffraction

Résumé en Français

Les réactions d'hydrogénation en catalyse colloïdale impliquent en général l'utilisation de métaux réduits tels que le nickel ou les platinoïdes (Re, Ru, Os, Rh, Ir, Pd, Pt). Bien que très efficaces, ces catalyseurs peuvent présenter différents inconvénients tels que l'utilisation d'éléments rares et coûteux, leur faible stabilité à l'air (caractère pyrophorique), une faible chimiosélectivité ou encore une résistance modérée à l'empoisonnement. Afin de contourner ces limites, nous nous sommes intéressés dans cette thèse à l'utilisation de nanoparticules de composés métalliques (carbures, oxydes, phosphures) pour l'hydrogénation en solvant de différentes molécules modèles telles que le phénylacétylène, le styrène ou le nitrobenzène.

L'activité catalytique des composés étudiés étant attendue comme plus faible que celle des métaux réduits, nous avons tenté de l'améliorer *via* l'ajout d'un co-catalyseur moléculaire. La stratégie poursuivie est inspirée du développement de la catalyse par les paires de Lewis frustrées (Frustrated Lewis Pairs, FLP), *i.e.* la rupture hétérolytique de liaisons chimiques par deux partenaires, un acide et une base de Lewis, tous deux encombrés stériquement (Figure 1A). Le concept, initialement développé en chimie moléculaire, a récemment été adapté en catalyse hétérogène où les deux sites actifs sont en surface d'un matériau, de type oxyde par exemple (CeO_2 , In_2O_3).¹ Nous tentons ici de réaliser une FLP colloïdale où l'un des deux partenaires est une nanoparticule inorganique (acide de Lewis) et l'autre un composé moléculaire (base de Lewis) (Figure 1B). Le choix du partenaire inorganique pour la catalyse a été réalisé suivant trois grands axes :

- des matériaux déjà connus pour leur activité catalytique en solvant, par exemple Mo_2C ou W_2C pour l'hydrogénation du furfural, et $\text{Ni}_2\text{P}/\text{Ni}_{12}\text{P}_5$ pour celle d'alcènes et de nitroarènes
- des matériaux dont le centre métallique est connu pour être un acide de Lewis, comme des oxydes de tungstène ($\text{W}_{18}\text{O}_{49}$) ou de molybdène (MoO_x)
- des matériaux dont l'activité catalytique tout solide de type FLP a déjà été démontrée, en phase gaz à haute température ($> 200\text{ }^\circ\text{C}$) pour In_2O_3 , et en solvant pour CeO_{2-x}

Dans tous les cas, l'activation de H_2 a été explorée en solvant à la fois en absence et en présence de co-catalyseurs de type bases de Lewis moléculaires, telles que la triphénylphosphine.

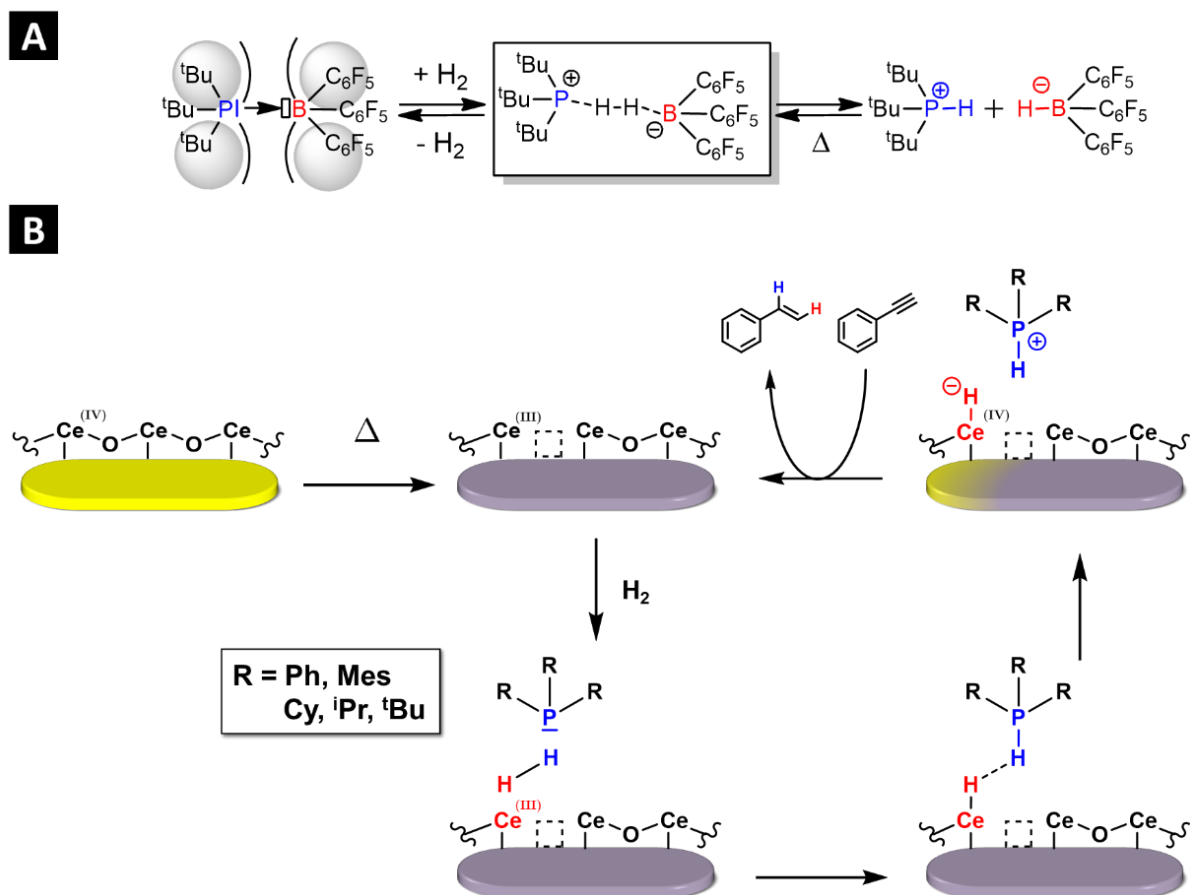


Figure 1. (A) Rupture hétérolytique d'une liaison H-H par FLP moléculaire.¹ (B) Illustration d'une catalyse hypothétique de type FLP entre un site acide de Lewis situé sur une nanoparticule de CeO_{2-x} et une base de Lewis encombrée, pour l'hydrogénation du phénylacétylène.

Dans la première partie de cette thèse, nous avons ciblé la synthèse de nanoparticules de carbures métalliques des groupes IV (Zr, Hf), V (Nb, Ta) et VI (Mo, W) pour l'hydrogénation d'oléfines. Les matériaux ont été obtenus par métathèse solide-solide entre un chlorure métallique (MCl_x) et du potassium, soit inséré dans du graphite (KC_8), soit dispersé dans de l'acétylène black (KC_4) (Chapitre II).^{2,3} Les deux poudres sont mélangées sous atmosphère inerte et réagissent spontanément pour former des nanoparticules de $\text{M}(0)$ et $\text{MC}/\text{M}_2\text{C}$ supportées sur carbone, et de la sylvite (KCl) comme coproduit (Figure 2). La poudre est alors lavée pour retirer le chlorure de potassium. Cette voie de synthèse sans solvant présente des avantages à la fois sur le plan de la nature des objets produits pour la catalyse (pas de ligands de surface, nanoparticules à haute surface spécifique et finement dispersées) et sur le plan de la synthèse elle-même si l'on se réfère aux critères de la chimie verte (pas de solvant, pas de chauffage extérieur, déchets non toxiques). Nous avons pu estimer la température de réaction lors de la combustion par des considérations thermodynamiques. L'énergie libérée est calculée *via* la formule de

Hess à partir des enthalpies de formation des réactifs et des produits, et la capacité calorifique du milieu est fixée principalement par la sylvite et le graphite. Une température théorique, dite adiabatique, peut ainsi être déduite : la réaction la plus exothermique avec WCl_6 est limitée par l'évaporation de KCl à 1500 °C et la moins exothermique avec ZrCl_4 se produit à environ 1000 °C.

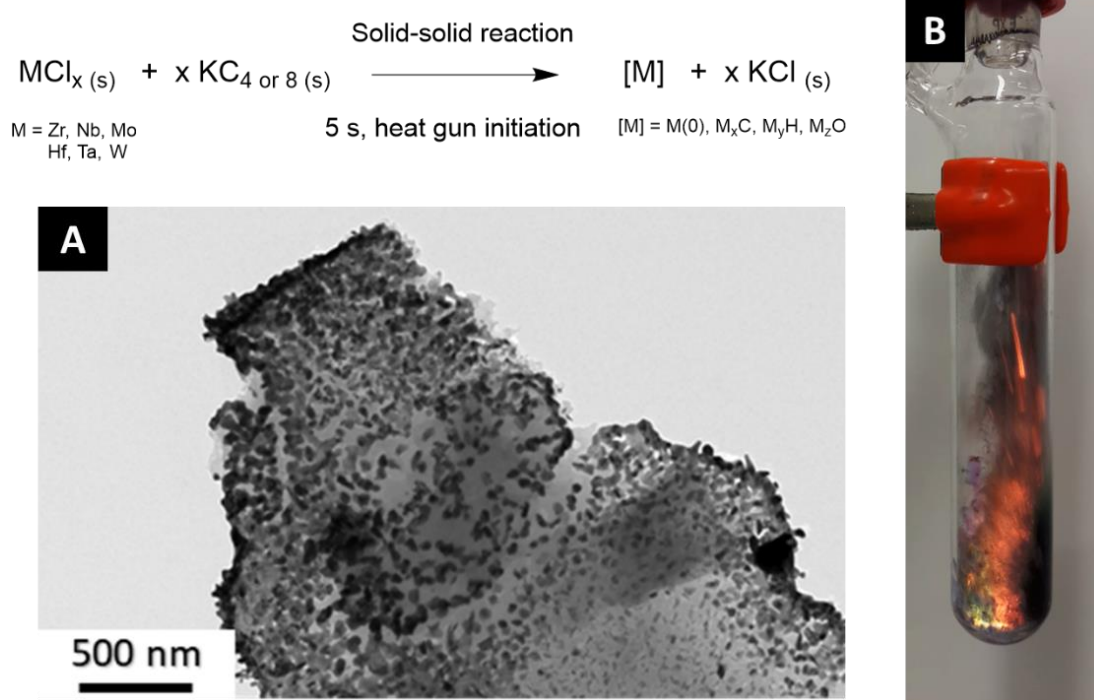


Figure 2. (A) Image MET d'un échantillon de Mo_2C supporté sur graphite par métathèse solide-solide entre 5 KC_8 et MoCl_5 . (B) Photo de la réaction lors de la combustion.

La spéciation de phase en fonction de divers paramètres de réaction (support carbone, granulométrie des précurseurs, phase gaz, échelle) a été étudiée par DRX : le point le plus remarquable est l'augmentation de la proportion de carbures vis-à-vis du métal lorsque la température de réaction augmente. De plus, nous avons découvert par sérendipité l'obtention possible d'hydrures métalliques pour les métaux du groupe IV (ZrH_2 et $\text{HfH}_{1.7}$) et V ($\text{NbH}_{0.8}$ et Ta_2H) pour les réactions conduites dans le vide. Des études complémentaires sur la morphologie des nanoparticules par HRTEM et sur la composition du matériau avant neutralisation nous ont permis de proposer un mécanisme en plusieurs étapes (Figure 3). Des nanoparticules métalliques sont d'abord formées et carburées *in situ* du fait des hautes températures puis les surfaces métalliques non carburées réagissent au contact des solvants de lavage (eau et éthanol) pour former des hydrures. Enfin, nous avons montré par XPS que la surface du matériau est oxydée au contact de l'air.

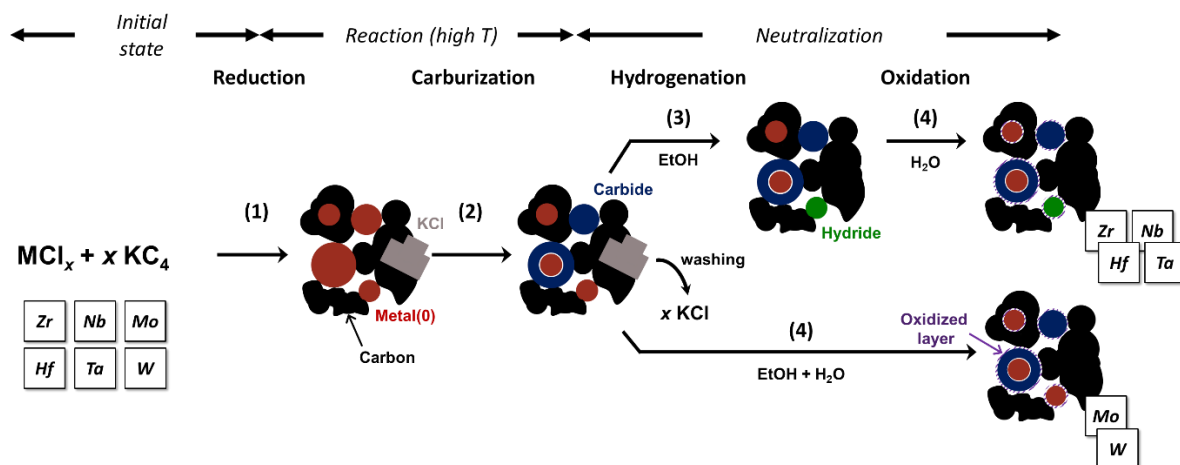


Figure 3. Proposition de mécanisme pour la formation de nanoparticules métalliques, de carbures et d'hydrures. Haut : éléments susceptibles de former des hydrures. Bas : éléments ne formant pas d'hydrures.

Parmi les matériaux synthétisés dans le Chapitre II, les carbures de molybdène et de tungstène Mo_2C/C et W_2C/C sont les catalyseurs les plus prometteurs vis-à-vis de l'activation de H_2 si l'on considère les travaux de Boudart sur l'hydrogénation en phase gaz ou la littérature sur le furfural (Chapitre III).⁴ Des résultats préliminaires ont démontré que Mo_2C /graphite est actif pour l'hydrogénation du butadiène en butène en phase gaz à partir de 120 °C. Lors de la première rampe de chauffe, il est apparu que l'activité était anormalement élevée aux alentours de 100 °C, supposément à cause d'une élévation locale de la température due à la réduction d'une couche d'oxyde. Les carbures W_2C /acetylene black et Mo_2C /graphite ont également été étudiés respectivement pour l'hydrogénation en solvant du styrène et du phénylacétylène. Dans le premier cas, le produit majoritaire de la réaction consiste en un dimère, le (E)-1,3-diphenyl-1-butene, présumément obtenu par catalyse acide avec des traces de H^+ sur le graphite, mais la formation d'éthylbenzène n'a pas été détectée. Dans le deuxième cas, la réaction menée à 100 °C sous 7, 15 et 30 bar de H_2 n'a mené qu'à la formation de traces de styrène.

Dans la deuxième partie de cette thèse, nous avons produit par voie hydrothermale des nanoparticules d'oxyde de cérium (CeO_{2-x}) (Chapitre IV) et d'indium (In_2O_3) (Chapitre V) pour l'activation de H_2 . Dans le Chapitre IV, nous avons voulu reproduire dans un premier temps le matériau utilisé par Qu *et al.* pour l'hydrogénation en solvant d'alcènes et d'alcynes comme point de départ de notre étude.⁵ Les auteurs reportent une synthèse en deux étapes d'un oxyde de cérium riche en défauts, assurant donc une proportion importante de $Ce^{(III)}$ en surface. Une fois les conditions de synthèse optimisées, nous avons été en mesure de reproduire un

matériau semblable à celui reporté par Qu *et al.* (Figure 4). Il est toutefois apparu que l'attribution des phases en DRX proposée par les auteurs de l'étude n'est pas cohérente : après une semaine à l'air à température ambiante, le matériau initial, $\text{Ce}(\text{OH})_3$, a jauni et le diffractogramme a évolué vers une phase non reportée dans les bases de données et non mentionnée dans la littérature. Nous avons caractérisé le matériau par différentes techniques (DRX, XAS, XPS et IR) et ainsi démontré l'oxydation de $\text{Ce}^{(\text{III})}$ en $\text{Ce}^{(\text{IV})}$ malgré l'absence de formation de CeO_2 . Cette évolution du matériau diverge des travaux reportés de la littérature.

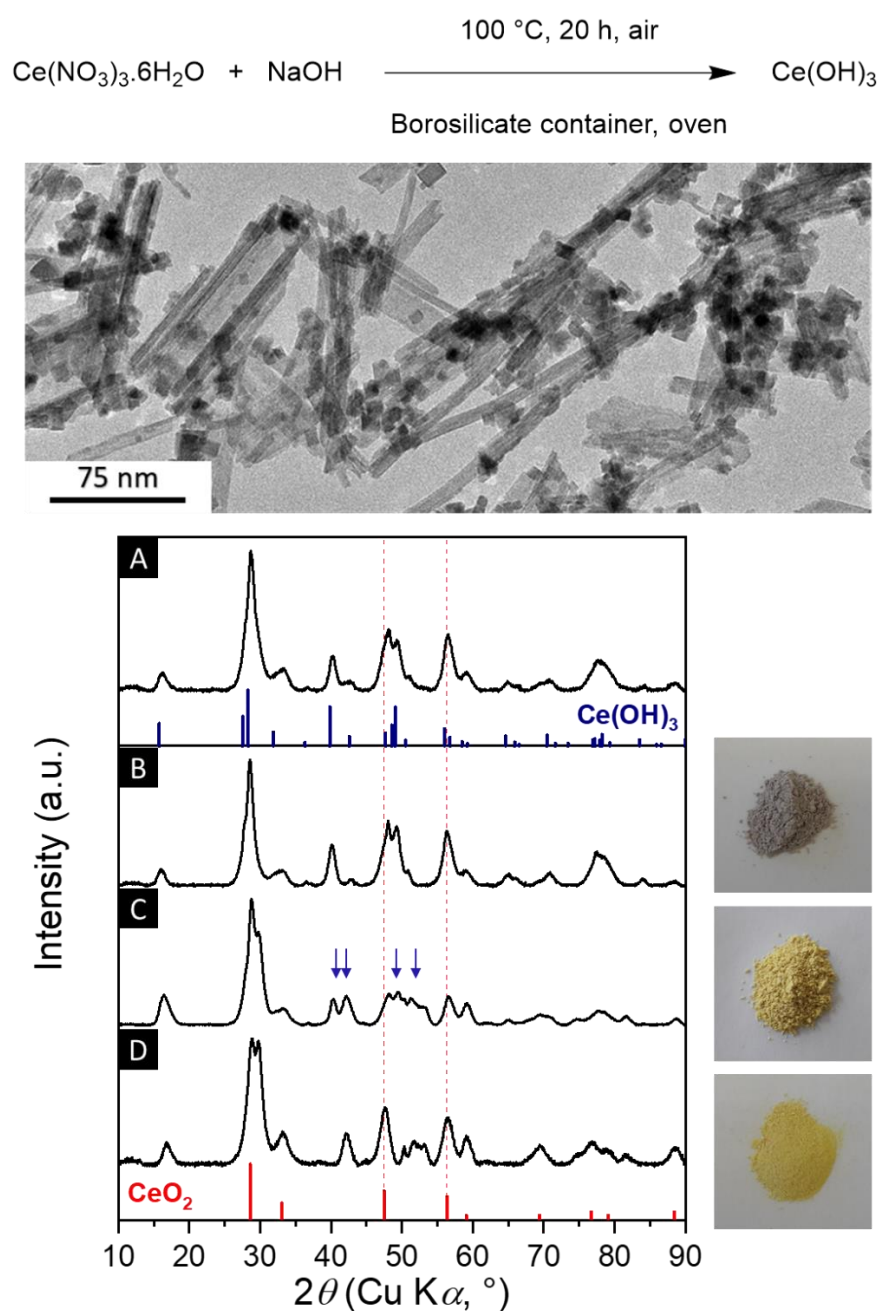


Figure 4. Synthèse de trihydroxyde de cérium et d'oxyde de cérium par voie hydrothermale (avec cliché MET). Diffractogrammes RX de (A) $\text{Ce}(\text{OH})_3$ deux heures après synthèse, (B)

Ce(OH)₃ stocké sous Ar pendant quatre jours, (C) Ce(OH)₃ stocké à l'air pendant un jour, (D) Ce(OH)₃ stocké à l'air pendant quatre jours. Les flèches bleus soulignent la présence simultanée de deux phases : Ce(OH)₃ et Ce(OH)₃ « vieilli ».

Dans un second temps, nous avons soumis les matériaux préalablement synthétisés, CeO₂ et Ce(OH)₃ vieilli, à une étape de calcination sous Ar à 200 °C afin d'augmenter le nombre de défauts d'oxygène en surface du matériau et ainsi générer des sites réactifs Ce^(III). Pour les nanobâtonnets de CeO₂, une étude XPS sur la région Ce 3d a démontré une augmentation du ratio de Ce^(III) de surface de 30 % à 50 %. Nous avons enfin pu montrer par XPS que l'addition de H₂, même à très basse pression (0.14 mbar), sur CeO_{2-x} est responsable d'une oxydation des sites Ce^(III) de surface (le ratio de Ce^(III) en surface passe de 75 % à 50 %), interprétée comme la formation d'hydruure de surface sur les lacunes d'oxygène (Figure 5).⁶ Les différents catalyseurs à base d'oxyde de cérium, éventuellement calcinés sous Ar, ont enfin été étudiés pour la semi-hydrogénation du phénylacétylène en styrène à 100 °C sous 7 bar de H₂ dans le toluène. Des rendements de l'ordre de 5-15 % ont été obtenus mais la large barre d'erreur ne permet pas de conclure quant à l'impact de l'addition de PPh₃.

Dans le chapitre V, deux catalyseurs à base d'indium ont été synthétisés par voie hydrothermale à 100 °C depuis des précurseurs de sels de nitrates d'indium. Suivant les travaux d'Ozin *et al.*, le dopage à 1 % de la phase cubique In₂O₃ par des atomes de bismuth a été réalisée.⁷ Le catalyseur c-Bi_{0.02}In₂O₃ a été étudié pour l'hydrogénation du phénylacétylène sous 7 bar de H₂ à 100 °C, 150 °C et 200 °C. Une faible activité catalytique a été détectée (rendement inférieur à 10 %) pour les températures supérieures à 100 °C ainsi que la formation d'acétophénone. L'ajout de triphénylphosphine n'a pas eu d'effet déterminant sur le produit de la catalyse. Le deuxième catalyseur, In₂O₃ rhomboédrique, n'a pas encore été étudié en catalyse.

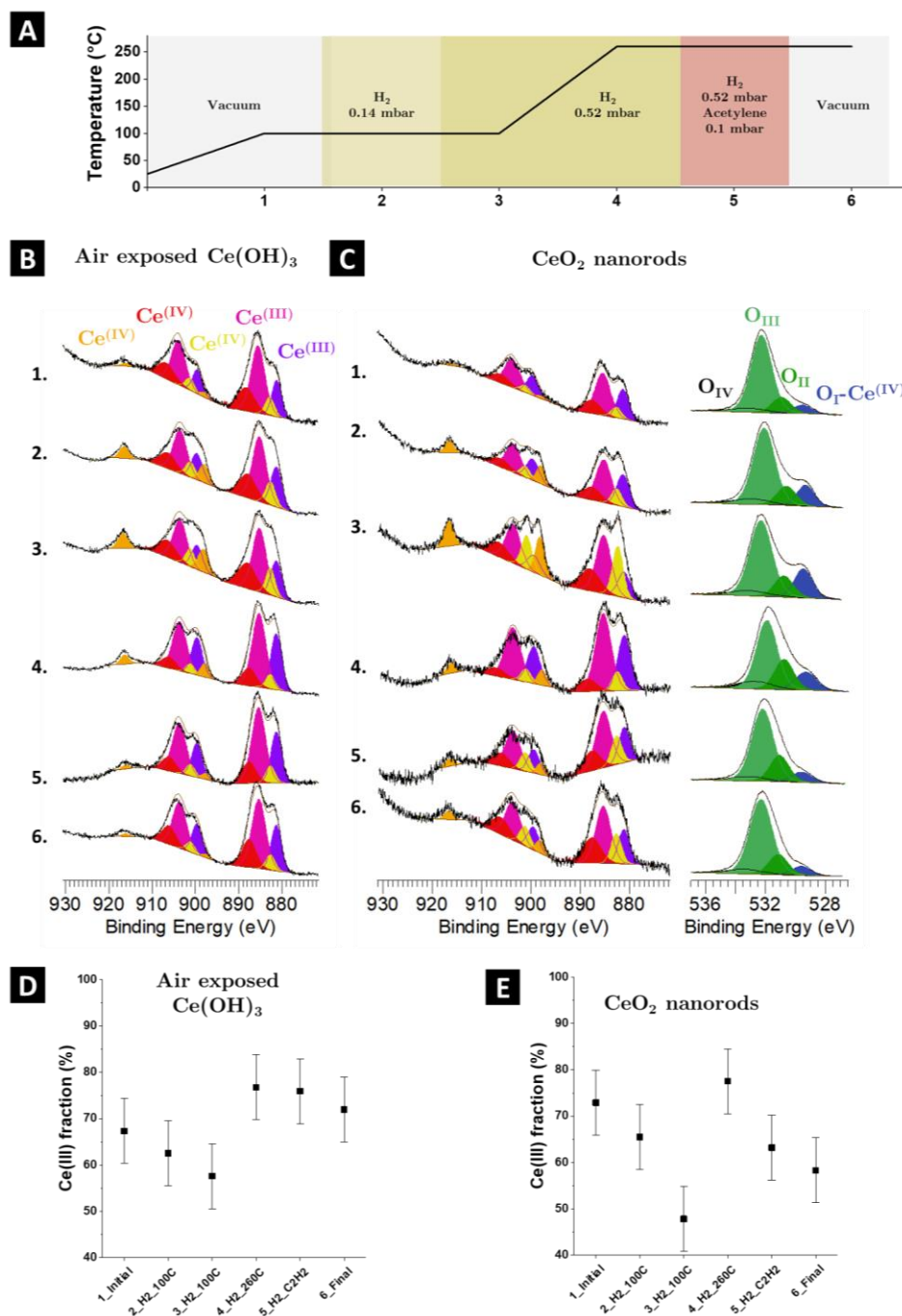


Figure 5. (A) Traitement température + gaz appliquée aux catalyseurs dans l'enceinte de l'appareil de NAP-XPS. (B,C) NAP-XPS de la région Ce 3d et O 1s pour les catalyseurs d'oxyde de cérium et (D,E) évolution du ratio Ce^(III)/Ce^(IV) en surface des catalyseurs.

La dernière partie de cette thèse est dédiée aux synthèses conduites dans des solvants à haute température d'ébullition tels que l'oleylamine (OAm), l'alcool oléique (OAl) ou l'acide oléique (OAc). Dans le chapitre VI, la synthèse de nanofils d'oxyde de tungstène, W₁₈O₄₉, a été adaptée du travail de Leite *et al.*⁸ et celle d'oxydes de molybdène du travail de Tatsuma *et al.*⁹ Pour la première, la réaction a

été reproduite avec succès après purification du précurseur, WCl_6 , qui contenait des traces de $\text{W}(0)$. Pour les secondes, la décomposition thermique de $\text{MoO}_2(\text{acac})_2$ dans l'oleylamine a conduit à une poudre dont l'analyse par diffraction RX n'est pas informative sur la composition chimique du matériau (Figure 6). L'analyse par microscopie électronique en transmission révèle la présence de nanoparticules de diamètre inférieur à 5 nm. Une synthèse similaire a été réalisée dans l'acide oléique. Aucune poudre n'a pu être isolée du fait de l'excellente stabilité colloïdale de la suspension. Les différents oxydes de molybdène synthétisés ont été étudiés en spectroscopie d'absorption X (XAS) afin de déterminer d'une part le degré d'oxydation (d.o.) et l'environnement chimique du molybdène, et d'autre part afin d'étudier le mécanisme de formation des nanoparticules. La synthèse dans l'oleylamine conduit à un d.o. compris entre +IV et +VI mais le produit ne semble pas être un mélange de MoO_2 et MoO_3 , ce qui indiquerait la présence d'oxydes intermédiaires. La réaction dans l'acide oléique conduit à un matériau dont le spectre XAS est très proche de celui de MoO_2 . Les nanofils d'oxyde de tungstène déficitaires en oxygène, $\text{W}_{18}\text{O}_{49}$, et les nanoparticules d'oxydes de molybdène produites dans l'oleylamine ont été utilisées pour l'hydrogénation en phase liquide du nitrobenzène et du phénylacétylène en conditions relativement dures (150 °C, 30 bar H_2). Aucune conversion n'a été obtenue pour le nitrobenzène et un rendement en styrène de 13 % et 26 % a été respectivement obtenu pour MoO_x et $\text{W}_{18}\text{O}_{49}$.

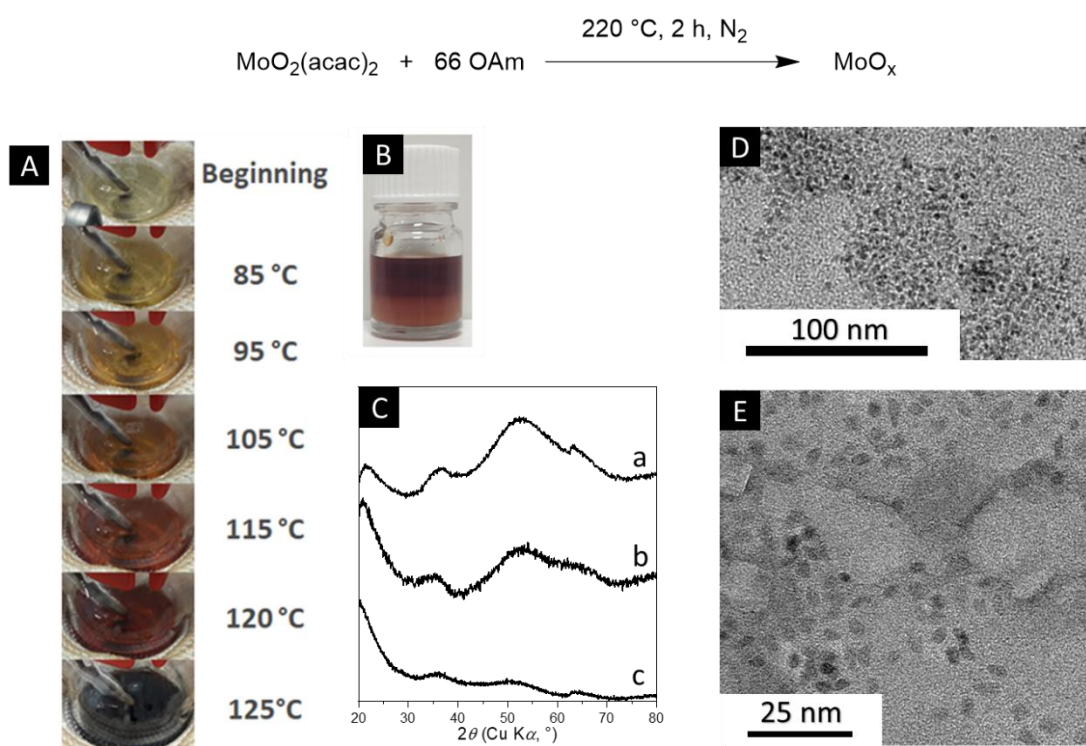


Figure 6. Synthèse de MoO_x par décomposition thermique de $\text{MoO}_2(\text{acac})_2$ dans l'oleylamine. (A) Evolution de la couleur de la suspension et (B) état final. (C) Diffractogramme RX des

produits de synthèse (a : DAM comme solvant, b,c : OAm). (D-E) Images MET des nanoparticules synthétisées dans l'oleylamine.

Dans le chapitre VII, la synthèse des nanoparticules de carbures et phosphures de nickel est adaptée du travail de Tracy *et al.*¹⁰ Elle consiste en une décomposition thermique de $\text{Ni}(\text{acac})_2$ à 250 °C pendant 2 h dans un mélange oleylamine/1-octadecène pour former des nanoparticules de carbure de nickel. Dans une deuxième étape et sans isolation préalable des nanoparticules, l'ajout d'un agent phosphurant, la trioctylphosphine (TOP), permet la phosphuration des nanoparticules à 300 °C en 30 min. La quantité de TOP ajoutée ainsi que la température d'injection mènent à différentes phases : Ni_2P ou Ni_{12}P_5 . Une famille de nanoparticules de compositions différentes (Ni_3C , Ni_2P et Ni_{12}P_5) mais de tailles similaires a ainsi été obtenue pour comparaison de leurs activités catalytiques. L'étude comparative a été initiée avec le carbure de nickel (Ni_3C) pour l'hydrogénation du nitrobenzène en aniline et du phénylacétylène en éthylbenzène dans différents solvants (Figure 7). Une hydrogénation quantitative a pu être obtenue à respectivement 60 °C et 100 °C dans l'éthanol, ce qui constitue la première mention de Ni_3C comme catalyseur « colloïdal » pour l'activation de H_2 .

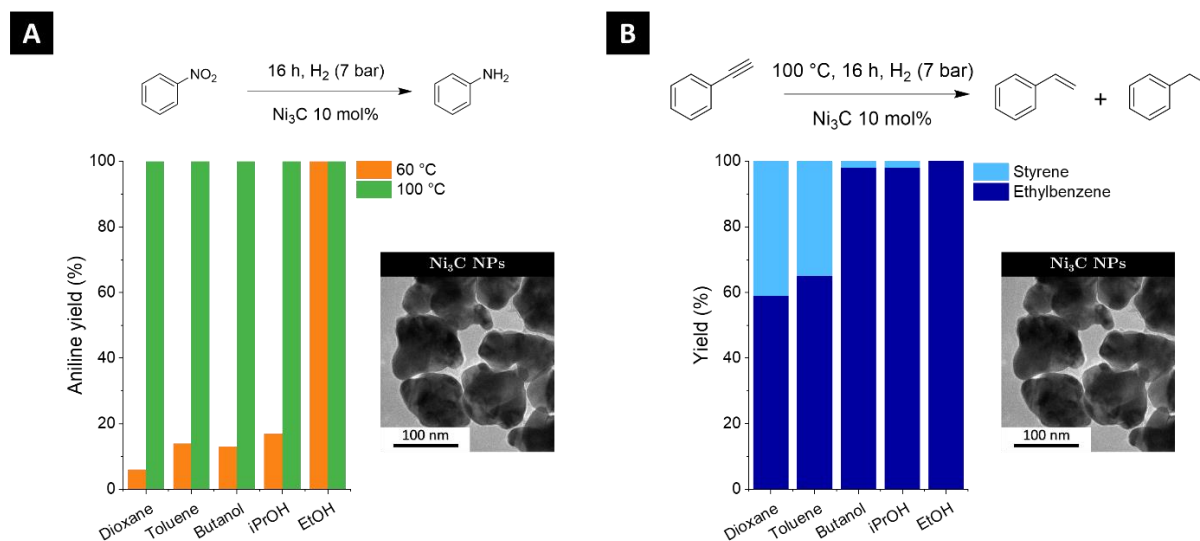


Figure 7. Hydrogénation (A) du nitrobenzène et (B) du phénylacétylène en présence de nanoparticules de Ni_3C dans différents solvants. Conversions déterminées par RMN.

En conclusion, nous avons synthétisé des nanoparticules appartenant à différentes familles (carbures, oxydes et phosphures) et selon différentes voies de synthèse (métathèse solide, hydrothermale, solvothermale) avec d'éventuels traitements post-synthèse (calcination). Les matériaux obtenus présentent donc une

diversité de phase mais également d'états de surface. Lors des tests catalytiques pour l'hydrogénation du phénylacétylène, CeO_2 est apparu comme actif à 100 °C sous 7 bar de H_2 bien qu'il soit encore difficile de trancher quant à l'effet de l'addition d'une phosphine. Le nitrobenzène et le phénylacétylène ont également pu être hydrogénés en présence de Ni_3C dans des conditions douces, respectivement 60 °C et 100 °C sous 7 bar de H_2 . Différentes perspectives sont envisagées : d'une part l'utilisation de conditions plus dures pour l'hydrogénation avec $\text{Mo}_2\text{C}/\text{C}$, $\text{W}_2\text{C}/\text{C}$, CeO_2 et In_2O_3 afin de pouvoir détecter une potentielle amélioration de la réactivité en présence de phosphine, d'autre part l'étude comparative du carbure Ni_3C et des phosphures Ni_2P et Ni_{12}P_5 pour l'activation de H_2 , éventuellement avec ajout d'une phosphine. Enfin, l'étude plus rationalisée du mécanisme de formation d'oxydes de Mo par décomposition thermique de $\text{MoO}_2(\text{acac})_2$ dans l'oleylamine ou l'acide oléique.

Références

1. Ma, Y. *et al.* Semi-solid and solid frustrated Lewis pair catalysts. *Chem. Soc. Rev.* **47**, 5541–5553 (2018).
2. Ressnig, D. *et al.* An expeditious synthesis of early transition metal carbide nanoparticles on graphitic carbons. *Chem. Commun.* **52**, 9546–9549 (2016).
3. Nartowski, A. M., Parkin, I. P., Craven, A. J. & MacKenzie, M. Rapid, Solid-State Metathesis Routes to Metal Carbides. *Adv. Mater.* **10**, 805–808 (1998).
4. Levy, R. B. & Boudart, M. Platinum-Like Behavior of Tungsten Carbide in Surface Catalysis. *Science*. **181**, 547–549 (1973).
5. Zhang, S. *et al.* Solid frustrated-Lewis-pair catalysts constructed by regulations on surface defects of porous nanorods of CeO_2 . *Nat. Commun.* **8**, 1–11 (2017).
6. Li, Z. *et al.* Oxidation of Reduced Ceria by Incorporation of Hydrogen. *Angew. Chemie Int. Ed.* **58**, 14686–14693 (2019).
7. Yan, T. *et al.* Bismuth atom tailoring of indium oxide surface frustrated Lewis pairs boosts heterogeneous CO_2 photocatalytic hydrogenation. *Nat. Commun.* **11**, 6095 (2020).
8. Gonçalves, R. H., Leite, L. D. T. & Leite, E. R. Colloidal WO_3 nanowires as a versatile route to prepare a photoanode for solar water splitting. *ChemSusChem* **5**, 2341–2347 (2012).
9. Lee, S. H., Nishi, H. & Tatsuma, T. Tunable plasmon resonance of molybdenum oxide nanoparticles synthesized in non-aqueous media. *Chem.*

- Commun.* **53**, 12680–12683 (2017).
10. Sarac, M. F., Wu, W. & Tracy, J. B. Control of Branching in $\text{Ni}_3\text{C}_{1-x}$ Nanoparticles and Their Conversion into Ni_{12}P_5 Nanoparticles. *Chem. Mater.* **26**, 3057–3064 (2014).

General introduction

Environmental issues have become of paramount importance for chemists during these past decades. They obviously include the limitation of the release of carbon dioxide and other greenhouse gases in the atmosphere. The global challenge of climate change should however not totally overshadow other critical points, such as materials scarcity (Figure 1) or anthropogenic pollution with metals in environment, due for instance to the mining activity or the waste disposal. These last points have a particular resonance for the inorganic chemistry community: a large number of catalytic processes in industrial chemistry indeed rely on the use of metal-containing catalysts. As catalysis is considered as one of the twelve principles of Green Chemistry, its use will undoubtedly increase in future. Its applications cover industrially relevant fields as vast as ammonia production *via* the Haber-Bosch process, polymerization reactions with the Ziegler-Natta process, fuels synthesis *via* the Fischer-Tropsch process or petroleum refinery through cracking on zeolites. More recently, environmental standards in auto industry have lowered the limit concentrations of NO_x, CO and hydrocarbons in exhaust emissions, increasing the use of platinum and rhodium in catalytic converters which now represents respectively 50 % and 80 % of their global productions.

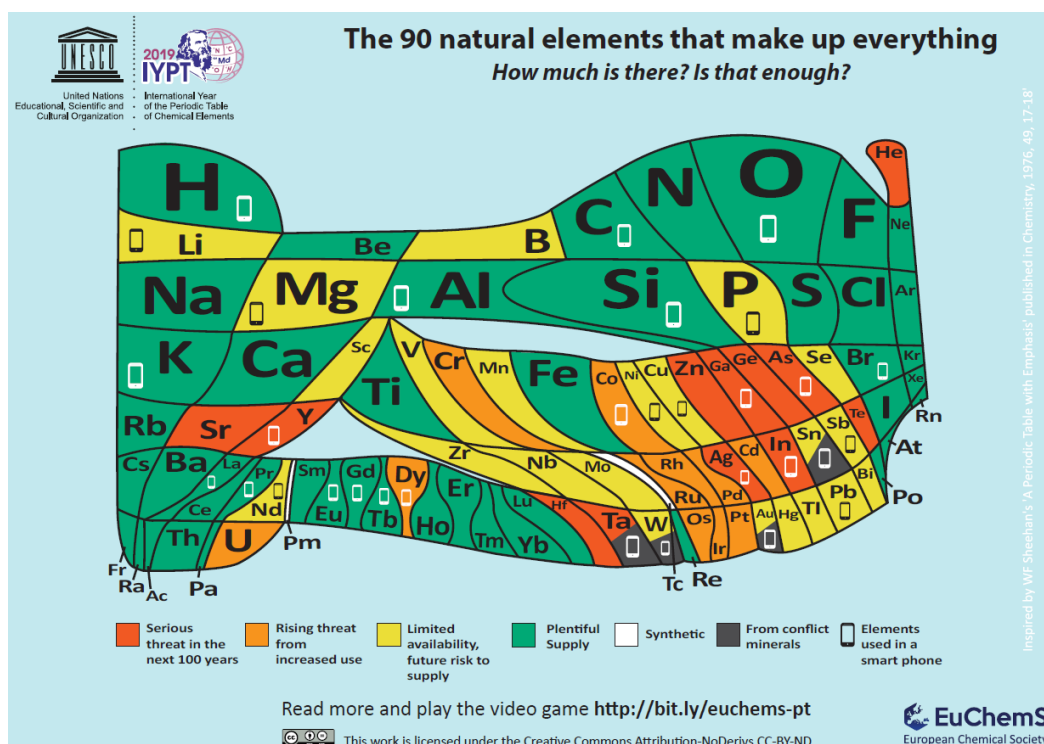


Figure 1. The periodic table of the element scarcity. The areas of the cases relate to the abundance of the atoms of each element on a logarithmic scale.

One particular example of industrial relevant catalyzed reaction is the hydrogenation: from petroleum refinery to biomass transformation and from fat hydrogenation to fine chemical syntheses, H_2 activation is crucial for several fields of the chemical industry. These hydrogenation reactions are generally catalyzed by either nickel, the undeniable star of the catalytic reduction, or platinoid elements (Ru, Os, Rh, Ir, Pd, Pt). Despite their high efficiency, the scarcity of these last ones makes them very demanded and expensive, with prices exceeding that of gold. Furthermore, their extraction may be subject of international tensions in the future considering 91 % of the known stocks worldwide are currently held by a single country, South Africa. There is currently a demand for more adaptable and sustainable catalysts. Adaptable first because the nature of the raw feedstocks in chemical industry will be more and more diverse, complex and non-stable in composition with the growing importance of the biomass and wastes in raw supplies. Sustainable then because the demand for the rarest of the chemical elements will be higher and higher with the increase and diversification of their uses: larger demand for chemicals and therefore for catalysts, stricter environmental standards requiring depollution modules and concurrence with new technologies (electronics, batteries, alternative energies). I believe catalysts choice will be less and less guided by the optimal performance but rather by a delicate balance between the performance and the environmental impact and cost of the catalyst production.

“Research and Development” departments in industry have the necessary striking force to screen and optimize the catalysts for all the relevant reactions. Nonetheless, the design of new concepts and the development of rational tools to study catalytic mechanisms still belong to the domain of academic research to my opinion. This is the reason why I believe our role, as academic researchers, is to lead this exploration for new active compounds and catalytic systems, with a particular focus on the materials which are still only accessible in laboratories. The boom of the “nano” research these past decades has permitted the synthesis of a large variety of metal-containing nanoparticles such as borides, carbides, nitrides and phosphides, not yet fully explored as to their catalytic potential. Besides, our understanding of the reaction mechanism at the surface of the catalyst and the progresses in materials science allow us to better design the surfaces of the materials, in particular as to the exposed facets, the defects or the presence of doping elements.

The strategy of the present work is to synthesize a variety of nanoparticles of various compositions (carbides, oxides, phosphides) to test their catalytic activity toward hydrogenation in solvent. We then envision a boost of their activity through the addition of a molecular co-catalyst which will help the heterolytic cleavage of the H_2 molecule. The concept is inspired from the recent development of the Frustrated Lewis Pair (FLP) chemistry, and adapted to inorganic surfaces: the H_2 molecule is located between a Lewis acid center and a Lewis basic center which are too sterically

hindered to form a Lewis adduct. The H–H bond is thus weakened and more easily cleaved in a hydride and a proton. A more in-depth description and analysis of the associated stakes will be done in first chapter. Our main objective in this thesis is not to build an efficient catalytic system that would be able to compete with the ones currently used in industry, but rather determine whether such a catalytic concept in colloidal chemistry is possible and determine what would be the critical parameters.

In **chapter I**, we first briefly reviewed the key concepts behind H₂ activation on metal-containing nanoparticles and we aggregated the main results obtained these past years in colloidal hydrogenation with non-purely metallic catalysts. The experimental part of this PhD thesis is then divided in six chapters grouped in three parts. Each part corresponds to one type of materials synthesis: solid-state syntheses for Part 1 (Chapter II and III), hydrothermal syntheses for Part 2 (Chapter IV and V) and solvothermal syntheses in high-boiling point solvents for Part 3 (Chapter VI and VII). We considered this division of the work as the most meaningful both for the materials syntheses and the catalytic aspect. The concepts used for rationalizing the catalyst syntheses indeed differ depending on the reaction medium. Besides, the state of the materials surface, crucial for catalysis, is highly dependent on the chosen pathway: few ligands are expected for solvent-free syntheses whereas surface hydroxyls and organic ligands are present for respectively hydrothermal and solvothermal reactions. We developed in **chapter II** a solvent-free synthesis of nanocarbides and nanohydrides of early transition metals by solid-state metathesis between metal chlorides and potassium graphite. Molybdenum and tungsten carbides previously synthesized were studied for hydrogenation of alkenes in gas and liquid phases in **chapter III**. We explored in **chapter IV** the syntheses of cerium hydroxide and oxide in aqueous solution. An unreported cerium hydroxide phase was obtained and characterized in depth. Different thermal treatments in view of the catalytic applications were studied. Reduced cerium oxide (CeO₂) was then explored for H₂ activation in the gas phase, and for semi-hydrogenation of phenylacetylene in solvent. We pursued in **chapter V** with the syntheses of indium oxide and bismuth-doped indium oxide in aqueous solution. Catalytic tests were also performed for semi-hydrogenation of phenylacetylene in solvent. The **chapter VI** deals with the syntheses of metal oxides (MoO_x and W₁₈O₄₉) in high-boiling point solvents (oleylamine, oleic acid and oleyl alcohol). In the case of the molybdenum oxide synthesis, an *in situ* X-Ray Absorption Spectroscopy (XAS) study was conducted to better understand the nature of the objects. Preliminary catalytic tests for hydrogenation of phenylacetylene and nitrobenzene were performed in solvent. We finally studied in **chapter VII** the syntheses of nickel carbide and phosphides nanoparticles in high-boiling point solvents (oleylamine, 1-octadecene, octyl ether and trioctylphosphine). The catalytic activity of Ni₃C was characterized for nitrobenzene and phenylacetylene hydrogenation in different solvents.

We adopted an exploratory approach to develop materials for hydrogenation reactions. Preliminary catalytic trials were therefore performed during the catalyst synthesis development and guided some of our synthetic choices. Most of the experimental work focused on the catalyst syntheses, this choice can be explained by three factors. First, the three-phase heterogeneous catalysis was a new competence in the laboratory and the experimental setup had to be installed in the course of the PhD, thereby postponing the first catalysis experiments. Then, we found by serendipity intriguing results during the catalysts development (unexpected phases for solid-state metathesis in Chapter II and unreported cerium-containing phase in Chapter IV) and we chose to study them more in-depth. Finally, as the experimental time was limited due to the exceptional situation in 2020 and 2021, we chose to favor the topics more susceptible to be ended in the course of the PhD, *i.e.* the materials syntheses. The choice of study of some metals or systems rather than others was also led by the opportunity to access synchrotron facilities, which allowed us to perform experiments not initially planned, though of high interest. This in particular justifies the Near Ambient Pressure X-Ray Photoelectron Spectroscopy (NAP-XPS) study of cerium oxide (Chapter IV) and the *in situ* XAS study of the solvothermal synthesis of molybdenum oxides (Chapter VI).

Chapter I

Literature review on metal-containing catalysts for hydrogenation in solvent

This chapter is built as a tutorial to understand what are the key concepts in colloidal hydrogenation reactions. It is structured as follows: we first briefly discuss the context of hydrogenation reactions with a focus on the limitations of purely metallic materials, the range of relevant substrates and the classical setups used in academic works. In the second part, we present the different reported mechanisms for H_2 activation on inorganic surfaces (heterolytic *versus* homolytic dissociation) as well as the characterization techniques (TPD, IR, INS, NMR, XPS) used to evidence the H_2 splitting. Third, we report a number of representative works on the use of metal-containing nanoparticles for liquid-phase hydrogenations. We finally explain our work philosophy as to the development of a colloidal catalysis based on the Frustrated Lewis Pair (FLP) chemistry.

I.1. Context of colloidal hydrogenation reactions

In the context of hydrogenation reactions, heterogeneous catalysis is often understood as a reaction where the substrate is in the gas phase while the catalyst is in the solid phase. For reactions performed in a solvent (or, more precisely, in a dispersion) with dispersed particles of catalyst, one can encounter the terms “liquid phase heterogeneous catalysis”, “three-phase hydrogenation catalysis” or “colloidal catalysis”. In these situations, the substrate is soluble in the solvent and the catalyst is a solid, highly dispersed or in suspension.¹

I.1.1 From conventional catalysts to catalysts with new compositions

Typical catalysts for hydrogenation reactions are finely divided late transition metals such as Ru, Os (Group VIII), Rh, Ir (Group IX) or Ni, Pd, Pt (Group X).^{1,2} These catalysts can be used as stand-alone particles, *i.e.* non supported colloids, or, more often, supported on a polymer or an inorganic nanostructured material (activated charcoal, graphite, zeolite, Al_2O_3 , SiO_2 , TiO_2). The support acts both as a catalyst modifier by exacerbating the activity or controlling the selectivity and as an aid to recover it after reaction. These metal catalysts are particularly efficient which renders challenging the selective or partial hydrogenation often required in fine chemistry.¹ For instance, Pd has to be deactivated by supporting it on $CaCO_3$ or $BaSO_4$ and treating it with $Pb(OAc)_2$ or PbO (Lindlar[®] catalyst) to avoid the total hydrogenation of

alkynes in alkanes.³ Besides, the high surface area and reactivity of finely divided Ni and Pd catalysts, commonly used in industry and academic works, make them pyrophoric and therefore difficult to handle on large scales. The scarcity of the rarest of these metals, the platinoids (Ru, Os, Rh, Ir, Pd, Pt), coupled with a growing demand, makes them more and more expensive and objects of international tensions. For instance, South Africa alone concentrates 91 % of their known stocks.⁴ More abundant metals, generally early transition or first row metals (Mn, Fe, Co, Ni, Cu), should therefore be envisioned as lower-cost alternatives, in a strategy of diversification of catalysts.⁵

The limited resistance of the previously mentioned reduced metals to poisonous elements from the reaction crude (oxygen, nitrogen, carbon, sulfur) or from poisoning molecules (carbon monoxide, phosphines, amines) leads to deactivation issues.⁶ In contrast, the catalytic activity of early transition metal carbides for instance is generally more tolerant to the insertion of nitrogen or sulfur atoms.⁷ The corresponding nitrides and sulfides are indeed also active, to the contrary of those of noble metals. This deactivation issue of the metallic catalysts is expected to be more and more pregnant with the increasing use of biomass and the increase of concentrations of impurities (N and S) in the fossil-based feedstocks (petroleum is extracted from deeper stocks than before).⁸

The catalytically active surfaces of purely metallic nanoparticles may be modified during the catalysis, either by a surface oxidation or by an *in situ* light element incorporation leading to carbide, phosphide or sulfide surface species. For instance, Sautet *et al.* reported a study on the surface carbidization of nickel catalysts when exposed to a slight pressure of hydrocarbon molecules.⁹ The dissolution of small amounts of carbon in the subsurface region of the catalyst drastically modifies its electronic structure. This effect has an impact on the adsorption energy of substrates and thus on the chemoselectivity. In those cases, the active catalytic sites are no longer reduced metal atoms and should be better described by metal-containing materials, comforting the interest in nanoparticles fully composed of these species.

All the aforementioned points justify the current research for new phases in hydrogenation reactions and for rationalization of the known active phases. Most of the works so far focused on relatively hard conditions of reaction relevant for oil refinery or biomass hydroprocessing. However, as will be developed later, a growing number of works report their use in more sensitive chemistries such as those of fine chemicals or sugars.

I.1.2 Substrate molecules

Hydrogenation reactions consist in the addition of hydrogen atoms in a molecule. This incorporation of H may result in the reduction of an insaturation ($C=C$, $C\equiv C$,

C=O, C=N, C≡N, NO₂) or in a C–X bond cleavage (X = C, N, O, S). In this last case, the term hydrogenolysis may be found.¹⁰ The scope of hydrogenation reactions in solvent covers a wide range of substrates with different stakes and challenges.

Petroleum refinery. During the petroleum refinery, hydrodesulfurization (HDS) and hydrodenitrogenation (HDN) are required to remove all traces of sulfur and nitrogen from the raw feedstocks.⁸ Typical impurities consist in thiols, thiophenes (dibenzothiophene) and sulfides for sulfur and amines (carbazole), pyridines, quinolines and porphyrins for nitrogen. Their removal by HDS and/or HDN produces respectively hydrogen sulfide (H₂S) and ammonia (NH₃). These hydroprocessing reactions are usually run at high temperatures and elevated H₂ pressures. The purification of the oil is needed first to avoid any poisoning of the catalysts used in the downstream refinery steps and then to limit the final release of pollutant gases such as SO_x or NO_x during combustion. Hydrodeoxygenation (HDO) processes are used for C–O bond cleavage, but in a lesser extent in petroleum refinery. They are nonetheless the subject of a growing interest these past decades due to the development of biorefinery, as detailed just below. Typical industrial catalysts are similar for HDS, HDN and HDO reactions and consist in cobalt or nickel promoted molybdenum or tungsten disulfides supported on metal oxides (γ-Al₂O₃, SiO₂, zeolites).^{8,11} We do not intend to exhaustively report the works on hydroprocessing as this vast field has already been the topic of numerous reviews and books. We can nonetheless stress the variety of the current research with the use of transition metal nitrides, carbides or phosphides.^{12,13}

Biomass valorization. In volume, most of the bio-sourced molecules originate from carbohydrate monomers or polymers (sugars, cellulose, hemi-cellulose), phenolic polymers (lignin) and fatty esters (vegetal oils) (Figure 1).¹⁴ The transformation of these chemicals has two main possible outcomes: as energy carriers or fuels (energy-driven refinery) or as higher-added value chemicals for further transformation (material-driven refinery). In the first case, a decrease of the oxygen content is targeted in order to improve the calorific value of the compound. In the second case, hydrogenation reactions must be performed in order to obtain similar molecules than the ones currently obtained from petroleum refinery. The molecules originating from biomass are indeed more oxidized than the ones from fossil resources. For both energy- and material-driven refineries, the acid-mediated dehydration reaction and the hydrodeoxygenation process (HDO) are essential. Two carbonyl compounds derived from carbohydrates should be considered in particular as to hydrogenation: the furfural (FAL) and the 5-hydroxymethylfurfural (HMF). These two furanic aldehydes are obtained from acid-catalyzed dehydration of xylose and hexose, themselves obtained from cellulose and hemicellulose.^{15,16} The reductive upgrading of FAL and HMF leads to more than 30 industrially-relevant molecules, including methylfuran and dimethylfuran which are good substitutes to ethanol as liquid biofuel.¹⁷ Lignin is a complex polymer composed of methoxylated phenols (coumaryl, coniferyl and sinapyl

alcohols). Handling and interpreting by ^1H NMR the chemical transformations of lignin in the context of academic research is quite challenging due to its complexity. Model molecules are thus studied instead of lignin. In order to represent the chemical diversity of the lignocellulosic polymers, these model molecules include phenol (Ph-OH), anisole (Ph-OCH_3), guaiacol (HO-Ph-OCH_3) and benzyloxybenzene ($\text{Ph-O-CH}_2\text{-Ph}$). Finally, the hydrodecarboxylation (HDC) of natural fatty acids allows the production of renewable liquid fuels. Considering the complexity of actual raw feedstocks, only a selection of fatty acids were chosen as model substrates in academia, they include stearic (C_{18}), palmitic (C_{16}) and lauric (C_{12}) acids for the saturated compounds and oleic and linoleic acids for the unsaturated ones.

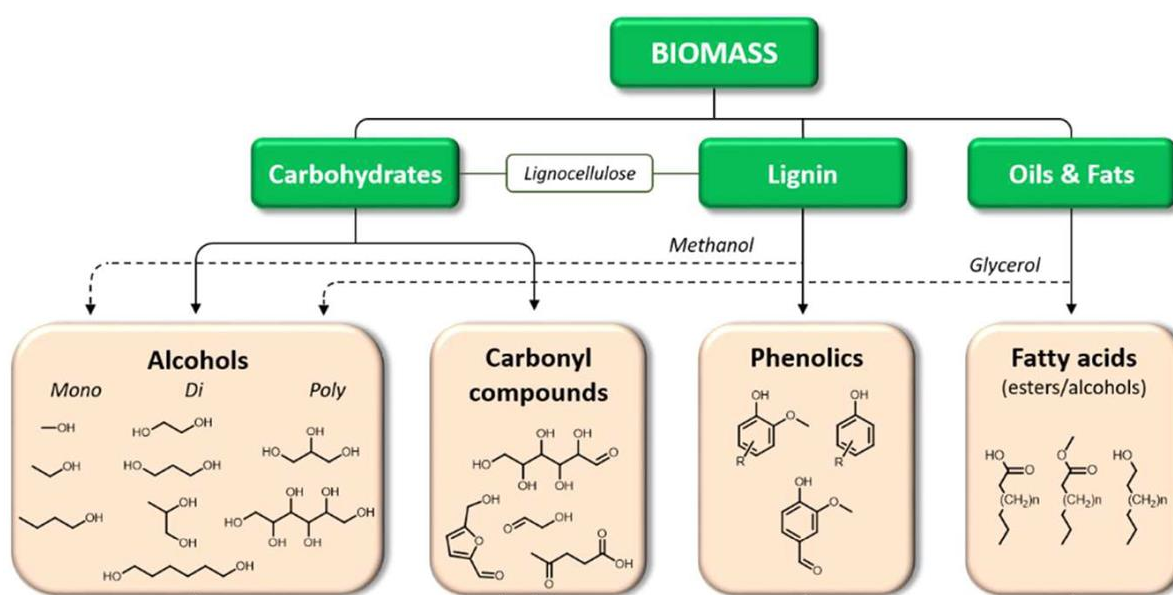


Figure 1. Overview of various bio-based platform molecules. Adapted from reference [14].

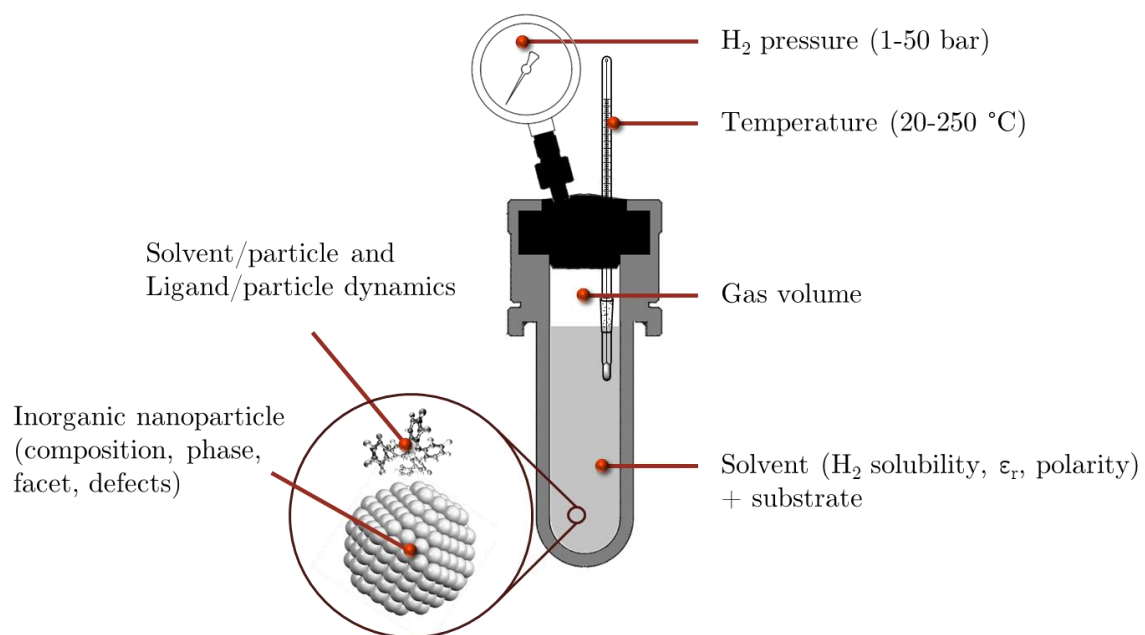
Fine chemicals. Hydrogenation reactions of unsaturated compounds in fine chemistry (drugs, dyes, agrochemicals, fragrances...) are very common steps for which chemoselectivity is crucial considering the high density of functions in the substrates molecules. For instance, the partial hydrogenation of alkynes and nitriles is known for being challenging as the olefinic bond is generally more easily reduced than the $\text{C}\equiv\text{C}$ and $\text{C}\equiv\text{N}$ ones. Usual substrates include alkenes and alkynes, aromatic rings, nitriles, imines, carbonyl moieties (aldehydes, ketones, esters, carboxylic acids), phenols, epoxides and nitro compounds.² Furthermore, removal of several protection groups such as activated ethers occurs through a hydrogenolysis step. Most of the academic works reporting the use of new catalysts generally optimize the reaction conditions on phenyl-derivative model substrates (styrene, phenylacetylene, benzonitrile, benzaldehyde, nitrobenzene...), easier to reduce than alkyl-connected groups. They then explore the

“strength” of the catalyst by screening a number of activated or deactivated moieties. The chemoselectivity may finally be illustrated on industrial-relevant molecule transformation such as citral selective hydrogenation in citronellal (C=C reduction) or geraniol (C=O reduction).¹⁸

Phenylacetylene semi-hydrogenation. The selective semi-hydrogenation of phenylacetylene in styrene is a specific case which is an important industrial process for the alkyne removal from styrene feed stocks.¹⁹ Phenylacetylene indeed deactivates the styrene polymerization catalyst, thereby lowering the quality of the produced polystyrene: it must be considered as a poisonous impurity in the styrene monomer. The main challenge for this particular compound is therefore the selectivity of the reaction as the catalyst should be active only on traces (phenylacetylene) and not on the main compound of the mix (styrene). This is achieved by a fine tuning of the adsorption energies of the two molecules on the catalyst.

I.1.3 Experimental setups for hydrogenation

In academic works, liquid phase hydrogenation reactions are usually performed in batch with an autoclave. The autoclave is charged with the liquid phase in equilibrium with a gas phase of pure H₂ at a given pressure (Scheme 1). Autoclaves in glass generally accommodate pressures up to *ca.* 10 bar whereas steel autoclaves are needed for higher pressures (up to 100 bar). Reactivity obtained at pressures as low as 1 atm makes possible the use of regular glassware equipped with a rubber balloon instead of pressurized setups. This point renders the work accessible to a much broader audience. Indicating the volume of the gas phase is necessary to determine the number of moles of H₂ and therefore the molar ratio H₂:substrate. Due to the small size of H₂ molecules and the limited intermolecular interactions, the model of ideal gas may be applied and the number of moles of H₂ is directly proportional to the pressure on a fairly large range of pressure. The molar concentration under 1 bar at 20 °C is of 41.0 mmol.L⁻¹ and that at 100 bar is overestimated by only 6 % (3.8 mol.L⁻¹ instead of 4.1 mol.L⁻¹).²⁰



Scheme 1. Classical setup for hydrogenation reaction in solvent with critical points.

I.2. Theoretical and experimental tools to study H₂ dissociation

I.2.1 Microscopic description

Elemental steps. Hydrogenation reactions are usually decomposed in several elemental steps describing (1) the physical/molecular adsorption of H₂ at the surface of the catalyst, (2) its chemical adsorption, *i.e.* the bond cleavage, (3) the adsorption of the substrate, (4) the hydrogen transfer and (5) the product desorption. The H₂ activation refers to steps (1-2). The chemisorption differs from the physisorption by a substantial modification of the bonds in the adsorbate molecule, the H–H bond here. All the states of this mechanism are characterized by a Gibbs free energy G , usually referred to as the free energy, and the different steps present an activation barrier E_{act} . A negative change in free energy, ΔG , denotes a favorable evolution *i.e.* the reaction is thermodynamically favored. A low energy barrier denotes an easy reaction *i.e.* the reaction is kinetically favored. Their values are commonly expressed in eV or in kJ/mol (1 eV \equiv 96 kJ/mol) and are usually obtained *via* theoretical calculations by Density Functional Theory (DFT), or *via* kinetic experiments.

When modelling the reaction, a “zero energy” has to be set because free energy is not absolute. Two conventional choices exist: the zero energy may either refer to the energy of a clean surface and H₂ in the gas phase, or to the physisorbed state H₂^{*}. The difference is small considering the low energy engaged in the physisorption of H₂, typically of the order of magnitude of 0.1 eV.²¹ The degree of activation of H₂ is given by the length of the H–H bond: a weakening of the H–H bond is associated with its elongation. For instance, upon H₂ activation on WC first at the top of a W site, the H–H bond length evolved from 75 pm, its standard value in H₂ (gas), to 96 pm.²² In some cases, as β -Mo₂C(001), stable molecular H₂ adsorption without the dissociation in two hydrogen atoms is not possible on any site and the H₂ dissociation is barrier-less: the molecule dissociates spontaneously without any activation barrier.²³ The larger the adsorption energy, the more favorable the H₂ dissociation, leading to higher coverage adsorption. In an ideal case, the surface–H bond should be strong enough to favor the H₂ cleavage and weak enough to allow the H transfer to the substrate a in second time. Indeed, the higher in energy the surface–H state, the lower the activation barrier of the hydrogen transfer step and the more thermodynamically favorable the reaction: this is the Sabatier principle. The H₂ activation (steps 1-2) is slowed down if the substrate molecules are adsorbed too strongly or if the product desorbs too slowly as these molecules impend the access to the surface to H₂. Ideally, the rate of H₂ activation should exceed that of product desorption, itself exceeding that of reactant adsorption.¹¹ A rapid product desorption also limits the risk of over-hydrogenation, as for phenylacetylene total hydrogenation in ethylbenzene.¹⁹

Molecular hydrogen dissociation. Two limit mechanisms, homolytic and heterolytic, are proposed for molecular hydrogen dissociation on surfaces. Both mechanisms are reported for metal oxides, and will be illustrated below on these materials, but the transposition is possible at least to metal nitrides²⁴ and sulfides.¹¹

- (1) the homolytic (radical) mechanism produces two hydrogen atoms $\text{H} \cdot$
- (2) the heterolytic (polar) mechanism produces a proton H^+ and a hydride H^-

In the homolytic mechanism, the two $\text{H} \cdot$ combine with oxygen atoms to form two hydroxyl groups $\text{O}-\text{H}$ and the charge neutrality of the material is respected by the reduction of one or two metal sites (the reduced metal centers are either isolated or delocalized in the conduction band) (Figure 2A, a)).^{25,26} This dissociation mechanism is therefore thought to be possible only for reducible metal compounds such as TiO_2 or CeO_2 (both M^{3+} and M^{4+} states are stable). In the heterolytic mechanism, the $\text{H}-\text{H}$ bond is broken along a $\text{M}-\text{O}$ bond and yields to an $\text{O}-\text{H}$ bond and a $\text{M}-\text{H}$ bond (Figure 2A, b)). This latter species is regarded as a surface hydride H^- considering the difference in electronegativity ($\chi(\text{M}) < \chi(\text{H})$). The degree of oxidation of the metal M has not formally changed as the $\text{M}-\text{O}$ was cleaved too and this mechanism is possible for both non-reducible metal oxides such as ZrO_2 , MgO , CaO , SiO_2 or Al_2O_3 and reducible ones such as ZnO , Ga_2O_3 or Cr_2O_3 .²⁶ The heterolytic dissociation of H_2 may lead to the homolytic product *via* a subsequent transfer of the hydrogen atom from the metal to an oxygen: this transfer was demonstrated for TiO_2 , CeO_2 , Co_3O_4 but also for metal-supported MgO .^{21,25,27-29} The two pathways, homolytic and heterolytic, with subsequent H migration are illustrated on Figure 2 for a $\text{Co}_3\text{O}_4(110)$ facet (Figure 2B). Finally, on defective surfaces with reduced metal centers, the H_2 molecule may dissociate in two hydride species associated with the oxidation of the metal, as proven for ZrO_2 and CeO_2 (Figure 2A, c)).^{26,30}

The presence of a $\text{M}-\text{H}$ stretching vibration band in infrared spectroscopy or inelastic neutron scattering suggests a heterolytic dissociation of H_2 (*vide infra*). The absence of experimental evidence of a $\text{M}-\text{H}$ species is nonetheless not sufficient to exclude the radical mechanism considering a possible rearrangement. The polarity of the $\text{M}-\text{O}$, or $\text{M}-\text{S}$ bond in the case of metal sulfides, induces a charge separation in the H_2 molecule in the transition state and thus favors its heterolytic splitting in (H^+, H^-) rather than its homolytic splitting (Figure 3A). The H_2 activation mechanism is therefore highly dependent on the nature of the $\text{M}-\text{X}$ bond. The reader may refer to different DFT studies conducted on H_2 dissociation on Co_3O_4 ,²¹ TiO_2 ,^{27,28} ZrO_2 ,³¹ MgO ,^{29,32,33} CeO_2 ,^{25,34} Ce_2O_3 ,³⁵ MoS_2 ,³⁶ Ni_2P ,³⁷ Mo_2C ,^{23,38} and WC .²²

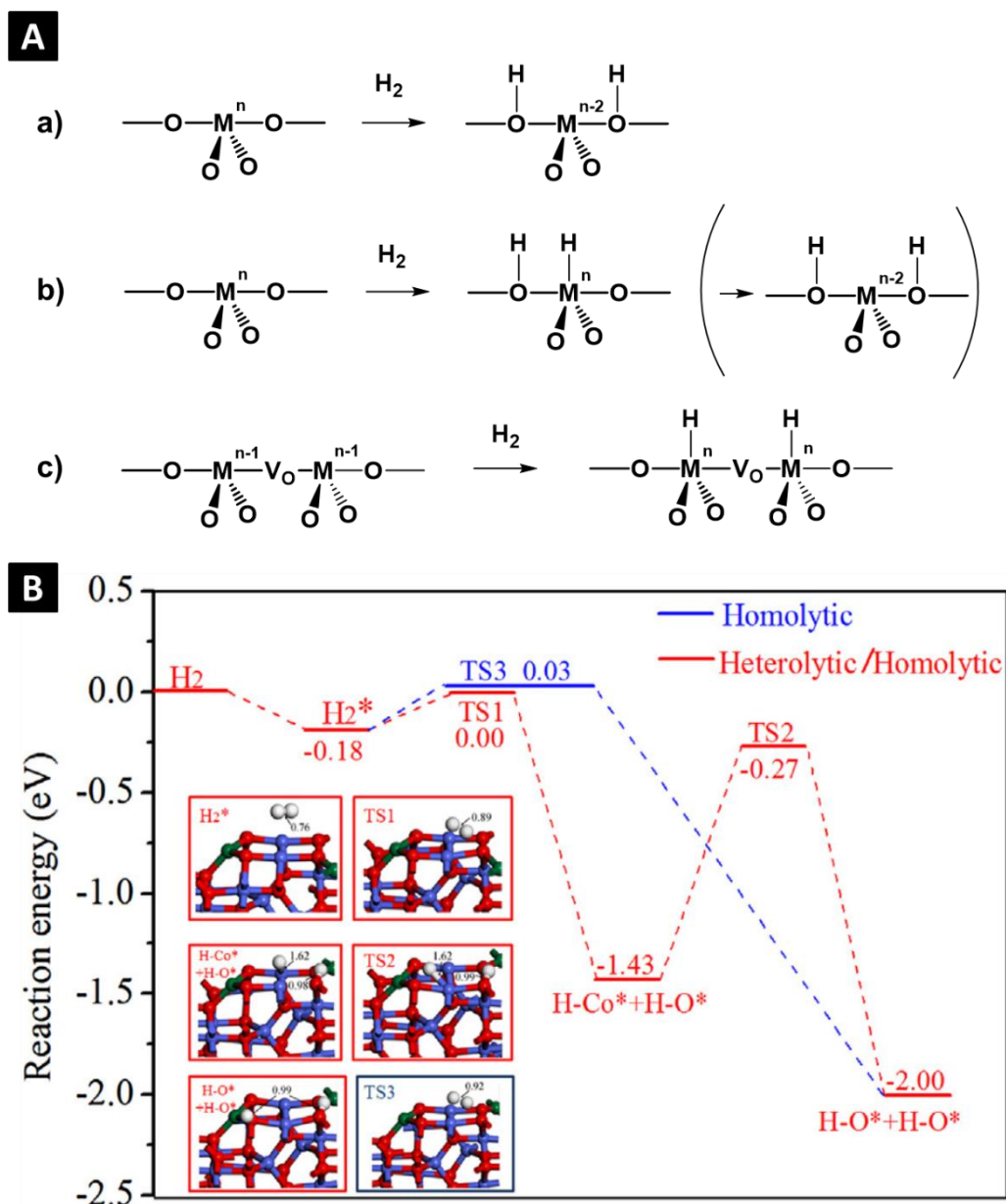


Figure 2. (A) a) Homolytic and b) Heterolytic activation of H₂ on metal oxide surfaces. c) H₂ activation on reduced metal oxide. (B) Energy profiles for homolytic and heterolytic H₂ dissociation pathways with the corresponding optimized geometries for the related states on perfect Co₃O₄(110) surface. The unique step of the homolytic pathway (blue curve) is exothermic ($\Delta_{\text{ads}}G = -1.82$ eV) with an energy activation of $E_{\text{act}} = 0.21$ eV. In the case of the heterolytic pathway (red curve), the first step is exothermic ($\Delta_{\text{ads}}G = -1.25$ eV) with an energy activation of $E_{\text{act}} = 0.18$ eV. After the heterolytic dissociation, the H atom linked to the Co atom migrates to a contiguous O atom to produce the homolytic product. This step is exothermic ($\Delta G = -0.57$ eV) but with a high activation energy of $E_{\text{act}} = 1.16$ eV, making it kinetically unfavorable. Reproduced from reference [21].

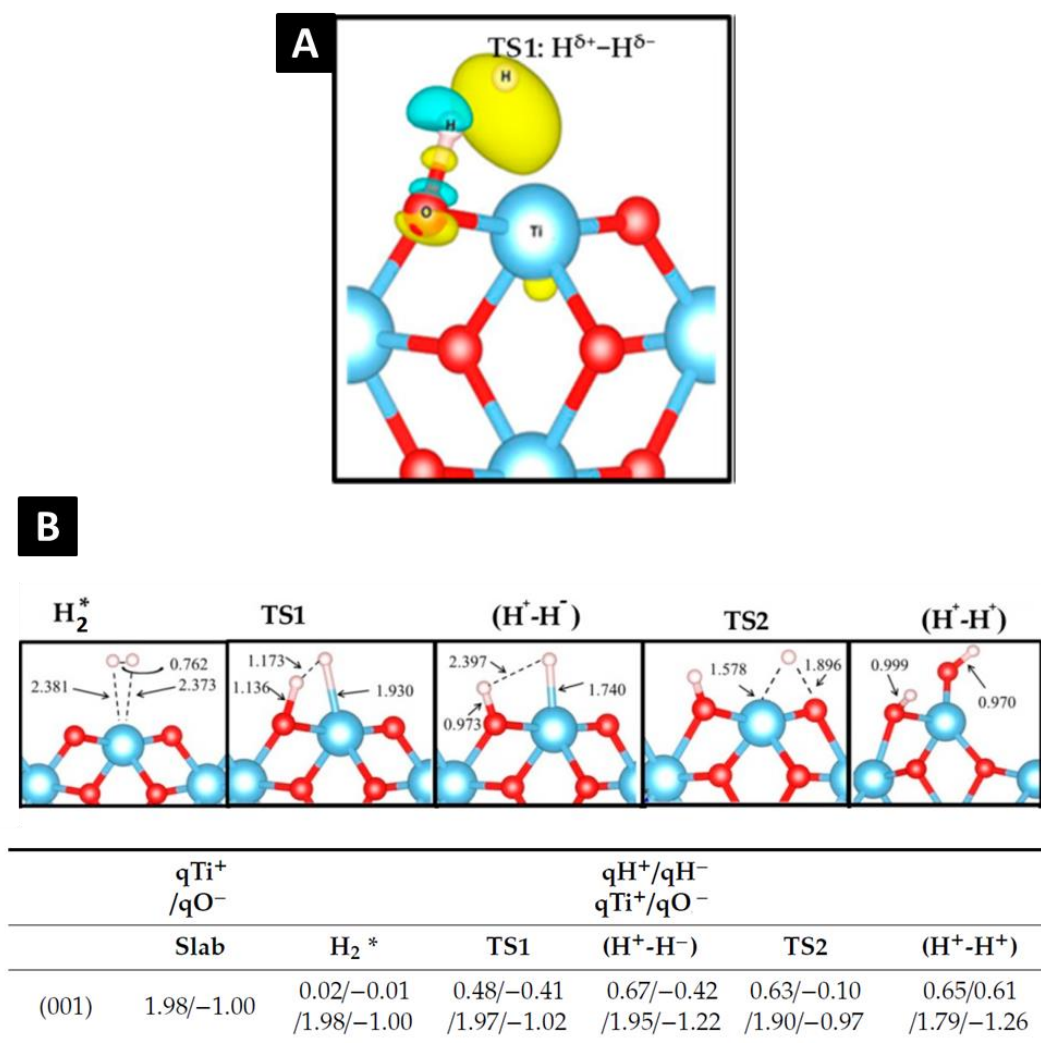


Figure 3. (A) Charge density difference of transition state illustrating the formation of the $\text{H}^{\delta+}-\text{H}^{\delta-}$ tight ion pair on the $\text{TiO}_2(001)$ surface. Yellow and green iso-surfaces show an electronic density gain and depletion, respectively. (B) Bader charges ($|e|$) of H, Ti and O in the H_2 dissociation process and in subsequent transfer from Ti to O process. Adapted from reference [27].

Catalytic site. Catalytically active sites are of different nature on surface. They generally correspond to metal atoms which are not fully coordinated (typically 6 neighbors for many transition metals) and display dangling bonds, hence the term of coordinatively unsaturated site (CUS) (Figure 4A). These sites exist owing to the presence of singularities on the surface such as edges, corners, steps and kinks or vacancies on terraces (Figure 4B). The CUS term is often found in literature for H_2 activation by MoS_2 due to the importance of sulfur vacancies in the corresponding catalysts but the concept is valid for all materials.^{38,39}

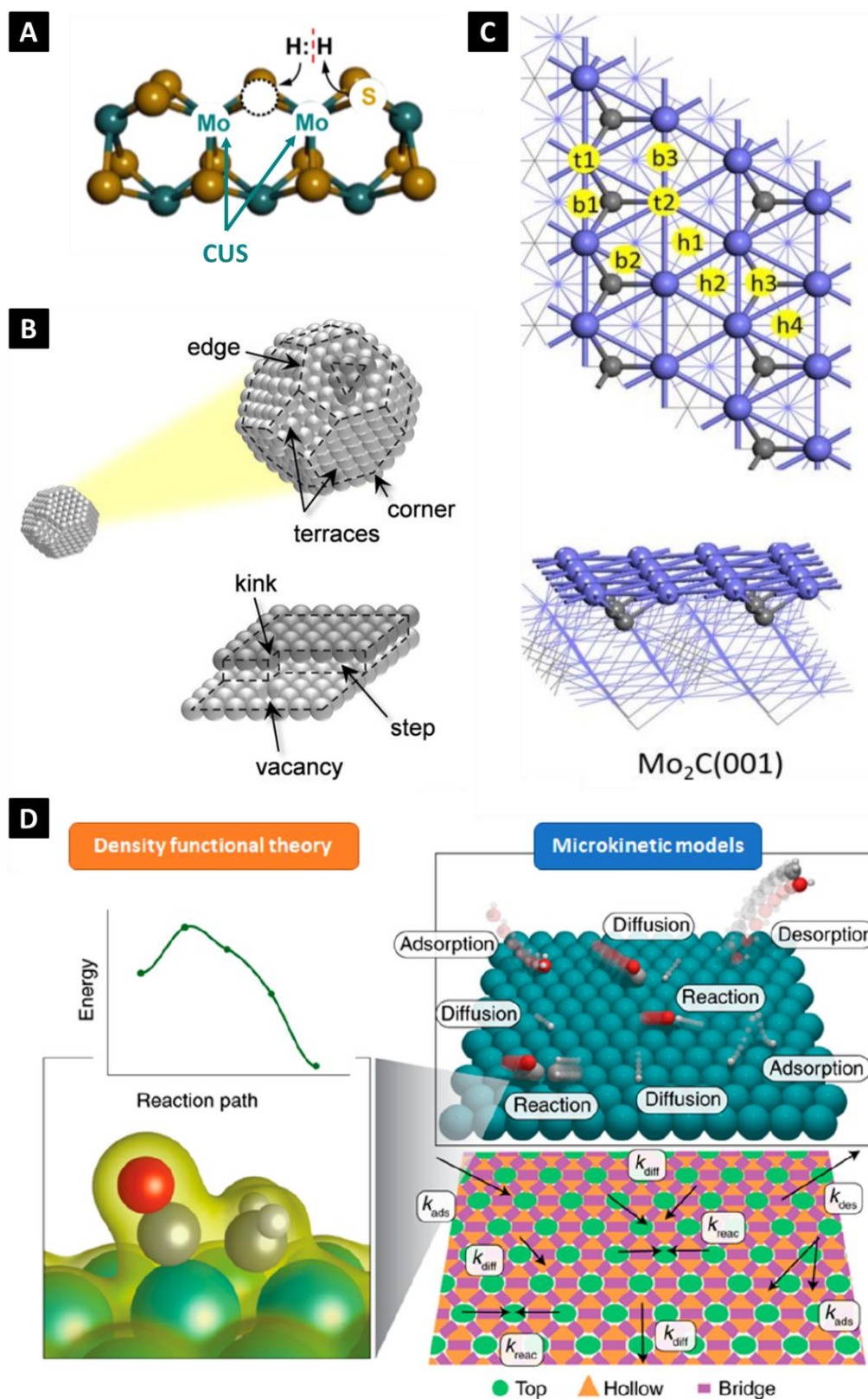


Figure 4. (A) Coordinatively unsaturated sites of Mo situated at a sulfur vacancy in MoS₂. (B) Panel of possible singularities on nanoparticle surfaces. (C) Top and side views of the Mo₂C(001) surface structure and possible adsorption sites (**t** for top, **b** for bridge, **h** for 3-fold hollow sites). (D) Illustrative scheme of the dynamic character of the system. Adapted from respectively references [39], [2], [23] and [40].

Different positions exist for the hydrogen location before and after H–H bond cleavage. The H atoms do not necessarily stay at the top of an atom (site **t**) but may also occupy a bridge position between two atoms (site **b**) or even a hollow site between three atoms or more (site **h**) (Figure 4C).²³ Sites **t** are not always on metal atoms, the H may also be at the top of a carbon atom for instance, as in the case of WC(0001) or Mo₂C(101).^{22,38} The low coordination of CUS renders the heterolytic cleavage easier as the M–H bond stabilizes the metal atom.²⁷ Post-dissociation migration of the hydrogen atoms may also occur before they react with a substrate molecule (Figure 4D).

Orbital description & electron Density of States (DOS). So far, the description of the mechanisms we presented relied on concepts inherited from homogeneous catalysis with discrete species, precise degrees of oxidation and charges. But the complexity and versatility of heterogeneous catalysis precisely relies on the complex interaction between the substrate, a molecule, and a material surface whose electron description should integrate its band structure according to Nørskov *et al.*⁴¹ One of the challenges is therefore to develop concepts and descriptors of the properties monitoring the activity and selectivity of the catalysts. Achieving this point would permit the rationalization of the already known catalytic materials and the development of new ones. The *d*-band model has proved its efficiency to understand the substrate adsorption and/or activation on a metal-containing surface. It relies on the interactions between the orbitals of the substrate and the *s* and *d* states of the surface (Figure 5). The strength of the M–H bond, and thus the adsorption of the substrate, is characterized by the filling of the antibonding orbitals between the adsorbate state and the metal *d* states (stressed in orange). The surface may be considered as a reservoir of electron at the Fermi level E_{Fermi} and these electrons are susceptible to fill the antibonding orbitals of the surface–substrate complex. The Fermi level also corresponds to the *d* band center. As the antibonding states are always higher in energy than the *d* states, the higher in energy the *d* states are (relative to the Fermi level), the emptier the antibonding states and the stronger the M–H bond. Variations in the width of the *d* band of the material are compensated by a shift in energy of the *d* band. There is therefore a great interest in the determination and engineering of the electron density of states (DOS) of the catalyst.

Different strategies may be considered such as the insertion of light elements in the metal lattice or the doping with other metal atoms.³⁷ Electron-enriched metal sites tend to have a lower Fermi level and therefore render the H desorption more favorable. On the contrary, electron-deficient metal sites lead to higher Fermi level and therefore render the H₂ adsorption more favorable. The doping of metallic phases with light elements generally decreases the electron density on the metal atoms considering the difference in electronegativities between the transition metals and the *p*-block elements, thereby favoring the H₂ dissociation.

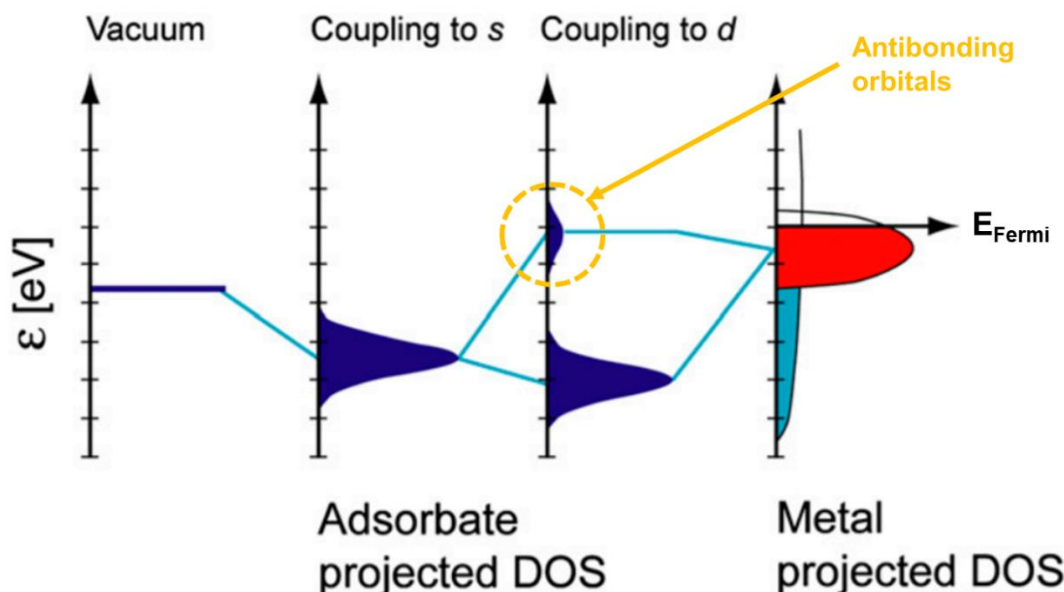


Figure 5. Bond formation at a transition-metal surface. Schematic illustration of the formation of a chemical bond between an adsorbate valence level (left) and the s and d states of a transition-metal surface (right). Adapted from reference [41].

Finally, the description of the material surface with orbitals and band structures is a reminder that the homolytic/heterolytic models proposed are simplifications, especially concerning the charges born by the different atoms. The Bader analysis thus indicates the electronic density estimated around a particular atom by DFT calculations and they do not correspond to integer values. A certain degree of delocalization of the charges is expected for covalent and metallic materials, and eventually for ionic ones such as metal oxides. For instance, for the heterolytic cleavage of H_2 on $\text{TiO}_2(001)$, the system is described as an ion pair (H^+-H^-) or (H^+-H^+) whereas the charges never exceed 0.7 on the H atom (Figure 3B).²⁷ Moreover, the charge conservation is not respected if only the four atoms directly involved are considered (O, Ti, 2 H): this is the sign of a delocalization of the charges to nearby atoms or to the whole nanoparticles.

Parameters. For a given chemical composition of a catalyst, the free energies of the transition states and of the intermediate species, and thereby the H–H splitting, depend on different characteristics. Both the crystal facet engineering and the defect engineering matter for designing the most active catalyst, and DFT calculations prior to the synthesis help the determination of the best catalyst:

- (1) **the crystal phase.**
- (2) **the crystal facet exposed.** Depending on the exposed facet, the accessible surface atoms may vary. For instance, $\beta\text{-Mo}_2\text{C}$ (001) and (100) facets are

terminated only by Mo atoms whereas (101) and (201) facets present a mix of C and Mo atoms.²³

- (3) **the presence of vacancies and defects.**
- (4) **the presence of metal dopants (Fe, Co, Ni...).** These atoms may modify the electronic structure and thereby the H₂ activation even without being directly involved and forming M–H bond.^{37,42}
- (5) **the surface coverage** with adsorbates (H atoms or substrate). Several H₂ molecule may dissociate at the surface of the catalyst at the same time, the saturation is reached when the stepwise adsorption energy of the n+1 molecule of H₂ equals 0: $\Delta_{\text{ads}}G(n+1) = G(2n+2 \text{ H}^*/\text{slab}) - (G(2n \text{ H}^*/\text{slab}) + G(\text{H}_2)) = 0$. The activity of the catalyst generally decreases with the H₂ coverage but the nature of the adsorption may also vary: molecular *vs* dissociative for instance.^{37,38}

I.2.2 Experimental techniques for H₂ activation characterization

The vast majority of the techniques presented here in order to characterize the activation of H₂ on the material surface are performed under vacuum or in the gas phase. This limitation clearly makes the *operando* study of heterogeneous catalysts in solution challenging if not impossible today.

I.2.2.1. Thermal technique

H₂-Temperature Programmed Desorption (H₂-TPD). This technique allows the determination of the energy of adsorption of H₂ at the surface of the catalyst and the eventual formation of subsurface hydrides.⁴³ This technique is performed in the gas phase after a treatment of the material under high vacuum. The material surface is first saturated with H₂ molecules at room temperature, the temperature is then gradually increased and the amount of desorbed H₂ is recorded. Two main points are informative in the measurement:

- Area under the TPD profile. In most of the systems, this area is proportional to the amount of adsorbed H₂ molecules, from which can be determined the surface coverage $\theta(\text{H}_2)$.
- Peak maximum position (T_{max}). The temperature at which there is a maximum of H₂ desorption, noted T_{max} , is related to the activation energy for desorption: the higher T_{max} , the larger the activation energy. H₂ adsorption is generally spontaneous, with virtually no activation energy, consequently, the activation energy of desorption equals the energy of adsorption.

The vast majority of real systems do not present a single peak but rather complex features. Each peak corresponds to one specific adsorption site characterized by a density of sites (area) and an adsorption energy (T_{max}). These adsorption sites may even consist in the formation of subsurface hydride species for materials such as Pd or Ni. To the best of our knowledge, there is no common experimental method which would provide the same data for H₂ adsorption energy in solvent.

I.2.2.2. Vibrational spectroscopies

Structures of surface isolated hydrides in heterogeneous catalysis are less understood than hydrides in molecular complexes, mostly due to the difficulty in revealing structures on/in solids and because of the large number of potential active sites and geometries.^{26,44} Vibrational spectroscopy experiments can nonetheless evidence the existence of metal-H bond or X-H bond where X is a light element. The position in energy of the band is also informative on the bond strength.

Infrared spectroscopy (IR). Cop  ret *et al.* recently reviewed the splitting of H₂ on a large number of bulk metal oxides and summarized the typical IR and Raman

bands ν_{M-H} expected or observed, with the associated binding types (top, bridge, terminal).²⁶ DFT calculations may also be used as qualitative guide to identify the M-H frequencies obtained experimentally.^{27,34} Diffuse Reflectance Infrared Fourier Transform Spectroscopy (DRIFTS) is an infrared technique which does not necessitate any treatment of the sample prior to measurements, it can therefore be used for operando studies. For instance, Ozin *et al.* recorded the DRIFTS spectra of the hydroxyl and hydride fingerprint regions in the case of indium oxide catalyst put in presence of H_2 (1 bar, room temperature) (Figure 6A,C-D).⁴⁵ They thus evidenced the formation of $In-H^-$ and protonated hydroxyl species $In-OH_2^+$ on different metal sites or with different geometries (ϕ_1 to ϕ_6 for hydride, ν_1 to ν_4 for hydroxyl).

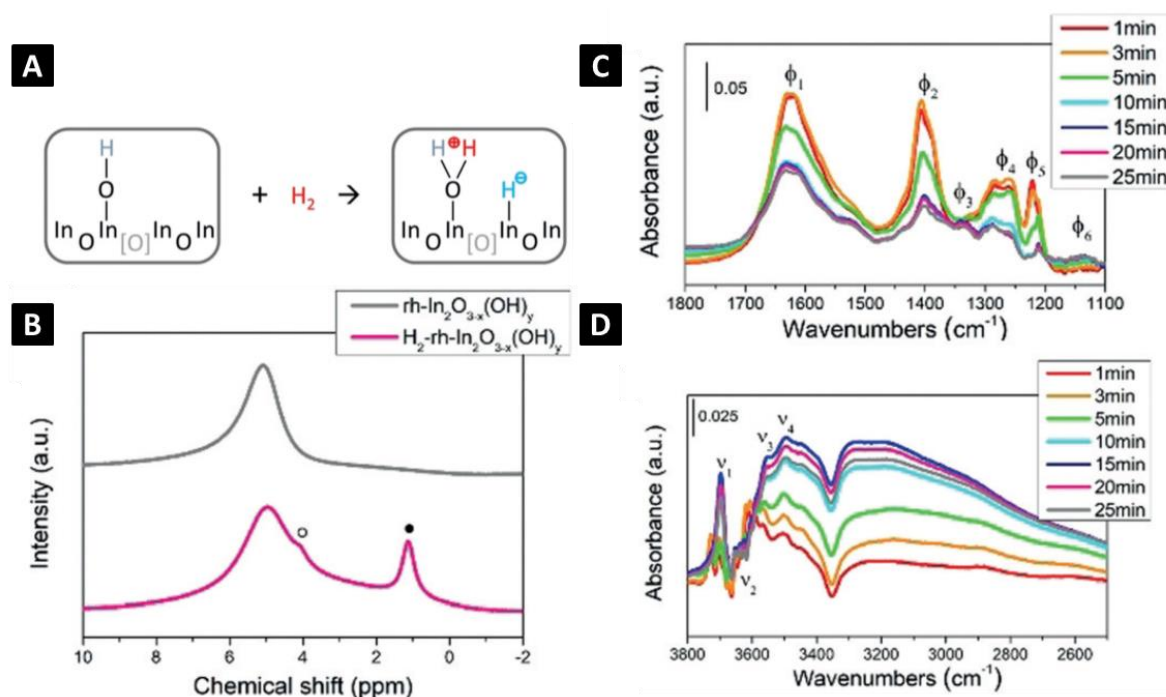


Figure 6. (A) Illustration of the heterolysis reaction pathway for the dissociation of H_2 on $rh-In_2O_{3-x}(OH)_y$, (B) Solid-state 1H MAS NMR spectra of $rh-In_2O_{3-x}(OH)_y$ where filled dot (1.14 ppm) can be assigned to $In-H^-$ and circle (4.05 ppm) to $In-OH_2^+$. Grey and pink spectra correspond to respectively before and after exposure to H_2 (1 bar) at room temperature. (C-D) Operando DRIFTS study of $rh-In_2O_{3-x}(OH)_y$ under H_2 atmosphere at room temperature (C: hydride region, D: hydroxyl region). Adapted from reference [45].

Inelastic Neutron Scattering (INS). Neutron scattering is very well suited for studying hydrogen environment as the incoherent neutron cross section of H is higher than any other atoms, meaning neutron scattering signal is dominated by that of hydrogen. Wu *et al.* recently reviewed the use of INS for hydrides characterization in heterogeneous catalysis, in particular for metal oxides and sulfides.⁴⁴ Contrarily to IR or Raman spectroscopies, all modes of vibration or rotation can be detected with INS. This technique is nonetheless less used considering the difficulty to access a neutron

source. Among different works, we can mention the direct observation of cerium hydride Ce–H species on cerium dioxide by Ramirez-Cuesta *et al.* and that of Mo–H species on molybdenum nitride by Thompson *et al.*^{24,46} This was the first time the H₂ heterolytic dissociation on CeO₂ was formally proved as other vibrational techniques failed to detect the hydride species.

I.2.2.3. Direct probing of the hydrogen

¹H Magic Angle Spinning Nuclear Magnetic Resonance (¹H MAS NMR). Upon activation of H₂ at the surface of a material, the solid state ¹H MAS NMR spectrum may display new peaks corresponding to surface species (M–OH⁺, M–OH₂⁺, M–H[–]). Hosono *et al.* reported a work on the NMR characterization of hydride species in metal oxides and demonstrated the attribution is not straightforward.⁴⁷ The electronic density around the H nuclei is indeed different from what is expected from the formal oxidation states: the density near the hydrogen atom in M–OH⁺ for instance exceeds that of hydrogen in M–H[–]. This NMR characterization was used to characterize the H₂ splitting on indium oxide by Ozin *et al.* (Figure 6A–B).⁴⁵ Two peaks grew after the addition of H₂ (1 bar) on the catalyst: one was attributed to a hydride species In–H[–] and another to a protonated hydroxyl group In–OH₂⁺. Such a technique may therefore comfort a heterolytic dissociation mechanism over a homolytic one.

I.2.2.4. Indirect probing *via* the metal center

A large number of characterization techniques for atom environments and oxidation degree over inorganic solid surfaces rely on the interaction between the studied atom and X-rays or high energy electrons. They therefore cannot be used for direct study of hydrogen atoms considering the low atomic number of the element and therefore its limited interaction with the X-rays and with the electrons. To circumvent this issue, the presence of adsorbed hydrogen may be indirectly detected on the metal center.

X-ray Photoelectron Spectroscopy (XPS). XPS is a powerful technique allowing the determination of the chemical composition and electronic configuration of atoms at the extreme surface of a material.⁴⁸ The degree of oxidation and the evolution of the close chemical environments of all the atoms can therefore be monitored with time. This technique was extensively used for the study of gas phase heterogeneous catalysts. Its main limitation is the need for Ultra-High Vacuum (UHV) as an X-ray beam is required and its interaction with gas molecules of atmosphere would extinguish it. With powerful beams, typically those available in synchrotron facilities, a low pressure of gas, up to *ca.* 5 mbar, can be introduced while measuring the surface state of the sample. This mode is termed Near Ambient Pressure XPS (NAP-XPS). For instance, Freund *et al.* used NAP-XPS to demonstrate H₂ could be split at the Ce^(III) sites on reduced cerium oxide catalyst to form surface hydride species.³⁰ Such a mechanism implies the oxidation of the Ce^(III) atoms in Ce^(IV) ones. This effect was indeed observed

on the Ce 3d region which a $\text{Ce}^{(\text{III})}$ fraction decreasing upon exposure to H_2 (Figure 7). The technique can *a priori* be applied to any system which may present a modification of the degree of oxidation of the metal center, and is therefore well suited to prove the heterolytic dissociation of H_2 or its splitting on oxygen vacancy sites.

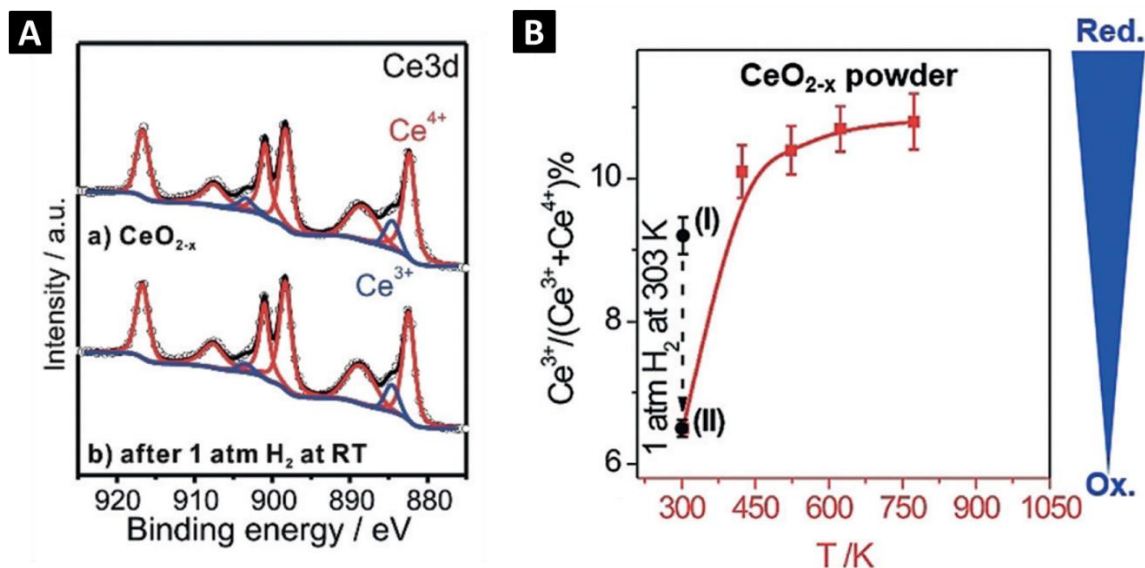


Figure 7. (A) Ce 3d XP spectra of CeO_{2-x} powder before (a) and after (b) exposure to 1 atm H_2 at r.t. (B) Ce^{3+} concentration in CeO_{2-x} (I) before and (II) after H_2 treatment (1 atm, 1 h, r.t.) and subsequent heating, determined from Ce 3d region XPS. Adapted from reference [30].

I.2.2.5. Chemical reactivity

H_2/D_2 scrambling. The catalytic activity of a material toward H_2 activation may be evidenced by the formation of HD, detected by mass spectrometry, when exposed to a H_2/D_2 mix. These experiments are usually performed in flux in the gas phase.⁴⁹ Studying the production and the release of HD as a function of temperature can thus be informative on the formation of transient surface hydride species and on the strength of the interaction between the surface and H/D (interaction strength and surface coverage). When looking at the H_2/D_2 exchange rate on metal oxides, no direct connection could be drawn between the efficiency of the exchange and the nature of the activation mechanism (heterolytic *versus* homolytic).²⁶

I.2.3 Reactions in solvent: where is the difference?

I.2.3.1. Solubility of H_2 in solvents

Molecular hydrogen concentration in the liquid phase depends on mainly three factors: the pressure of H_2 in the gas phase, the temperature and the nature of the solvent. Figure 8 displays the evolution of the molar H_2 concentration as a function of temperature and H_2 pressure for several common solvents. First, it appears the range of concentration in H_2 is close for all the solvents, between 2 and 6 mmol/L under

1 atm of H_2 at 25 °C, and that there is no clear trend concerning the polarity of the solvent. While there may be a more favorable solubilization of H_2 in non-polar solvents (*n*-alkanes, toluene), this effect is counterbalanced by physical characteristics of the liquids such as their density or molar mass. Then, H_2 concentration increases for all solvents with temperature, on average of 50 % between 25 °C and 100 °C. Finally, in agreement with Henry's law, the concentration in H_2 is proportional to the partial pressure in H_2 in the gas phase. All these results indicate that H_2 may be dissolved in non-negligible quantities in all common solvents and that increasing the H_2 pressure is a more efficient way to solubilize H_2 than increasing the temperature. This analysis however does not prejudge of the best conditions for the catalysis itself: the temperature has also a critical importance to kinetically favor the solubilization of H_2 and to overcome the activation barriers of its activation. The solubility of H_2 evolves linearly with the pressure in the gas phase so the progressive consumption of H_2 diminishes its concentration in the liquid phase, thereby lowering the reaction rate. Although this correction is usually small when high H_2 pressures are used, it may be significant for atmospheric pressures or close.

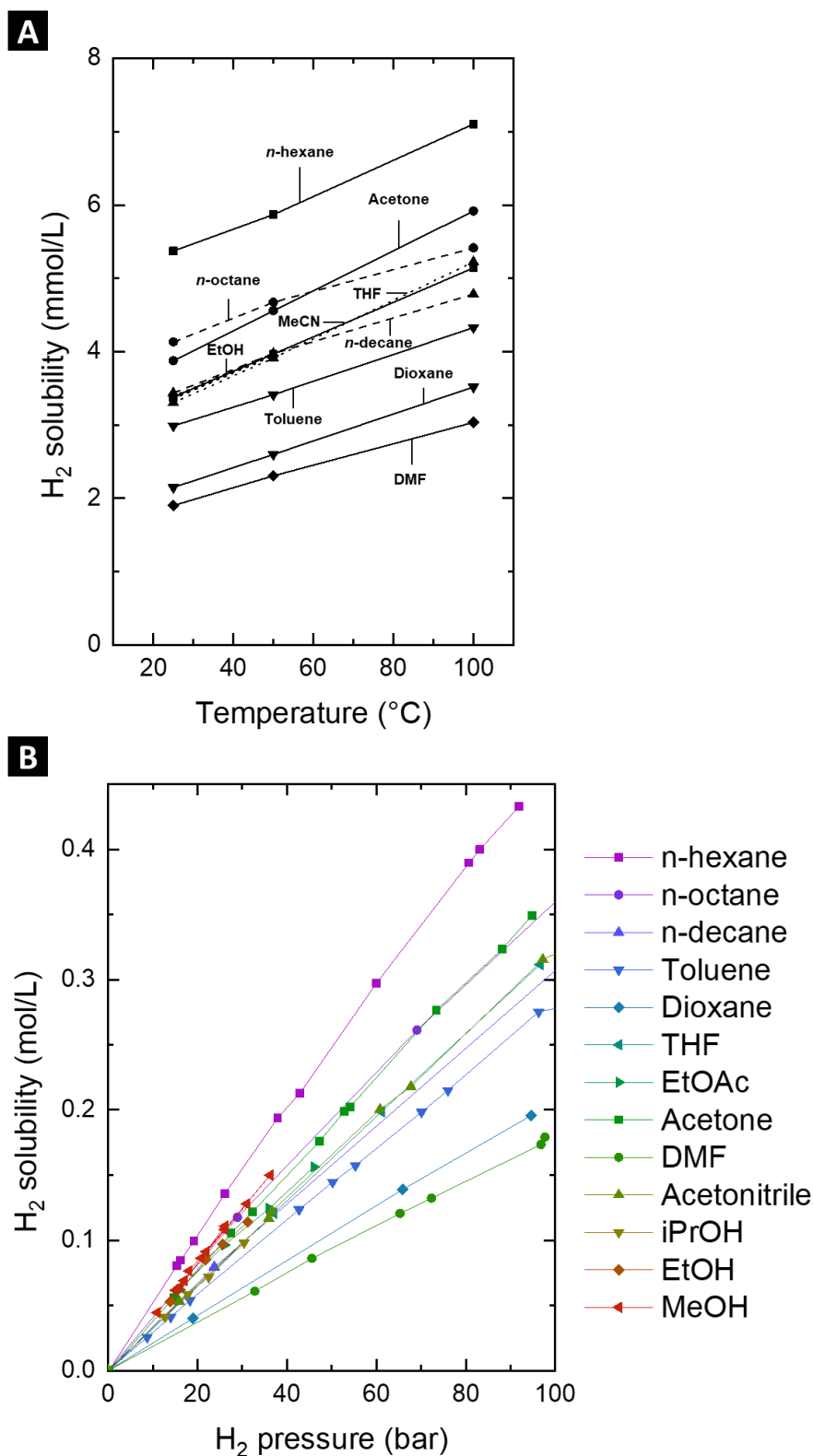


Figure 8. H_2 solubility in various solvents (A) under 1 atm of H_2 at different temperatures and (B) at 25 $^{\circ}C$ under different pressures. The polarities of the solvents according to the Miller chart are the following: *n*-hexane (0.009), *n*-octane, *n*-decane, toluene (0.099), dioxane (0.164), THF (0.207), ethyl acetate (0.228), acetone (0.355), DMF (0.386), acetonitrile (0.46), isopropanol (0.617), ethanol (0.654), methanol (0.762). Data extracted from references ^[50,51].

I.2.3.2. Reaction medium: impact on adsorption and solvation energies

The presence of a liquid phase in heterogeneous catalysis may alter the free energies of the different states, and thereby the reaction mechanism, because of the interactions between the solvent molecules and the reagents/products/reaction intermediates. These modifications are generally related to the polarity of the solvent and its capacity to stabilize ions and ion pairs, rationalized through its dielectric constant ϵ_r . Modeling liquid-phase reactions is nonetheless more challenging than gas-phase reactions which are closer to the *in vacuo* conditions of DFT regular calculations.^{40,52,53} Nonetheless, barring an increase in calculation cost, different methods were developed to take into account the solvent: (1) implicit-solvent models, (2) explicit-solvent models and (3) microsolvation models (Figure 9). In case (1), also termed Continuum Solvation Models (CSM), the solvent molecules are not individually modelled but instead considered as a continuum, and correction terms in free energy calculations for solutes are added. This is a mean-field approach based on the dielectric constant of the liquid, it therefore finds limitations in the modelling of directional interactions such as hydrogen bonding and asymmetrically charged solvents. In case (2), all solvent molecules are modelled and their interactions with the catalyst and solutes are taken into consideration. Although straightforward, this approach is highly costly as to calculation time. Moreover, static calculations at 0 K cannot be representative of the dynamic character of the solvent. Molecular dynamic simulations can overcome this limitation but at the cost of a further increase in calculation time. Case (3) corresponds to a mix of cases (1) and (2), one may find the terms of (hybrid-)cluster-continuum models. The principle consists in modelling short-range directional interactions through the addition of a few explicit solvent molecules and the long-range electrostatic interactions by using continuum models. Calculation times are therefore kept reasonable.

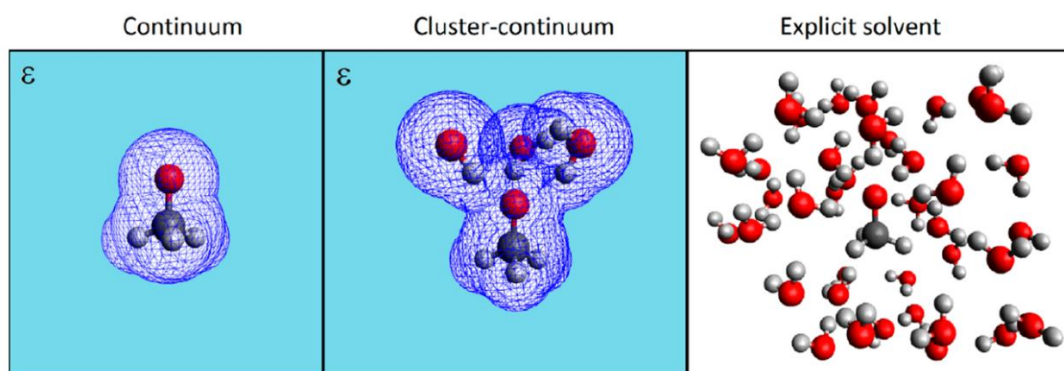


Figure 9. Different approaches to treat solvation of a methoxide ion in water: Continuum, Cluster-Continuum, and Explicit-Solvent. The light-blue background represents a dielectric continuum that approximates the solvent with a relative permeability of ϵ . The blue mesh represents the solute–solvent interface. Color code for atoms: dark gray, C; red, O; white, H.

Reproduced from reference [54].

I.3. Metal-containing catalysts for colloidal hydrogenation

This section does not intend to exhaustively list the use of non-purely metallic active phases for H_2 activation in solvent but rather indicate what are the currently most studied materials. If a material led to numerous works, we only mention the pioneering studies. We chose to mention the main reviews and some works realized under mild conditions.^{1,5,55-58}

Metal-containing compounds are expected to possess a different reactivity from the parent metals through mainly two effects:⁵⁹

- (a) Ligand effect: the introduction of light elements in the metal lattices increases the lattice parameters, thereby decreasing the extent of the M–M interaction and narrowing the d -electron band. The modification of the d -orbitals is amplified by the charge transfer from the light element to the metal and the hybridization of the d -orbitals of the metal and the sp -orbitals of the light element. The electron deprived metal sites are therefore less susceptible to fill the antibonding orbitals of M–H, which favors the H_2 activation.⁵⁸
- (b) Ensemble effect: the presence of a second element in the material modifies the geometric arrangement of the metal atoms at the surface and therefore may create different adsorption sites. Furthermore, the presence of light element vacancies increases the number of coordinatively unsaturated sites (CUS), expected to be more catalytically active.

The type of bonding in materials may be defined among ionic, metallic and covalent. The ionic character is characterized by a high difference in electronegativity between the different elements composing the material and the metallic character by a low average electronegativity. Depending on the percentage of importance of each component, the material is placed on the Van Arkel-Ketelaar triangle (Figure 10). The Pauling electronegativities of boron ($\chi(\text{B}) = 2.04$) and phosphorus ($\chi(\text{P}) = 2.19$) are closer to those of transition metals than the other light elements ($\chi(\text{C}) = 2.55$, $\chi(\text{N}) = 3.04$, $\chi(\text{O}) = 3.44$ and $\chi(\text{S}) = 2.58$), a more pronounced covalent or metallic character is therefore expected, associated with a better electron delocalization. On the contrary oxides present a more marked ionic character. Nitrides and carbides present an intermediate nature. Finally, silicides ($\chi(\text{Si}) = 1.90$) are generally considered as intermetallic compounds with a predominant metallic character for the bonding. As previously developed, the mechanism at stake for H_2 dissociation at the surface of the particle has two extreme descriptions: the homolytic dissociation and the heterolytic one. This distinction may be put in relation with the nature of the bonding in the material: heterolytic dissociation would be more often observed for ionic bonding, *i.e.*

for oxides, sulfides and eventually nitrides and homolytic for covalent and metallic compounds, *i.e.* phosphides, carbides, silicides, borides and eventually nitrides.

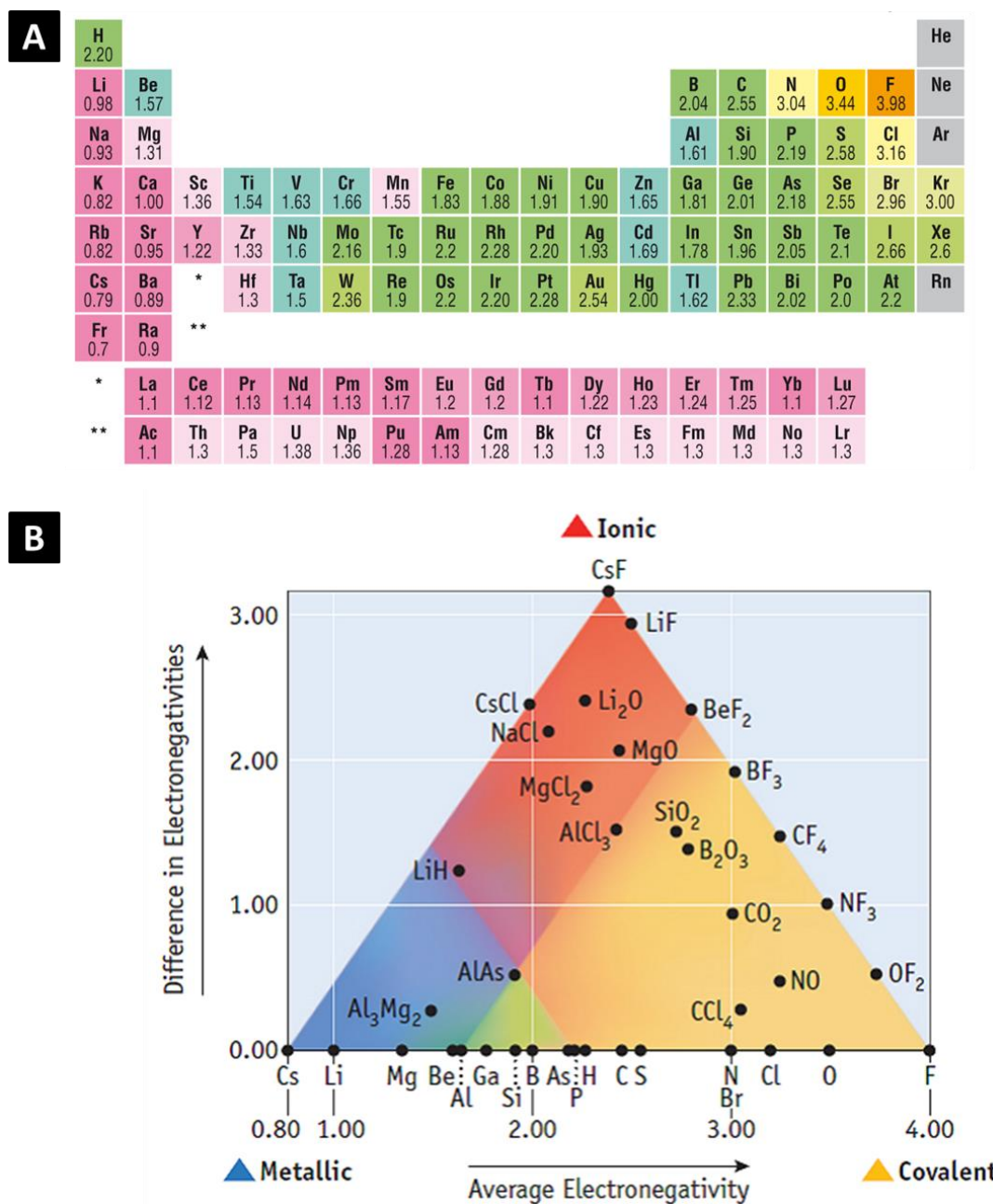


Figure 10. (A) Pauling electronegativities of elements. (B) Van Arkel-Ketelaar triangle.

I.3.1 Metal borides

Boron alloys of nickel and cobalt have been extensively reported for hydrogenation reactions, including HDO, HDS and HDN processes.^{56,58,60,61} Works mentioning metal borides generally do not refer to a specific crystallographic phase but

rather to amorphous nanoscale materials. If such, they are denoted M–B where M is the metal. A high number of the reactions were performed with substrates in the gas phase but we can nonetheless stress the use of Ni–B and Co–B alloys for hydrogenation of sulfolene, sugars (glucose, fructose, maltose), aldehydes and ketones (furfural, crotonaldehyde, benzaldehyde, cinnamaldehyde), nitro compounds and nitriles in solvent, all summarized by the reviews of Tao *et al.* and Sanchez *et al.*^{58,61} For instance, the hydrogenation of nitrobenzene was reported with amorphous nickel boride, Ni–B, under mild conditions (90 °C, 10 bar H₂, EtOH),⁶² and that of citral with Co₂B/Ni₇B₃ (150 °C, 15 bar H₂, hexane). Different chemoselectivities were obtained in the last case: Co₂B preferentially hydrogenates C=O bonds while Ni₇B₃ is selective for C=C bonds.¹⁸

Ref.	Material	Substrate	Solvent	P(H ₂)	T, t
Borides					
18	Co ₂ B	Citral (C=O)	Hexane	15 bar	150 °C, 4 h
18	Ni ₇ B ₃	Citral (C=C)	Hexane	15 bar	80-150 °C, 4 h
63	Ni–B	Nitrobenzene	MeOH	4 bar	65-100 °C, 2 h
62	Ni–B	Nitrobenzene	EtOH	10 bar	90 °C, <i>n.a.</i>
Silicides					
64,65	NiSi _x	Phenylacetylene	EtOH	4 bar	50 °C, 5 h
66	Ni ₂ Si	Nitroarenes/Nitriles Aldehydes/Ketones Alkenes/Alkynes	H ₂ O/MeOH	10- 50 bar	40-130 °C, 20 h
67	M ₂ Si (Fe, Co, Ni)	Cinnamaldehyde	EtOH	10 bar	90 °C, 4 h
Phosphides					
68	Fe ₂ P@C	Nitroarenes	H ₂ O/THF	50 bar	120 °C, 12 h
69	Co ₂ P/CN _x	Nitroarenes	H ₂ O/THF	50 bar	60 °C, 6 h
70	Co ₂ P	Nitriles	iPrOH/NH ₃	1-40 bar	130-150 °C, 20 h
71	Co ₂ P	Furfural	H ₂ O	40 bar	130 °C, 2 h
72	Co ₂ P	Aldehydes/Ketones	H ₂ O/NH ₃	1-10 bar	100 °C, 6-48 h
49	Ni ₂ P	Alkynes	Dioxane	6 bar	85 °C, 10 h
73	Ni ₂ P	Nitroarenes	EtOH	10 bar	80 °C, 10 h
74,75	Ni ₂ P/MO _x	Maltose/Glucose	H ₂ O	1-20 bar	r.t.-100 °C, 24 h
76	Ni ₂ P, Ni ₅ P ₄	Alkynes	Toluene	10- 20 bar	30-70 °C, flux

Table 1. Examples of hydrogenation reactions in solvent catalyzed by metal borides, silicides and phosphides.

I.3.2 Metal silicides

The use of metal silicides compounds in catalysis was recently reviewed by Liang *et al.*⁵⁷ Their use in HDS reaction is considered in particular due to the high stability of the materials toward H₂S poisoning, even higher than that of carbides, nitrides and phosphides. Fewer works reported HDO reactions: Ni₂Si was used for lignin and diphenylether hydrogenation. As to fine chemistry, different metal silicides M₂Si@C (M = Fe, Co, Ni) were reported for the selective hydrogenation of cinnamaldehyde with a selectivity echoing that reported for the metal borides: Co₂Si@C preferentially hydrogenates polar C=O bonds, to the contrary of Ni₂Si@C, more active on C=C bonds.⁶⁷ Cobalt silicides (CoSi and CoSi₂), obtained by pyrolysis of CoCl₂ and Si, were proved to hydrogenate phthalic anhydride in the liquid phase (180-220 °C, 40 bar H₂, 4-hydroxybutanoic lactone).⁷⁷ The semi-hydrogenation of phenylacetylene in styrene was achieved with various Ni-Si compounds (NiSi₂, NiSi, Ni₂Si) under mild conditions (50-80 °C, 4-10 bar of H₂, EtOH).^{64,65} Finally, Beller *et al.* reported the use of nickel silicide catalysts for the hydrogenation of a large scope of substrates including nitroarenes, aldehydes, ketones, nitriles, quinolines, alkenes and alkynes (40-130 °C, 10-50 bar H₂, H₂O/MeOH mixture).⁶⁶ The catalyst was produced by pyrolysis of [Ni(OAc)₂] and 1,10-phenanthroline on metal oxides.

I.3.3 Metal phosphides

The introduction of phosphorus atoms into metals, also termed “phosphorus-alloying (P-alloying)” was found to significantly improved the catalytic activity of the parent metal for H₂ activation. Two roles were identified for the phosphorus: first, the stabilization of the metallic character of the catalyst in air, which is not the case for the purely metallic compounds, and then, the ligand effect previously described. DFT calculations indeed reveal the insertion of P increases the *d*-electron density near the Fermi level of the material.⁷³ The use of different binary and ternary metal phosphides (Ni-P, Co-P, Fe-P, Mo-P, W-P, Ni-Mo-P) for high temperature HDO of vegetal oils, phenol, anisole and guaiacol and for hydrotreating reactions has been reviewed by Sanchez *et al.*⁵⁸

Iron phosphide. Wan *et al.* reported the use of a carbon supported iron phosphide Fe₂P@C for hydrogenation of nitroarenes in anilines (120 °C, 50 bar, H₂O/THF mixture).⁶⁸ The catalyst was synthesized by pyrolysis of phosphorus-containing Fe-MOF (Metal Organic Framework) at 900 °C. This is to the best of our knowledge the only occurrence of iron phosphide catalyst for hydrogenation reaction if we exclude the hydrotreatment ones.

Cobalt phosphide. The first mention of the use of cobalt phosphide for colloidal hydrogenation is the work by Queen *et al.* on the hydrogenation of nitroarenes in anilines (60 °C, 50 bar H₂, H₂O/THF mixture).⁶⁹ The catalyst was synthesized by

pyrolysis of MOF nanocubes with red phosphorus to produce a $\text{Co}_2\text{P}/\text{CN}_x$ composite. The authors performed a hot extraction experiment which confirmed the catalysis is heterogeneous and does not occur through molecular species which would have leached from the nanoparticles. Jitsukawa *et al.* reported the use of cobalt phosphide Co_2P for the hydrogenation of aliphatic and aromatic nitriles in primary amines ($130\text{ }^\circ\text{C}$, 1 bar H_2 , $i\text{PrOH}$) (Figure 11A).⁷⁰ The nanoparticles were synthesized *via* a solvothermal route with CoCl_2 in hexadecylamine, 1-octadecene and triphenylphosphite. Cobalt phosphide CoP also displayed a catalytic activity although lower than Co_2P (Figure 11C). Other phosphides such as Ni_2P , Fe_2P and Cu_3P did not lead to any hydrogenation under similar conditions. DFT calculations indicated the free energy for the adsorption of H_2 on Co_2P is $\Delta_{\text{ads}}G = -1.13\text{ eV}$, which is even larger than on metallic Co. Once adsorbed on a *t* site (phosphorus atom), the H–H bond length increased from 0.79 \AA to 2.02 \AA , indicating a kinetically favored H_2 dissociation, in agreement with the experimental results. The good catalytic activity of Co_2P was attributed by spectroscopic studies to its metallic nature and to the increase in *d*-electron density near the Fermi level due to the phosphidization of Co. The use of ammonia as part of the solvent mixture was not discussed in the article even though it may be considered as a hydrogen donor. A similar catalyst was used for furanic aldehydes hydrogenation ($130\text{ }^\circ\text{C}$, 40 bar H_2 , H_2O).⁷¹ Finally, Mitsudome *et al.* recently reported the use of Co_2P nanorods, synthesized *via* a solvothermal pathway, for the reductive amination of carbonyl compounds ($100\text{ }^\circ\text{C}$, 1-10 bar H_2 , $\text{H}_2\text{O}/\text{NH}_3$).⁷²

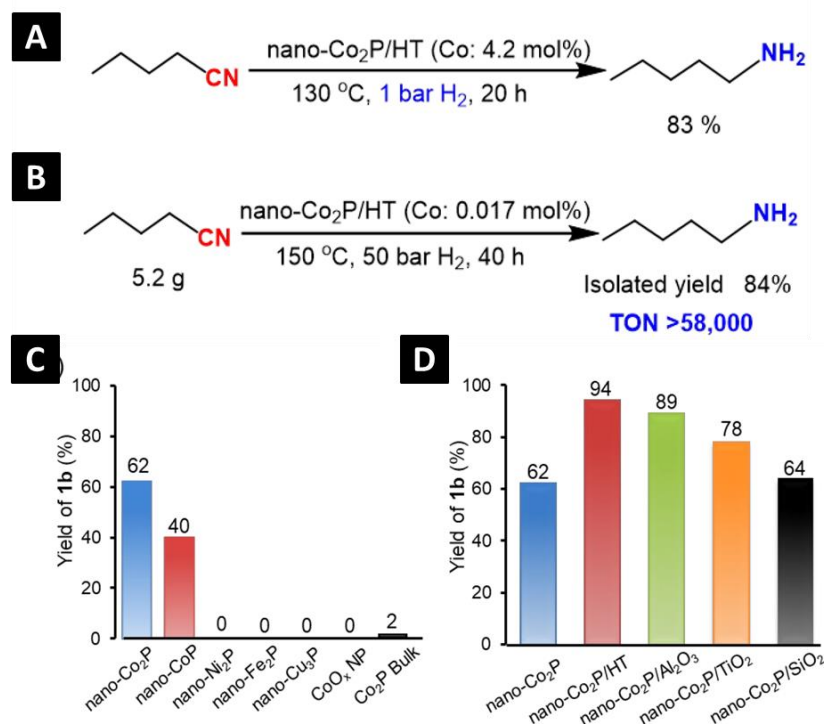


Figure 11. (A) Hydrogenation of pentanenitrile **1a** under ambient pressure of H_2 and (B) gram scale experiment. (C) Catalytic performance of various metal phosphides and Co oxide

nanoparticles in hydrogenation of **1a**. (D) Catalytic performance of nano-Co₂P and nano-Co₂P on different supports. Reaction condition: catalyst (metal: 4.2 mol%), **1a** (0.5 mmol), iPrOH (3 mL), NH₃ aq. (1.2 mL), 130 °C, 40 bar H₂, 1 h. Adapted from reference [70].

Nickel phosphide. Among the first works on colloidal hydrogenation with metal phosphides, Zhang *et al.* reported the possible use of silica supported nickel phosphides (Ni₂P and Ni₁₂P₅) for the selective reduction of cinnamaldehyde in hydrocinnamaldehyde (120 °C, 30 bar H₂, cyclohexane).⁷⁸ The selectivity for the C=C reduction rather than the C=O reduction was high (90 %). The others metal phosphides which were investigated (Fe₂P, CoP, Co₂P, MoP, WP) led to much lower yields (< 4 % *versus* 50-80 % for Ni-P). A few years later, Corma *et al.* demonstrated the catalytic activity of Ni₂P nanoparticles for the hydrogenation of phenylacetylene and styrene (85 °C, 6 bar H₂, dioxane).⁴⁹ The catalyst was found to be chemoselective for the formation of alkene and not alkane, to the contrary of Ni(0) catalysts. Pérez-Ramírez also reported the activity of Ni₂P and Ni₅P₄ in continuous-flow three-phase semi-hydrogenation of terminal alkyne (30-70 °C, 10-20 bar H₂, toluene).⁷⁶ The catalysts displayed an induction time of 2 h, attributed to the reduction of the oxide layer covering the surface, but then reached stable performance on stream for more than 24 h. They in particular studied the evolution of the reaction rates as a function of pressure and temperature. The use of Ni₂P as hydrogenating catalyst was then extended to nitroarenes in mild conditions (80 °C, 10 bar H₂, EtOH) by Zou *et al.*⁷³ The authors stressed the difficulty in releasing the H atoms once these are adsorbed at the surface of Ni₂P due to its strong affinity. To circumvent this issue, they suggest to tune the *d*-band of Ni by anchoring the nanoparticles on phosphorus-doped carbon (PC). DFT calculations confirmed the electron donation of carbon toward Ni. Consequently, the desorption energy of H decreased from -1.12 eV to -0.56 eV in Ni₂P/PC and the Ni-H bond length increased from 1.65 Å to 1.9 Å, making the properly said hydrogenation step more thermodynamically and kinetically favorable. Finally, Mitsudome *et al.* reported the possible use of metal oxide supported Ni₂P nanoparticles for the hydrogenation of sugars (glucose, maltose) in polyols under mild conditions (r.t.-100 °C, 1-20 bar, H₂O).^{74,75}

I.3.4 Metal carbides and nitrides

Metal carbides and nitrides are generally studied and commented together concerning their catalytic applications. They indeed display similar crystalline phases with close electronic configurations.^{7,12,56,79} One has to pay attention to the possibility of incorporating other atoms to form ternary phases. For instance, Mo₂C, W₂C and WC are known to incorporate O, N and S atoms, at least on the extreme surface of the catalyst, during respectively HDO, HDN and HDS reactions.⁷ This issue is nonetheless not necessarily critical as catalyst deactivation is generally limited. Tungsten

monocarbide (WC) was investigated for hydrogenation reactions by Levy and Boudart in 1973.⁸⁰ They elucidated the electronic structure of the material and highlighted its similarity with platinum. They thus reported the gas phase reduction of butadiene in butene. Unfortunately, WC activity is observed only at relatively high temperatures (150 °C to 400 °C) and WC as a stand-alone catalyst is rarely mentioned. Interesting results were nonetheless obtained when WC was doped with Ni or Co in particular for hydrodeoxygenation reactions. Group VI metal carbides (α -MoC, β -Mo₂C, WC and W₂C) are efficient catalysts for biomass derived molecules hydrogenation but mainly in the gas phase.⁸¹ Dongil recently reviewed the use of metal nitrides in heterogeneous catalysis.⁵⁹ The nitridation of metals of end of transition (Fe, Co, Ni, Cu) being more difficult than early transition metals, most of the works on hydrogenation reactions with metal nitrides focus on molybdenum and tungsten nitrides.¹²

Ref.	Material	Substrate	Solvent	P(H ₂)	T, t
Carbides					
82	α -MoC, β -Mo ₂ C	Furfural	Alcohol	10-20 bar	150 °C, 6 h
83	WC	Nitroarenes, Phenylacetylene	EtOH	10 bar	100 °C, flux
Nitrides					
84	β -Mo ₂ N	Nitroarenes	EtOH	11 bar	150 °C, flux
82	γ -Mo ₂ N	Furfural	Alcohol	10-20 bar	150 °C, 6 h
24	γ -Mo ₂ N-H _x	Crotonaldehyde	EtOH	<i>n.a.</i>	70 °C, 1 h
85	CoN _x /CN	Phenols	Dodecane	20 bar	200 °C, 2 h
86	CoN _x /CN	Nitroarenes	H ₂ O	5 bar	110 °C, 1 h
87	CoN _x	Nitroarenes	Scope	1-3.5 bar	40-110 °C, 12 h
88	Ni ₃ N	Benzonitrile Nitrobenzene	EtOH	25 bar	50-150 °C, flux
89	Ni ₃ N	Alkyne	EtOH	20 bar	100 °C, 5 h

Table 2. Examples of hydrogenation reactions in solvent catalyzed by metal carbides and nitrides.

Early transition metals. In the 1970s, Horányi *et al.* reported a series of works mentioning the catalytic activity of WC for the liquid-phase hydrogenation of organic compounds.⁹⁰⁻⁹² Even though the reaction temperature was only of 40-90 °C, the conditions were relatively harsh as the medium was a solution of sulfuric acid (H₂SO₄). The authors reported the reduction of nitroarenes and quinones but not of C=C nor C≡C bonds. To the best of our knowledge, the reactions were not reproduced. Later, nanostructured WC was reported for nitroarenes hydrogenation to aromatic amines

under mild conditions in continuous flow (100 °C, 10 bar H₂, EtOH).⁸³ The reaction was chemoselective as no reduction of C=C, C=O or C≡N bonds occurred. Ma *et al.* recently disclosed the furfural hydrogenation in furfuryl alcohol (FAL) and in 2-methylfuran (2-MF) by α -MoC and β -Mo₂C (150 °C, 10-20 bar H₂, alcohol).⁸² Depending on the molecular size of the alcohol, the product selectivity was different: 95 % of 2-MF were obtained with 2-butanol *versus* 95 % of FAL with MeOH (Figure 12A). The reaction required a pressure of H₂ to proceed but the alleged mechanism relies on a hydrogen transfer *via* the solvent (Figure 12B).

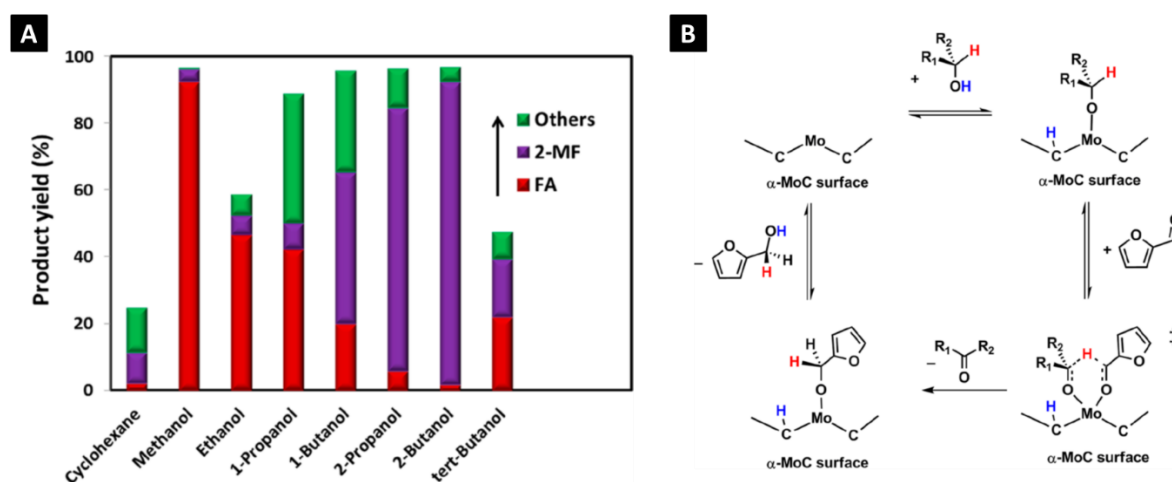


Figure 12. (A) Solvent effects on product yields of furfural hydrogenation on α -MoC catalysts (150 °C, 20 bar H₂, 1 mL furfural, 50 mL solvent, 150 mg α -MoC, 6 h; FA for furfuryl alcohol, 2-MF for 2-methyl furan). (B) Plausible Pathway for Transfer Hydrogenation of Furfural by an Alcohol on α -MoC Surfaces. Reproduced from reference [82].

Keane *et al.* reported the first use of molybdenum nitride, β -Mo₂N for liquid phase hydrogenation of nitroarenes in flux (150 °C, 11 bar H₂, EtOH).⁸⁴ The nitridation of metallic Mo is thought to be responsible for the good catalytic activity of Mo₂N. Indeed, the interstitial nitrogen atoms led to a higher d -electron density at the Fermi level and therefore an increased capacity for H₂ adsorption. The H₂ adsorption and dissociation on Group VI metal nitrides is not yet perfectly understood but several authors suggest a heterolytic dissociation on nitrogen deficient sites. H₂ chemisorption experiments led to the hypothesis of the formation of a stable hydride phase in the nitride sub-surface. This hypothesis was also formed by Thompson *et al.* who studied the H₂ uptake by γ -Mo₂N and the use of the formed compound, γ -Mo₂N-H_x, for the hydrogenation of crotonaldehyde.²⁴ Finally, Ma *et al.* reported the possible use of both phases, β -Mo₂N and γ -Mo₂N, for furfural hydrogenation in 2-methylfuran and furfuryl alcohol (150 °C, 20 bar H₂, iPrOH).⁸²

Late transition metals. We could not find any mention of a carbide of Fe, Co, Ni or Cu as a catalyst for H₂ activation in solvent, though the catalytic activity of some of these materials for Fischer-Tropsch process has been studied. Cobalt nitrides, CoN_x, were reported by Zhang *et al.* for hydrodeoxygenation of lignin-derived phenols (200 °C, 20 bar H₂, dodecane).⁸⁵ The catalyst was obtained by pyrolysis of Co(NO₃)₂ and cellulose. The authors also reported a cobalt nitride catalyst obtained by calcination of cobalt phthalocyanine for the hydrogenation of large scope of nitroarenes under very mild conditions (40-110 °C, 1-3.5 bar H₂), quantitative conversions were reached at 110 °C for many solvents (H₂O, THF, CH₃CN, EtOH, iPrOH, toluene, EtOAc).⁸⁷ A similar catalyst obtained by pyrolysis of Ce(NO₃)₂ and histidine over silica was used for nitroarenes hydrogenation (110 °C, 5 bar H₂, H₂O).⁸⁶ The most common nickel nitride phase, Ni₃N, was also reported by Giordano *et al.* for its hydrogenation activity toward nitrobenzene and benzonitrile (50 °C, 25 bar H₂, EtOH).⁸⁸ This material is however metastable: a treatment at 250 °C in a H₂/Ar (3:1) flux leads to the release of nitrogen as N₂ and NH₃ and Ni₃N totally decomposes at temperatures beyond 400 °C.⁹³ Bai *et al.* also reported the use of Ni₃N anchored on an N-doped carbon for the semi-hydrogenation of alkynes in alkenes (100 °C, 20 bar H₂, EtOH).⁸⁹

1.3.5 Metal oxides

Cerium oxide. While the use of ceria CeO₂ for nitroarenes hydrogenation was already mentioned with hydrazine as H source, the use of CeO₂ for H₂ activation in the liquid phase was first reported by Pérez-Ramírez *et al.* for a continuous flow alkyne hydrogenation by metal oxide supported CeO₂.⁹⁴ The catalyst was obtained by wet impregnation of TiO₂, Al₂O₃ or ZrO₂ with an acidified solution of cerium ammonium nitrate. XPS measurements indicated a Ce(III) percentage of 28 % at the surface of the catalyst. Alkyne conversions superior to 80 % were obtained only for H₂ pressures superior to 50 bar and for temperatures beyond 140 °C in toluene. However, the selectivity towards the alkenes was excellent for both aliphatic and aryl alkynes. Later, highly defective cerium oxide nanoparticles were reported by Qu *et al.* for their hydrogenation catalytic activity of alkenes and alkynes under milder conditions (6 bar, 100 °C, toluene) following a heterolytic dissociation mechanism (Figure 13).⁹⁵ The surface defects on cerium oxide are typically associated with surface Lewis acidic sites, composed of two adjacent Ce(III) atoms (Ce_I and Ce_{II} on Figure 13a), and basic sites, composed of surface lattice oxygens (O_{IIc}). The developed catalyst, termed PN-CeO₂ and presenting a Ce(III) surface fraction of 30 %, was in capacity to hydrogenate styrene but the activity was quenched in presence of Lewis acids or bases (pyrrole, pyridine) likely due to their adsorption on the Ce_I, Ce_{II} and O_{IIc} sites (Figure 13d). DFT calculations on ideal and reduced CeO₂(110) surfaces revealed the activation barrier for the heterolytic splitting of H₂ is lower for a defective structure (0.17 eV) than for an ideal one (0.65 eV) (Figure 13e).

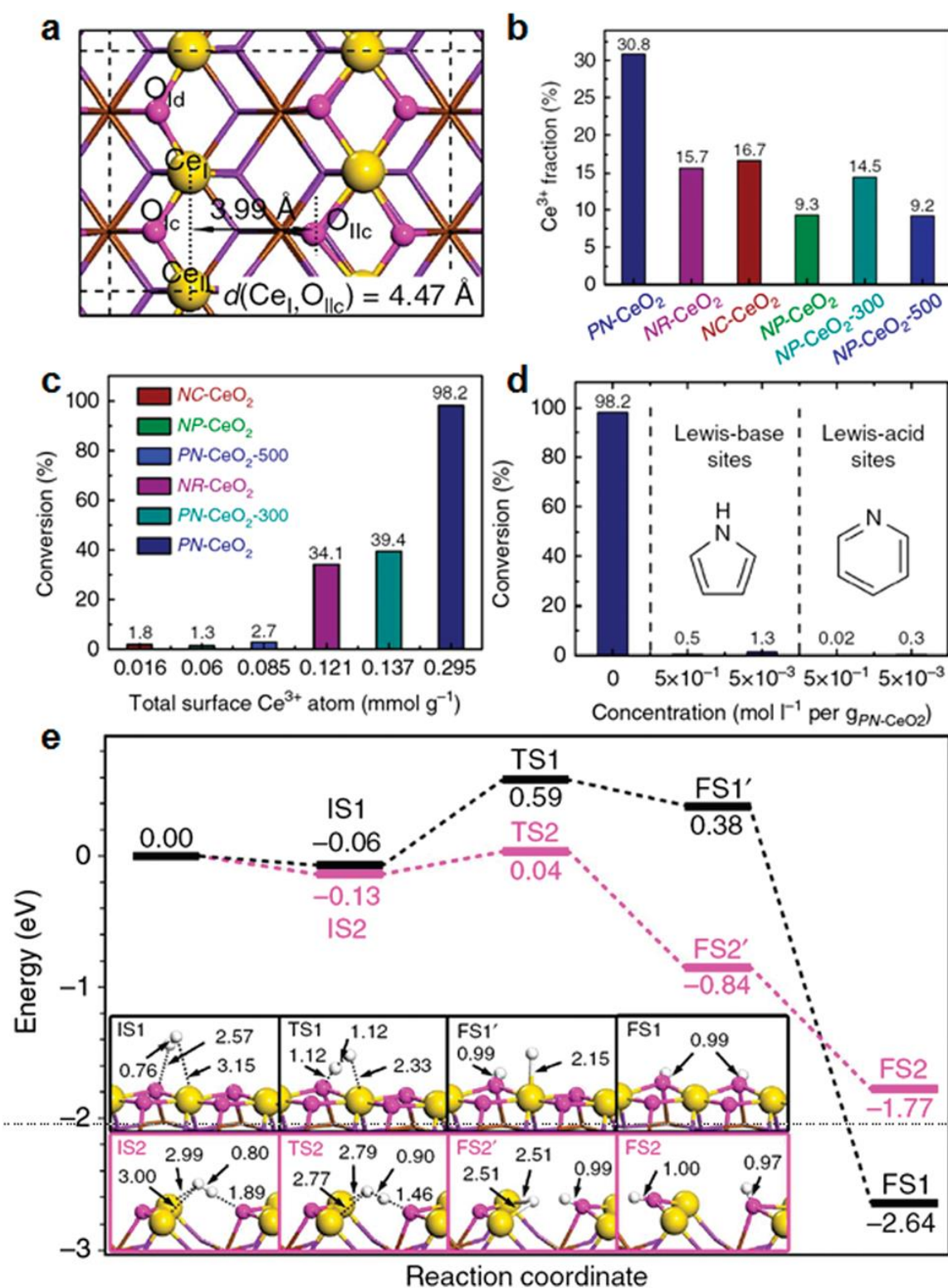


Figure 13. Surface regulations on CeO₂ for the construction of surface FLP-like catalytic sites and their performance for hydrogenation. (a) DFT calculations on the possibility by the surface regulations for the formation of independent surface Lewis acidic sites and Lewis basic sites on CeO₂(110) and the construction of surface FLP sites. (b) Surface fractions of Ce³⁺ for various CeO₂. (c) Catalytic hydrogenation activity versus the surface fractions of Ce³⁺. Reaction conditions: styrene (1.0 mmol), toluene (0.5 ml) and catalysts (20.0 mg) at 100 °C, 10 bar H₂, 14 h. (d) Influences of a molecular Lewis-base or Lewis-acid on the

catalytic activity of CeO_2 for the hydrogenation of styrene. (e) Energy profiles for H_2 dissociation on ideal $\text{CeO}_2(110)$ in the black curve and $\text{CeO}_2(110)$ with two oxygen vacancies in the red curve. The optimized structures of the initial states (IS), transition states (TS) and final states (FS) are labelled with bond distances (in Å). Reproduced from reference [95].

Ref.	Material	Substrate	Solvent	P(H_2)	T, t
Oxides					
96	$\text{WO}_{2.72}$	Alkenes	Cyclohexane	30 bar	100 °C, 3 h
96	$\text{WO}_{2.72}$	Nitroarenes	EtOH	30 bar	120 °C, 5 h
94	CeO_2/MO_x	Alkynes	Toluene	50 bar	140 °C, flux
95	CeO_{2-x}	Alkenes/Alkynes	Toluene	6-30 bar	100 °C, 14 h
97	$\gamma\text{-Fe}_2\text{O}_3$	Nitroarenes	$\text{H}_2\text{O}/\text{THF}$	50 bar	120 °C, 12 h
98	$\alpha\text{-Fe}_2\text{O}_3$, FeO , $\gamma\text{-Fe}_2\text{O}_3$, Fe_3O_4	Nitroarenes	$\text{H}_2\text{O}/\text{THF}$	30 bar	150 °C, 10 h
99,100	Co_3O_4	N-heteroarene, Nitriles, Aldehydes/Ketones	Toluene EtOH iPrOH	20-40 bar	100-130 °C, 20 h
Sulfides					
101	FeS_2	Nitroarenes	iPrOH	5 bar	60 °C, 7 h
102	NiS , Ni_7S_6 , Ni_4S_3	Nitrobenzene	EtOH	40 bar	150 °C, 24 h
103	FeS_2 , NiS_2 , CoS_2	Nitroarenes	MeOH	30 bar	110 °C, 12 h
104	MoS_2	Nitrobenzene	Toluene	30 bar	100 °C, 6 h
105	MoS_2	Nitroarenes	EtOH	20 bar	120 °C, 5 h
106	WS_2	Nitroarenes	$\text{H}_2\text{O}/\text{THF}$	20-50 bar	120 °C, 12 h

Table 3. Examples of hydrogenation reactions in solvent catalyzed by metal oxides and sulfides.

Tungsten oxide. In the case of tungsten trioxide WO_3 , DFT calculations show the adsorption of H_2 is unfavorable on $\text{WO}_3(001)$ ($\Delta_{\text{ads}}G = 0.436$ eV) and that the activation energy of the H_2 cleavage is high ($E_{\text{act}} = 1.643$ eV), in agreement with the low increase in H–H bond length (from 0.749 Å to 0.759 Å).⁹⁶ On the contrary, oxygen-deficient tungsten oxide $\text{WO}_{2.72}(001)$ leads to a favorable adsorption ($\Delta_{\text{ads}}G = -0.346$ eV) and a lower energy barrier for H_2 cleavage ($E_{\text{act}} = 0.902$ eV), in agreement with the larger weakening of the H–H bond (from 0.749 Å to 1.392 Å). These results clearly indicate that the presence of oxygen vacancies increases the hydrogenation catalytic activity of WO_3 . The calculations are validated by experimental data: $\text{WO}_{2.72}$ hydrogenates alkenes and nitroarenes under moderate conditions in ethanol or

cyclohexane (30 bar H_2 , $< 150\text{ }^\circ\text{C}$). Interestingly, the catalyst presents a better hydrogenation selectivity than $\text{Ni}(0)$ when several groups are present on the substrate molecule: for instance, $\text{WO}_{2.72}$ does not hydrogenate $\text{C}=\text{C}$ in aromatic rings where $\text{Ni}(0)$ does. We can nonetheless remind the propension of tungsten oxide to be *in situ* reduced by H_2 to form bronze phases H_xWO_3 .

Late transition metals. Beller *et al.* reported the use of iron oxide $\gamma\text{-Fe}_2\text{O}_3$ for the chemoselective hydrogenation of nitroarenes ($120\text{ }^\circ\text{C}$, 50 bar of H_2 , $\text{H}_2\text{O}/\text{THF}$ mixture).⁹⁷ The catalyst was produced by pyrolysis of $[\text{Fe}(\text{OAc})_2]$ and 1,10-phenanthroline on metal oxides. Based on X-ray photoelectron spectra of the N 1s region, the authors suggest the formation of FeN_x centers in addition of the iron oxide. These results were extended to different iron oxides, $\alpha\text{-Fe}_2\text{O}_3$, $\gamma\text{-Fe}_2\text{O}_3$, FeO and Fe_3O_4 , by Zou *et al.* in similar conditions ($150\text{ }^\circ\text{C}$, 30 bar H_2 , $\text{H}_2\text{O}/\text{THF}$ mixture).⁹⁸ The catalysts were prepared from FeCl_3 and ethylene glycol followed by a calcination step and displayed a microflower morphology. The normalized catalytic activity of all the iron oxides were in the same range. While $\alpha\text{-Fe}_2\text{O}_3$, FeO and Fe_3O_4 displayed similar activities for the first and the second run of the reaction, that of $\gamma\text{-Fe}_2\text{O}_3$ increased in the second run of the reaction. This effect was attributed to the partial reduction of the material according to XPS. Interestingly, phenylacetylene was quantitatively hydrogenated in styrene by Fe_3O_4 at $120\text{ }^\circ\text{C}$. Following a similar catalyst synthesis, Beller *et al.* also disclosed the catalytic activity of Co_3O_4 for the hydrogenation of quinolines and N-heteroarenes ($120\text{ }^\circ\text{C}$, 20-40 bar H_2 , toluene), and of nitriles, ketones and aldehydes ($100\text{-}130\text{ }^\circ\text{C}$, 20-40 bar H_2 , EtOH or iPrOH).^{99,100} The catalyst was produced by calcination of $[\text{Co}(\text{OAc})_2]$ with 1,10-phenanthroline over $\alpha\text{-Al}_2\text{O}_3$. As for iron oxide, CoN_x centers were detected by XPS.

I.3.6 Metal sulfides

As for metal oxides, both heterolytic and homolytic mechanisms are detected for H_2 activation on metal sulfides with a high importance given to structural defects. The topic has been reviewed in 2002 by Breysse *et al.*¹¹ The authors covered the most conventional catalysts, MoS_2 and WS_2 , eventually doped with Ni or Co, but also noble metal sulfides such as RuS_2 . Although the study concerns hydroprocessing and gas phase H_2 activation, most of the concepts may be applied to liquid phase hydrogenation. The presence of sulfhydryl S-H was evidenced by different spectroscopic techniques (IR, INS, MAS NMR) but the existence of M-H bonds is less convincing. The main point concerning MoS_2/WS_2 is the importance of the sulfur vacancies: the optimal Sulfur/Metal ratio for H_2 activation was determined to be 1.95 and not 2. On near stoichiometric sulfides, the predominant mechanism for H_2 activation is the homolytic dissociation on two sulfur atoms. The heterolytic dissociation mechanism involves sulfur atoms and coordinatively unsaturated metal sites (CUS) and are therefore not favored on stoichiometric materials. At high temperatures, one of the main limitations

of sulfur-defective MoS₂/WS₂ is the progressive substitution of sulfur atoms by oxygen atoms, provided by water traces for instance, which deactivate the surface. The activity is maintained by addition of H₂S or CS₂ in the reaction feed.

Early transition metals. Molybdenum and tungsten disulfides have been extensively studied for hydroprocessing or electrocatalysis but more rarely for hydrogenation reaction in the liquid phase in soft conditions. Two recent works report the use of sulfur deficient molybdenum disulfide (MoS_{2-x}) for the hydrogenation of nitroarenes. In the first one, by Xie *et al.*, MoS_{2-x} microflowers efficiently hydrogenated nitrobenzene in aniline (100 °C, 30 bar H₂, toluene).¹⁰⁴ Commercial MoS₂ displayed a lower, though non-negligible, activity under similar conditions. The authors attributed the enhanced activity of the sulfur deficient MoS₂ to the higher number of coordinatively unsaturated Mo sites and proposed a heterolytic splitting of H₂, resulting in the formation of Mo–H and S–H. In the second work, a one-pot nitro-reduction and reductive amination yielding a secondary amine was studied.¹⁰⁵ A nitroarene Ar₁-NO₂ and a benzaldehyde derivatives Ar₂-CHO react to form Ar₁-NH-CH₂-Ar₂ (120 °C, 20 bar H₂, EtOH). The authors also showed nitrobenzene was quantitatively hydrogenated in aniline in absence of aldehyde. The catalyst was exposed to different pretreatments and the authors correlated a high activity with a high number of sulfur and molybdenum vacancies. DFT calculations in this study revealed the adsorption free energy of H₂, $\Delta_{\text{ads}}G$, gradually decreased from -0.5 eV to -1.3 eV when sulfur vacancies were added to the model. In the meantime, the adsorption energy of the substrates also decreased, making the whole reaction thermodynamically more favorable. Schaak *et al.* reported the use of defect-rich WS₂ nanostructures for the hydrogenation of a broad scope of nitroarenes (120 °C, 20-50 bar H₂, H₂O/THF mixture).¹⁰⁶ As for metal oxides and MoS₂, the defects play an important role both for the activity of the material and for the good selectivity towards nitro group hydrogenation. Considering the higher proportion of defects in nanostructures than in bulk, the authors recommended the use of MoS₂ and WS₂ nanosheets and indeed, the same reaction with bulk WS₂ did not lead to any conversion. These two materials (MoS₂ and WS₂) are in particular known for the near-zero free energy of adsorption of H₂ on edge and defect sites ($\Delta_{\text{ads}}G \approx 0$ eV), *i.e.* the adsorption step is not thermodynamically limiting. DFT calculations showed the rate-determining step with WS₂ was the transfer of the hydrogen to the adsorbed substrate ($E_{\text{act}} = 0.97$ eV).

Late transition metals. A few examples of late transition metal sulfides were reported, mainly with Fe and Ni. Recent work by Guo *et al.* reported the catalytic activity of iron disulfide (FeS₂) nanoparticles, or pyrite, for nitroarenes hydrogenation (60 °C, 5 bar H₂, iPrOH).¹⁰¹ The catalyst was synthesized by solvothermal route from FeCl₂ and elemental sulfur. A negative adsorption enthalpy for H₂ was obtained by DFT calculations for the three possible configurations: both H on a Fe site ($\Delta_{\text{ads}}G = -0.91$ eV), both H on a S site ($\Delta_{\text{ads}}G = -0.29$ eV) or one H on S and one on Fe ($\Delta_{\text{ads}}G$

= -1.11 eV). H₂-TPD experiment indicated an adsorption energy of -0.97 eV, coherent with the DFT calculations. Schaak *et al.* extended these results to bulk off-the-shelf FeS₂ though under stronger conditions (120 °C, 50 bar H₂, H₂O/THF mixture).¹⁰⁷ The authors in particular stressed the selectivity towards other insaturations (C=C, C=O, C≡C, C≡N) and the simplicity of this readily available catalyst. Finally, flowerlike nickel sulfides (NiS, Ni₃S₄, Ni₇S₆) microparticles were reported for chloronitrobenzene hydrogenation (150 °C, 40 bar H₂, EtOH).¹⁰² Their syntheses were performed with NiCl₂ in a water/ethanolamine mixture with thiourea as the sulfur source.

I.4. Toward the “NanoFLP” system

I.4.1 Frustrated Lewis Pair catalysis

At the beginning of the 2000s, the activation of H_2 and other small molecules in solvent was studied by Stephan, Erker *et al.* by the mean of Frustrated Lewis Pairs (FLP).¹⁰⁸ The principle of this homogeneous catalysis is to put in presence two molecules acting as a Lewis base (LB) and a Lewis acid (LA) whose reactive centers are both sterically hindered (Figure 14A). They typically consist in a tertiary phosphine (P^tBu_3 , PCy_3 , $PMes_3$) or an amine (lutidine, tetramethylpiperidine) and a tertiary borane ($B(C_6F_5)_3$) or an alumane ($Al(C_6F_5)_3$). The Lewis pair would be stabilized by forming a Lewis adduct LB–LA but the formation of such a molecular complex is hampered by the bulky groups present on the two species. A “reactive pocket” is nonetheless formed with a Lewis acidic and basic sides and this catalytic site may heterolytically cleave chemical bonds such as H–H or C–O (Figure 14B). In the case of H_2 , the activated proton and hydride subsequently react to hydrogenate different substrates such as an imine in the seminal work of Stephan *et al.* (Figure 14C).¹⁰⁹

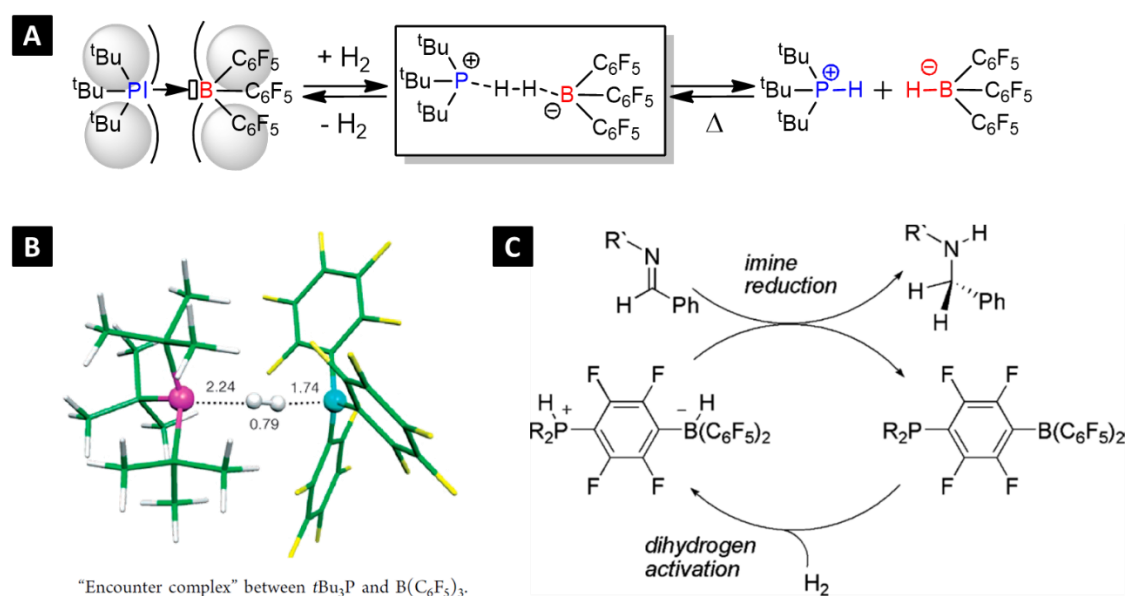


Figure 14. (A) Activation of H_2 *via* a Frustrated Lewis Pair. (B) Geometry of the encounter complex of P^tBu_3 and $B(C_6F_5)_3$ activating H_2 . (C) Hydrogenation of an imine after H_2 activation by FLP. Reproduced from references [108,109].

The FLP concept has been very fruitful these past two decades in homogeneous catalysis and has then reached the field of heterogeneous catalysis (Figure 15),¹¹⁰ although the formal attribution of these new catalytic systems to an FLP may be subject to discussion.¹¹¹ Different configurations were reported: (a-b) semi-solid systems

where either the base or the acid is a molecular species and (c-d) all-solid systems for which the basic and acid sites are both situated at the surface of the solid catalyst, the “frustration” originating from the rigidity of the atomic positions. For this last category, we can in particular mention the use of defective cerium oxides by Qu *et al.*^{95,112,113} (already mentioned in a previous section, Figure 13) and that of defective indium oxides by Ozin *et al.*^{111,114–116} This last case was briefly mentioned earlier in the characterization section (Figure 6A). The authors suggest the presence of oxygen vacancy sites is related to that of unsaturated surface In sites presenting a Lewis acid character. The H₂ molecule is then cleaved to form a hydridic In–H[–] and a protonic In–OH₂⁺ species. It was found a high concentration of oxygen defects increased the catalytic activity of the material.

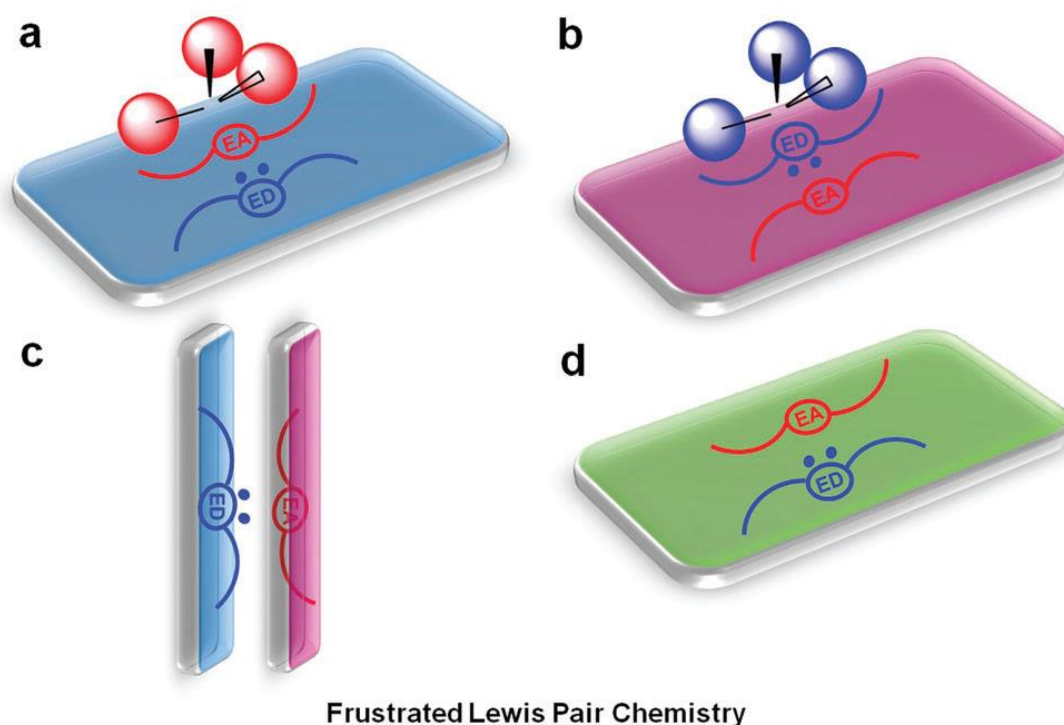


Figure 15. Schematic chemistry of semi-solid and solid FLPs: (a) semi-solid FLP catalyst with the combination of a molecular Lewis acid and a solid Lewis base; (b) semi-solid FLP catalyst with the combination of a molecular Lewis base and a solid Lewis acid; (c) all solid FLP catalyst based on a solid Lewis acid and a solid Lewis base; and (d) all solid FLP catalyst within one solid. Reproduced from [110].

I.4.2 Boosting the surface reactivity of nanoparticles with ligands

In a certain number of cases, the heterolytic cleavage of dihydrogen (H₂) on metallic or metal-containing nanoparticles in solvent is promoted *via* a metal-ligand cooperative mechanism: a Lewis basic site of the ligand binds the proton and the coordinated metal atom acts as a Lewis acid and takes the hydride.¹¹⁷ This mechanism naturally echoes the concept of semi-solid FLP with the combination of a Lewis base and a metal surface (Figure 15b). Few examples only were mentioned in literature but we will exemplify it with the case of gold surfaces.

Following the seminal work of Guo *et al.* on the hydrogenation of N-benzylidenemethylamine with Au powder (50 °C, 20 bar H₂, toluene),¹¹⁸ Rossi *et al.* reported the formation of active sites on Au nanoparticles *via* the addition of different N-containing bases (Figure 16A).¹¹⁹ The Au-piperazine system was found to be the most efficient and selective for the semi-hydrogenation of phenylacetylene in styrene with a Au:PhCCH:base molar ratio of 1:100:100. The complete reaction was achieved in 5 hours under mild conditions (80 °C, 6 bar H₂, EtOH), whereas no reactivity was observed without base. As described in Figure 16B, Rossi *et al.* proposed a mechanism inspired by the FLP chemistry: the H₂ molecules are heterolytically dissociated between the Au surface and the piperazine. The activation barrier for this step was estimated by DFT to be 0.32 eV, much lower than the activation on clean Au(111) surface (1.45 eV). The two following steps, *i.e.* the transfer of the hydride and of the proton on the alkyne, have activation barriers of respectively 0.74 eV and 0.13 eV. The authors of the study then reported the possible use of an Au@N-doped carbon/TiO₂ catalyst for the hydrogenation of biomass molecules (5-HMF and furfural) following a similar pathway.¹²⁰

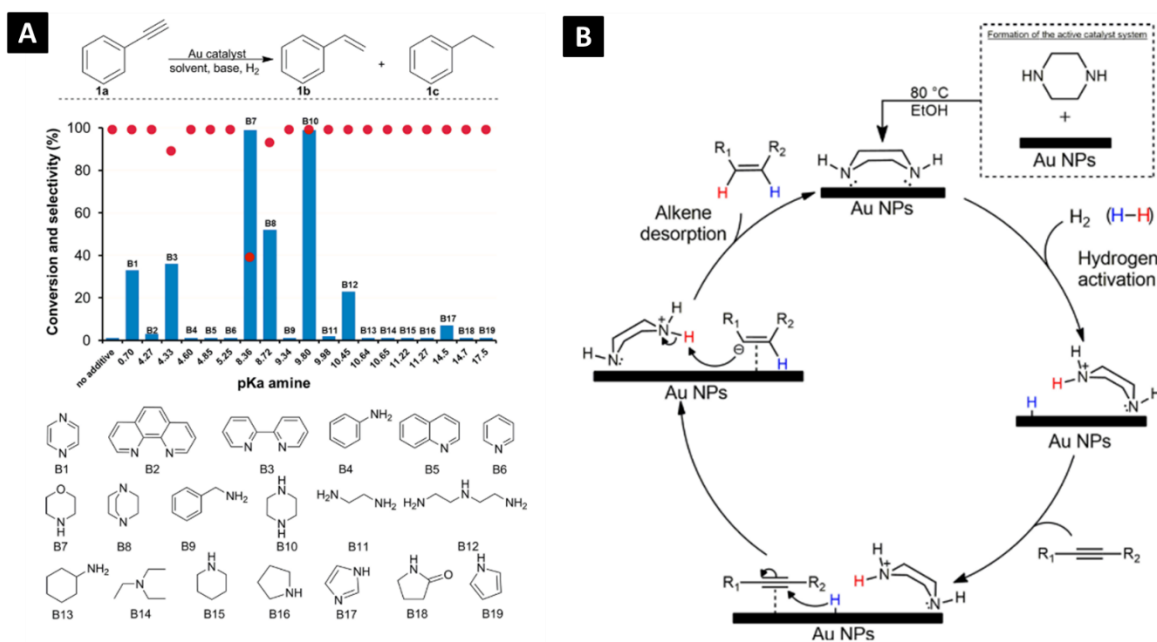


Figure 16. (A) Screening of nitrogen-containing bases for phenylacetylene hydrogenation with Au/SiO₂ catalyst. Reaction conditions: 1 mmol of 1a, 0.01 mmol of Au (50 mg of Au/SiO₂), 1 mmol of amine, 2 mL of ethanol, 100 °C, 6 bar of H₂, 24 h. (B) Proposed mechanism for gold-catalyzed catalytic hydrogenation of alkynes into cis-alkenes via a frustrated Lewis pair approach. Reproduced from [119].

Van Leeuwen *et al.* developed a similar system with the use of a Secondary Phosphine Oxide (SPO) ligand placed on the surface of gold nanoparticles (Figure 17).¹²¹ These ligands act both as a stabilizer for the nanoparticle suspension and as a co-catalyst: the authors indeed demonstrated the mechanism goes through an HCD. The oxygen atom of the SPO acts as Lewis base and captures the proton H⁺ while a surface hydride species H⁻ is formed on the gold surface. A selective hydrogenation of a large number of aldehydes was thus achieved under relatively mild conditions (40–60 °C, 40 bar H₂, THF/hexane mixture). A screening over different SPOs was performed and revealed that the degree of polarization of P=O is crucial for the HCD mechanism to occur. A strong polarity of the bond is required, typically obtained with aryl groups on the phosphorus center rather than alkyl ones.

The field of heterolytic cleavage of hydrogen on metal nanoparticles in cooperation with a ligand is still in its infancy, hence the relatively low number of published works and the inhomogeneity of the works. The interest for these catalytic systems is nonetheless growing rapidly and led to a few reviews.^{110,117,122}

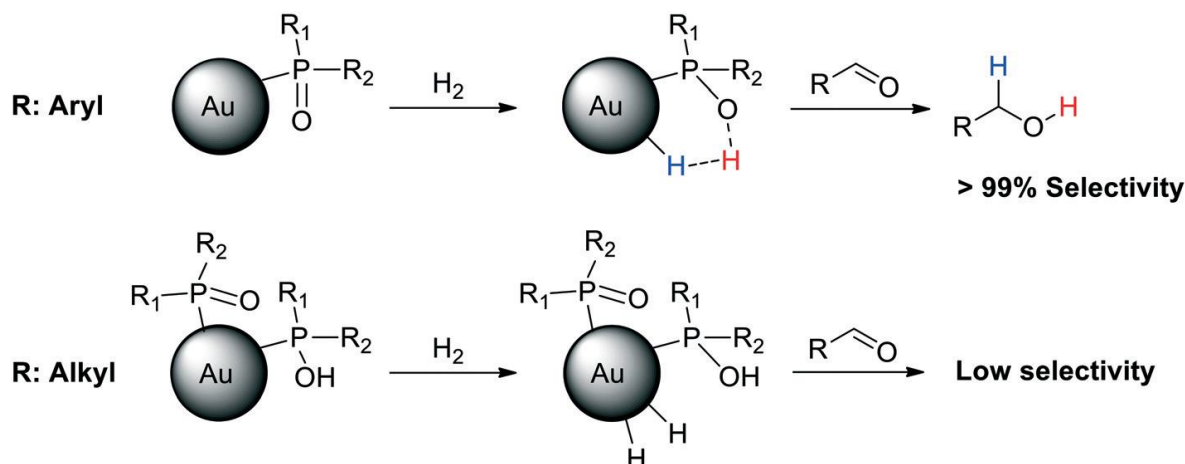


Figure 17. Au NPs ligated by aryl SPOs exhibit a strong polarity of the P=O bond, which favours the HCD and thus the selective hydrogenation of aldehydes. Au NPs ligated by alkyl SPOs show a low polarity of the P=O bond, which hinders the heterolytic H₂ activation.

These Au NPs display low selectivity in aldehyde hydrogenation. Reproduced from reference [121].

I.4.3 Philosophy of work

Most of the ligand-assisted colloidal catalysis developed so far for the heterolytic cleavage of hydrogen imply the use of noble metals such as Au or Ru.¹¹⁷ There is however to the best of our knowledge very few works mentioning the use of non-noble metal containing nanoparticles such as metal carbides, metal oxides or nickel derivatives compounds. The goal of this PhD thesis is therefore to explore the possible use of these materials for an FLP-like activation of H₂ in solvent *via* the implication of a molecular base. We chose to use tertiary phosphines (PPh₃, PCy₃) as Lewis bases in a first time and to vary the inorganic nanoparticle following three main strategies:

- Materials already known for their catalytic activity in solvent for H₂ activation, for instance Mo₂C or W₂C for furfural hydrogenation, or Ni₂P/Ni₁₂P₅ for nitroarenes and olefins reduction
- Materials whose metallic center is known for being a Lewis acid, such as tungsten oxides (W₁₈O₄₉) or molybdenum oxides (MoO_x)
- Materials already known for an all solid FLP catalytic activity, in gas phase at high temperature for In₂O₃, or in solvent for CeO_{2-x}

I.5. Bibliography

1. Delgado, J. A., Benkirane, O., Claver, C., Curulla-Ferré, D. & Godard, C. Advances in the preparation of highly selective nanocatalysts for the semi-hydrogenation of alkynes using colloidal approaches. *Dalt. Trans.* **46**, 12381–12403 (2017).
2. Vilé, G., Albani, D., Almora-Barrios, N., López, N. & Pérez-Ramírez, J. Advances in the Design of Nanostructured Catalysts for Selective Hydrogenation. *ChemCatChem* **8**, 21–33 (2016).
3. Lindlar, H. Ein neuer Katalysator für selektive Hydrierungen. *Helv. Chim. Acta* **35**, 446–450 (1952).
4. Månberger, A. & Johansson, B. The geopolitics of metals and metalloids used for the renewable energy transition. *Energy Strateg. Rev.* **26**, 100394 (2019).
5. Formenti, D., Ferretti, F., Scharnagl, F. K. & Beller, M. Reduction of Nitro Compounds Using 3d-Non-Noble Metal Catalysts. *Chem. Rev.* **119**, 2611–2680 (2019).
6. Bartholomew, C. H. Mechanisms of Nickel Catalyst Poisoning. in 81–104 (1987).
7. Führer, M., van Haasterecht, T. & Bitter, J. H. Molybdenum and tungsten carbides can shine too. *Catal. Sci. Technol.* **10**, 6089–6097 (2020).
8. Robinson, P. Tutorial on Hydroprocessing: Hydroprocessing Catalysts and Processes. in *AIChE Spring Meeting* (2012).
9. Sautet, P. & Cinquini, F. Surface of Metallic Catalysts under a Pressure of Hydrocarbon Molecules: Metal or Carbide? *ChemCatChem* **2**, 636–639 (2010).
10. Connor, R. & Adkins, H. Hydrogenolysis of oxygenated organic compounds. *J. Am. Chem. Soc.* **54**, 4678–4690 (1932).
11. Breyse, M., Furimsky, E., Kasztelan, S., Lacroix, M. & Perot, G. Hydrogen activation by transition metal sulfides. *Catal. Rev.* **44**, 651–735 (2002).
12. Furimsky, E. Metal carbides and nitrides as potential catalysts for hydroprocessing. *Appl. Catal. A Gen.* **240**, 1–28 (2003).
13. Oyama, S. T., Gott, T., Zhao, H. & Lee, Y.-K. Transition metal phosphide hydroprocessing catalysts: A review. *Catal. Today* **143**, 94–107 (2009).
14. Pelckmans, M., Renders, T., Van de Vyver, S. & Sels, B. F. Bio-based amines through sustainable heterogeneous catalysis. *Green Chem.* **19**, 5303–5331 (2017).

15. Scholz, D., Aellig, C. & Hermans, I. Catalytic Transfer Hydrogenation/Hydrogenolysis for Reductive Upgrading of Furfural and 5-(Hydroxymethyl)furfural. *ChemSusChem* **7**, 268–275 (2014).
16. Nakagawa, Y., Tamura, M. & Tomishige, K. Catalytic Reduction of Biomass-Derived Furanic Compounds with Hydrogen. *ACS Catal.* **3**, 2655–2668 (2013).
17. Hao, Y.-C. *et al.* Promoting nitrogen electroreduction to ammonia with bismuth nanocrystals and potassium cations in water. *Nat. Catal.* **2**, 448–456 (2019).
18. Kalyon, N. *et al.* Catalytic activity of nanoscale borides: Co₂B and Ni₇B₃ in the liquid-phase hydrogenation of citral. *J. Catal.* **352**, 436–441 (2017).
19. Zhou, Z., Hu, J., Zhang, R., Li, L. & Cheng, Z. Revisiting the reaction kinetics of selective hydrogenation of phenylacetylene over an egg-shell catalyst in excess styrene. *Chem. Eng. Sci.* **138**, 663–672 (2015).
20. Linstrom, P. J. & W.G., M. *NIST Chemistry WebBook, NIST Standard Reference Database Number 69.* (2021).
21. Zhang, Y.-C. *et al.* Unraveling the facet-dependent and oxygen vacancy role for ethylene hydrogenation on Co₃O₄ (110) surface: A DFT+U study. *Appl. Surf. Sci.* **401**, 241–247 (2017).
22. Xi, Y., Huang, L., Forrey, R. C. & Cheng, H. Interactions between hydrogen and tungsten carbide: a first principles study. *RSC Adv.* **4**, 39912 (2014).
23. Shi, Y., Yang, Y., Li, Y.-W. & Jiao, H. Activation mechanisms of H₂, O₂, H₂O, CO₂, CO, CH₄ and C₂H_x on metallic Mo₂C(001) as well as Mo/C terminated Mo₂C(101) from density functional theory computations. *Appl. Catal. A Gen.* **524**, 223–236 (2016).
24. Wyvratt, B. M. *et al.* Reactivity of Hydrogen on and in Nanostructured Molybdenum Nitride: Crotonaldehyde Hydrogenation. *ACS Catal.* **6**, 5797–5806 (2016).
25. García-Melchor, M. & López, N. Homolytic Products from Heterolytic Paths in H₂ Dissociation on Metal Oxides: The Example of CeO₂. *J. Phys. Chem. C* **118**, 10921–10926 (2014).
26. Copéret, C., Estes, D. P., Larmier, K. & Searles, K. Isolated Surface Hydrides: Formation, Structure, and Reactivity. *Chem. Rev.* **116**, 8463–8505 (2016).
27. Wei, B., Tielens, F. & Calatayud, M. Understanding the Role of Rutile TiO₂ Surface Orientation on Molecular Hydrogen Activation. *Nanomaterials* **9**, 1199 (2019).
28. Hu, G., Wu, Z. & Jiang, D. First Principles Insight into H₂ Activation and

- Hydride Species on TiO₂ Surfaces. *J. Phys. Chem. C* **122**, 20323–20328 (2018).
29. Chen, H.-Y. T., Giordano, L. & Pacchioni, G. From Heterolytic to Homolytic H₂ Dissociation on Nanostructured MgO(001) Films As a Function of the Metal Support. *J. Phys. Chem. C* **117**, 10623–10629 (2013).
 30. Li, Z. *et al.* Oxidation of Reduced Ceria by Incorporation of Hydrogen. *Angew. Chemie Int. Ed.* **58**, 14686–14693 (2019).
 31. Hofmann, A., Clark, S. J., Oppel, M. & Hahndorf, I. Hydrogen adsorption on the tetragonal ZrO₂(101) surface: a theoretical study of an important catalytic reactant. *Phys. Chem. Chem. Phys.* **4**, 3500–3508 (2002).
 32. Song, Z. & Xu, H. Unusual dissociative adsorption of H₂ over stoichiometric MgO thin film supported on molybdenum. *Appl. Surf. Sci.* **366**, 166–172 (2016).
 33. Song, Z. *et al.* Heterolytic dissociative adsorption state of dihydrogen favored by interfacial defects. *Appl. Surf. Sci.* **433**, 862–868 (2018).
 34. Matz, O. & Calatayud, M. Breaking H₂ with CeO₂: Effect of Surface Termination. *ACS Omega* **3**, 16063–16073 (2018).
 35. Matz, O. & Calatayud, M. H₂ Dissociation and Oxygen Vacancy Formation on Ce₂O₃ Surfaces. *Top. Catal.* **62**, 956–967 (2019).
 36. Travert, A. *et al.* Hydrogen Activation on Mo-Based Sulfide Catalysts, a Periodic DFT Study. *J. Am. Chem. Soc.* **124**, 7084–7095 (2002).
 37. Wang, G. *et al.* DFT insights into hydrogen activation on the doping Ni₂P surfaces under the hydrodesulfurization condition. *Appl. Surf. Sci.* **538**, 148160 (2021).
 38. Wang, T., Li, Y.-W., Wang, J., Beller, M. & Jiao, H. Dissociative Hydrogen Adsorption on the Hexagonal Mo₂C Phase at High Coverage. *J. Phys. Chem. C* **118**, 8079–8089 (2014).
 39. Schachtl, E., Kondratieva, E., Gutiérrez, O. Y. & Lercher, J. A. Pathways for H₂ Activation on (Ni)-MoS₂ Catalysts. *J. Phys. Chem. Lett.* **6**, 2929–2932 (2015).
 40. Chen, B. W. J., Xu, L. & Mavrikakis, M. Computational Methods in Heterogeneous Catalysis. *Chem. Rev.* **121**, 1007–1048 (2021).
 41. Norskov, J. K., Abild-Pedersen, F., Studt, F. & Bligaard, T. Density functional theory in surface chemistry and catalysis. *Proc. Natl. Acad. Sci.* **108**, 937–943 (2011).
 42. Riley, C. *et al.* Design of Effective Catalysts for Selective Alkyne Hydrogenation by Doping of Ceria with a Single-Atom Promotor. *J. Am. Chem. Soc.* **140**, 12964–

- 12973 (2018).
43. Rakić, V. & Damjanović, L. Temperature-Programmed Desorption (TPD) Methods. in 131–174 (2013). doi:10.1007/978-3-642-11954-5_4.
 44. Polo-Garzon, F. *et al.* Neutron Scattering Investigations of Hydride Species in Heterogeneous Catalysis. *ChemSusChem* **12**, 93–103 (2019).
 45. Wang, L. *et al.* Room-Temperature Activation of H₂ by a Surface Frustrated Lewis Pair. 9501–9505 (2019) doi:10.1002/anie.201904568.
 46. Wu, Z. *et al.* Direct Neutron Spectroscopy Observation of Cerium Hydride Species on a Cerium Oxide Catalyst. *J. Am. Chem. Soc.* **139**, 9721–9727 (2017).
 47. Hayashi, K., Sushko, P. V., Hashimoto, Y., Shluger, A. L. & Hosono, H. Hydride ions in oxide hosts hidden by hydroxide ions. *Nat. Commun.* **5**, 3515 (2014).
 48. Carenco, S. Describing inorganic nanoparticles in the context of surface reactivity and catalysis. *Chem. Commun.* **54**, 6719–6727 (2018).
 49. Carenco, S. *et al.* Nickel phosphide nanocatalysts for the chemoselective hydrogenation of alkynes. *Nano Today* **7**, 21–28 (2012).
 50. Brunner, E. Solubility of hydrogen in 10 organic solvents at 298.15, 323.15, and 373.15 K. *J. Chem. Eng. Data* **30**, 269–273 (1985).
 51. Wainwright, M. S., Ahn, T., Trimm, D. L. & Cant, N. W. Solubility of Hydrogen in Alcohols and Esters. *J. Chem. Eng. Data* **32**, 22–24 (1987).
 52. Motagamwala, A. H. & Dumesic, J. A. Microkinetic Modeling: A Tool for Rational Catalyst Design. *Chem. Rev.* **121**, 1049–1076 (2021).
 53. Marenich, A. V., Cramer, C. J. & Truhlar, D. G. Universal Solvation Model Based on Solute Electron Density and on a Continuum Model of the Solvent Defined by the Bulk Dielectric Constant and Atomic Surface Tensions. *J. Phys. Chem. B* **113**, 6378–6396 (2009).
 54. Pliego, J. R. & Riveros, J. M. Hybrid discrete-continuum solvation methods. *WIREs Comput. Mol. Sci.* **10**, (2020).
 55. Song, J. *et al.* Review on selective hydrogenation of nitroarene by catalytic, photocatalytic and electrocatalytic reactions. *Appl. Catal. B Environ.* **227**, 386–408 (2018).
 56. Alexander, A. M. & Hargreaves, J. S. J. Alternative catalytic materials: carbides, nitrides, phosphides and amorphous boron alloys. *Chem. Soc. Rev.* **39**, 4388–4401 (2010).
 57. Chen, X. & Liang, C. Transition metal silicides: fundamentals, preparation and

- catalytic applications. *Catal. Sci. Technol.* **9**, 4785–4820 (2019).
58. Carenco, S., Portehault, D., Boissière, C., Mézailles, N. & Sanchez, C. Nanoscaled metal borides and phosphides: Recent developments and perspectives. *Chem. Rev.* **113**, 7981–8065 (2013).
 59. Dongil, A. B. Recent Progress on Transition Metal Nitrides Nanoparticles as Heterogeneous Catalysts. *Nanomaterials* **9**, 1111 (2019).
 60. February, R. *et al.* Synthetically Useful Reactions wlfh Metal Boride and Aluminide Catalysts. *Chem. Rev.* **5**, 763–780 (1988).
 61. Pei, Y. *et al.* Synthesis and catalysis of chemically reduced metal–metalloid amorphous alloys. *Chem. Soc. Rev.* **41**, 8140 (2012).
 62. Li, H., Zhao, Q., Wan, Y., Dai, W. & Qiao, M. Self-assembly of mesoporous Ni–B amorphous alloy catalysts. *J. Catal.* **244**, 251–254 (2006).
 63. Collins, D. J., Smith, A. D. & Davis, B. H. Hydrogenation of nitrobenzene over a nickel boride catalyst. *Ind. Eng. Chem. Prod. Res. Dev.* **21**, 279–281 (1982).
 64. Yang, K., Chen, X., Guan, J. & Liang, C. Nickel silicides prepared from organometallic polymer as efficient catalyst towards hydrogenation of phenylacetylene. *Catal. Today* **246**, 176–183 (2015).
 65. Chen, X. *et al.* Synthesis and Catalytic Properties for Phenylacetylene Hydrogenation of Silicide Modified Nickel Catalysts. *J. Phys. Chem. C* **114**, 16525–16533 (2010).
 66. Ryabchuk, P. *et al.* Intermetallic nickel silicide nanocatalyst—A non-noble metal–based general hydrogenation catalyst. *Sci. Adv.* **4**, eaat0761 (2018).
 67. Zhang, L. *et al.* Cobalt Silicides Nanoparticles Embedded in N-Doped Carbon as Highly Efficient Catalyst in Selective Hydrogenation of Cinnamaldehyde. *ChemistrySelect* **3**, 1658–1666 (2018).
 68. Zhu, Y., Yang, S., Cao, C., Song, W. & Wan, L.-J. Controllable synthesis of carbon encapsulated iron phosphide nanoparticles for the chemoselective hydrogenation of aromatic nitroarenes to anilines. *Inorg. Chem. Front.* **5**, 1094–1099 (2018).
 69. Yang, S. *et al.* MOF-Derived Cobalt Phosphide/Carbon Nanocubes for Selective Hydrogenation of Nitroarenes to Anilines. *Chem. - A Eur. J.* **24**, 4234–4238 (2018).
 70. Mitsudome, T. *et al.* A cobalt phosphide catalyst for the hydrogenation of nitriles. *Chem. Sci.* **11**, 6682–6689 (2020).

71. Ishikawa, H. *et al.* Air-Stable and Reusable Cobalt Phosphide Nanoalloy Catalyst for Selective Hydrogenation of Furfural Derivatives. *ACS Catal.* **11**, 750–757 (2021).
72. Sheng, M. *et al.* Single-Crystal Cobalt Phosphide Nanorods as a High-Performance Catalyst for Reductive Amination of Carbonyl Compounds. *JACS Au* **1**, 501–507 (2021).
73. Gao, R. *et al.* Ultradispersed Nickel Phosphide on Phosphorus-Doped Carbon with Tailored *d*-Band Center for Efficient and Chemoselective Hydrogenation of Nitroarenes. *ACS Catal.* **8**, 8420–8429 (2018).
74. Yamaguchi, S. *et al.* Support-Boosted Nickel Phosphide Nanoalloy Catalysis in the Selective Hydrogenation of Maltose to Maltitol. *ACS Sustain. Chem. Eng.* **9**, 6347–6354 (2021).
75. Yamaguchi, S. *et al.* Air-stable and reusable nickel phosphide nanoparticle catalyst for the highly selective hydrogenation of D-glucose to D-sorbitol. *Green Chem.* **23**, 2010–2016 (2021).
76. Albani, D. *et al.* Ensemble Design in Nickel Phosphide Catalysts for Alkyne Semi-Hydrogenation. *ChemCatChem* **11**, 457–464 (2019).
77. Zhang, L. *et al.* Rapid microwaves synthesis of CoSi_x/CNTs as novel catalytic materials for hydrogenation of phthalic anhydride. *J. Solid State Chem.* **217**, 105–112 (2014).
78. Wang, H., Shu, Y., Zheng, M. & Zhang, T. Selective Hydrogenation of Cinnamaldehyde to Hydrocinnamaldehyde over SiO₂ Supported Nickel Phosphide Catalysts. *Catal. Letters* **124**, 219–225 (2008).
79. Hwu, H. H. & Chen, J. G. Surface chemistry of transition metal carbides. *Chem. Rev.* **105**, 185–212 (2005).
80. Levy, R. B. & Boudart, M. Platinum-Like Behavior of Tungsten Carbide in Surface Catalysis. *Science* **181**, 547–549 (1973).
81. Pang, J. *et al.* Transition metal carbide catalysts for biomass conversion: A review. *Appl. Catal. B Environ.* **254**, 510–522 (2019).
82. Deng, Y. *et al.* Solvent Tunes the Selectivity of Hydrogenation Reaction over α -MoC Catalyst. *J. Am. Chem. Soc.* **140**, 14481–14489 (2018).
83. Braun, M. & Esposito, D. Hydrogenation Properties of Nanostructured Tungsten Carbide Catalysts in a Continuous-Flow Reactor. *ChemCatChem* **9**, 393–397 (2017).
84. Cárdenas-Lizana, F. *et al.* Selective three-phase hydrogenation of aromatic nitro-

- compounds over β -molybdenum nitride. *Catal. Today* **173**, 53–61 (2011).
85. Liu, X. *et al.* Selective Hydrodeoxygenation of Lignin-Derived Phenols to Cyclohexanols or Cyclohexanes over Magnetic $\text{CoN}_x\text{@NC}$ Catalysts under Mild Conditions. *ACS Catal.* **6**, 7611–7620 (2016).
 86. Wei, X. *et al.* Solid-state nanocasting synthesis of ordered mesoporous CoN_x -carbon catalysts for highly efficient hydrogenation of nitro compounds. *Nanoscale* **10**, 16839–16847 (2018).
 87. Zhou, P. *et al.* High performance of a cobalt–nitrogen complex for the reduction and reductive coupling of nitro compounds into amines and their derivatives. *Sci. Adv.* **3**, e1601945 (2017).
 88. Clavel, G., Molinari, V., Kraupner, A. & Giordano, C. Easy Access to Ni_3N - and Ni-Carbon Nanocomposite Catalysts. *Chem. - A Eur. J.* **29**, 9018-9023 (2014).
 89. Shi, X. *et al.* Fabrication of Ni_3N nanorods anchored on N-doped carbon for selective semi-hydrogenation of alkynes. *J. Catal.* **382**, 22–30 (2020).
 90. Horányi, G., Vértés, G. & Fézler, G. Tungsten Carbide as Catalyst for Liquid (aqueous) Phase Heterogeneous Catalytic Hydrogenation. *Zeitschrift für Phys. Chemie* **83**, 322–324 (1973).
 91. Horányi, G. & Rizmayer, E. M. Novel evidence for the selective behaviour of tungsten carbide in liquid phase heterogeneous catalytic hydrogenation. *React. Kinet. Catal. Lett.* **13**, 21–26 (1980).
 92. Vértés, G., Horányi, G. & Szakács, S. Selective catalytic behaviour of tungsten carbide in the liquid-phase hydrogenation of organic compounds. *J. Chem. Soc., Perkin Trans. 2* 1400–1402 (1973).
 93. Gage, S. H., Trewyn, B. G., Ciobanu, C. V., Pylypenko, S. & Richards, R. M. Synthetic advancements and catalytic applications of nickel nitride. *Catal. Sci. Technol.* **6**, 4059–4076 (2016).
 94. Vilé, G. *et al.* Stereo- and Chemoselective Character of Supported CeO_2 Catalysts for Continuous-Flow Three-Phase Alkyne Hydrogenation. *ChemCatChem* **6**, 1928–1934 (2014).
 95. Zhang, S. *et al.* Solid frustrated-Lewis-pair catalysts constructed by regulations on surface defects of porous nanorods of CeO_2 . *Nat. Commun.* **8**, 1–11 (2017).
 96. Song, J. *et al.* Oxygen-Deficient Tungsten Oxide as Versatile and Efficient Hydrogenation Catalyst. *ACS Catal.* **5**, 6594–6599 (2015).
 97. Jagadeesh, R. V. *et al.* Nanoscale Fe_2O_3 -Based Catalysts for Selective Hydrogenation of Nitroarenes to Anilines. *Science* **342**, 1073–1076 (2013).

98. Niu, H. *et al.* Iron Oxide as a Catalyst for Nitroarene Hydrogenation: Important Role of Oxygen Vacancies. *Ind. Eng. Chem. Res.* **55**, 8527–8533 (2016).
99. Chen, F. *et al.* Selective Catalytic Hydrogenation of Heteroarenes with N-Graphene-Modified Cobalt Nanoparticles ($\text{Co}_3\text{O}_4\text{-Co/NGr@}\alpha\text{-Al}_2\text{O}_3$). *J. Am. Chem. Soc.* **137**, 11718–11724 (2015).
100. Chen, F. *et al.* Stable and Inert Cobalt Catalysts for Highly Selective and Practical Hydrogenation of $\text{C}\equiv\text{N}$ and $\text{C}=\text{O}$ Bonds. *J. Am. Chem. Soc.* **138**, 8781–8788 (2016).
101. Ma, B. *et al.* Pyrite nanoparticles: an Earth-abundant mineral catalyst for activation of molecular hydrogen and hydrogenation of nitroaromatics. *RSC Adv.* **6**, 55220–55224 (2016).
102. Cao, F. *et al.* One-pot synthesis of flowerlike Ni_7S_6 and its application in selective hydrogenation of chloronitrobenzene. *J. Mater. Chem.* **20**, 1078–1085 (2010).
103. Wei, Z. *et al.* The synergic effects at the molecular level in CoS_2 for selective hydrogenation of nitroarenes. *Green Chem.* **20**, 671–679 (2018).
104. Li, Z., Zhang, D., Ma, J., Wang, D. & Xie, C. Fabrication of MoS_2 microflowers for hydrogenation of nitrobenzene. *Mater. Lett.* **213**, 350–353 (2018).
105. Zhang, Y. *et al.* Sublimation-Induced Sulfur Vacancies in MoS_2 Catalyst for One-Pot Synthesis of Secondary Amines. *ACS Catal.* **9**, 7967–7975 (2019).
106. Sun, Y. *et al.* Defect-mediated selective hydrogenation of nitroarenes on nanostructured WS_2 . *Chem. Sci.* **10**, 10310–10317 (2019).
107. Morse, J. R., Callejas, J. F., Darling, A. J. & Schaak, R. E. Bulk iron pyrite as a catalyst for the selective hydrogenation of nitroarenes. *Chem. Commun.* **53**, 4807–4810 (2017).
108. Stephan, D. W. Frustrated Lewis Pairs: From Concept to Catalysis. *Acc. Chem. Res.* **48**, 306–316 (2015).
109. Stephan, D. W. “Frustrated Lewis pairs”: a concept for new reactivity and catalysis. *Org. Biomol. Chem.* **6**, 1535 (2008).
110. Ma, Y. *et al.* Semi-solid and solid frustrated Lewis pair catalysts. *Chem. Soc. Rev.* **47**, 5541–5553 (2018).
111. Ghuman, K. K. *et al.* Surface Analogues of Molecular Frustrated Lewis Pairs in Heterogeneous CO_2 Hydrogenation Catalysis. *ACS Catal.* **6**, 5764–5770 (2016).
112. Huang, Z. *et al.* Understanding All-Solid Frustrated-Lewis-Pair Sites on CeO_2 from Theoretical Perspectives. (2018).

113. Zhang, S. *et al.* Interfacial Frustrated Lewis Pairs of CeO₂ Activate CO₂ for Selective Tandem Transformation of Olefins and CO₂ into Cyclic Carbonates. *J. Am. Chem. Soc.* **141**, 11353–11357 (2019).
114. Dong, Y. *et al.* Tailoring Surface Frustrated Lewis Pairs of In₂O_{3-x}(OH)_y for Gas-Phase Heterogeneous Photocatalytic Reduction of CO₂ by Isomorphous Substitution of In³⁺ with Bi³⁺. *Adv. Sci* **6**, 1700732 (2018).
115. Yan, T. *et al.* Bismuth atom tailoring of indium oxide surface frustrated Lewis pairs boosts heterogeneous CO₂ photocatalytic hydrogenation. *Nat. Commun.* **11**, 6095 (2020).
116. Wang, L. *et al.* Room-Temperature Activation of H₂ by a Surface Frustrated Lewis Pair. *Angew. Chemie Int. Ed.* **58**, 9501–9505 (2019).
117. Cano, I., Martínez-Prieto, L. M. & van Leeuwen, P. W. N. M. Heterolytic cleavage of dihydrogen (HCD) in metal nanoparticle catalysis. *Catal. Sci. Technol.* **11**, 1157–1185 (2021).
118. Lu, G. *et al.* Gold catalyzed hydrogenations of small imines and nitriles: enhanced reactivity of Au surface toward H₂ via collaboration with a Lewis base. *Chem. Sci.* **5**, 1082–1090 (2014).
119. Fiorio, J. L., López, N. & Rossi, L. M. Gold–Ligand-Catalyzed Selective Hydrogenation of Alkynes into cis-Alkenes via H₂ Heterolytic Activation by Frustrated Lewis Pairs. *ACS Catal.* **7**, 2973–2980 (2017).
120. Silva, R., Fiorio, J., Vidinha, P. & Rossi, L. Gold Catalysis for Selective Hydrogenation of Aldehydes and Valorization of Bio-Based Chemical Building Blocks. *J. Braz. Chem. Soc.* **30**, 2162–2169 (2019).
121. Cano, I., Chapman, A. M., Urakawa, A. & van Leeuwen, P. W. N. M. Air-Stable Gold Nanoparticles Ligated by Secondary Phosphine Oxides for the Chemoselective Hydrogenation of Aldehydes: Crucial Role of the Ligand. *J. Am. Chem. Soc.* **136**, 2520–2528 (2014).
122. Rossi, L. M., Fiorio, J. L., Garcia, M. A. S. & Ferraz, C. P. The role and fate of capping ligands in colloiddally prepared metal nanoparticle catalysts. *Dalt. Trans.* **47**, 5889–5915 (2018).

Part 1

Solvent-free syntheses

Chapter II

Solid-state metathesis of carbide and hydride nanoparticles

*Note: the results discussed in this chapter are reported under another form in the following article: “Early Transition Metal Nano-carbides and Nano-hydrides from Solid-State Metathesis initiated at Room Temperature”, by R. F. André, F. D’Accriscio, A. P. Freitas, G. Crochet, C. Ulhaq, M. Bahri, O. Ersen, C. Sanchez and S. Carencio, **Green Chemistry**, just accepted (2021).*

II.1. Refractory compounds syntheses by solid-state metathesis

Transition metal carbides (TMC) are interstitial alloys formed by the incorporation of carbon atoms into the close-packed lattices of transition metals (TM). Due to their catalytic activity similar to Pt-group metals, molybdenum carbide (Mo_2C) and tungsten carbides (WC and W_2C) are studied as a substitute to rare and expensive metals, in particular for electrochemical¹ and hydrogenation reactions.^{2,3} Most of the TMC syntheses require an extended reaction time (up to one week) at elevated temperatures ($> 800\text{ }^\circ\text{C}$) between the metal precursor and a carbon source such as graphite, a polymer or light hydrocarbons.⁴ To limit the oxidation of the material, the reaction is usually conducted under a reductive or an inert atmosphere. The high temperatures and the long reaction times are critical for these syntheses to overcome the solid-state diffusion barrier of carbon into metal. They represent a costly step in terms of energy.

Energy-saving alternative pathways were established during the past decades for the production of ceramics and refractive materials, and are now used by manufacturers.⁵⁻⁷ For instance, Self-propagation High-temperature Syntheses (SHS) were extensively studied by Merzhanov *et al.* in the 1980s.⁷ In an SHS, the reaction liberates enough heat so that the solid-state reaction is self-sustained at high temperature, without need for external heating. Highly exothermic reactions are needed to enter in this regime. Although the reaction is initiated at low temperatures, the reaction temperature can go above $1300\text{ }^\circ\text{C}$ within a second, leading to highly crystalline products, and rapidly decreases to room temperature. SHS were initially used on compressed powder mixtures, yielding bulk TMC among other compounds, and were then extended to TMC nanoparticles (NPs).^{8,9}

Transition metal halide salts have been used as the metallic source due to their simplicity and in order to obtain highly exothermic reactions. When these particular reagents are used, SHS reactions are called Solid-State Metathesis (SSM) reactions. They permit the formation of refractive compounds containing a light element, such as carbides, nitrides, silicides or phosphides. SSM reactions were studied by Kaner, Parkin *et al.*^{6,10} When using a metal chloride, a reducing agent is needed to reduce the metallic center. It is usually a derivative of an alkaline or earth-alkaline metal in combination with the light element to be inserted. The heat released by the reaction of the two solid partners allows an exchange of atoms between the two compounds to yield the targeted phase, hence its name “metathesis”.¹¹ Various works report the use of MgB_2 for borides,¹² CaC_2 , SrC_2 , Al_4C_3 for carbides,^{8,9} Li_3N , NaN_3 for nitrides,^{13–15} Mg_2Si , CaSi_2 for silicides,¹⁶ Na_3P for phosphides,¹⁷ Na_2S for sulfides,¹⁸ *etc.* The metal chloride (MCl_x) and the reducing agent are introduced in stoichiometric conditions as regard to the electron transfer, *i.e.* x electrons provided by x alkaline metal atoms or $x/2$ earth-alkaline metal atoms for one MCl_x . In some cases, the excess of light element (B, C, N, Si, S or P) is recovered under its elemental form as a byproduct of the reaction, *e.g.* graphitic carbon or N_2 . The reaction is driven by the high lattice energy of the coproduced chloride salt (LiCl , NaCl , KCl , CaCl_2 , AlCl_3).^{8,9,15,18,19} When the precursor is a TM oxide, the reaction is called a Modified Solid-State Metathesis (MSSM) and is driven by the formation of the alkaline oxide, such as Li_2O , CaO or SrO .^{14,20} In both cases, SSM and MSSM, the reaction enthalpy is largely negative (500-2000 kJ/mol per atom of metal), hence the high exothermicity and reaction temperatures. The reaction is either initiated by mixing or grinding of the reagents for the more reactive mixtures, or by gradually heating the powder mixture up to the point the partners suddenly react: this temperature is called the ignition temperature T_{ig} .

Our group recently developed an expeditious way to access finely divided NPs dispersed on a carbon support *via* an SSM reaction initiated under ambient conditions between a metal chloride (MCl_x) and metallic potassium dispersed in carbon, KC_8 or KC_4 .¹⁹ Potassium-graphite (KC_8) is an intercalation compound of potassium atoms in graphite, it was first reported in the 1920s²¹ and was then widely used as a reagent or a catalyst considering its excellent properties as a reducing agent.^{22,23} Potassium in acetylene black (KC_4) is not an intercalation compound but is obtained by impregnation of liquid potassium into 50 nm large particles of acetylene black. The potassium-containing compound (KC_8 or KC_4) reduces the metal chloride to form KCl along with metal(0) or carbide NPs. The KC_4/KC_8 process presents many advantages in terms of green chemistry: no solvent, no high or prolonged heating, non-toxic reagents and innocuous wastes. Moreover, it is versatile and can be applied to numerous early transition metals (Ti, V, Mo, W in the initial work,¹⁹ Zr, Nb, Mo, Hf, Ta, W in the present one).

The influence of the different process parameters was not studied so far and is the object of the present work, which also provides a rationalization of the results in the framework of SSM reactions. The present study also investigates the formation of carbides with additional elements: Zr, Hf, Nb and Ta. While exploring different reaction conditions, a synthetic path to metal hydride nanoparticles was found by serendipity. We exploit here the specificities of KC_4 and KC_8 to tune the phase speciation of the reaction product. We first discuss the nature of the products of the reaction performed with metals of the Group IV (Zr, Hf), Group V (Nb, Ta) and Group VI (Mo, W). The products were analyzed by a combination of spectroscopies and microscopies. We put these results in light of thermodynamic considerations based on the enthalpies of reaction. We demonstrate that the reaction is not under thermodynamic control. Then, we explore the influence of different process parameters (nature of carbon support, precursor granularity, gas phase, scale...) on the metal speciation by Powder X-ray Diffraction (PXRD). Finally, we propose a mechanism for the NPs synthesis and subsequent modifications.

II.2. Solid-state metathesis and chemical trends with KC_8 and KC_4

II.2.1 Combustion reaction

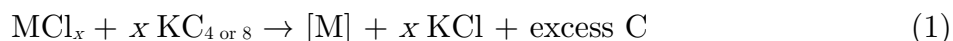
Synthesis II.1. Preparation of KC_8 or KC_4 . In a Schlenk tube and in glovebox, 1 g of metallic potassium cut in pieces (25.57 mmol, 1 equiv.) and 2.46 g of dry graphite (204.56 mmol, 8 equiv.) (or 1.23 g of dry acetylene black 50 % compressed (102.28 mmol, 4 equiv.)) were mixed. The tube was put under static vacuum and heated with a heat gun under vigorous stirring for at least 1 h in order to obtain a homogeneous powder. Metallic potassium melts and was incorporated into the carbon phase to form a bronze powder for KC_8 or a black powder for KC_4 . The obtained powder (100 % yield) was then stored under inert atmosphere.

[*Caution*] Potassium and final compounds are pyrophoric: the reaction must be conducted in the absence of dioxygen and water. The KC_8 and KC_4 reagents should be used within the month in order to provide reproducible results.

Synthesis II.2. Solid-state metathesis with KC_8 or KC_4 . In a Schlenk tube and in glovebox, 100 mg of KC_4 (1.15 mmol, 1 equiv.) were mixed with metal chloride MCl_x (1.15/x mmol, 1/x equiv.) by gentle hand-shaking (caution: the mixture may explode at room temperature) and the Schlenk tube was taken out of the glovebox. The gas phase was eventually removed or changed for N_2 . The reaction was initiated by gentle heating with a heat gun. Once the reaction was over, the Schlenk tube was let to cool down to room temperature and filled with N_2 (caution: the mixture is still

pyrophoric). The solid was neutralized by careful addition of ethanol (10 mL) and subsequent addition of water (20 mL). Moderate heating and bubbling occurred during a few minutes. The mixture was shaken and eventually sonicated before being centrifuged (9,000 rpm, 10 min, 20 °C). The supernatant was removed and the black solid was let to dry at air.

In Synthesis II.2., the reaction is a solid-state combustion where the reducing agent is potassium (K), either dispersed in acetylene black at 0.25 equivalent (corresponding composition: KC_4) or inserted in graphite (KC_8). The oxidant is a metal chloride of general formula MCl_x ($M = Zr, Nb, Mo, Hf, Ta, W$). In Eq. 1, MCl_x and the reducing agent are introduced in stoichiometric proportions, *i.e.* one equivalent of K per electron to provide to the chloride for its full reduction. The oxidation number of the metal M is reduced to (0) to form NPs supported on carbon, with KCl salt and carbon as the main coproducts. Here, [M] denotes a species containing a metal(0), a metal carbide, a metal hydride or a metal oxide.



The solid reagents were mixed by handshaking in a Schlenk tube under argon. Alternatively, the gas phase was changed for N_2 , or removed to perform the reaction under static vacuum, before shaking the Schlenk. Mixtures with metal chlorides of Group V and VI spontaneously ignited within seconds or minutes under vacuum while an initial activation with gentle heating (below 75 °C) was required for Group IV metals. Snapshots of the reactions performed with $ZrCl_4$ and KC_4 under Ar displayed an initiation point in the powder followed by a progression of the reaction front in the powder, at the speed of *ca.* 5 cm/s (Figure 1), confirming the classification of the reaction as a Self-propagation High-temperature combustion Synthesis (SHS). Similar behaviors were observed with the other metals. In all cases but more particularly for reactions with KC_4 under vacuum, a black particulate solid was spread over the walls of the reaction tube, due to the explosivity of the reaction. Iridescences were also observed on the glass vessel: they can be explained by the formation of a thin layer of a compound (probably metallic potassium or KCl) which has been previously sublimed by the heat released by the reaction. The traces of unreacted pyrophoric KC_4 or KC_8 were finally neutralized with ethanol, and the powder was washed with water to remove KCl and traces of unreacted metal chloride. During the washing step, the supernatants sometimes displayed characteristic colors of metal complexes (blue for W, brown for Mo, grey for Zr, Nb, Hf and Ta), indicating that not all the reagents were consumed.

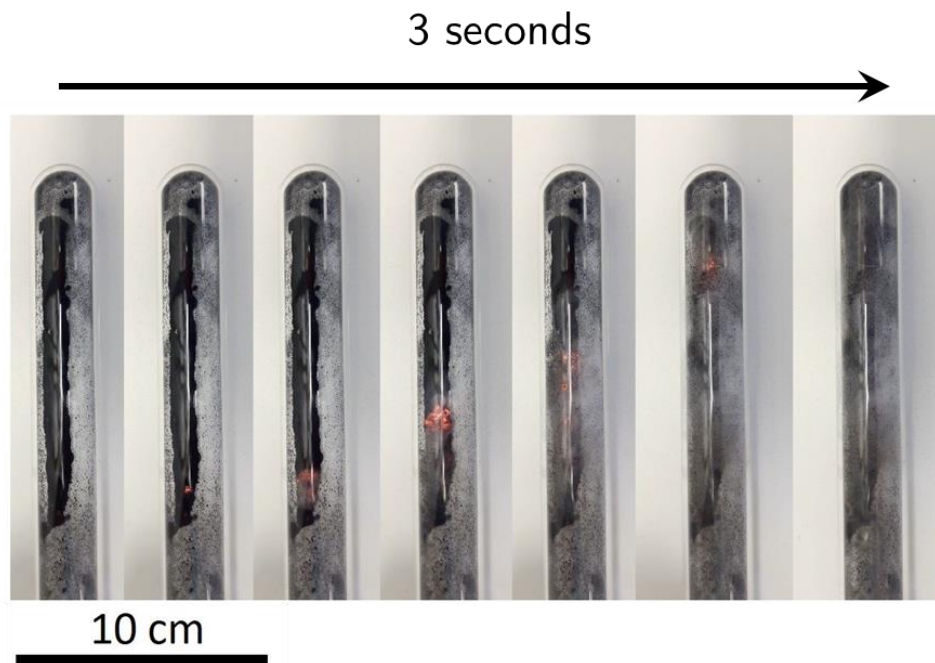


Figure 1. A sequence of photographs showing the ignition and reaction stage of a SSM reaction (Synthesis II.2.) between $\text{ZrCl}_4 + 4 \text{KC}_4$ under Ar, covering a time span of about 3 seconds. The reaction was initiated through external heating by using a heat gun.

II.2.2 Structural and morphological characterization

Figure 2 displays the Powder X-Ray Diffraction (PXRD) patterns of the crystalline inorganic products of the reactions between the metal chlorides and KC_4 under argon (Synthesis II.2.). All the metal chloride precursors used in this study, to the exception of MoCl_3 , are either soluble or hydrolyzed in water, the traces of unreacted precursor are therefore not detected by PXRD in the final product. Despite of the washing step, traces of sylvite (KCl) appear on all the diffractograms and the its diffraction peak at 28.3° was used as a common calibration peak for the angle position 2θ of the detector. For the interpretation of diffractograms, although PXRD is not a quantitative method, we assumed the phases leading to the strongest diffraction peaks are the major crystalline ones. We worked under the assumptions that the phases identified in PXRD are representative of the sample, that there is only a limited amount of amorphous material and that the oxidation layer of the objects exposed to air is small enough to be neglected in a first approach.

Group IV metals. Metallic zirconium and hafnium can form a variety of phases but only $\alpha\text{-Zr}$ and $\alpha\text{-Hf}$ are detected here (Figure 2A-B, peaks at respectively 36.4° and 37.0° indicated by red dashed lines). These phases are the low-temperature metallic phases: the phase transition towards the high-temperature ones $\alpha \rightarrow \beta$ occurs at respectively 862°C and 1780°C for $\text{Zr}(0)$ and $\text{Hf}(0)$.²⁴ The other major species

detected for these two reactions are the metal hydrides (peaks at respectively 32.4° and 33.0° , indicated by green dashed lines), attributed to ZrH_2 and $\text{HfH}_{1.74}$, which are the closest reported hydride phases in the JCPDS (Joint Committee on Powder Diffraction Standards) database. The exact stoichiometries are here undetermined as transition metal hydrides are insertion compounds with hydrogen atoms in the interstitial positions: the number of hydrogen atoms per metal atom can range from 0.8 to 2 for Zr and Hf with little impact on the PXRD spectra. On diffractogram A, peaks at 33.0° and 38.3° (indicated by blue dashed lines) are attributed to ZrC . Early transition metal carbides are known to be nonstoichiometric due to carbon vacancies: zirconium and hafnium carbides are solid solutions with a continuum of stoichiometries from $\text{MC}_{0.5}$ to $\text{MC}_{1.0}$ with small variations of the cell parameters (respectively 0.17 % and 0.5 % of variation between the two extremes).⁴ The peaks are broadened here due to the small size of the crystallites: the precise stoichiometry of the carbide cannot be stated.²⁵ All the powders were washed with ethanol and water and then exposed to air, surface oxidation is therefore expected. Accordingly, the diffractograms display a peak at respectively 30.2° and 30.4° (indicated by violet dashed lines) attributed to ZrO_2 and HfO_2 respectively (Figure 2A-B). Although the Scherrer formula could not be applied using these peaks, their broadness indicates a small crystallite size or an amorphous phase.

Group V metals. On diffractograms C and D of Figure 2, peaks at respectively 34.4° and 34.9° (indicated by blue dashed lines) are attributed to Nb_6C_5 and TaC . By reaction of metal with graphite, different phases of niobium and tantalum carbides can be obtained below 1500°C : $\text{M}(0)$, $\beta\text{-M}_2\text{C}$, M_6C_5 , $\zeta\text{-M}_4\text{C}_3$ and $\delta\text{-MC}$.²⁶ Diffraction patterns of Nb_6C_5 , $\zeta\text{-Nb}_4\text{C}_3$ and $\delta\text{-NbC}$ are close and our experimental diffraction patterns could match each of them. We arbitrarily chose to indicate Nb_6C_5 and TaC . TaO is isostructural with TaC and presents the same lattice parameters: its presence cannot be excluded at this point. Metal hydrides $\text{NbH}_{0.8}$ and $\text{TaH}_{0.5}$ are also detected at respectively 36.1° and 37.6° (indicated by green dashed lines). $\text{NbH}_{0.8}$ pattern is a better match than NbH and other H-rich niobium hydrides. We hypothesize the pronounced triangular shape of the peaks obtained with TaCl_5 is due to the superposition of broad and thin diffraction peaks, resulting from the polydispersity in size of the crystallites.

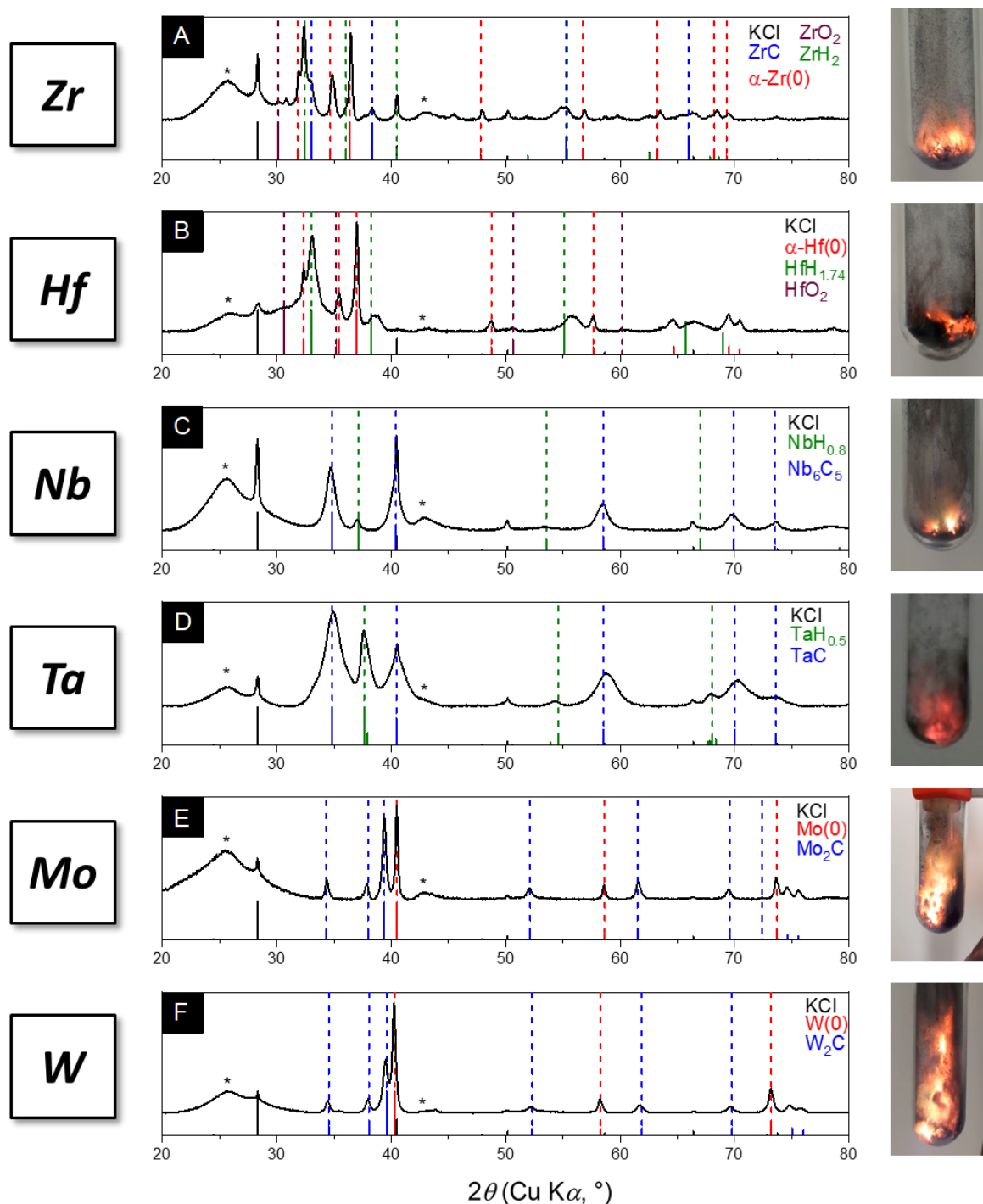


Figure 2. (Left) PXRD patterns of washed powders obtained by the reaction of KC_4 and metal chlorides under Ar according to Synthesis II.2.: (A) $ZrCl_4$, (B) $HfCl_4$, (C) $NbCl_5$, (D) $TaCl_5$, (E) $MoCl_5$, (F) WCl_6 . Asterisks indicate the acetylene black peaks. (Right) Snapshots of the explosion observed in the corresponding reaction.

Group VI metals. On diffractograms E and F, peaks at respectively 40.5° and 40.3° (indicated by red dashed lines) are attributed to $Mo(0)$ and $W(0)$. KCl salt generates a diffraction peak at 40.5° which is almost underneath the first diffraction

peak of metallic molybdenum and tungsten, hence the shoulder which appears at the right of the peak of W(0) at 40.3° . Metal carbides M_2C (indicated by blue dashed lines) are also present for both metals. Tungsten and molybdenum carbides contain small amounts of carbon vacancies and the phase stoichiometries are more precise than for Group IV and V metal carbides. Starting from $MoCl_5$, a single phase of hexagonal β - Mo_2C is obtained, which corresponds to the most common molybdenum carbide and the most thermally stable, the other one being α - MoC . In spite of the excess of carbon, the major phase obtained with tungsten is β - W_2C and not WC .²⁷

Overview. All the reactions described above result in metallic, metal carbide and/or metal hydride phases. The reactions with the six chloride salts were also conducted under static vacuum: they displayed fairly similar behaviors and results than the reactions conducted under argon. Phase speciation for metals in the same column present strong similarities:

(1) metal chlorides of the Group IV (Zr and Hf) form a mixture of mainly the metal(0) and the metal hydride MH_x , but also of the metal carbide MC for Zr and of traces of the metal oxide MO_2 ,

(2) metal chlorides of the Group V (Nb and Ta) form the metal hydride MH_x , or the metal carbide MC in varying proportions under vacuum and in Ar,

(3) metal chlorides of the Group VI (Mo and W) form mainly the metal(0) and the carbide M_2C .

Morphology description. Scanning Electron Microscopy (SEM) images revealed a homogeneous aspect of the samples at a length-scale larger than the micron. All samples were studied by Transmission Electron Microscopy (TEM), after washing, for morphology description and most of the sample correspond to either 5-25 nm large nanoparticles supported on carbon or nanostructured zones with structuration length of the same order of magnitude (Figure 3). These nanostructured zones look like the sintering of several particles. No objects larger than the initial size of the carbon support particles were observed. The different objects are systematically obtained from a batch to another: the diversity therefore does not originate from variability between experiments but rather from an inhomogeneity of the reaction medium. In a few samples of syntheses from $MoCl_5$ and WCl_6 , metal-containing particles present a core-shell morphology (core and shell of typically 10 nm) whose origin and composition are discussed later in this study.

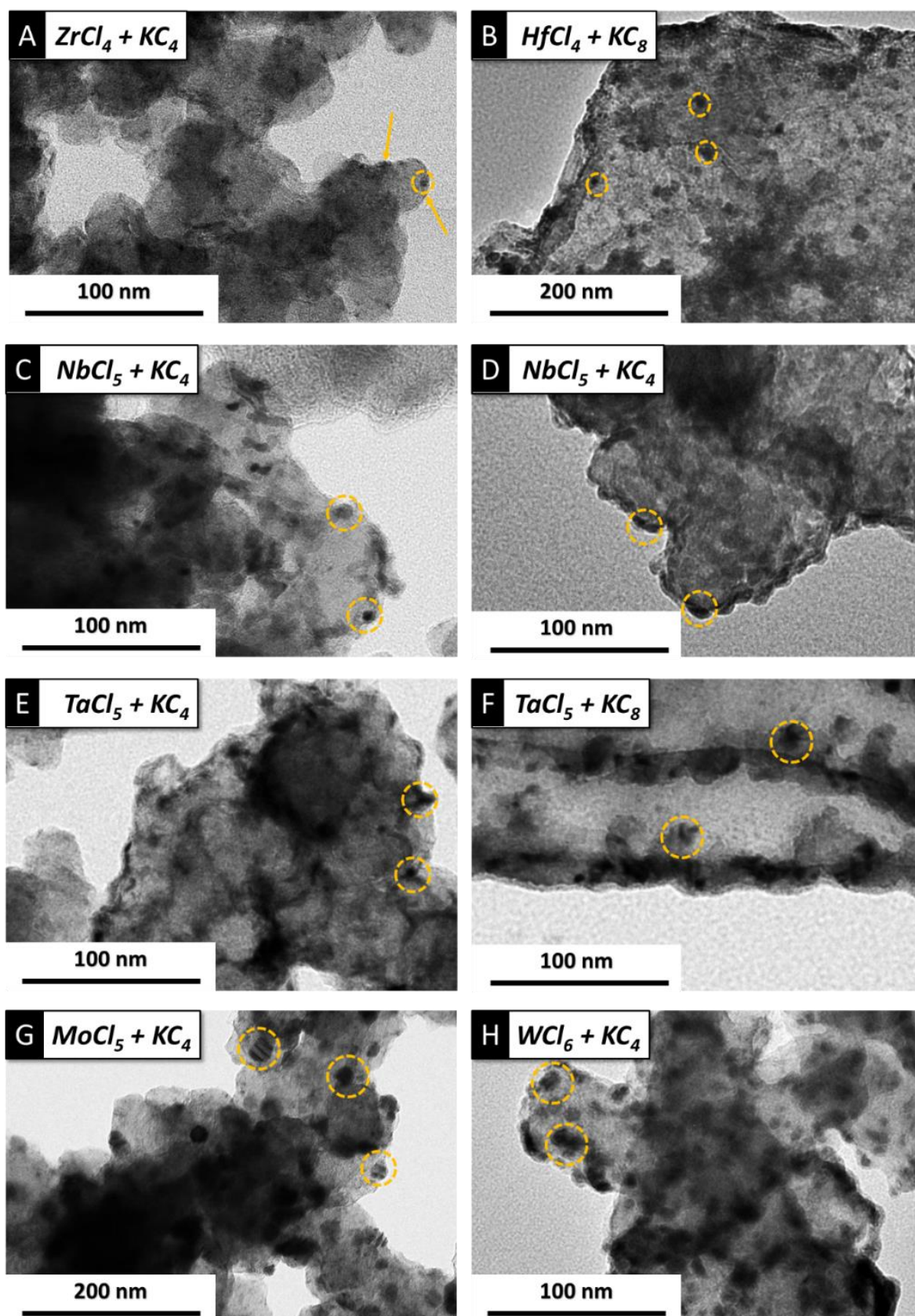


Figure 3. TEM images of different particles supported on carbon supports from reaction between KC_4/KC_8 and metal chlorides (Synthesis II.2.). KC_4 corresponds to an acetylene black support and KC_8 to a graphite one.

Surface oxidation state. X-ray Photoelectron Spectroscopy (XPS) performed on NPs synthesized under Ar from MoCl_5 and KC_4 , and subsequently washed with water and exposed to air, unsurprisingly confirms the presence of surface oxidation with a species at 232.7 eV ($3d_{5/2}$ peak) in the Mo 3d region (Figure 4A). Details on the experimental conditions are given in Appendix I ES.1.9. The presence of reduced molybdenum was noted with a peak at 228.4 eV ($3d_{5/2}$ peak). It can be attributed both to Mo(0) and Mo_2C species. Considering the penetration depth of the XPS technique (1-2 nm for Mo), only the extreme surface of the nanoparticles was probed here.²⁸ Because XPS is a surface-sensitive method, the molybdenum sample was also analyzed with X-ray Absorption Near-Edge Spectroscopy (XANES) at the Mo K-edge (experimental conditions given in Appendix I ES.9.) in order to determine the average oxidation state of the atoms in the nanoparticles. On Figure 4B, the spectrum of the sample is compared with three reference samples: metallic Mo(0), MoO_2 and MoO_3 . None of these compounds has a spectroscopic signature close to that of the sample. However, the edge position of the Mo nanocarbide is located at 20 007.5 eV, closer to the Mo(0) metallic edge (20 003.9 eV) than to these of the oxides MoO_2 and MoO_3 (20 016.5 eV and 20 020.5 eV, respectively). The spectrum of the sample is even closer to the spectrum of molybdenum carbide from literature.^{29,30} In particular, features (a), (b) and (c) on Figure 4B (respectively, a shoulder *ca.* 20 011 eV, an inflexion point *ca.* 20 033 eV and a maximum *ca.* 20 039 eV) are similar to the ones observed for the samples MoC-G and Mo_2C -G from reference [30]. Overall, Mo_2C describes the best the average environment of Mo atoms in the sample, in agreement with PXRD observations. XANES thus confirms that the main product is reduced molybdenum, although this was not clear from XPS measurements. This discrepancy is explained by the fact XPS can only probe the extreme surface containing oxidized species. The limited depth of oxidation of the nanoparticles is supported by the fact we observed distinct diffraction fringes of Mo_2C phase on nanoparticles as small as 5 nm in diameter. Samples of other metals were also analyzed by XPS: the metal is mostly observed at an elevated oxidation degree (+4 for Zr and Hf, +5 for Nb and Ta, +6 for W).

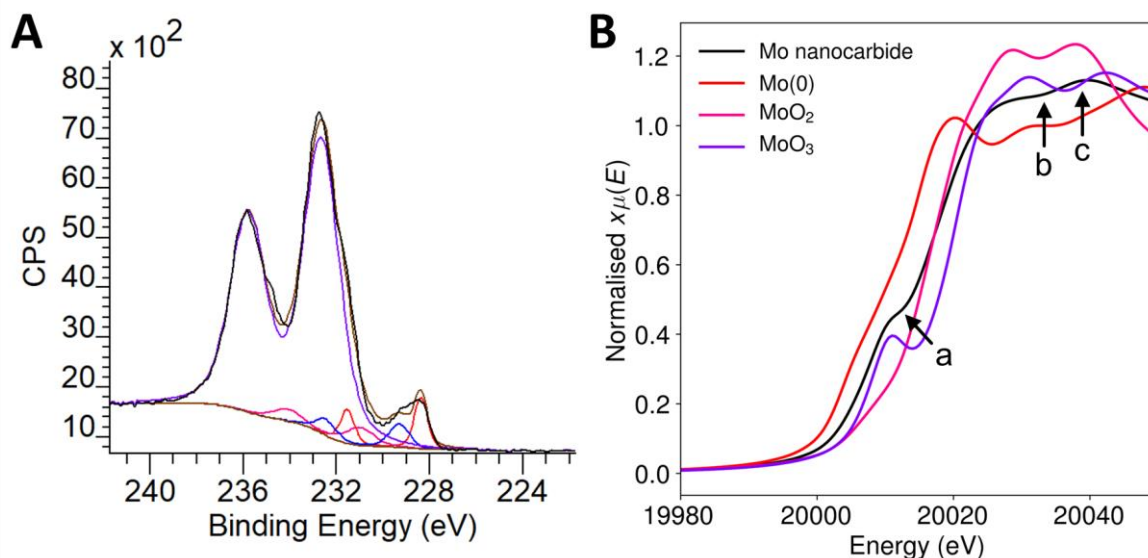


Figure 4. Redox state of sample Mo nanocarbide from XPS and Mo K-edge XANES measurements. (A) XPS of the Mo 3d region, black: measured signal, red: contributions attributed to Mo(0), blue: Mo(+II), magenta: Mo(+IV), purple: Mo(+VI), brown: sum of all 4 contributions. (B) Mo K-edge XANES measurements, black: sample Mo nanocarbide pellet, red: Mo(0) sheet, magenta: MoO₂ pellet, purple: MoO₃ pellet. Features (a), (b) and (c) are features characteristic of the signal of molybdenum carbide.

II.2.3 Determination of reaction temperature by thermodynamic considerations

Ignition and combustion temperatures. Reactions with ZrCl₄ and HfCl₄ are less explosive than the ones with NbCl₅, TaCl₅ and MoCl₅, themselves less explosive than the one with WCl₆ (Figure 2, snapshots). The combustion temperature, *i.e.* the highest temperature reached during the explosion, is expected to be one of the key parameters for the phase speciation of the metal. Considering the brevity of the reaction, *ca.* one second, and its high exothermicity, a large amount of energy is liberated in a short period of time and a small space, leading to high temperatures. As a first approach of the released energy by the SSM reaction, we can compare the differences of standard electrochemical potentials ($\Delta E^\circ = E^\circ(\text{MCl}_x) - E^\circ(\text{K})$) between K and MCl_x for the different metal chlorides. Standard potentials are not reported for all the chloride salts, we therefore compare the ΔE° with metal oxides of similar degrees of oxidation (ZrO₂, HfO₂, Nb₂O₅, Ta₂O₅, WO₃) (Table 1, column 1). A larger difference in standard potentials corresponds to an easier and more exothermic reduction of the corresponding metal chloride and thus to a more violent reaction. Metal oxides from the same column have similar redox potentials and ΔE° increases from Group IV to Group VI (1.4 V for Group IV, 2.2 V for Group V and above 2.8 V

for Group VI). This trend is consistent with the increase in exothermicity observed on Figure 2.

N°	1	2	3	4	5
Metal salt	ΔE° potassium-oxides	Released energy (kJ/mol)	Adiabatic temperature T_{ad}	Chloride salt T_m	Carbide Gibbs energy of formation at 1500 °C (kJ/mol)
ZrCl ₄	1.38 V	642	990 °C	331 °C (subl.)	-181 (ZrC)
HfCl ₄	1.42 V	633	970 °C	432 °C	*
NbCl ₅	2.29 V	1231	1490 °C	205 °C	-133 (NbC)
TaCl ₅	2.18 V	1170	1420 °C	216 °C	-140 (TaC)
MoCl ₃	*	824	1500 °C	410 °C	-63 (Mo ₂ C)
MoCl ₅	2.89 V **	1502	1500 °C	194 °C	-63 (Mo ₂ C)
WCl ₆	2.84 V	1841	1500 °C	275 °C	-38 (W ₂ C) and -33 (WC)

*No data available. **For Mo(V): we used the average E° of MoO₂ (0.15 V) and MoO₃ (0.07 V)

Table 1. Thermodynamic considerations for the reactions conducted on the different metal chlorides with stoichiometric proportions of KC₄. (1) Difference in standard potential E° between potassium (-2.93 V) and the corresponding oxide. The redox half-equations are given in water with M(0) as the reducing agent.³¹ (2) Absolute value of molar reaction enthalpy of the reaction of formation of the metal.³² (3) Adiabatic temperature T_{ad} determined with Eq. 2 and considering the eventual melting and evaporation of KCl. (4) Melting temperature of the corresponding chloride salt (for ZrCl₄, sublimation temperature). (5) Standard Gibbs energy of formation, per atom carbon, of the most common carbide phases from elemental reagents (M(0) and graphite).

A more rigorous approach for the exothermicity of the reactions is the calculation of the reaction enthalpy. To calculate it, we define the ignition temperature T_{ig} as the temperature at which the reaction is triggered in the powder mixture. The heat released by the reaction at T_{ig} , noted $|\Delta_{\text{reaction}} H_{T_{ig}}^0|$, corresponds to the absolute value of the enthalpy of reaction, *i.e.* the difference in enthalpy of formation between the reagents and the products. It can be calculated using Hess's law, the useful data for the calculations of released energy by the reaction are given in Appendix II, TC.2. and the results in Table 1, column 2. The high exothermicity

of the reaction is due to the large negative enthalpy of formation of the coproduced salt KCl. To simplify the thermodynamic calculations, we made the assumption that M(0), KCl and graphitic carbon are the only products and we did not take into account the formation of carbides from M(0) and graphite, which is also exothermic but in a much smaller extent. We assumed the conversion is total. The change in the enthalpy of formation of the different chloride salts between room temperature and the ignition temperature T_{ig} (always inferior to 75 °C) can be neglected as it is below 1 % between room temperature and 75 °C (*cf.* Ellingham approximation). Reactions with chlorides of metals of Group IV liberate less heat than reactions with metals of Group V and Group VI, the more exothermic reaction being the one with WCl_6 . The estimated energies released during the explosion are consistent with the visual observations of the reaction and with the evolution of ΔE° .

Adiabatic temperature. We define the adiabatic temperature T_{ad} as the theoretical maximum temperature reached by the mixture if we consider the system as thermally isolated. T_{ad} is a theoretical temperature, to be distinguished from the actual temperature during the reaction, termed combustion temperature and noted T_{comb} . It seems reasonable to consider the system as pseudo-adiabatic considering the brevity of the reaction. All the energy released by the reaction is then dissipated in the heating of the powder and eventual endothermic state changes (melting and evaporation of KCl). As the enthalpy is a state function, T_{ad} may be defined independently on how the system actually reaches its final state (Figure 5).⁷ We note C_p the heat capacity of the products (KCl salt, graphite and metal(0)): it is a function of the temperature and of the physical state of the compounds. The models we chose for their values are given in Appendix II, TC.2.. T_{ad} is determined by Eq. 2: if T_{ad} is beyond the melting point T_{fus} (770 °C) or the boiling point T_{vap} (1500 °C) of KCl, we also have to take into account the enthalpy of fusion $\Delta H_{\text{fus}}^0(\text{KCl})$ and the enthalpy of evaporation $\Delta H_{\text{vap}}^0(\text{KCl})$ of the salt.⁶ All the other compounds (metals, carbides and graphite) have melting or degradation temperatures far beyond the boiling point of potassium chloride and their physical state do not change on the temperature range relevant here.

$$|\Delta_{\text{reaction}} H_{T_{\text{ig}}}^0| = \int_{T_{\text{ig}}}^{T_{\text{fus}}} C_p(T) dT + x \Delta H_{\text{fus}}^0(\text{KCl}) + \int_{T_{\text{fus}}}^{T_{\text{ad}}} C_p(T) dT \quad (2)$$

This method does not pretend to give an exact value of the combustion temperature T_{comb} , however it gives an upper limit: the adiabatic temperature T_{ad} . The actual combustion temperatures are certainly lower due to a not total conversion and to the heat transfers towards the Schlenk tube walls and to the gas phase if there is one. A similar study about the sulfuration of MoCl_5 with Na_2S to form Mo_2S gave an adiabatic temperature of 1450 °C (boiling point of NaCl) and optical pyrometry measurements indicated an actual temperature close to 1100 °C.⁶

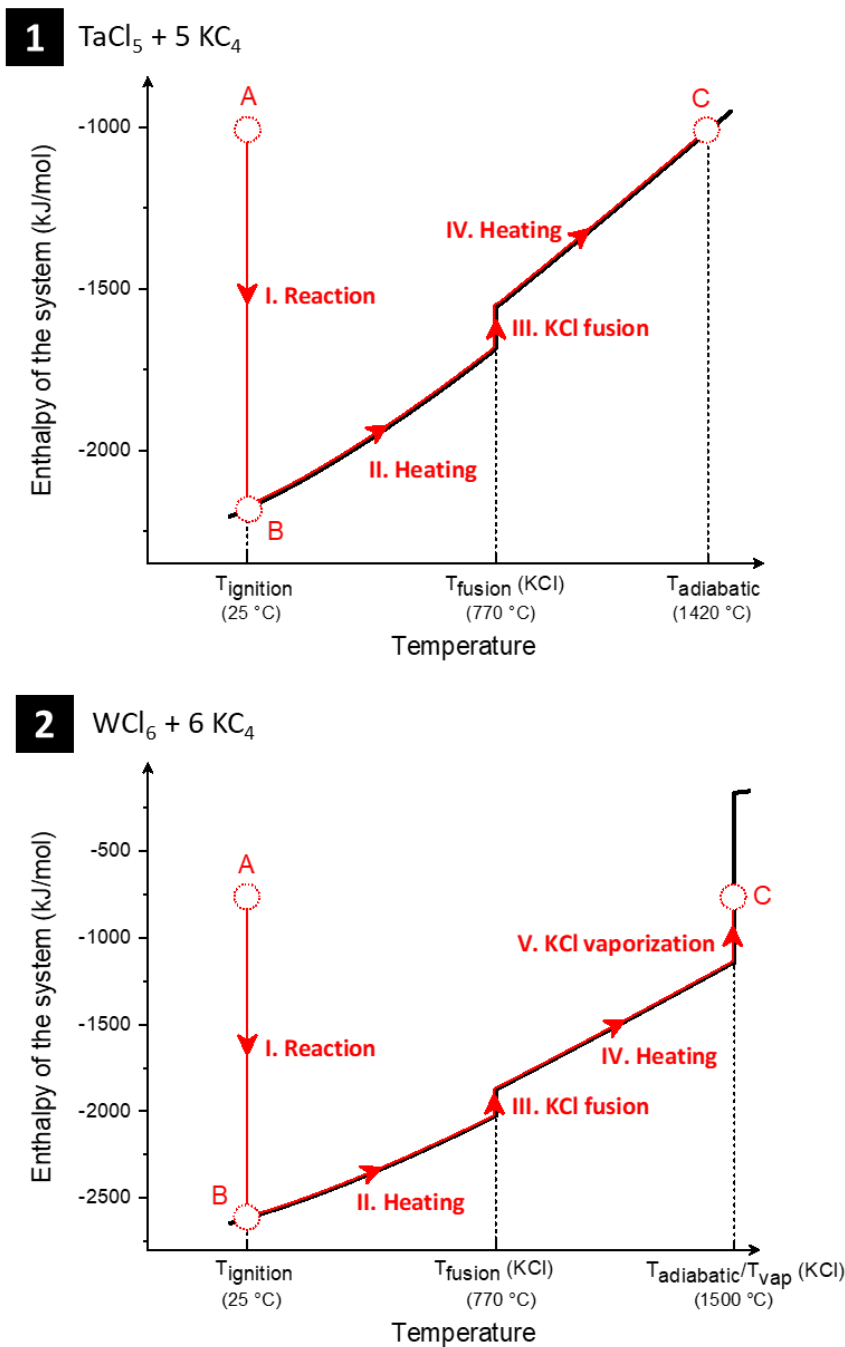
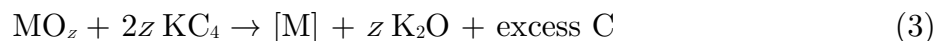


Figure 5. Illustrations of a hypothetical thermodynamic pathway of the reaction (1) $\text{TaCl}_5 + 5 \text{KC}_4 \rightarrow \text{Ta}(0) + 5 \text{KCl} + 20 \text{C}$ and (2) $\text{WCl}_6 + 6 \text{KC}_4 \rightarrow \text{W}(0) + 6 \text{KCl} + 24 \text{C}$. (A) Initial state before reaction starts, (B) hypothetical state just after reaction but before temperature elevation, (C) final state of the system at the adiabatic temperature T_{ad} . A and C have equal total enthalpies.

The reaction was conducted here on small quantities (≈ 0.2 mmol of chloride salt) and the released energy was eventually absorbed by the Schlenk tube, whose temperature elevation did not exceed 50°C . All the reactions presented here have T_{ad} close or above 1000°C (Table 1, column 3) except metals from Group IV whose

adiabatic temperatures are approximately 400 °C lower than those of the other metals. The combustion temperatures are high enough to exceed the metal chloride melting points (Table 1, column 4): as soon as the reaction initiated, the metal chloride melts and triggers the reaction in its vicinity. This melting propagates the reaction zone and maintains a high temperature until all the reagents are consumed (Figure 1).

Modified Solid-State Metathesis (MSSM). A similar reaction was attempted on carbon dispersed potassium (KC_4) and molybdenum oxide (MoO_3) precursor instead of molybdenum chloride (MoCl_5). This Modified Solid-State Metathesis (MSSM, “modified” as the precursor is an oxide and not a chloride) presents the advantages of a cheap and stable precursor. The reaction failed to produce carbides or any other products even if the mixture was heated above 100 °C. If we consider Eq. 3, the reaction enthalpy for MoO_3 is -160 kJ/mol. By comparing this value with the enthalpies of reaction with metal chlorides, comprised between -623 kJ/mol and -1841 kJ/mol, we can conclude the low exothermicity of the reaction with MoO_3 impends the self-propagation *via* high temperatures.



Calculations made for the other metal oxides led to less exothermic reactions than with MoCl_5 , or even endothermic ones (all the results are given in Appendix II, TC.2.). The difference between MSSM and SSM in our case is the important difference in standard enthalpy of formation of the coproduced salt (-394 kJ/mol for K_2O vs. -818 kJ/mol for 2 KCl). Sylvite (KCl) is a thermodynamic well, which leads to a strongly exothermic reaction, contrarily to K_2O . MSSM for carbide synthesis was nonetheless successfully reported in other studies when the reducing agent was CaC_2 or SrC_2 : this is made possible by the large enthalpy of formation of CaO and SrO (-635.7 kJ/mol and -592 kJ/mol respectively).²⁰ The experimental validation of the reactivity of KC_4 , KC_8 , CaC_2 and SrC_2 with metal chlorides and of only CaC_2 and SrC_2 with metal oxides confirms the pertinence of our model for calculating enthalpies of reaction.

Thermodynamic control versus process control. All the Gibbs energies of formation of the carbide phases from the metal(0) and elemental carbon ($\Delta G_f^0(\text{carbides})$) are negative (Table 1, column 5) and the system presents large excess of graphitic carbon, at least 20 atoms of C per metal atom. If the system had reached a thermodynamic equilibrium, there should be no metal(0) left to the benefit of carbide. On the contrary, metal(0) and hydride phases, deriving from metal(0), were detected. These phases were even obtained in higher proportions for Group IV metals than for Group VI ones whereas the Gibbs energy of formation of the carbide is higher for Mo_2C and W_2C than for ZrC and HfC . This consideration

comforts our hypothesis that the reaction is under kinetic control and not thermodynamic one. In this system, the reaction products speciation is in great part determined by the combustion temperature and the quality of the reagents contact, these two points being themselves related to different process parameters.

II.3. Study of the process parameters impact

The reaction between the chloride salts and potassium is not under thermodynamic control as previously shown. We therefore studied the influence of different process parameters on the metal phase speciation. PXRD is not a quantitative method so the pie-charts displaying the phase speciation of the crystalline part in this section must be regarded as trends rather than absolute ratios. Methods for exactly quantifying the proportion of each phase are beyond the scope of this study as only the evolution of the proportions is relevant here. For readability reasons, comparisons of diffractograms are displayed only on a small angle range showing relevant peaks. The reactions were all performed twice and the results are rather reproducible although the reactions are delicate to conduct. The commented trends are stable and consistent through the different studied metals.

Carbon source. The nature of the carbon support, acetylene black *vs.* graphite, was identified as having an importance on the proportion of carbide *vs.* metal(0) for Group VI metals. In the case of MoCl_5 , there is more carbide when the reaction is performed with potassium graphite (KC_8) than with potassium acetylene black (KC_4) (Figure 6A). Similar results are obtained with WCl_6 (data not shown). The difference in enthalpy of formation of KC_4 and KC_8 is of 2.5 kJ/mol so the relative change in reaction enthalpy is below 2 %: the heat released by the reaction is virtually the same for KC_4 and KC_8 . The quantity of carbon is however doubled, increasing the heat capacity of the medium and thereby limiting the combustion temperature. The decrease in the adiabatic temperature from KC_4 to KC_8 is between 200 °C and 400 °C (Appendix II, TC.2.). If we consider the carbide phase as the phase favored by high temperatures, this explanation based on the reaction enthalpy goes against the observed trend as the proportion of carbide should increase with adiabatic temperature and should therefore be higher with KC_4 , which is not the case. The origin of the difference between KC_4 and KC_8 reactions could not be definitely identified but several hypotheses are proposed. The graphitic carbon may be more easily decomposed than acetylene black and thus diffuses more quickly in metal NPs. The contact between the two precursors powders may be more intimate for graphite than for acetylene black due for instance to the grain size and self-cohesion of the powder. Finally, as KC_8 is more compact than KC_4 , the explosion disperses less the mixture of powders (as observed with a naked eye) and the heat dissipation may be lower for KC_8 leading to higher temperatures locally, hence a better carbon insertion.

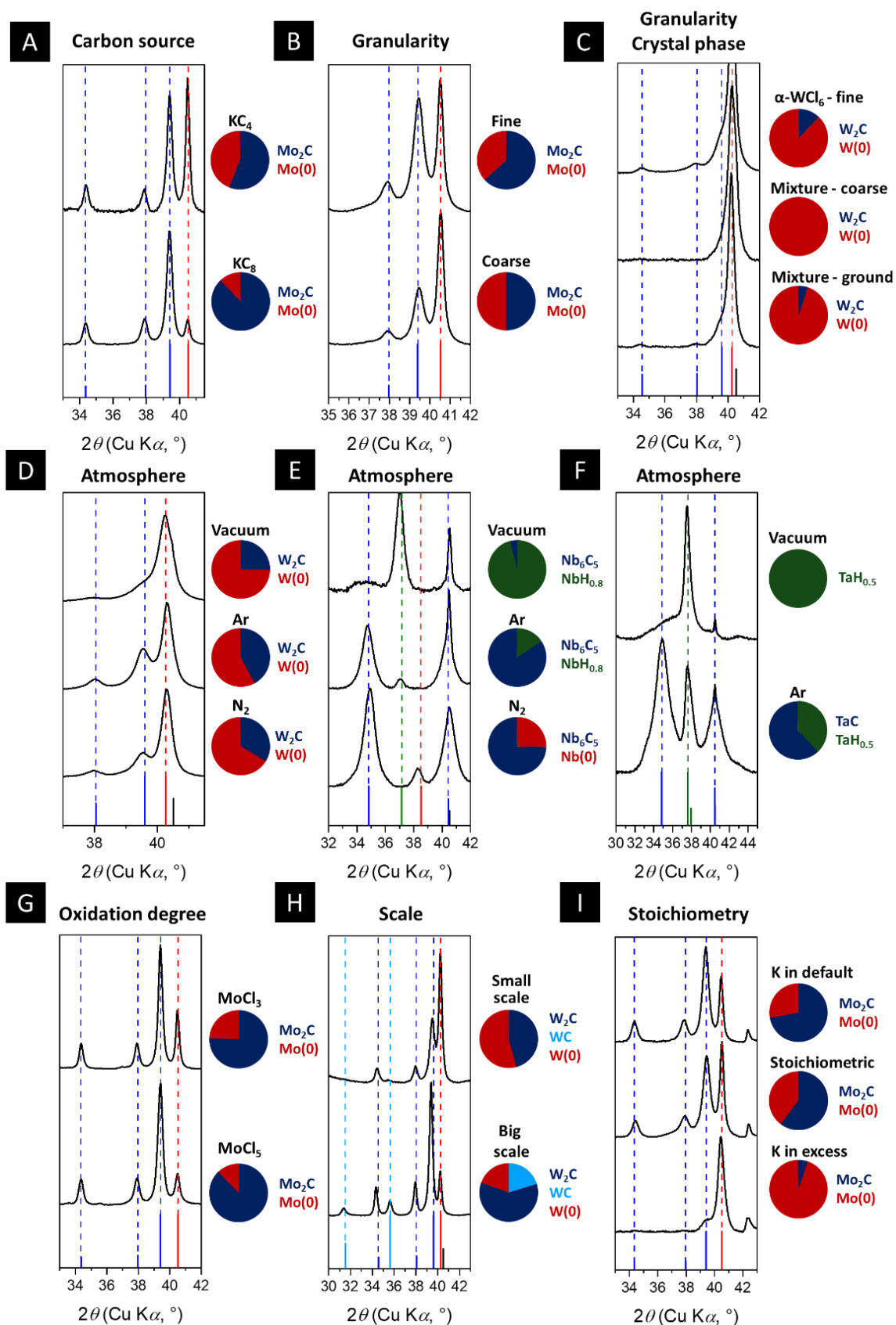


Figure 6. Details of diffractograms of powders obtained by reaction with metal chlorides under different conditions. (A) MoCl_5 under Ar with KC_4/KC_8 , (B) MoCl_5 fine/coarse under vacuum with KC_8 (C) WCl_6 fine/coarse/ground under vacuum with KC_4 , (D) WCl_6 under

vacuum/Ar/N₂ with KC₄ (E) NbCl₅ under vacuum/Ar/N₂ with KC₄, (F) TaCl₅ under vacuum/Ar with KC₄, (G) MoCl₃/MoCl₅ under Ar with KC₈, (H), WCl₆ under Ar with KC₄ at small/big scale and (I) MoCl₅ under Ar with KC₈ in default/in stoichiometric proportion/in excess. Pie charts are guides for the eyes of the repartition in the different phases.

Precursor grain size. Particle size of MoCl₅ and WCl₆ was found to influence the phase speciation of the products, in favor of the metal for an increasing grain size (Figure 6B-C). To generate bigger crystal grains, two precursors, MoCl₅ and WCl₆, were recrystallized under vacuum at 210 °C and the products were collected and used as is without grinding (more details in Appendix I, ES.1.). Due to the air degradation of the precursors, no quantitative measurements of the grain size of the recrystallized powders of MoCl₅ and WCl₆ were performed but the commercial powder has granularity below 1 mm whereas that of recrystallized precursors is above. An increase in the precursor grain size leads to a lower contact area between the reagents which may result in a lower conversion if not all the precursor has reacted. The loss in heat released by the reaction may lead to a lower combustion temperature and therefore explain the lower conversion to carbide.

Precursor crystal phase. As the reaction occurs between two solids, we investigated whether the crystal phase of the precursor has an impact on the products. Tungsten hexachloride (WCl₆) displays two crystal phases: the α -rhombohedral phase (corresponding to the commercial product) and the β -hexagonal phase.³³ The recrystallization of α -WCl₆ at 210 °C under vacuum led to a mixture of α -WCl₆ and β -WCl₆ (the phase transition at atmospheric pressure is tabulated at 177 °C). Although no absolute quantification of the two phases was performed by PXRD, we can estimate the major phase of the recrystallized compound is β -WCl₆ (data shown in Appendix I, ES.1.), assuming they lead to a similar signal. To limit the influence of the granularity, the recrystallized mixture of α -WCl₆ and β -WCl₆ was ground to obtain a finer powder, however not as fine as the commercial α -WCl₆ as extensive grinding triggers a reaction on WCl₆ (beige-red coloration of the powder instead of deep purple). The peaks of tungsten carbide W₂C (34.5°, 38.0° and 39.6°) were not visible for coarse precursor grains but they reappeared on the diffractogram of the reaction with “ground” WCl₆ (Figure 6C). This indicates the difference in metal speciation between commercial α -WCl₆ and the mixture of α -WCl₆ and β -WCl₆ from the recrystallization is probably due to precursor granularity and not to crystal phase. This result is supported by a difference of enthalpies of formation between α -WCl₆ and β -WCl₆ of only 21 kJ/mol at room temperature, accounting for a negligible change in the enthalpy of reaction of 1 %.

Inert gas (Ar/N₂) versus vacuum. The metal speciation radically changes whether the reaction is performed under vacuum or in Ar or N₂-filled Schlenk tubes. In the case of MoCl₅ and WCl₆, the absence of gas phase leads to a higher proportion of metal(0) *vs.* metal carbide M₂C whereas the ratio M(0)/M₂C seems less affected by the nature of the gas (Ar or N₂) (Figure 6D). For Group V metals (Nb and Ta), the only product detected was a hydride (NbH_{0.8} and TaH_{0.5}) when there is no gas phase (Figure 6E-F). The presence of hydrides may be surprising considering there is theoretically no stoichiometric source of hydrogen but we hypothesized the hydride NPs originate from the metallic NPs, this point will be discussed in detail later. The differences in the diffractograms between the experiments with the two gases are smaller than between gas and vacuum. Therefore, the impact of this parameter on the reaction does not originate from a chemical phenomenon linked to the nature of the gas molecules but rather from a physical phenomenon. We did not consider the heat dissipation by the gas phase as a credible explanation. Indeed, Ar has a molar heat capacity of 12.5 J/mol/K which corresponds to a heat capacity of 12.5 mJ/K for the entire volume (25 mL) of the Schlenk tube. The energy needed to elevate the temperature of the gas of 1000 °C is 12.5 J whereas the minimum energy released by the reaction of 0.29 mmol of HfCl₄ (the less exothermic reaction) is 152 J. If the entire gas volume of the Schlenk was immediately heated to the combustion temperature, it would account for only 8 % of the total released energy. We do not believe such a decrease of energy is enough to strongly modify the phase speciation. Another possible explanation is the self-cohesion of the powder mixture: as mentioned earlier, a black particulate solid is spread over the Schlenk tube during the explosion and this is particularly true for reactions under vacuum. This spreading may lead to a higher heat dissipation or a lower conversion and therefore to lower combustion temperatures. Finally, the melting and boiling points of KCl decrease under vacuum which may also limit the combustion temperature. Even though we cannot decide the mechanism at stake here, this process parameter (gas phase) is clearly critical.

We noticed that the reactions more often self-ignited (*i.e.* without heat gun activation) under vacuum, or sometimes during the gas evacuation, than similar reactions under inert gas. Conducting the reaction under vacuum leads to a lower ignition temperature (high reactivity) but also to a lower combustion temperature (low proportion of carbides *vs.* metal(0) and hydrides compared to reactions under Ar or N₂).

Oxidation number. The reaction performed with a molybdenum chloride of lower degree of oxidation (MoCl₃ *vs.* MoCl₅) led to the same metallic and carbide phases (Figure 6G). We also detect traces of unreacted MoCl₃ which did not hydrolyze or degrade, even in water, to the contrary of MoCl₅. Experiments showed a comparable phase speciation of the molybdenum. The heat released by the reaction of KC₈ with MoCl₃ (817 kJ/mol) is only 55 % of the heat released by the reaction with

MoCl_5 (1489 kJ/mol) but the total heat capacity of the mixture with MoCl_3 is 70 % that of the one with MoCl_5 , we can therefore expect similar combustion temperatures. We conclude the impact of the initial oxidation number is limited if close combustion temperatures are reached.

Scale. The reactions of this study were conducted on the scale of 100 mg of KC_4 or 155 mg of KC_8 . The scale up of the reaction has an important impact on the phase speciation, at least for Mo and W. Figure 6H shows the diffractograms obtained for the reaction conducted on WCl_6 and KC_4 under Ar with 100 mg and 500 mg of KC_4 . The proportion of metallic particles is lowered when the scale is increased, to the benefit of carbide. Furthermore, another carbide, WC, was detected in addition of W_2C . We hypothesized the increase in mass of the reaction medium diminishes losses of heat by dissipation. Higher combustion temperatures may be attained, leading to a more complete carburization of the metallic NPs and more carbon-rich carbide phases. Indeed, WC is usually obtained at higher temperatures than W_2C .³⁴

Stoichiometry. We finally explored the potential impact of a default or an excess of the reducing agent (KC_8) *vs.* the metal source in the case of MoCl_5 . The same crystal phases were obtained, whatever the K: MoCl_5 stoichiometry (0.5, 1 or 2). A higher proportion of carbide was observed when the potassium was introduced in default or in stoichiometric amount. The presence of the same crystallographic phases indicates the reaction of reduction of the metal salt by KC_8 does not go through stable species with intermediary oxidation states but directly to the metallic or the metal carbide nanoparticles. As the heat released by the reaction is limited by the reagent in default, whereas the heat capacity is imposed by the whole mixture, the combustion temperature would normally be maximal for a K: MCl_x ratio of 1. Thermodynamic calculations give an adiabatic temperature of respectively 1100 °C, 1250 °C and 830 °C for the K: MoCl_5 ratio of 0.5, 1 and 2. The reaction with the lowest adiabatic temperature, *i.e.* corresponding to the potassium introduced in excess, was indeed the one producing the smallest amount of carbide *vs.* the metal(0).

II.4. Mechanism proposal

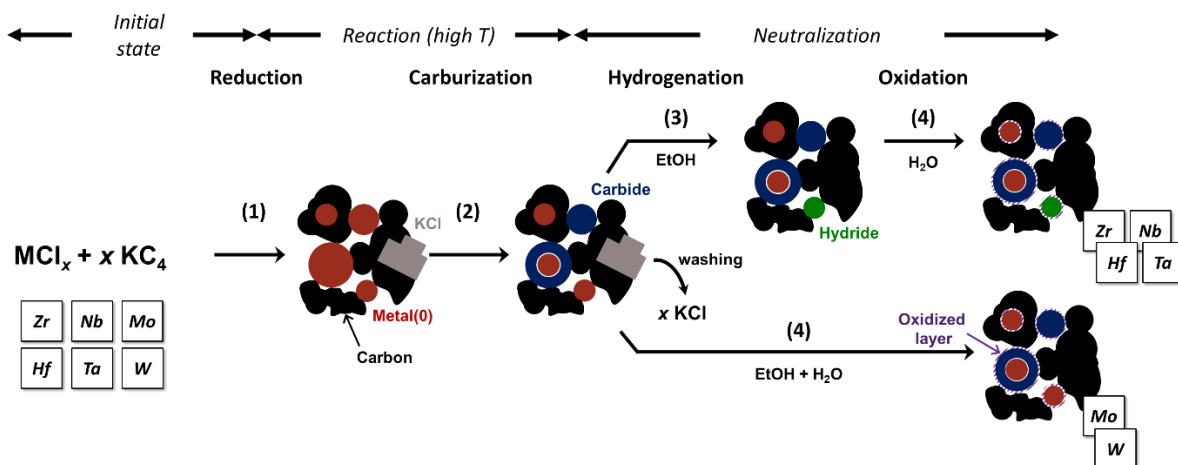
Reaction initiation. The initiation of the reaction, *i.e.* the self-ignition of the mixture, depends mainly on two parameters: the nature of the chloride salt and the gas phase. The more reactive compound is WCl_6 followed by MoCl_5 , NbCl_5 , TaCl_5 and then ZrCl_4 , HfCl_4 , MoCl_3 . Under vacuum, only ZrCl_4 , HfCl_4 and MoCl_3 needed heat gun activation, the other precursors self-ignited within a few minutes or during gas evacuation. Under Ar, the required heating increased from WCl_6 to MoCl_3 . Roughly, metal chlorides with high melting point require a stronger heating, with an exception for WCl_6 which is the most reactive but has a higher melting point (275 °C) than MoCl_5 (194 °C), TaCl_5 (216 °C) and NbCl_5 (205 °C) (Table 1, column 4). MacKenzie *et al.* attributed the self-ignition temperature to the lowest temperature at which one of the two reagents undergoes a physical state change.⁸ Tungsten hexachloride WCl_6 undergoes a crystallographic phase transition $\alpha \rightarrow \beta$ at a lower temperature (177 °C) than the melting point of the second more reactive precursor, MoCl_5 . The trend mentioned by MacKenzie is therefore in agreement with our observations. Interestingly in our case, even though the trend is respected (including WCl_6 if we take into account the solid phase transition), there is no need to attain the actual physical state change temperature to trigger the reaction. We could not explain such a high reactivity with KC_4 - KC_8 . Applying vacuum decreases the melting points of all the chloride salts: we hypothesize this effect is significant enough to explain the higher reactivity observed under vacuum than in Ar.

Reduction step. In this study, metallic phases are reported for all the metals (Figure 2). For a series of reactions, the crude was analyzed by PXRD in capillary under argon after reaction but before neutralization with ethanol or water (Figure 8). Potassium chloride (KCl) is systematically detected in high proportions, the reduction of the metal chlorides in metallic or carbide phases is therefore allowed by the oxidation of KC_4 or KC_8 in K^+ . If alternative pathways exist, they were not detected. The presence of metallic phases comforts the hypothesis made by the community according to which the solid-state carbide metathesis reactions go along a sequential reduction-recombination pathway and that the metallic state is an intermediate of the reaction (Eq. 3).²⁵ The carbon element is not directly transferred from KC_4 or KC_8 to the metal chloride. Most of the nanoparticles formed during this step are supported on the carbon (Scheme 1, step (1)).



Carburization step. To the exception of Hf, carbide phases were reported for all metals but in varying proportions depending on the group of the metal and on the process parameters. The reactions with Group VI metals tend to produce more

carbides than Group IV and Group V metals and the carbide phase was usually obtained in higher proportions when process parameters favored high temperatures (fine granularity of the precursors, presence of a gas phase or large scale). We also detected traces of WC in addition of W_2C on reactions led on large scales between WCl_6 and KC_4 (Figure 6H). Under thermodynamic control, tungsten monocarbide (WC) is synthesized at higher temperatures than ditungsten carbide (W_2C). We suggest all the carbide phases are obtained by carburization of the preformed metallic NPs. This carburization corresponds to the diffusion of carbon atoms from the graphite or the acetylene black to the metallic NPs (Scheme 1, step (2)).



Scheme 1. Proposed reaction mechanism. Top: elements that form metal hydrides, bottom: elements that do not form metal hydrides.

On several samples with WCl_6 , core-shell structures were observed with TEM (Figure 7A-B). According to the contrast, the core is more electron-rich than the shell. Diffraction fringes appear on STEM micrograph for the core (Figure 7B) and the corresponding distance (2.2 \AA) could correspond to W (2.24 \AA theoretically). Energy Dispersive X-ray Spectroscopy (EDS) performed on the different zones reveals that they all contain high amounts of carbon, which was expected considering the presence of graphite in the whole sample, and negligible amounts of oxygen (Figure 7C-F). Although EDS is not quantitative for light elements, the hypothesis of a tungsten oxide (WO_3) shell can be excluded. The shell and the core could not be discriminated by EDS: both contain significant amounts of tungsten. No diffraction fringes could be observed in the shell, preventing a direct phase identification: we cannot be decided based on these micrographs whether the shell contains a carbide phase or inclusion of tungsten atoms into a carbon shell. However, as the number of tungsten atom per volume unit slightly decreases when W(0) is transformed in W_2C , a core-shell structure $W@W_2C$ would be consistent with the observed contrast (dark for core, light for shell).

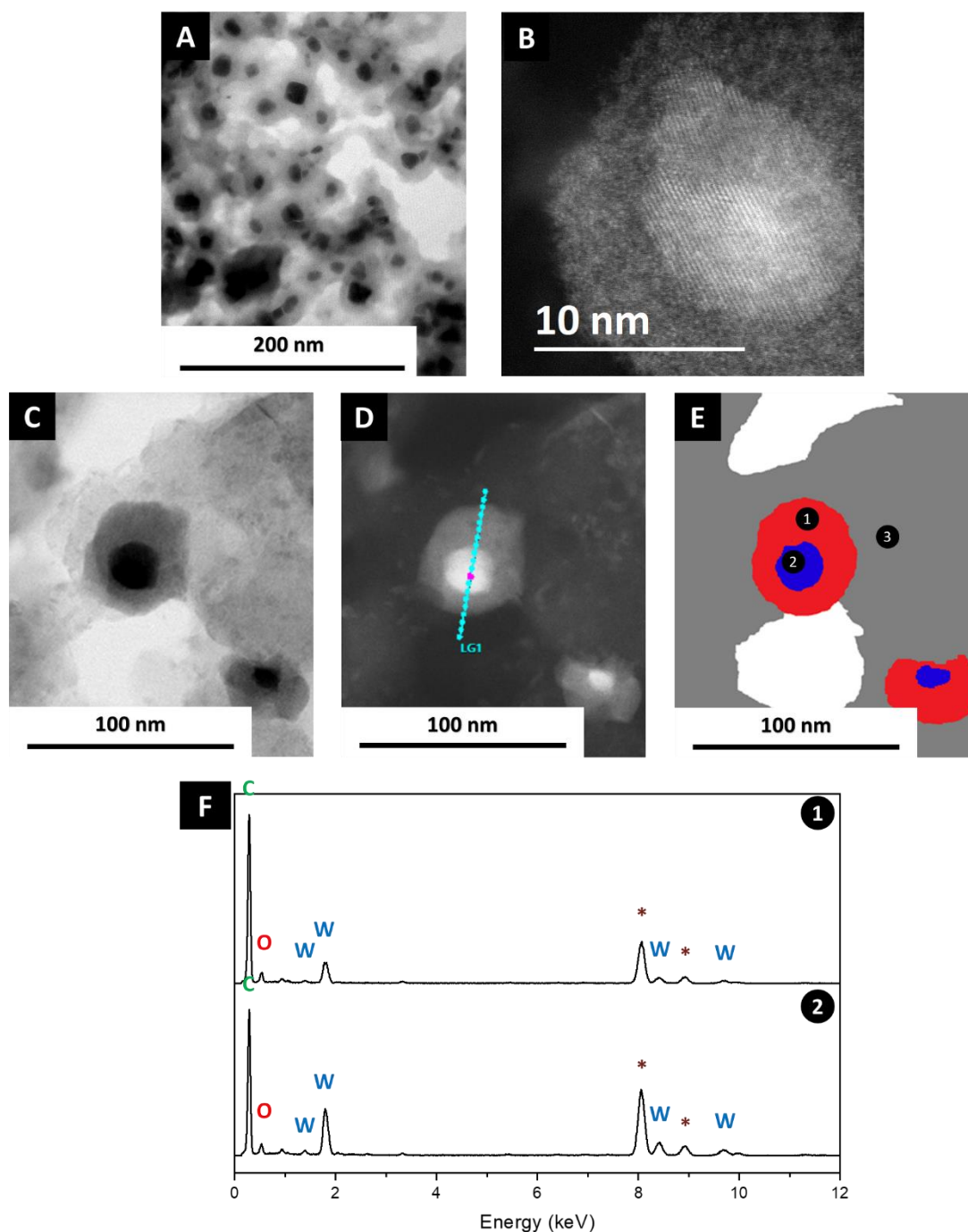


Figure 7. Core-shell particles *via* the reaction of WCl_6 with KC_8 under vacuum. (A, C) Bright-Field and (B, D) High Angle Annular Dark-Field Scanning Transmission Electron Microscopy of tungsten-containing NPs supported on graphite. (E) Scheme of the sample with suggested phases (blue = metallic tungsten, red = W_2C or carbon with tungsten atoms and grey = graphite). (F) EDS spectra of the zones (1) and (2) (the asterisks correspond to Cu, from the EDS anode).

Hehemann *et al.* studied the mechanism of carburization of tungsten metal particles by acetylene black into tungsten carbides WC and W_2C .³⁵ The commonly

accepted pathway is a two-stage process starting with the formation of ditungsten carbide (W_2C) followed by carburization in WC: $W(0) \rightarrow W_2C \rightarrow WC$. Carbon diffuses more rapidly in W_2C than in WC, the carbon initially in contact with the metallic particle reacts to form a thin outer shell of WC. From this WC shell, metallic tungsten is converted to W_2C . As long as the metallic core has not completely reacted, the WC outer shell does not significantly grow and stays thin. If the complete carburization of $W(0)$ is not attained, the major phase is thus W_2C . In our study, according to PXRD, the final product is a mixture of the “intermediate” W_2C and of $W(0)$ which leads us to hypothesize that $W(0)$ nanoparticles are not fully carburized. The only partial transformation of the metallic NPs is due to both the brevity of the reaction (< 1 s) and the too low temperatures. All the other studies on similar SSM reactions comports tungsten carbides report the WC phase with no formation of the $W(0)$ phase. However, higher ignition points are reported (> 200 °C) and the powder mixture is heated after reaction (at least 1 h at 500 °C).^{8,9} We hypothesize a similar mechanism is operating for other metals, core-shell $Mo@Mo_2C$ structures were for instance observed by reaction of a carburizing agent (1-chlorobutane) on metallic NPs.³⁶

Hydrogenation reaction. One of the major products for reactions with $ZrCl_4$, $HfCl_4$, $NbCl_5$ and $TaCl_5$ is the metal hydride (Figure 2). Due to their electronegativity, early transition metals (Groups IV and V) easily form hydrides. No common metal hydride phases are reported in literature for Mo and W under standard pressures, *i.e.* below 1 GPa.^{37,38} However, one key point of the reduction of metal chlorides with KC_4 or KC_8 is the theoretical absence of oxygen and hydrogen atoms in the mixture before the neutralization step with EtOH. To elucidate the origin of the metal hydrides (MH_y), we conducted a series of PXRD in capillary under argon on powders from reactions with $ZrCl_4$, $NbCl_5$ and $TaCl_5$, before exposure to ethanol or air (Figure 8A-C). For the three metal chlorides, a metallic phase ($Zr(0)$, $Nb(0)$ and $Ta(0)$) and a hydride phase (ZrH_2 , $NbH_{0.8}$ and $TaH_{0.5}$) were present, the same phases as the ones present after neutralization. Not all the peaks could be attributed for diffractograms in capillary but as these peaks are not present anymore after the washing step, they certainly correspond to air- or water-sensitive compounds. Because there is theoretically no H atom in the reaction before the neutralization, the hydrogens probably come from impurities in the graphite or acetylene black.

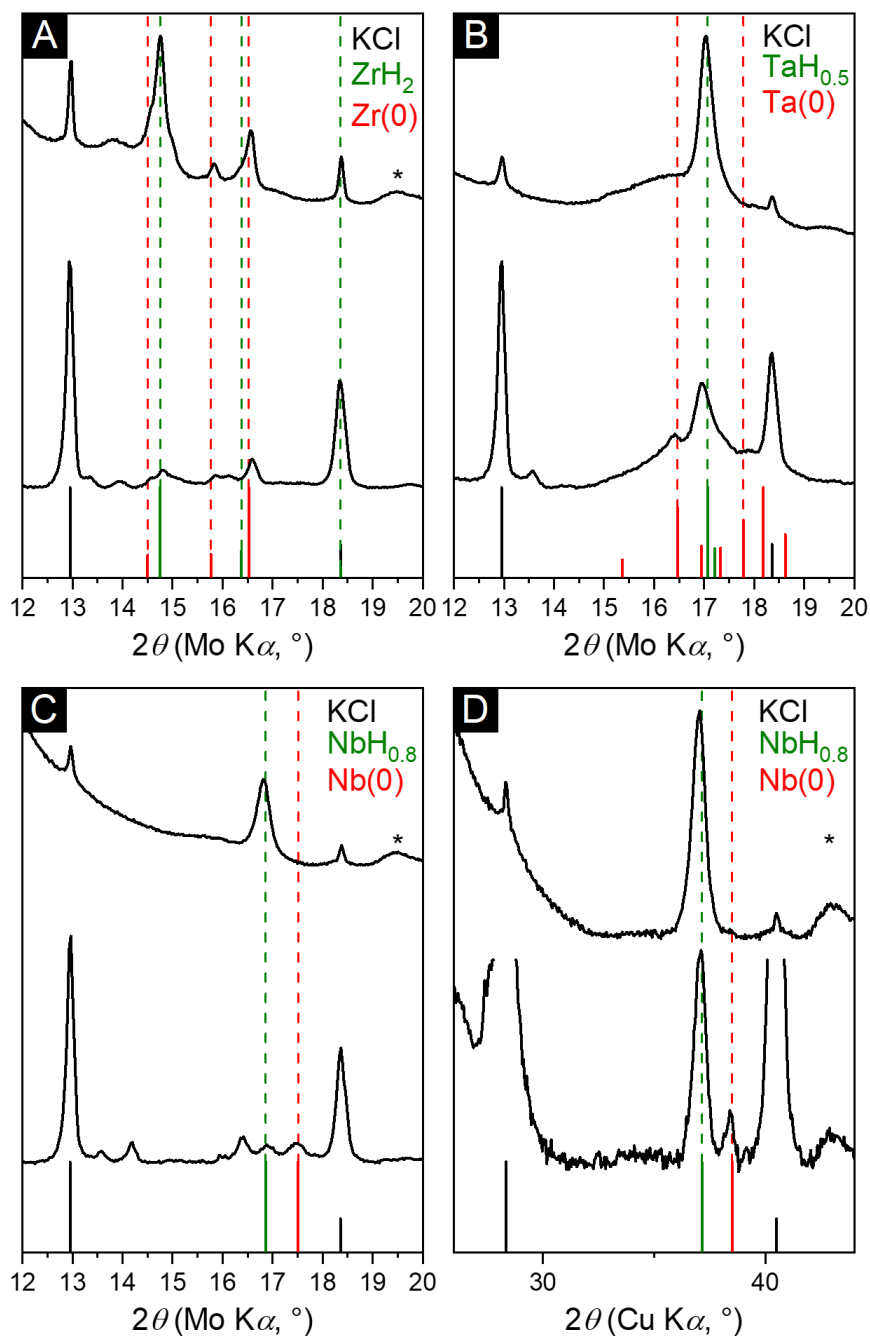
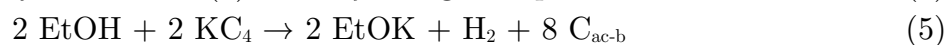


Figure 8: PXRD pattern of the products of the reaction with a stoichiometric mixture $MCl_x + x KC_4$ performed under vacuum. (A) $ZrCl_4$, after neutralization (top) and before neutralization (under Ar in capillary) (bottom). (B) $TaCl_5$, after neutralization (top) and before neutralization (under Ar in capillary) (bottom). (C) $NbCl_5$, after neutralization (top) and before neutralization (under Ar in capillary) (bottom). (D) $NbCl_5$ after neutralization with EtOH and water (top) and before neutralization after exposure to air (bottom).

Prolonged bubbling was observed during the addition of ethanol on the crude mixture (neutralization step). It may originate either from the neutralization of potassium, producing thereby H_2 gas (Eq. 5), or from the surface oxidation of the metallic nanoparticles. NPs of metals such as Zr(0), Hf(0), Nb(0) or Ta(0) are indeed

particularly reactive with protic solvents. PXRD of the samples after neutralization display a decrease of the M(0) peak and an increase of the MH_y peak (Figure 8A-C). Hydride formation can therefore be explained by hydrogenation of the metallic NPs formed upon reaction and which have not been carburized (Scheme 1, step (3)).¹ Two mechanisms are possible: either ethanol directly reacts with the metallic surface to provide H atoms and form organic species (Eq. 4) or ethanol reacts with leftover KC_4 or KC_8 to produce *in situ* H_2 (Eq. 5)³⁹ which diffuses in the metal (Eq. 6). This last hypothesis (Eq. 5 + 6) is less probable as significant amounts of KC_4 or KC_8 are needed to form the hydrides. For instance, $ZrCl_4$ reacts with 4 equiv. of KC_4 to form $Zr(0)$ and 2 others equiv. of KC_4 would be needed to form ZrH_2 .



The exothermicity of the hydrogenation reaction is coherent with the moderate temperature elevation of the Schlenk when the solvent is added.³⁷ Contrarily to the usual hydride syntheses, there is no need for prolonged period of reaction at high temperatures probably because of the small size of the nanoparticles: diffusion of hydrogen atoms in the metal is fast. Figure 8C-D display diffractograms of the reaction of $NbCl_5$ with 5 KC_4 : the reaction crude under inert atmosphere (Figure 8C, bottom), after exposure to air (Figure 8D, bottom) and after washing (Figure 8D, top). A simple exposure to traces of water from atmosphere is enough to start producing hydrides, although metallic phase is still present, whereas there is exclusively metal hydride after the washing step.

The distribution of the phases within each NP is still unclear as it could contain metal hydride, metal(0) and metal carbide. In particular, we could not determine if metal(0) detected after the neutralization (Figure 2A,B for Zr, Hf and Figure 6E, N_2 for Nb) was not hydrogenated because it was inaccessible due to an oxide, a hydride or a carbide shell or because it was imbedded in the carbon support. In the case of the reaction of $NbCl_5$ with KC_4 under Ar, $Nb(0)$ was detected but not the hydride (Figure 6E). This may be due to the formation of a carbide shell around the nanoparticles, preventing the solvent and/or H_2 to access the metallic part and consequently react with it. This description of the hydrogenation step comforts our choice of discussing together the metallic and hydride phases when we commented the impact of exothermicity on the possible formation of the carbide phase.

Most of the research on metal hydride materials is focused on Group I (Li, Na, K), Group II (Be, Mg, Ca), Group X (Ni, Pd, Pt) and Group XIII (B, Al) metals and

¹ The reader has to be careful with the KCl residual peaks which may be at the same positions as other peaks, typically one of ZrH_2 : we suggest to look at the main peak at 14.8° for this phase.

essentially for hydrogen storage applications, *i.e.* in dry environments with microparticles. There are therefore few descriptions of transition metal hydride surfaces in solvent such as H₂O or EtOH. The metal hydride nanoparticles synthesized here were stable over several weeks based on their XRD patterns, however, surface oxidation may occur, acting as a passivation barrier.

Oxidation reaction. In PXRD, crystalline metal oxides were detected both for ZrCl₄ and HfCl₄ (Figure 2) but not for all the other metals. The diffraction peaks are extremely broad, indicating a thin oxide layer at the surface of the NPs. All the XPS results indicate the presence of an oxidized layer but limited to the extreme surface of the NPs (Scheme 1, step (4)). This oxidation is limited by the soft conditions at which it occurs: the neutralization step is done at ambient temperature, under a protection of N₂ and with EtOH. For metals of Group V and VI, as no crystalline oxide phase was detected, we attribute the oxidized species detected by XPS to a surface oxycarbide or to hydroxylated surface metal atoms. XRD allows the detection of crystalline phases and is not suitable to characterize the presence of amorphous ones: amorphous oxides are likely to be present along with crystalline hydrides.

II.5. Reagent choice and potential products

Scale up. If a scale up is envisioned, the natural combustion temperature of the system may differ from the desired one. When temperatures lower than the adiabatic ones are targeted, a common technique consists in diluting the initial mixture with an inert salt, such as NaCl or KCl, which will act as a heat absorber, due to the salt melting enthalpy. On the contrary, when higher temperatures are targeted, one can surround the reactive powder by another SHS-active mixture, which will liberate heat too when the reaction will be triggered. This last technique is termed “chemical oven” and limits the cooling by heat transfer. Together, these two strategies, inert salt addition and “chemical oven”, allow the monitoring of the combustion temperature and therefore the phase speciation. They are more suited to scales larger than the ones used in the present work.⁵ At first view, the explosivity of the reaction may be in conflict with the twelfth principle of Green Chemistry calling for safer chemistry procedures. Three aspects must be discussed: the high temperatures reached by the medium, the pyrophoricity of the reagents and the explosivity due to gas dilatation. The first point is inherent to many chemistries and in particular that of refractory compound synthesis: we believe industries are already in capacity to deal with it as large scale applications, *i.e.* more than 10 000 tons per year, are already reported using SHS principle.⁵ For the second point, one great advantage of the synthesis is that KC_4 and KC_8 may be formed in situ from metallic potassium and then mixed with the metal chloride, thereby limiting the need to transport highly reactive compounds. Finally, considering the risk of thermal dilatation of the gases in the closed vessel, we suggest to run the reaction in vacuum if the phase speciation is compatible with such conditions or to connect the vessel to a Schlenk line (or a container of inert gas), which will act as a “pressure buffer”. With such precautions, no particular risk is expected while running the experiment.

Reagent choices. This study is the continuation of works from the 1990s using Al_4C_3 , CaC_2 or SrC_2 carbides as reducing agents, but with potassium derived compounds (KC_4 and KC_8).^{8,19,25} While the three first ones are carbides *stricto sensu* (equivalent terms, methide and acetylide, may also be found), KC_4 is an impregnation compound without particular known crystallographic structure and KC_8 is a Graphite Intercalation Compound (GIC). Although there are a few occurrences of potassium carbide K_2C_2 in the literature, this compound appears to be much less studied and common than KC_8 . On the contrary, GICs include LiC_6 , CaC_6 , SrC_6 and others. Carbides and GICs have undoubtedly different structures and properties but for the study of solid-state metathesis, we considered the comparison was relevant as they have comparable elemental compositions and both present a reductive character. KC_8 and KC_4 were chosen as they are easily prepared on a gram scale in one step

from potassium and graphite at 100 °C under Ar, which is not the case of CaC_6 (metallic calcium melts at 842 °C *vs.* 63 °C for metallic potassium).

We could not determine why the use of KC_4 or KC_8 allows the ignition to be done at ambient, or close, conditions but this is an obvious energy-saving advantage. The ignition temperatures of the reactions reported in our present work are between room temperature and 75 °C, while the similar reactions using calcium carbide CaC_2 as the reducing agent was initiated at 200 °C at the lowest and necessitates a heating at 500 °C for at least one hour to fully crystallize the products.⁹ To the best of our knowledge, all the other carbide syntheses *via* the SSM route have ignition temperatures of 200 °C at least. Ignition at room temperatures are reported but for other families of materials, such as nitrides or sulfides.⁵ We hypothesize the combination of the low ignition temperatures (< 75 °C) and the absence of heating after reaction explain the unexpected production of hydrides (ZrH_2 , $\text{HfH}_{1.7}$, $\text{NbH}_{0.8}$ and $\text{TaH}_{0.5}$) *via* metallic particles, never reported for SSM. These hydride phases do not *strico sensu* result from the SSM as they are the products of the hydrogenation of small metallic particles. However, they are among the smallest metal hydride NPs reported as these phases are usually synthesized by metal microparticles hydrogenation with H_2 .

We mentioned earlier the use of metal oxides as precursors, instead of metal chlorides. Although the substitution of the metal chloride by a similar metal oxide would have been of high interest, in particular in terms of green chemistry (simpler reagents, not air or water sensitive, no use of Cl), we demonstrated the MSSM was not possible when the reducing agent is potassium for thermodynamic reasons (formation of K_2O). On the contrary, MSSM with CaC_2 and metal oxides was successfully reported by Nartowski *et al.* in the case of V_2O_3 , Nb_2O_5 , Ta_2O_5 , MoO_3 .²⁰ The authors nonetheless indicated the mixtures ignited at much higher temperatures than with metal chlorides (480-650 °C for MSSM *vs.* 200-350 °C for SSM) and that there was no thermal flash at the ignition. They noticed instead a darkening of the powder over 20 seconds. This may be interpreted as a lower exothermicity. Moreover, a longer annealing step was needed for MSSM (12 h at 1000 °C instead of 1 h at 500 °C for SSM). All these observations are coherent with our thermodynamic calculations. Indeed, among the metals studied both in this article and by Nartowski *et al.* (Nb, Ta, Mo, W), the theoretical enthalpies of reaction are between -144 kJ/mol and +282 kJ/mol for MSSM with KC_8 (no reaction), between -974 kJ/mol and -409 kJ/mol for MSSM with CaC_2 (moderate reaction), between -1305 kJ/mol and -707 kJ/mol for SSM with CaC_2 (explosive reaction) and between -1826 kJ/mol and -817 kJ/mol for SSM with KC_8 (explosive reaction) (ES).

Transition and f-block metals. Similar works on SSM of metal carbide nanoparticles report attempts to use metal chlorides of late transition (beyond

column VI) but all failed to produce carbides. This systematic result was named the “chromium enigma”. One advanced explanation is the poor stability of the corresponding metal carbides with high temperature in comparison with early transition metals: the carbides are formed but immediately melt or degrade. We present in

Table 2 the melting temperatures of the majority of the stable carbide phases of transition metals in relation with the adiabatic temperature for a hypothetical reaction between KC_8 and the corresponding metal chloride. First, it appears the melting temperatures of the carbides of all the metals studied in this work, and from a previous study in our group,¹⁹ (Ti, Zr, Hf, V, Nb, Ta, Mo, W) are above the boiling point of KCl and thereby above the adiabatic temperature, to the noticeable exception of MoC (1220 °C), which was indeed not obtained in our study. Then, for scandium and yttrium carbides, the melting temperature (respectively 1864 °C and 1645 °C) are well above the adiabatic temperatures (520 °C and 460 °C) but there are doubts about the possibility to ignite the reaction considering the low enthalpies of reaction for SSM between ScCl_3 or YCl_3 and KC_8 (-272 kJ/mol and -235 kJ/mol). These enthalpies of reaction are comparable with the ones obtained for MSSM reactions with KC_8 and which were unsuccessful. Lanthanide and actinide elements, to the exception of Pm, form at least one stable carbide, the most common ones being M_2C_3 and MC_2 .⁴⁰ M_2C_3 carbides are generally stable up to *ca.* 1500 °C while MC_2 decomposes at *ca.* 2200 °C. The limiting point here seems to be the same as for Sc and Y: the low enthalpy of reaction. The example of LaCl_3 , expected to be representative of all lanthanides, leads to a reaction enthalpy of only -147 kJ/mol.

Concerning Cr and Mn, the situation is in the middle: the degradation temperatures are around the boiling point of KCl (1500 °C) and therefore technically accessible although the adiabatic temperature is systematically below. Nartowski *et al.* reported the synthesis of Cr_3C_2 when using CaC_2 .²⁵ Iron presents several carbide phases between Fe_2C and Fe_4C , all metastable. The only relevant one here is the cementite Fe_3C whose degradation is particularly slow, literature indicating a limit degradation temperature of 1252 °C.⁴¹ Cobalt presents two main metastable carbide phases, CoC_2 and CoC_3 , for which the literature defines a degradation temperature of respectively 469 °C and 491 °C.⁴² Nickel presents only one metastable carbide phase, Ni_3C . The compound does not melt but is decomposed into Ni(0) and C. As the phase is metastable, there is no defined degradation temperature but the usual range of degradation temperatures is 300-500 °C.⁴³ Nickel and cobalt carbides would be undoubtedly degraded if formed during the SSM but the case of iron carbide is borderline. There is up to now no mention of a common carbide phase for Ru, Rh, Pd, Re, Os, Ir and Pt. Metals of column XI (Cu, Ag, Au) form explosive acetylide M_2C_2 and those of column XII (Zn, Cd, Hg) form not well characterized carbides, these compounds are therefore beyond the scope of this work.

Metal	Carbide	Melting temperature	Adiabatic temperature	Metal	Carbide	Melting temperature	Adiabatic temperature
Sc	ScC	2270 °C	520 °C (ScCl ₃)	Cr	Cr ₃ C ₂	1811 °C	930 °C (CrCl ₃)
	Sc ₄ C ₃	1864 °C			Cr ₇ C ₃	1766 °C	
Y	YC ₂	2415 °C	460 °C (YCl ₃)		Cr ₂₃ C ₆	1576 °C	
	Y ₂ C ₃	1645 °C		Mo	MoC	1220 °C	1250 °C (MoCl ₅)
La	LaC ₂	2360 °C	320 °C (LaCl ₃)		Mo ₂ C	2605 °C	
	La ₂ C ₃	1415 °C		W	WC	2785 °C	1280 °C (WCl ₆)
Ti	TiC	3067 °C	770 °C (TiCl ₃)		W ₂ C	2785 °C	
Zr	ZrC	3445 °C	770 °C (ZrCl ₄)	Mn	Mn ₇ C ₃	1333 °C	770 °C (MnCl ₂)
Hf	HfC	3928 °C	770 °C (HfCl ₄)		Mn ₅ C ₂	1171 °C	
V	VC	2656 °C	900 °C (VCl ₃)		Mn ₃ C	1052 °C	
	V ₈ C ₇	2650 °C			Mn ₂₃ C ₆	1034 °C	
	V ₂ C	2191 °C			Fe	Fe ₃ C	
Nb	NbC	3608 °C	1040 °C (NbCl ₅)	Co	Co ₂ C	469 °C (d)	1040 °C (CoCl ₂)
	Nb ₂ C	2504 °C			Co ₃ C	491 °C (d)	
Ta	TaC	3965 °C	1000 °C (TaCl ₅)	Ni	Ni ₃ C	300-500 °C (d)	1050 °C (NiCl ₂)
	Ta ₂ C	3330 °C					

Table 2. Melting temperatures of all common carbide phases of transition metals and adiabatic temperature for a hypothetical SSM reaction between KC₈ and the different chloride salts. Fe, Co and Ni developing only metastable carbide phases, the decomposition temperatures are indicated instead of the melting temperatures. Data are taken from references ^{24,44,45}.

II.6. Conclusion

We demonstrated the possible use of KC_4 and KC_8 to produce a variety of carbon-supported nanoparticles (metal(0), carbide, hydride) derived from early transition metals (Zr, Hf, Nb, Ta, Mo and W). We showed the possibility to partially modify the combustion temperature and therefore the phase speciation of the reaction by playing on several process parameters. This is particularly interesting as the usual parameters used in chemistry such as the concentration, the reaction temperature and the reaction time are not relevant for solid-state metathesis reactions. Furthermore, this study of the process parameters resulted in a proposed mechanism in four steps: reduction, carburization, hydrogenation and surface oxidation. Using thermodynamic considerations, we demonstrated that the simplest reagents were used and we delineated the scope of this process in terms of reachable compounds. In comparison to the state of the art, our process presents significant gains in energy while preserving the scalability, the versatility, the atom economy and the absence of toxic wastes.

II.7. Bibliography

1. Zhong, Y. *et al.* Transition Metal Carbides and Nitrides in Energy Storage and Conversion. *Adv. Sci.* **3**, 1500286 (2016).
2. Hwu, H. H. & Chen, J. G. Surface chemistry of transition metal carbides. *Chem. Rev.* **105**, 185–212 (2005).
3. Levy, R. B. & Boudart, M. Platinum-Like Behavior of Tungsten Carbide in Surface Catalysis. *Science* **181**, 547–549 (1973).
4. Ushakov, S. V., Navrotsky, A., Hong, Q.-J. & van de Walle, A. Carbides and Nitrides of Zirconium and Hafnium. *Materials (Basel)*. **12**, 2728 (2019).
5. Merzhanov, A. G. The chemistry of self-propagating high-temperature synthesis. *J. Mater. Chem.* **14**, 1779 (2004).
6. Wiley, J. B. & Kaner, R. B. Rapid Solid-State Precursor Synthesis of Materials. *Science* **255**, 1093–1097 (1992).
7. Yi, H. C. & Moore, J. J. Self-propagating high-temperature (combustion) synthesis (SHS) of powder-compacted materials. *J. Mater. Sci.* **25**, 1159–1168 (1990).
8. Nartowski, A. M., Parkin, I. P., Craven, A. J. & MacKenzie, M. Rapid, Solid-State Metathesis Routes to Metal Carbides. *Adv. Mater.* **10**, 805–808 (1998).
9. Nartowski, A. M., Parkin, I. P., MacKenzie, M., Craven, A. J. & MacLeod, I. Solid state metathesis routes to transition metal carbides. *J. Mater. Chem.* **9**, 1275–1281 (1999).
10. Parkin, I. P. Solid state metathesis reaction for metal borides, silicides, pnictides and chalcogenides: Ionic or elemental pathways. *Chem. Soc. Rev.* **25**, 199–207 (1996).
11. Meyer, H.-J. Solid state metathesis reactions as a conceptual tool in the synthesis of new materials. *Dalt. Trans.* **39**, 5973 (2010).
12. Rao, L., Gillan, E. G. & Kaner, R. B. Rapid synthesis of transition-metal borides by solid-state metathesis. *J. Mater. Res.* **10**, 353–361 (1995).
13. Fitzmaurice, J. C., Hector, A. & Parkin, I. P. Rapid synthesis of TiN, HfN and ZrN from solid-state precursors. *Polyhedron* **12**, 1295–1300 (1993).
14. Song, B. *et al.* Facile and General Route to Nitrides by a Modified Solid-State Metathesis Pathway. *Chem. Mater.* **19**, 1497–1502 (2007).

15. O'Loughlin, J. L., Wallace, C. H., Knox, M. S. & Kaner, R. B. Rapid Solid-State Synthesis of Tantalum, Chromium, and Molybdenum Nitrides. *Inorg. Chem.* **40**, 2240–2245 (2001).
16. Nartowski, A. M. & Parkin, I. P. Solid state metathesis synthesis of metal silicides; reactions of calcium and magnesium silicide with metal oxides. *Polyhedron* **21**, 187–191 (2002).
17. Jarvis, R. F., Jacubinas, R. M. & Kaner, R. B. Self-Propagating Metathesis Routes to Metastable Group 4 Phosphides. *Inorg. Chem.* **39**, 3243–3246 (2000).
18. Bonneau, P. R., Jarvis, R. F. & Kaner, R. B. Rapid solid-state synthesis of materials from molybdenum disulphide to refractories. *Nature* **349**, 510–512 (1991).
19. Ressnig, D. *et al.* An expeditious synthesis of early transition metal carbide nanoparticles on graphitic carbons. *Chem. Commun.* **52**, 9546–9549 (2016).
20. Nartowski, A. M., Parkin, I. P., Mackenzie, M. & Craven, A. J. Solid state metathesis: Synthesis of metal carbides from metal oxides. *J. Mater. Chem.* **11**, 3116–3119 (2001).
21. Fredenhagen, K. & Cadenbach, G. Die Bindung von Kalium durch Kohlenstoff. *Zeitschrift für Anorg. und Allg. Chemie* **158**, 249–263 (1926).
22. Bergbreiter, D. E. & Killough, J. M. Reactions of potassium-graphite. *J. Am. Chem. Soc.* **100**, 2126–2134 (1978).
23. Lalancette, J.-M., Rollin, G. & Dumas, P. Metals Intercalated in Graphite. I. Reduction and Oxidation. *Can. J. Chem.* **50**, 3058–3062 (1972).
24. *Alloy Phase Diagrams*. (ASM International, 2016).
25. Nartowski, A. M., Parkin, I. P., MacKenzie, M., Craven, A. J. & MacLeod, I. Solid state metathesis routes to transition metal carbides. *J. Mater. Chem.* **9**, 1275–1281 (1999).
26. Cuppari, M. & Santos, S. Physical Properties of the NbC Carbide. *Metals (Basel)*. **6**, 250 (2016).
27. Kurlov, A. S. & Gusev, A. I. Tungsten carbides and W-C phase diagram. *Inorg. Mater.* **42**, 121–127 (2006).
28. Sarma, D. D., Santra, P. K., Mukherjee, S. & Nag, A. X-ray photoelectron spectroscopy: A unique tool to determine the internal heterostructure of nanoparticles. *Chem. Mater.* **25**, 1222–1232 (2013).
29. Lee, J. S. & Yie, J. E. An XANES study of carbides of molybdenum and

- tungsten. *Korean J. Chem. Eng.* **8**, 164–167 (1991).
30. He, C. & Tao, J. Exploration of the electrochemical mechanism of ultrasmall multiple phases molybdenum carbides nanocrystals for hydrogen evolution reaction. *RSC Adv.* **6**, 9240–9246 (2016).
 31. Vanýsek, P. CRC Handbook of Chemistry and Physics. in *CRC Handbook of Chemistry and Physics, 93rd edition* 5-80/89 (CRC, Boca Raton, FL, 2012).
 32. Chase, M. W. *NIST-JANAF Thermochemical Tables, 4th Edition.* (1998).
 33. Taylor, J. C. & Wilson, P. W. The structure of β -tungsten hexachloride by powder neutron and X-ray diffraction. *Acta Crystallogr. Sect. B Struct. Crystallogr. Cryst. Chem.* **30**, 1216–1220 (1974).
 34. Mühlbauer, G., Kremser, G., Bock, A., Weidow, J. & Schubert, W.-D. Transition of W_2C to WC during carburization of tungsten metal powder. *Int. J. Refract. Met. Hard Mater.* **72**, 141–148 (2018).
 35. McCarty, L. V., Donelson, R. & Hehemann, R. f. A diffusion model for tungsten powder carburization. *Metall. Trans. A* **18**, 969–974 (1991).
 36. Chien, C.-H. *et al.* Preparation of $Mo_2C@a-C$ core-shell powders via carburization of Mo particles by 1-chlorobutane and hexachlorobenzene. *Mater. Lett.* **61**, 3593–3596 (2007).
 37. Young, K. Metal Hydrides. in *Reference Module in Chemistry, Molecular Sciences and Chemical Engineering* 1–23 (Elsevier, 2018).
 38. Kuzovnikov, M. A., Meng, H. & Tkacz, M. Nonstoichiometric molybdenum hydride. *J. Alloys Compd.* **694**, 51–54 (2017).
 39. Schlögl, R. & Boehm, H. P. The reaction of potassium-graphite intercalation compounds with tetrahydrofuran. *Carbon N. Y.* **22**, 341–349 (1984).
 40. Gschneidner, K. A. & Calderwood, F. W. The carbon-rare earth systems. *Bull. Alloy Phase Diagrams* **7**, 421–436 (1986).
 41. Okamoto, H. The C-Fe (carbon-iron) system. *J. Phase Equilibria* **13**, 543–565 (1992).
 42. Ishida, K. & Nishizawa, T. The C-Co(Carbon-Cobalt) system. *J. Phase Equilibria* **12**, 417–424 (1991).
 43. Bayer, B. C. *et al.* In Situ Observations of Phase Transitions in Metastable Nickel (Carbide)/Carbon Nanocomposites. *J. Phys. Chem. C* **120**, 22571–22584 (2016).
 44. Shatynski, S. R. The thermochemistry of transition metal carbides. *Oxid. Met.*

- 13**, 105–118 (1979).
45. Kosolapova, T. Y. *Carbides*. (Springer US, 1995).

Chapter III

Catalysis with carbon-supported metal carbides

The synthesis of finely dispersed molybdenum and tungsten carbides nanoparticles supported on carbon was achieved in chapter II (Synthesis II.2.). These two materials, Mo_2C and W_2C , have already been studied in the context of hydrogenation reactions both in the gas phase and in solvent.¹⁻³ Following our “NanoFLP” target, *i.e.* the boosting of the catalytic activity of metal-containing compounds through the addition of sterically hindered molecular bases, we tested different metal carbides for hydrogenation of styrene and phenylacetylene in solvent. In a second time, the addition of co-catalysts is envisioned.

III.1. Hydrogenation of butadiene

Note: the work described in this section was performed thanks to a collaboration with Dr. Laurent Delannoy from the Laboratoire de Réactivité de Surface at Sorbonne Université. He performed the gas phase catalytic tests.

In the first section, we attempted a known hydrogenation reaction in the gas phase with Mo_2C /graphite in order to assess the possible access by the molecules to the active phase. Indeed, the XPS analysis performed in chapter II proved the presence of an oxidized shell at the surface of $\text{Mo}_2\text{C}/\text{C}$ and the TEM pictures of the catalysts suggest the nanoparticles are imbedded in a carbon shell. This preliminary study was conducted on butadiene as molybdenum carbide was reported to selectively hydrogenate butadiene in butene at 35 °C in a mixture $\text{H}_2/\text{C}_4\text{H}_6/\text{N}_2$ (9.1/4.5/86.4).⁴ We expect here a hydrogenation of butadiene in C_4 hydrocarbons (1-butene, cis-butene, trans-butene and butane).

Experimentally, the Mo_2C /graphite catalyst (Synthesis II.2. with KC_8 and MoCl_3), mixed with carborundum SiC (20 mg of catalyst/180 mg of SiC), was disposed between two silica wool plugs in a Quartz U-shaped tube reactor (Figure 1). The catalytic loading [Mo] in the Mo_2C /graphite-SiC is expected to be 2.5 wt.% based on the mass of the precursors. The system was purged with N_2 during 3 h before switching to the reactive mixture at 1 bar (3,000 ppm of butadiene in $\text{H}_2:\text{He}$ (20:80)). The oven, initially at 20 °C, was heated to 300 °C with a heating ramp of 2 °C/min. Every 30 °C, the reactive mixture was sampled and the catalytic activity was determined by Gas Chromatography-Flame Ionization Detector (GC-FID).

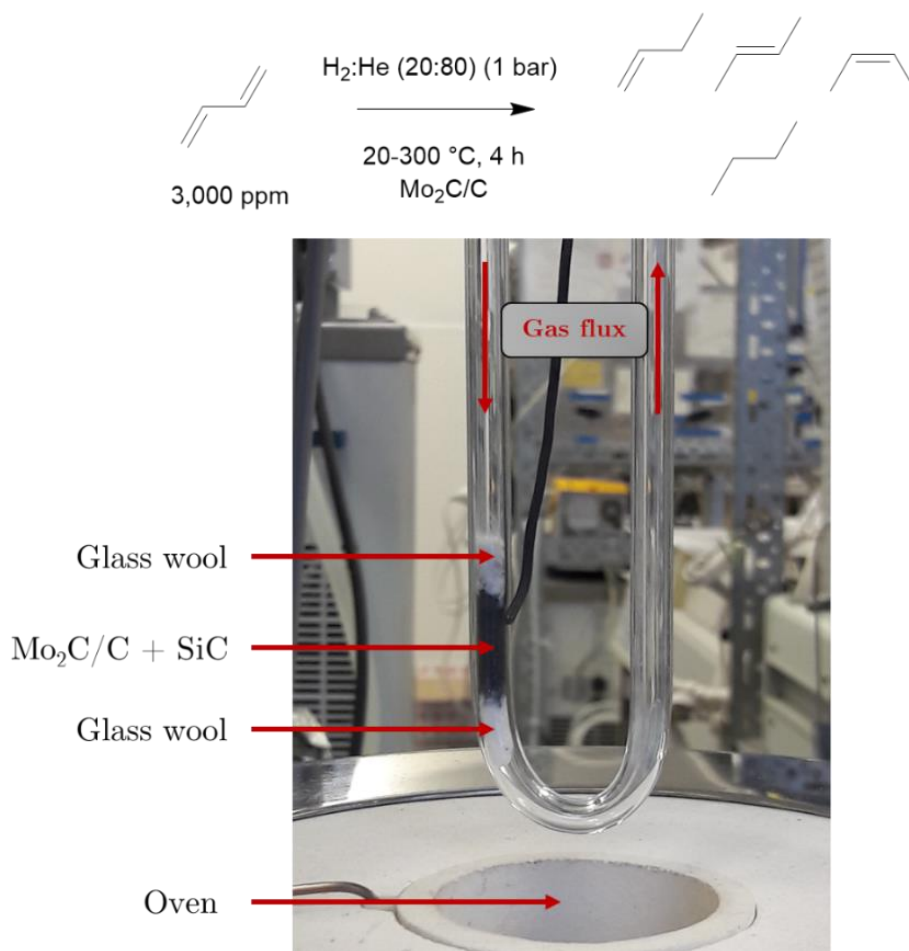


Figure 1. Gas-phase hydrogenation of butadiene with Mo₂C/graphite in a flux of H₂:He (20:80).

No conversion of butadiene was observed at temperatures below 120 °C (Figure 2A). During the first heating ramp, total conversion of butadiene was observed at 120 °C, with a non-negligible formation of butane (10 %), which is the fully hydrogenated product. This attests of the catalytic activity of Mo₂C. A total conversion for such moderate temperatures seemed nonetheless abnormally high, especially considering the diminution at 150 °C to only 23 %. We suspected a modification of the surface occurred. We therefore stopped the heating ramp at 150 °C and went back to 120 °C until stabilization of the conversion, at *ca.* 4 % after one hour. We then pursued the heating ramp up to 300 °C (Figure 2B). The conversion of the butadiene gradually increased up to 30 % at 210 °C and then decreased to 15 % at 300 °C. With increasing temperature, the selectivity towards the mono-hydrogenated product “trans-2-butene” decreased to the benefit of “cis-2-butene”. The proportion of butane, which started to be formed at 210 °C, increased with temperature although staying a minor species.

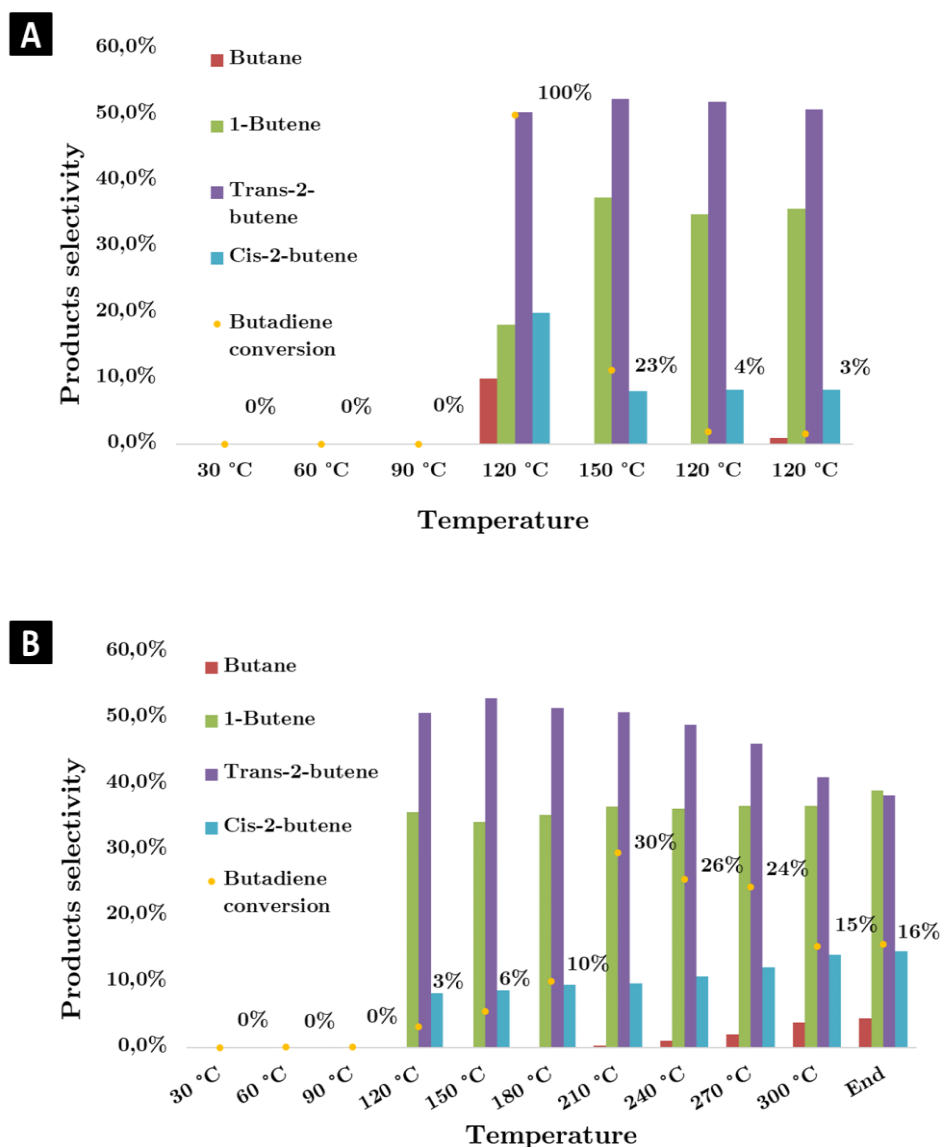


Figure 2. Hydrogenation of butadiene by Mo₂C/C: selectivity and conversion as a function of temperature. (A) First heating ramp and (B) second heating ramp.

We hypothesized the particularly high catalytic activity observed at 120 °C during the first heating ramp was due to a local intense heating. Although the oven was only at 120 °C, the oxidized surface of the nanoparticles, characterized by XPS in the previous chapter, was probably reduced *in situ* by H₂. This reduction is exothermic, resulting in higher temperature for the catalytic sites, hence the high conversion of butadiene in butene and butane. This high activity was not observed during the second heating ramp because all the oxide shell was reduced. Much modest conversions were then measured at 120 °C (3 % butadiene conversion, no butane formation).

Although this study was not further pushed, the preliminary results indicate first that the synthesized material is actually active for hydrogenation reactions in gas phase under relatively mild conditions (0.2 bar H_2 , $< 200\text{ }^\circ\text{C}$). Then, they suggest that an activation step at temperatures beyond $120\text{ }^\circ\text{C}$ under H_2 is required to access the Mo_2C material beneath the oxidized shell.

III.2. Liquid phase catalysis

The Mo₂C/graphite synthesized in Synthesis II.2. with MoCl₃ and KC₈ was shown to display a catalytic activity in butadiene hydrogenation in the gas phase. We therefore attempted the hydrogenation in solvent of simple olefins, styrene and phenylacetylene. Conversion and yield were determined by ¹H NMR without isolation of the product. Catalytic data should therefore be interpreted with a consequent error bar: this is not problematic as the focus of the study was put on the possibility or not to perform the reaction and not on a fine optimization of the reaction conditions.

III.2.1 Styrene dimerization

The carbon supported catalysts W₂C/ac-b and Mo₂C/graphite developed in Chapter II (Synthesis II.2.) were studied for hydrogenation of styrene.¹ Their metal loadings are expected to be respectively 39 wt.% and 25 wt.% according to the mass of the precursors. First attempts were made in toluene at 100 °C under 7 bar of H₂ following Catalysis III.1.

Catalysis III.1. Hydrogenation of styrene. Under Ar, 50 mg of catalyst powder from Synthesis II.2. (0.05 equiv. of [W] for W₂C/ac-b or 0.07 equiv. of [Mo] for Mo₂C/graphite) were introduced in a 25 mL autoclave. To the autoclave were added 230 µL of styrene (2 mmol, 1 equiv.) and 1 mL of solvent. The autoclave was closed and the atmosphere was changed for H₂ (7 bar) after 2 cycles vacuum/H₂ (1 bar). The autoclave was then introduced in a preheated oil bath at 100 °C for 16 h. After reaction, the autoclave was let to cool down naturally to r.t. before opening. An aliquot of the liquid phase was studied by ¹H NMR in CDCl₃.

A blank reaction confirmed the absence of reactivity of acetylene black as no conversion of styrene was detected after 16 h at 100 °C in toluene (Table 1, entry 1). While attempting at reducing the styrene under different conditions, no ethylbenzene was formed for none of the preliminary tests but instead a collection of products, including one major species with a 40 % selectivity (Figure 3). This species was attributed to the linear dimer (E)-1,3-diphenyl-1-butene, recognizable in ¹H NMR with its specific pattern at *ca.* 6.6 ppm. The ¹H NMR spectrum of the product was previously attributed and the pattern corresponds to the ethylenic protons.^{5,6} Mo₂C/graphite was also studied for this reaction led to the same product as for W₂C/ac-b with a low conversion yield (Table 1, entry 2). In presence of W₂C/ac-b, conversion and selectivity seem unaffected by the nature of the gas phase as similar values are obtained under an oxidative atmosphere (air), an inert one (Ar) or a reductive one (H₂, 7 bar) (Table 1, entries 3-5). However, the catalytic activity is

¹ These catalytic trials were performed before the gas phase experiment, hence the absence of reductive pre-treatment.

highly affected by the nature of the solvent: styrene dimerizes in toluene, is oxidized in DMSO and does not react in 1-butanol (Table 1, entries 3, 6-7). All the results displayed were obtained with the same batch of $W_2C/ac-b$. When we attempted to reproduce the results with different batches of $W_2C/ac-b$, the same products were obtained but with very variable yields, with sometimes only traces of dimer and merely no conversion of styrene.

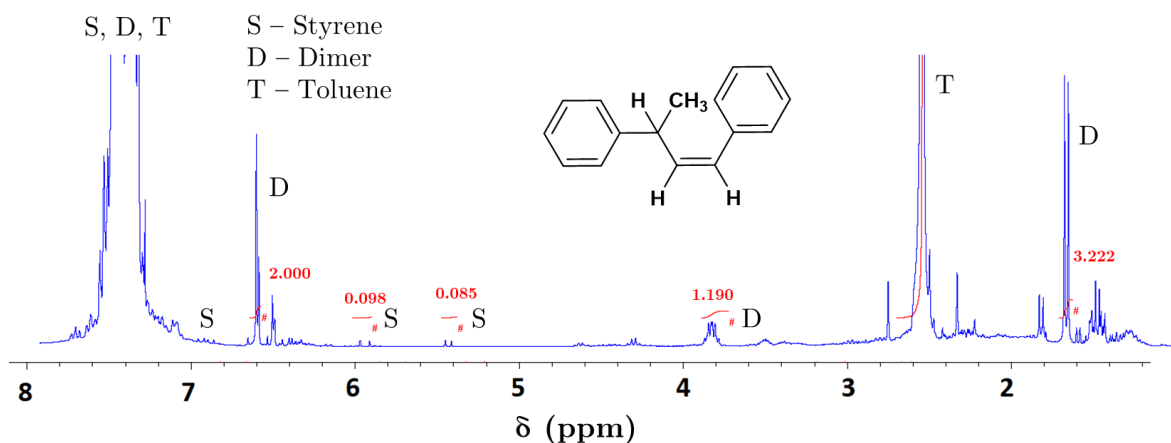
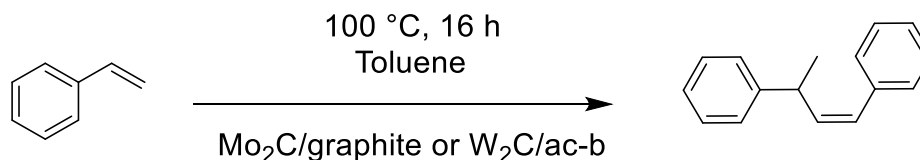


Figure 3. Typical 1H NMR spectrum of Catalysis III.1. with $W_2C/ac-b$, in toluene under H_2 .



	Catalyst	Solvent	Gas	Styrene conversion (%)	Styrene dimer selectivity (%)
1	ac-b	Toluene	Air	0	-
2	$Mo_2C/graphite$	Toluene	Air	12	52
3	$W_2C/ac-b$	Toluene	Air	98	37
4	$W_2C/ac-b$	Toluene	Ar	98	44
5	$W_2C/ac-b$	Toluene	H_2 (7 bar)	97	45
6 ^a	$W_2C/ac-b$	DMSO	Air	29	0
7	$W_2C/ac-b$	1-butanol	Air	0	-

Table 1. Solvent and gas effect on styrene dimerization by molybdenum and tungsten carbides. Reaction conditions: 230 μL of styrene (2 mmol), 50 mg of catalyst, 1 mL of solvent, 100 $^{\circ}C$, 16 h in autoclave (25 mL). Conversion and yield determined by NMR.

^aStyrene oxide and benzaldehyde were obtained.

No catalytic activity was obtained when a base such as butylamine or a tertiary phosphine (PCy_3 or P^tBu_3) was added (Table 2) to the reaction medium. These two molecules are both a Brønsted and a Lewis base so we could not determine whether the loss of catalytic activity is due to an abstraction of all the potential surface acidic protons by the base or to a saturation of the catalyst surface with the ligands, impeding the approach of the substrate.

	Catalyst	Organic base	Styrene conversion (%)	Selectivity (%)		
				Benzaldehyde	Styrene oxide	Styrene dimer
1	$\text{W}_2\text{C}/\text{ac-b}$	-	98	0	0	37
2 ^a	$\text{W}_2\text{C}/\text{ac-b}$	Butylamine	0	-	-	-
3 ^b	$\text{W}_2\text{C}/\text{ac-b}$	PCy_3	0	-	-	-
4 ^b	$\text{W}_2\text{C}/\text{ac-b}$	P^tBu_3	0	-	-	-

Table 2. Study of the addition of an organic base on styrene dimerization by tungsten carbide supported on acetylene black, following Catalysis III.2. Reaction conditions: 230 μL of styrene (2 mmol), 50 mg of catalyst, 1 mL of toluene, 100 °C, air, 16 h. Conversion and yield determined by NMR. ^a2 drops of butylamine. ^bAddition of 50 mg of phosphine (PCy_3 or P^tBu_3).

We interpreted the results as following: the styrene dimerization was catalyzed by residual Brønsted sites on the carbon-supported nanoparticles. Such residual protons were probably generated during the washing step of the catalysts, explaining why the catalytic results were very poorly repeatable. The addition of Brønsted bases such as 1-butanol, amines or phosphines neutralized the catalytic sites, thereby leading to no catalysis even with a batch known for being active otherwise. Supplementary experiments with strong acids such as trifluoroacetic (TFA) or trichloroacetic acids were run in similar conditions and indeed led to the (E)-1,3-diphenyl-1-butene dimer, in addition with other unidentified products.

A literature survey was conducted and comforted our hypothesis. Head-to-tail dimerization of vinylarene molecules, such as styrene, was reported with a variety of catalytic systems. Initially, styrene dimerization was obtained with strong Brønsted acids such as sulfuric acid or phosphoric acid but the selectivity towards the linear dimer was too low. The first developed homogeneous catalysts with good selectivities were transition metal complexes with Pd,^{5–12} Ni,^{13,14} or Co.¹⁵ It appeared the activity drastically increased in presence of triflate salts $\text{In}(\text{OTf})_3$,^{7,8} $\text{Cu}(\text{OTf})_2$,⁸ $\text{Ag}(\text{OTf})$,¹¹ or acids such as $\text{BF}_3 \cdot \text{Et}_2\text{O}$ ^{6,9,10} or TFA.⁵ Transition metal-free routes were developed

with the exclusive use of acids such as InBr_3 ,¹⁶ TfOH ,^{17,18} AcClO_4 ,^{18,19} or HClO_4 .¹⁷ As to heterogeneous catalysts, there is, to the best of our knowledge, only mention of zeolites.^{20–22} Grigor'eva *et al.* extensively studied this reaction in the past decades and reported the possible dimerization of vinylarenes, in particular of styrene and α -methylstyrene. They reported linear and cyclic dimers and trimers while realizing the reaction between 80 °C and 120 °C in chlorobenzene or neat.

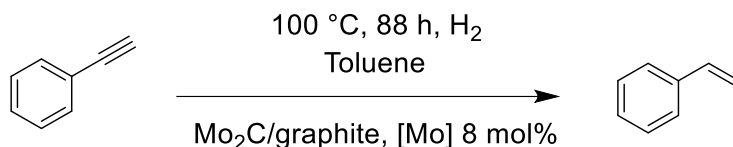
Considering the very poor reproducibility of the catalytic results (large series of unsuccessful reactions were performed, although not shown here), the dimerization of the styrene and the absence of hydrogenation activity under these conditions, we did not push further in this direction.

III.2.2 Phenylacetylene semi-hydrogenation

The hydrogenation of styrene with metal carbide NPs in the previous section proved to be unsuccessful and one main problem arose: the competitive dimerization/polymerization of the alkene. We therefore attempted here the hydrogenation of a close alkyne, the phenylacetylene. The same catalyst as the one used for gas phase hydrogenation was used: molybdenum carbide supported on graphite, $\text{Mo}_2\text{C}/\text{graphite}$ (metal loading of 25 wt.%). The reactions were conducted at higher H_2 pressures in a steel autoclave following Catalysis III.2.

Catalysis III.2. Semi-hydrogenation of phenylacetylene. In air, 60 mg of catalyst powder $\text{Mo}_2\text{C}/\text{graphite}$ (Synthesis II.2. with MoCl_3 and KC_8 , $[\text{Mo}]$ 25 wt.%, 0.08 equiv. $[\text{Mo}]$) were introduced in a 25 mL steel autoclave (Teflon reaction cuve). To the autoclave was added 220 μL of phenylacetylene (2 mmol, 1 equiv.) and 1 mL of toluene. The autoclave was closed and the atmosphere was changed for H_2 (7, 15 or 30 bar) after 2 cycles vacuum/ H_2 (1 bar). The autoclave was then introduced in a preheated oil bath at 100 °C for 88 h. The pressure increased to *ca.* 40 bar. After reaction, the autoclave was let to cool down naturally to r.t. before opening. An aliquot of the liquid phase was studied by ^1H NMR in CDCl_3 .

The semi-hydrogenation of phenylacetylene in styrene occurred in the conditions of Catalysis III.2. but with very low yields, below 2 % even when H_2 pressure was set to 30 bar. There is nonetheless no degradation of the phenylacetylene in byproducts. Such low conversions impend us from concluding $\text{Mo}_2\text{C}/\text{graphite}$ is an active catalyst for H_2 activation under these conditions.



	Catalyst	H ₂ pressure	Styrene yield (%)
1	Mo ₂ C/graphite	7 bar	Traces
2	Mo ₂ C/graphite	15 bar	1.2 %
3	Mo ₂ C/graphite	30 bar	1.5 %

Table 3. Semi-hydrogenation of phenylacetylene with Mo₂C/graphite. Reaction conditions: 220 μL of phenylacetylene (2 mmol), 60 mg of Mo₂C/graphite (0.16 mmol [Mo] estimated, 8 mol%), 1 mL of toluene, H₂ (x bar, x mmol), 100 $^{\circ}\text{C}$ during 88 h in autoclave (25 mL).

Conversion and yield determined by NMR.

III.2.3 Conclusion on hydrogenation reactions in solvent

The hydrogenation reactions of olefins with Mo₂C and W₂C nanoparticles supported on graphite or acetylene black were unsuccessful with no reduction at all of styrene in ethylbenzene at 100 $^{\circ}\text{C}$ under 7 bar of H₂ and only traces of styrene formation from phenylacetylene at 100 $^{\circ}\text{C}$ under 30 bar of H₂.

We nonetheless demonstrated in the first part that the Mo₂C/graphite catalyst is active for butadiene hydrogenation for temperatures above 120 $^{\circ}\text{C}$ with an optimum at *ca.* 200 $^{\circ}\text{C}$, and that a reduction of the oxidized shell is needed. We therefore suggest the study of phenylacetylene and styrene hydrogenations at elevated temperatures, *i.e.* 150-200 $^{\circ}\text{C}$, before concluding as to the inefficiency of the developed materials for these reactions. Furthermore, the hydrogenation of aromatic aldehydes such as benzaldehyde or furfural could be attempted as β -Mo₂C is known to be an active catalyst of furfural hydrogenation under 20 bar H₂ at 150 $^{\circ}\text{C}$ in isopropanol.²

III.3. Bibliography

1. Levy, R. B. & Boudart, M. Platinum-Like Behavior of Tungsten Carbide in Surface Catalysis. *Science* **181**, 547–549 (1973).
2. Deng, Y. *et al.* Solvent Tunes the Selectivity of Hydrogenation Reaction over α -MoC Catalyst. *J. Am. Chem. Soc.* **140**, 14481–14489 (2018).
3. Braun, M. & Esposito, D. Hydrogenation Properties of Nanostructured Tungsten Carbide Catalysts in a Continuous-Flow Reactor. *ChemCatChem* **9**, 393–397 (2017).
4. Yang, Q., Qiu, R., Ma, X., Hou, R. & Sun, K. Surface reconstruction and the effect of Ni-modification on the selective hydrogenation of 1,3-butadiene over Mo₂C-based catalysts. *Catal. Sci. Technol.* **10**, 3670–3680 (2020).
5. Ma, H. *et al.* Highly efficient Pd(acac)₂/TFA catalyzed head-to-tail dimerization of vinylarenes at room temperature. *Tetrahedron Lett.* **52**, 1569–1573 (2011).
6. Myagmarsuren, G., Tkach, V. S., Shmidt, F. K., Mohamad, M. & Suslov, D. S. Selective dimerization of styrene to 1,3-diphenyl-1-butene with bis(β -diketonato)palladium/boron trifluoride etherate catalyst system. *J. Mol. Catal. A Chem.* **235**, 154–160 (2005).
7. Tsuchimoto, T., Kamiyama, S., Negoro, R., Shirakawa, E. & Kawakami, Y. Palladium-catalysed dimerization of vinylarenes using indium triflate as an effective co-catalyst. *Chem. Commun.* **3**, 852–853 (2003).
8. Peng, J. *et al.* Dimerization of styrene to 1,3-diphenyl-1-butene catalyzed by palladium–Lewis acid in ionic liquid. *J. Mol. Catal. A Chem.* **255**, 16–18 (2006).
9. Tkach, V. S., Myagmarsuren, G., Suslov, D. S., Mesyef, M. & Shmidt, F. K. Palladium carboxylate/boron trifluoride etherate catalyst system for the selective dimerization of styrene. *Catal. Commun.* **8**, 677–680 (2007).
10. Suslov, D. S., Tkach, V. S., Bykov, M. V. & Belova, M. V. Selective dimerization of styrene to 1,3-diphenylbutene-1 in the presence of [(acac)Pd(PAr₃)₂]BF₄/BF₃OEt₂ catalytic systems. *Pet. Chem.* **51**, 157–163 (2011).
11. Choi, J. H., Kwon, J. K., RajanBabu, T. V. & Lim, H. J. Highly Efficient Catalytic Dimerization of Styrenes via Cationic Palladium(II) Complexes. *Adv. Synth. Catal.* **355**, 3633–3638 (2013).

12. Suslov, D. S. *et al.* [Pd(acac)(MeCN)₂]BF₄: air-tolerant, activator-free catalyst for alkene dimerization and polymerization. *RSC Adv.* **5**, 104467–104471 (2015).
13. Dawans, F. Dimerisation stereospécifique du styrène en présence de bis(trifluoroacétate de nickel π -allyle). *Tetrahedron Lett.* **12**, 1943–1946 (1971).
14. Yi, C., Hua, R. & Zeng, H. Efficient and selective nickel(II)-catalyzed tail-to-head dimerization of styrenes affording 1,3-diaryl-1-butenes. *Catal. Commun.* **9**, 85–88 (2008).
15. Wang, C.-C., Lin, P.-S. & Cheng, C.-H. Cobalt-catalyzed dimerization of alkenes. *Tetrahedron Lett.* **45**, 6203–6206 (2004).
16. Peppe, C., Schulz Lang, E., de Andrade, F. M. & de Castro, L. B. Indium(III) Bromide-Catalyzed Chemoselective Dimerization of Vinylarenes. *Synlett* 1723–1726 (2004).
17. Yue, H.-L., Zhao, X.-H., Jiang, L., Shao, Y. & Mei, L.-J. Highly efficient TfOH-catalyzed head-to-tail dimerization of vinylarenes. *Synth. Commun.* **46**, 179–186 (2016).
18. Nishii, H. & Higashimura, T. Dimerization of methylstyrenes by acetyl perchlorate and trifluoromethanesulfonic acid. *J. Polym. Sci. Polym. Chem. Ed.* **15**, 1179–1188 (1977).
19. Higashimura, T. & Nishii, H. Selective Dimerization of Styrene To 1,3-Diphenyl-1-Butene By Acetyl Perchlorate. *J Polym Sci Polym Chem Ed* **15**, 329–339 (1977).
20. Benito, A., Corma, A., García, H. & Primo, J. Dimerization of styrene catalyzed by acid 12-membered ring zeolites. *Appl. Catal. A Gen.* **116**, 127–135 (1994).
21. Grigor'eva, N. G. *et al.* Dimerization of vinylarenes on zeolite catalysts. *Pet. Chem.* **49**, 16–22 (2009).
22. Grigor'eva, N. G., Bubennov, S. V., Khalilov, L. M. & Kutepov, B. I. Codimerisation of styrene and α -methylstyrene in the presence of zeolites. *Appl. Catal. A Gen.* **407**, 85–90 (2011).

Part 2

Hydrothermal syntheses

Chapter IV

Syntheses of defective cerium oxide nanoparticles for H₂ activation

Cerium oxides have been extensively studied in the context of catalysis due to the versatility of the degree of oxidation of cerium.¹ Cerium is indeed stable both as Ce^(III) and Ce^(IV) which makes it unique among the rare earth metals. The oxidation Ce^(III) → Ce^(IV) in cerium oxides occurs under ambient conditions with atmospheric dioxygen.² The most common cerium oxide is CeO₂ but this raw formula actually covers a large variety of composition as oxygen vacancies are intrinsically present in cerium oxide and are charge-compensated by the presence of Ce^(III). A rigorous description would therefore be Ce^(IV)_{1-x}Ce^(III)_xO^(-II)_{2-0.5x}. The percentage x of Ce^(III) may vary from 0 % up to 40 % for nanoparticles prepared *via* usual synthetic pathways.¹ The amount of Ce^(III) may be increased *a posteriori* by treatments such as calcination in inert atmosphere,³ or reaction with reducing agents like ascorbic acid.⁴ The color of the material depends on the oxidation state of the surface cerium atoms: the violet and the yellow colors are respectively associated to Ce^(III) and Ce^(IV).² Reduced cerium oxides are typically violet or grey while oxidized ones are yellow or off white.

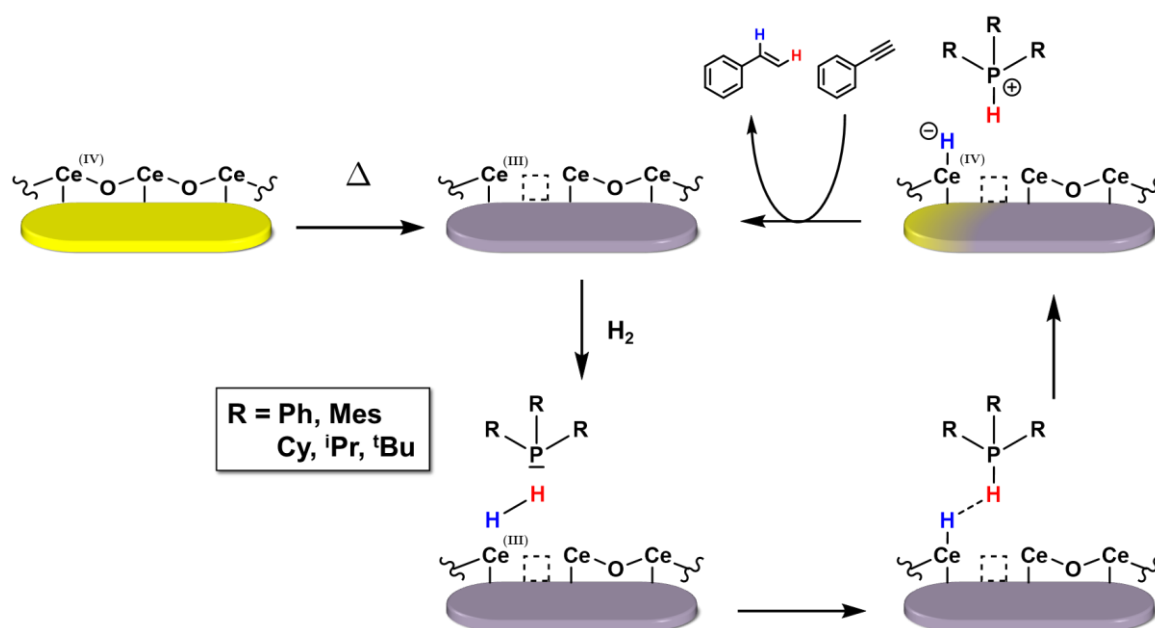
The hydrothermal synthesis of cerium oxide nanoparticles below 50 nm has been the object of multiple works.^{1,2,5,6} These syntheses use a variety of precursors (CeCl₃, Ce(NO₃)₃, Ce(SO₄)₂) and precipitating agents (NaOH, KOH, NH₄OH), and with different reaction conditions including the temperature (typically 100-250 °C), the nature of the reaction vessel (Teflon autoclave, Borosilicate vessel, Nalgene vessel), the treatment of the initial suspension and the washing step, among others.² In most cases, the synthesis parameters allow the control to some extent of the shape, the size and the defect density of the nanocrystals. Unfortunately, discrepancies and conflicting results emerged, stressing the high sensitivity of these syntheses to the reaction conditions. The easiness and the dynamic character of the reduction/oxidation processes in CeO₂ render delicate the study and characterization of the degree of oxidation by techniques such as X-ray Photoelectron Spectroscopy (XPS).⁷

As developed in Chapter I, Qu *et al.* recently reported the use of cerium oxide nanoparticles for hydrogenation of alkenes and alkynes in toluene under soft conditions.⁸ This study is among the most disruptive of this past decade as to activation of H₂ with metal oxides in the liquid phase. The authors demonstrated the catalytic activity essentially relies on the presence of defects in the CeO₂ structure. The active sites are situated at the vicinity of an oxygen vacancy (V_o) with two Ce^(III) at the surface of the nanoparticles. To create such sites, a high density of Ce^(III) is required,

typically more than 30 % on the surface. The surface oxygen vacancies on cerium oxide were reported to favor H_2 activation by heterolytic cleavage and to stabilize the so-formed hydride Ce-H .⁹ This last species could not be characterized by infrared spectroscopy but was recently evidenced by Freund *et al.* by XPS in the case of a highly defective cerium oxide.¹⁰

Guo *et al.*¹² and Rossi *et al.*^{13–15} reported hydrogenation reactions of alkenes and alkynes with gold nanoparticles whose catalytic activity is exacerbated by the presence of imines or amines. They both suggest the mechanism at stake is a Frustrated Lewis Pair (FLP)-like one and that one H^+ is captured by the imine/amine while the H^- counterpart stays on the gold surface. The hydride and the proton then successively react with the substrate molecule. No such mechanism was however reported so far for metal oxide materials, or any other compound displaying an ionic character.

As Qu *et al.* managed an all solid FLP-like splitting of H_2 at the surface of cerium oxide and Freund *et al.* proved the stability of Ce-H hydride species, we wondered whether the H_2 activation could be performed between a cerium atom in CeO_2 and a phosphine ligand according to an FLP-like mechanism. We imagined a heterolytic cleavage of H_2 with H^+ captured by the phosphine and H^- on the surface of the nanoparticle as a surface hydride (Scheme 1). This theoretical mechanism relies on the ability of cerium to easily switch from $\text{Ce}(\text{III})$ to $\text{Ce}(\text{IV})$ and vice versa. As cerium oxide is known for its catalytic activity for hydrogenation of acetylene in gas phase¹⁶ and of phenylacetylene in solvent, though with moderate activity,⁸ we chose this last molecule (PhCCH) as model substrate.



Scheme 1. Hypothetical H_2 activation at the surface of a defective cerium oxide nanoparticle for hydrogenation of phenylacetylene according to an FLP-like mechanism.

Different objectives were thus pursued in this chapter:

- (1) The reproduction of the material reported by Qu *et al.* as a starting point
- (2) The optimization of the ratio of surface Ce^(III) in CeO₂ for H₂ activation by different reductive post-synthesis treatments
- (3) The study of the impact of the addition of phosphine ligands on the catalytic activity for hydrogenation of phenylacetylene

We first attempted at reproducing the material obtained by Qu *et al.* *via* a two-step protocol (Section IV.1.). When a reproducible synthesis of the targeted material was finally achieved, with similar XRD pattern than the reported one, it appeared there were discrepancies in the analysis of the XRD data between our work and that of Qu *et al.* As the intermediate material at the end of the first step was not reported or discussed in literature, we performed an in-depth characterization (Section IV.2.). The cerium oxide samples from Sections IV.1. and IV.2. were then subjected to thermal treatments to increase the surface Ce^(III) ratio (Section IV.3). The catalysts were finally studied for the activation of H₂ in the gas phase (Section IV.4.1.) and for the hydrogenation of phenylacetylene in solvent (Section IV.4.2.).

IV.1. Tailored hydrothermal synthesis of defective cerium oxide catalyst

IV.1.1 Cerium oxide nanorods

Cerium oxide nanoparticles were synthesized by hydrothermal treatment of $\text{Ce}(\text{NO}_3)_3 \cdot 6\text{H}_2\text{O}$ with a 6 M NaOH solution at 100 °C, followed by extensive washing with water.⁶

Synthesis IV.1. Cerium oxide nanorods. In a 250 mL Borosilicate vessel, 3.91 g of $\text{Ce}(\text{NO}_3)_3 \cdot 6\text{H}_2\text{O}$ (9 mmol, 1 equiv.) were dissolved in 30 mL of distilled water to yield a colorless limpid solution. Meanwhile, 43 g of NaOH pellets (1.075 mol, 6 M) were dissolved in 150 mL of water and the resulting solution was slowly added to the cerium nitrate solution. A yellow-brown precipitate appeared at the first drops, followed by a yellow gel and a grey gel and finally a violet suspension. The turbid violet solution was stirred 30 min and distributed in 4 Nalgene vessels of 50 mL, which were then put in a preheated oil bath at 100 °C for 20 h. After reaction, the solution was let to cool down naturally to r.t. A grey-violet powder sedimented at the bottom of the vessel, the supernatant was colorless. The whole suspensions were brought together and centrifugated (9,000 rpm, 10 min, 20 °C). The grey powder was washed 6 times with 30 mL of H_2O and once with 30 mL of EtOH: along the washings, the powder gradually turned beige. The obtained beige powder (1.45 g, 94 % yield) was then dried under N_2 and stored under air.

According to XRD, the material obtained with Synthesis IV.1. is isostructural with cerium oxide CeO_2 [PDF card N°00-034-0394], with a crystallite size *ca.* 12 nm, calculated with the Scherrer formula applied to the peaks at 29°, 33°, 47° and 69° (Figure 1A). TEM images reveal the product consists in polycrystalline nanorods and nanocubes (Figure 1B-C) with typical sizes ranging from 100 nm to 200 nm for nanorods length and 12 nm for their diameter, and of 10-20 nm for nanocubes diameter. Selection Area Electron Diffraction (SAED) comforts the XRD attribution to CeO_2 (Figure 1D). As cerium oxide is known for its large tolerance to oxygen vacancies, the XRD attribution does not give information on the actual average oxidation degree of the cerium. This material will be referred to as CeO_2 nanorods.

After reaction, the sediment in the reaction vessel was grey-violet and the powder gradually turned beige during the several washings with water. The grey-violet color before the washing step indicated the material was partially reduced, at least in surface, and the color change that surface cerium atoms were oxidized by contact with atmospheric O_2 . Their oxidation may occur without structural modifications, *i.e.* the CeO_2 phase was probably already formed before the washing but with a consequent number of oxygen defects to accommodate the surface $\text{Ce}^{\text{(III)}}$ atoms. When the powder was dried in oven at 60 °C in air after the washing steps, as frequently done in

literature, it turned deep yellow. The drying step is therefore not innocent and not limited to the simple removal of water molecules.

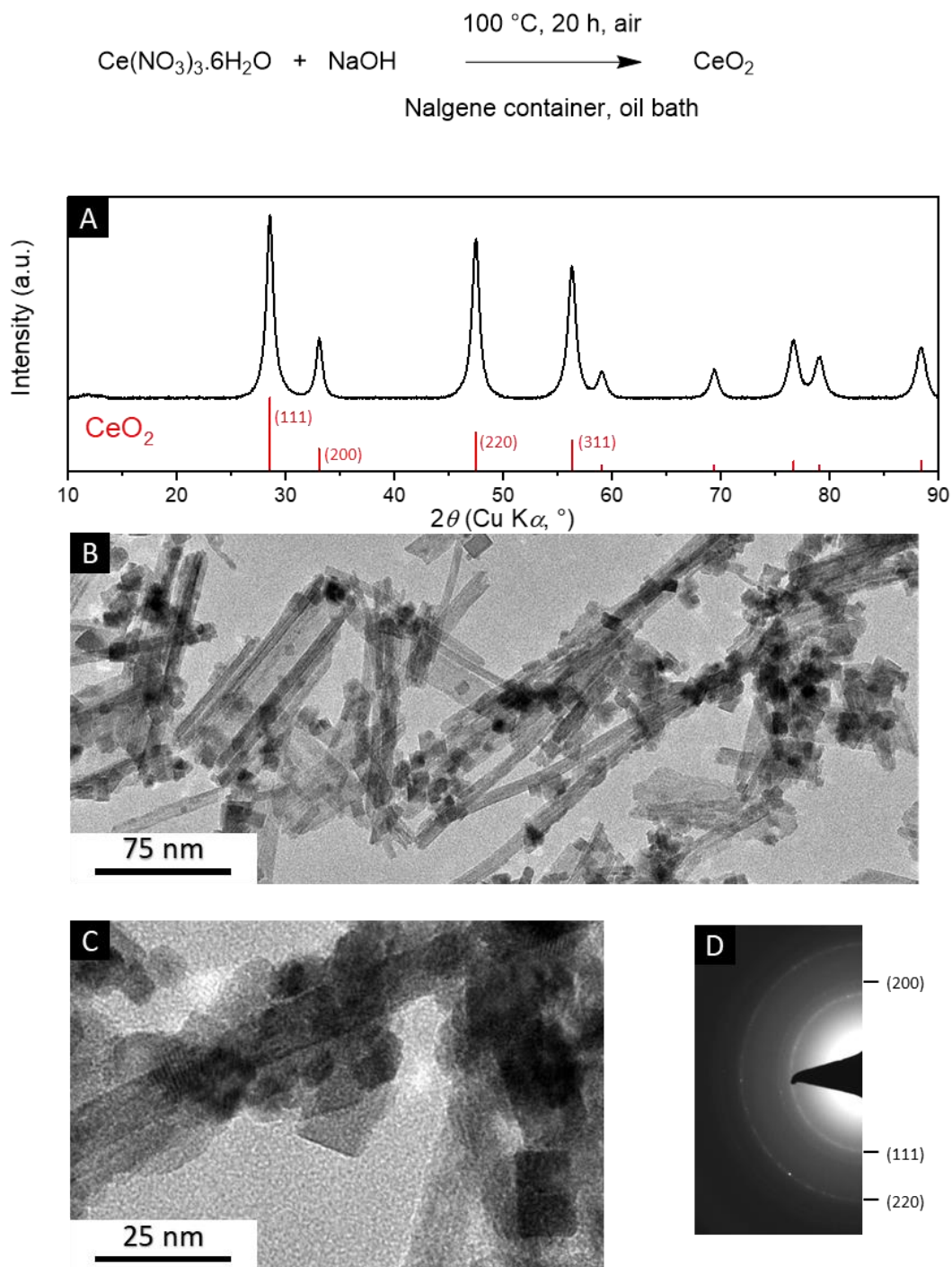


Figure 1. Synthesis of CeO_2 nanoparticles according to Synthesis IV.1. (A) XRD pattern with lattice planes attribution, (B-C) TEM images and (D) electron diffraction pattern.

The turbid violet solution obtained after stirring but before reaction at 100 °C was isolated to be studied. Initially violet, it turned ochre after two washings with water and one with ethanol and then yellow in less than 24 h when stored in air. XRD indicates the material is cerium oxide CeO_2 with 5 nm crystallite size (Figure 2a) and TEM images reveal sheet-like particles. Cerium nitrate is known to form cerium trihydroxide $\text{Ce}(\text{OH})_3$ in the presence of basic solutions, then $\text{Ce}(\text{OH})_3$ decomposes in CeO_2 when exposed to air, with broad features in XRD.^{2,5} We hypothesize such an evolution occurred in our case, explaining the presence of CeO_2 but with different morphology than the particles obtained after hydrothermal treatment at 100 °C.

Alternatively, the heating step was conducted at 75 °C in a 50 mL Nalgene vessel or at 100 °C in a 25 mL Teflon autoclave. Both gave the same results than the heating at 100 °C in the Nalgene vessel, on the basis of XRD (Figure 2b-d). However, the reaction conducted at a higher temperature of 180 °C in the Teflon autoclave produced quasi exclusively nanocubes with larger size according to XRD and TEM, around 25 nm (Figure 2e). Finally, the reaction was once conducted in a regular glass reaction tube and the glass leached due to the high pH: this was obvious as micron sized rolled up objects were observed in TEM and a cancrinite phase ($\text{Al}_3\text{Na}_4\text{O}_{14.35}\text{Si}_3$) was the major species in XRD.

We concluded cerium oxide nanorods could be obtained when the reaction temperature is *ca.* 100 °C. Higher temperatures (180 °C) leads to the same crystallographic phase but a different morphology, large nanocubes, which presents a lower surface/volume ratio, detrimental to catalysis. The use of a Teflon autoclave or a Nalgene vessel does not seem to lead to significantly different materials but the use of regular glass should be prohibited for this reaction due to leaching issues. We retained the conditions “100 °C in Nalgene vessel” for the production of cerium oxide for catalysis.

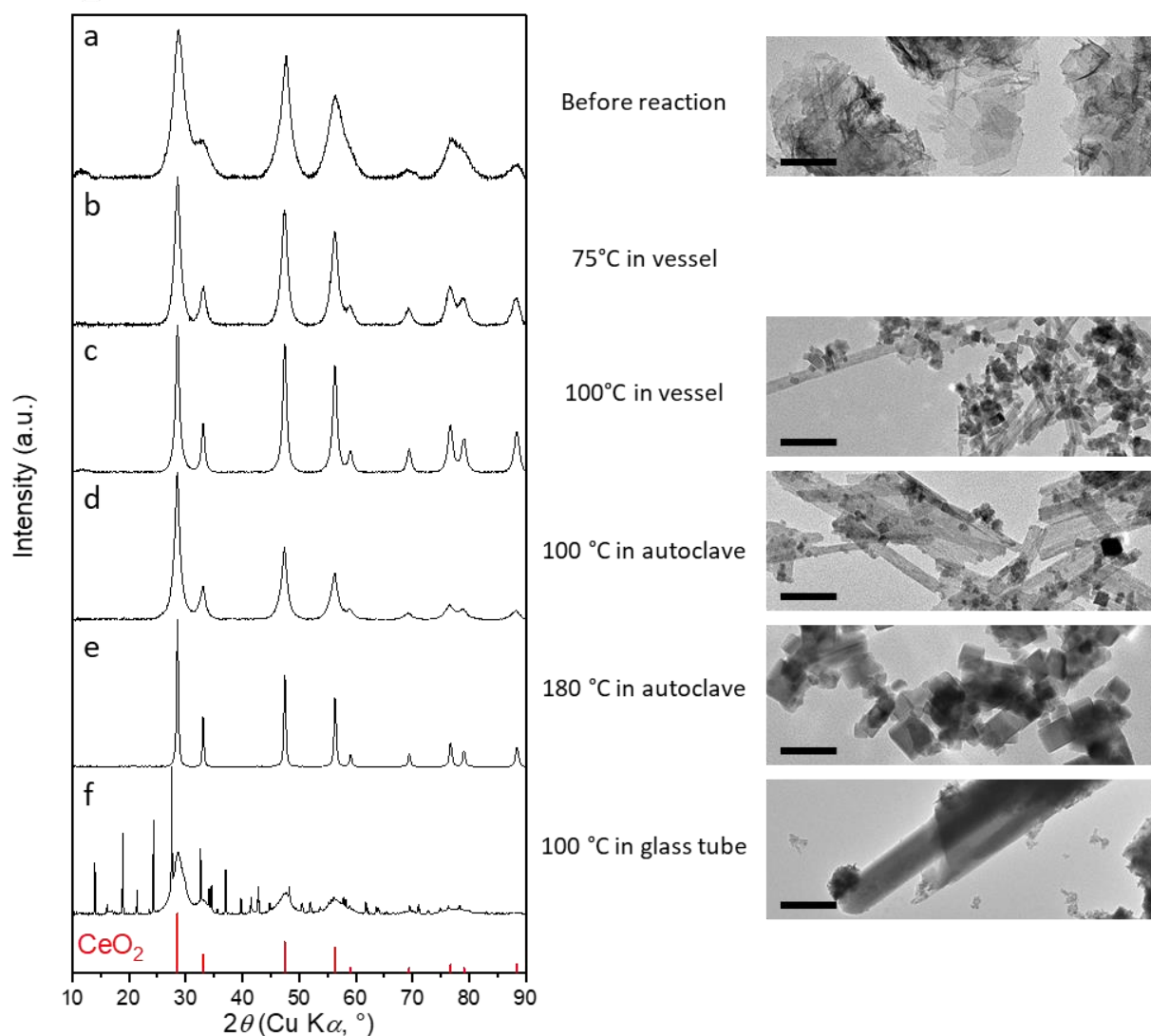


Figure 2. Synthesis of CeO₂ under different conditions with structural and morphological characterizations by XRD (left) and TEM (right). (a) Washed grey gel obtained after 30 min of stirring. Powder obtained after 20 h in a Nalgene vessel (b) at 75 °C or (c) 100 °C. Powder obtained after 20 h in a Teflon autoclave (d) at 100 °C or (e) 180 °C. (f) Powder obtained after 20 h in a glass reaction tube at 100 °C. Scale bars on TEM images represent 50 nm except for (f) where it represents 500 nm. The calculated Scherrer sizes on XRD are respectively 5 nm, 8 nm, 12 nm, 9 nm and 25 nm for (a-e).

IV.1.2 Toward Ce^(III) rich cerium oxide and cerium hydroxide

We then attempted to reproduce the materials synthesized by Qu *et al.*, which displayed excellent properties as to hydrogenation of alkenes and alkynes in toluene.^{3,8} Their protocol consists in two steps: first the synthesis of a “non-porous CeO₂ nanorods precursor” (NP-CeO₂ precursor) by hydrothermal treatment of Ce(NO₃)₃ · 6H₂O with NaOH at 100 °C for 20 h in a Pyrex bottle in an oven, then its dehydration in CeO₂ by hydrothermal treatment at 160 °C during 12 h. The NP-CeO₂ precursor was

identified by Guo *et al.* as a mixture of $\text{Ce}(\text{OH})_3$ and CeO_2 , this point will be discussed later.³ The diffraction pattern is particularly recognizable due to the peaks at *ca.* 52°, forming a thin peak and a quasi-plateau (Figure 3).

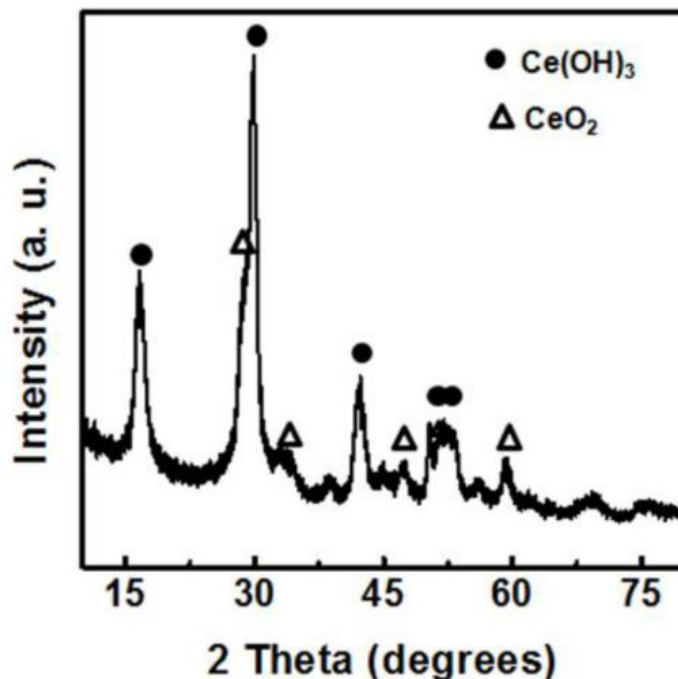


Figure 3. XRD pattern of the targeted material with phase attribution, from reference [8].

In order to favor the formation of $\text{Ce}(\text{OH})_3$ phase instead of CeO_2 , obtained in Synthesis IV.1, we explored the influence of different parameters such as (1) the nature of the reaction vessel (Nalgene/Borosilicate), (2) the nature of the precipitating agent (NaOH/KOH), (3) the concentration of the base and (4) the reaction temperature (75 °C/100 °C).

The reaction was first conducted with $[\text{NaOH}] = 6 \text{ M}$ or with $[\text{KOH}] = 4.3 \text{ M}$ in either a Borosilicate vessel or a Nalgene vessel. This last one is supposedly less air-tight than the Borosilicate one. Reactions in Nalgene vessels led to XRD-pure CeO_2 and the peaks were thinner than in Borosilicate vessels (Figure 4a-b *vs* c-d). For reactions conducted in Borosilicate vessels, a lower proportion of CeO_2 was obtained with KOH than with NaOH (Figure 4c-d), in favor of the phase with the characteristic pattern at *ca.* 52°. We therefore used KOH and Borosilicate vessels for the following experiments. The reaction was then conducted with a KOH concentration of 4.3 mol/L and of 0.43 mol/L, both corresponding to pH above 13, and either at 75 °C or 100 °C (Figure 4e-h). The proportion of CeO_2 was higher for low KOH concentrations both at 75 °C and 100 °C. The proportion of CeO_2 was also higher when the reaction temperature was set to 100 °C both at low and high KOH concentrations. As a consequence, we

kept the KOH concentration at 4.3 mol/L and the reaction temperature at 100 °C for the following experiments. We can nonetheless notice the robustness of the reaction as similar diffractograms were obtained even when varying the nature and the concentration of the precipitating agent and the reaction temperature.

As previously mentioned, we noticed the powder gradually turned yellow during the several washings with water. To determine whether these washings significantly increase the proportion of CeO₂ of the material, we performed XRD measurements on the samples both before and after washing (data not shown). We did not observe any growth of the CeO₂ phase due to the washing. However, before the washing step, a potassium carbonate phase was detected, probably originating from the reaction of atmospheric CO₂ with the highly basic wet powder.

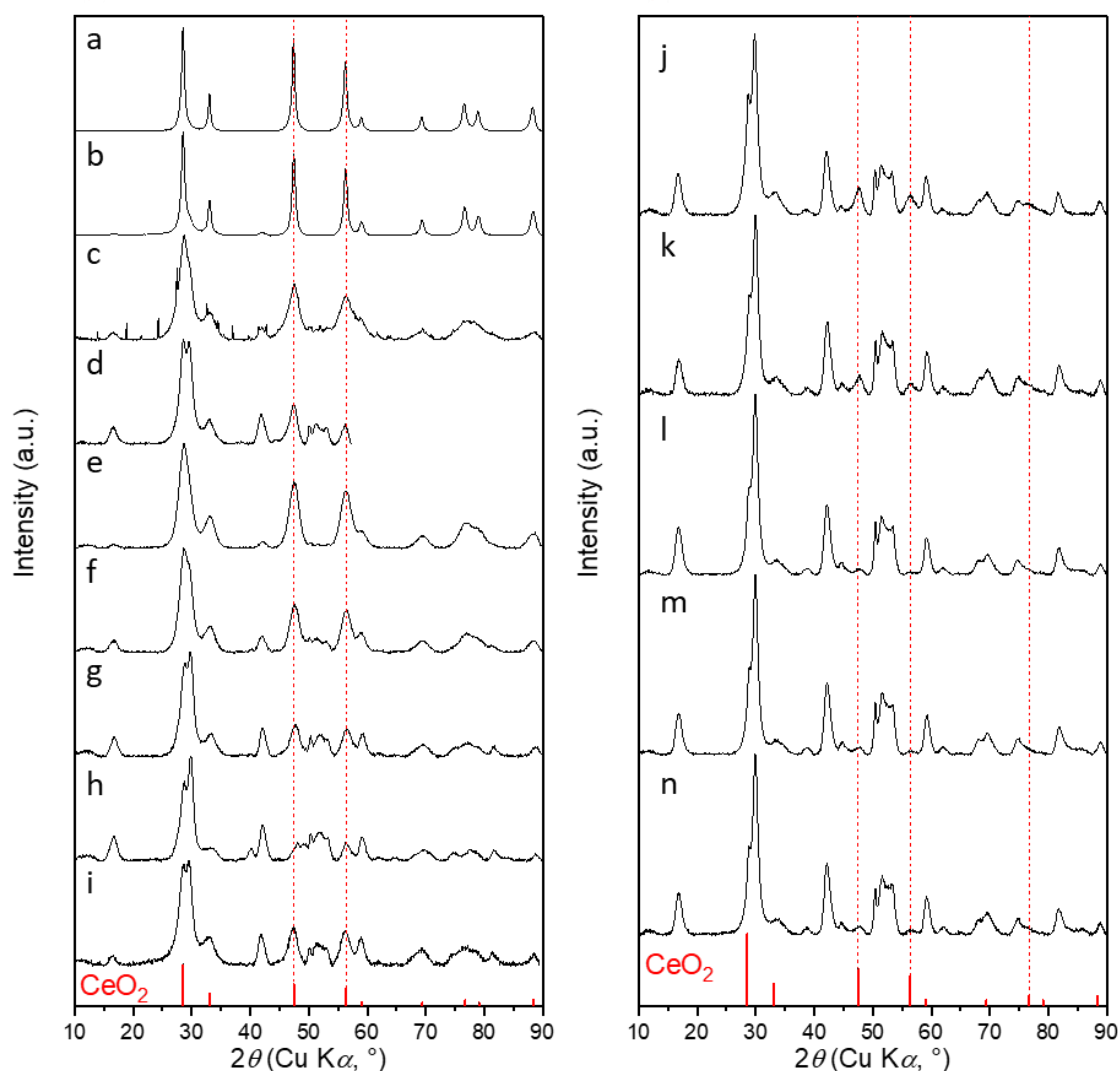


Figure 4. XRD measurements of cerium oxide/hydroxides powders for reactions performed at 100 °C, (a) with [NaOH] = 6 M in a 50 mL Nalgene vessel, (b) with [KOH] = 4.3 M in a Nalgene vessel (50 mL), (c) with [NaOH] = 6 M in a Borosilicate vessel (66 mL) and (d) with

[KOH] = 4.3 M in a Borosilicate vessel. Reactions performed in a Borosilicate vessel (e) with [KOH] = 0.43 M at 75 °C, (f) with [KOH] = 0.43 M at 100 °C, (g) with [KOH] = 4.3 M at 75 °C, (h) with [KOH] = 4.3 M at 100 °C (i) with [KOH] = 4.3 M at 100 °C in cryodegassed water. Reactions performed in Borosilicate vessel (66 mL) at 100 °C with [KOH] = 4.3 M, (j) 12 mL Borosilicate vessel filled, in air, (k) 36 mL Borosilicate vessel filled, in air, (l) 12 mL Borosilicate vessel filled, in N₂, (m) 36 mL Borosilicate vessel filled, in N₂ and (n) 66 mL Borosilicate vessel fully filled with the solution. As a guide to the eye, the red dotted lines stress the peak positions of CeO₂ not superimposed with the other phases.

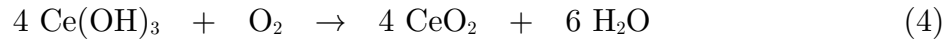
Wang *et al.* reported that a solution of Ce(NO₃)₃ and NaOH under stirring turns yellow in 20 min if exposed to air while it stays grey-violet if maintained in a sealed vessel.² We therefore hypothesized the oxidation of all the Ce^(III) from the cerium nitrate precursor occurs with the dissolved O₂ in water and from the oxygen present in the gas phase in equilibrium inside the closed vessel. The solubility of O₂ in pure water is $s(\text{O}_2) = 0.28 \text{ mmol/L}$ at 20 °C and decreases if salinity increases. Considering the reaction is conducted in air in a reaction volume V_{reaction} in a closed vessel V_{vessel} , and with $V_{\text{mol}} = 24 \text{ L/mol}$ the molar volume of a gas, the maximal available amount of dioxygen $n(\text{O}_2)$ is given by Eq. (1), (2) and (3).

$$n(\text{O}_2) = n_{\text{dissolved}} + n_{\text{gas}} \quad (1)$$

$$n_{\text{dissolved}} = s(\text{O}_2) \cdot V_{\text{reaction}} \quad (2)$$

$$n_{\text{gas}} = 0.2 (V_{\text{vessel}} - V_{\text{reaction}})/V_{\text{mol}} \quad (3)$$

For instance, with $V_{\text{reaction}} = 36 \text{ mL}$ and $V_{\text{vessel}} = 66 \text{ mL}$, we obtain $n_{\text{dissolved}} = 0.010 \text{ mmol}$ and $n_{\text{gas}} = 0.25 \text{ mmol}$. For this reaction volume, 1.8 mmol of Ce(NO₃)₃ were introduced. If we consider Eq. (4) for the oxidation of Ce^(III) in Ce^(IV), 0.25 equiv. of O₂ are required per cerium atom, *i.e.* 0.45 mmol in the example case.



We first note the amount of initially dissolved O₂ would only oxidize 2 % of the cerium atoms. We can therefore neglect its contribution in a first approach, meaning the deoxygenation of water is probably not crucial to limit the formation of Ce^(IV). For comparison, we ran the reaction in water deoxygenated by N₂ bubbling during 4 h and in water degassed by 3 freeze-pump-thaw cycles. As more CeO₂ was obtained with cryodegassed water, we decided to only use deoxygenated water by N₂ bubbling (Figure 4h-i). Then, we note that if the entirety of the O₂ available in the gas phase is consumed for cerium oxidation, which seems unlikely, it would result in the oxidation of 55 % of the material (Table 1, entry 2).

	Liquid volume / Gas volume	Gas phase	$n(\text{O}_2)$	$n(\text{Ce}^{\text{III}})$	Maximal theoretical Ce^{IV} percentage
1	12 mL/44 mL	Air	0.45 mmol	0.6 mmol	100 %
2	36 mL/30 mL	Air	0.25 mmol	1.8 mmol	55 %
3	12 mL/44 mL	N_2	0 mmol	0.6 mmol	0 %
4	36 mL/30 mL	N_2	0 mmol	1.8 mmol	0 %
5	66 mL/0 mL	<i>n.a.</i>	0 mmol	3.3 mmol	0 %

Table 1. Theoretical oxidation ratio of the cerium atoms for a reaction conducted in a 66 mL air-tight Borosilicate vessel in the case of a reaction solution with $[\text{Ce}] = 0.05 \text{ mol/L}$.

To investigate whether this explanation of the origin of the cerium oxidation is valid, we ran 5 experiments all originating from the same $\text{Ce}(\text{NO}_3)_3 + \text{KOH}$ solution batch. Three levels of filling of the Borosilicate vessel were chosen: 12 mL, 36 mL and 66 mL (*i.e.* the totality of the container) and for the non-entirely filled conditions, the gas phase was either air or N_2 . In all cases, the CeO_2 was present but was the minor phase (Figure 4j-n): when the gas phase was air (j-k), the proportion of CeO_2 was higher, and the higher the gas volume, the more intense the CeO_2 peaks. For reactions conducted with N_2 in the gas phase or with no gas phase (l-n), there is no significant difference between the diffractograms. We validated the fact a part of the oxidation of Ce^{III} in Ce^{IV} originates from the O_2 initially present in the gas phase in equilibrium with the solution, at least for reactions conducted in Borosilicate vessels. Not all the atmospheric O_2 is consumed as the CeO_2 stays at the state of traces. The residual presence of CeO_2 , even with theoretically no O_2 available, may be explained by either O_2 traces or by alternative oxidation pathways. Besides, CeO_{2-x} is known to accommodate defects up to $x = 0.5$, which would correspond to Ce_2O_3 , *i.e.* only Ce^{III} . This analysis comforts a work from Qu *et al.* in 2016: conducting a similar synthesis of cerium oxide under different O_2 partial pressures (from 1 bar to 0 bar), they showed the percentage of Ce^{III} in the final CeO_2 increases from 19.7 % to 25.4 %.¹⁷

In conclusion, we demonstrated we could produce both regular CeO_2 and the NP- CeO_2 precursor targeted for our catalysis study. For this latter material, an optimization allowed us to establish a reproducible protocol which led to almost no CeO_2 and quasi exclusively the targeted material.

IV.2. Structural study of cerium hydroxide $\text{Ce}(\text{OH})_3$ aging

IV.2.1 Structural characterization

By limiting the presence of O_2 in the reaction medium and playing on several parameters, we successfully limited the proportion of CeO_2 in the sample. For the rest of this section, the synthesis conditions for cerium trihydroxide are the following (Synthesis IV.2.).

Synthesis IV.2. Cerium trihydroxide $\text{Ce}(\text{OH})_3$. In a 66 mL Borosilicate vessel and under a flux of N_2 , 780 mg of $\text{Ce}(\text{NO}_3)_3 \cdot 6\text{H}_2\text{O}$ (1.8 mmol, 1 equiv.) were dissolved in 6 mL of deoxygenated water by N_2 -bubbling during 4 h to yield a colorless limpid solution. Meanwhile, 8.64 g of KOH (154 mmol, 4.3 M) were dissolved in 30 mL of deoxygenated water and the resulting solution was slowly added to the cerium nitrate solution. A yellow-brown precipitate appeared at the first drops, followed by a yellow gel and a grey gel and finally a violet suspension. The vessel was closed under N_2 and let to react during 30 min at r.t. and was then put in a preheated oven at 100 °C for 20 h. After reaction, the solution was let to cool down naturally to r.t. A grey powder sedimented at the bottom of the vessel, the supernatant was colorless. The solution was centrifugated under air. The powder was washed 6 times with 30 mL of H_2O and once with 30 mL of EtOH without excessive shaking nor use of sonication during redispersion.¹ The obtained grey powder (326 mg, 95 % yield) was then dried under N_2 and stored under argon.

X-ray diffraction. The obtained material from Synthesis IV.2. evolved over time if stored in air. From initially grey, the powder gradually turned yellow in a few days whereas it stayed grey if stored in Ar. In the fresh sample (synthesis less than 2 hours ago), cerium trihydroxide $\text{Ce}(\text{OH})_3$ [PDF card N°00-055-0556] peaks account for most of the signal (Figure 5A). The diffraction pattern does not evolve significantly when the material is stored in Ar, even after one week (Figure 5B), but is modified if stored in air (Figure 5C-D). XRD measurements on the sample after several months in air do not display any further modification (data not shown). We will refer to fresh and aged $\text{Ce}(\text{OH})_3$ for respectively the material stored in Ar immediately after synthesis and the one exposed to air for at least one week. All diffractograms presented in the previous section correspond to aged samples.

The presence of CeO_2 cannot be excluded *a priori* on the fresh sample as all its diffraction peaks are beneath those of $\text{Ce}(\text{OH})_3$. However, in aged samples, peaks at 47° and 56° are revealed (stressed by red dotted lines). On one particular batch, no

¹ One batch was washed thoroughly with non-deoxygenated water with vigorous agitation in air and then dried under a flux of N_2 . An XRD was recorded and nearly no CeO_2 was detected (data not shown), the precautions concerning the washing step are therefore probably excessive but we chose to keep them.

signal at all is observed at 47° and 56° (Figure 6B): we concluded first that these two “non-observed” peaks correspond to CeO_2 traces and not to a new phase and then that there is no production of CeO_2 during aging. This aging phenomenon was observed on all our batches with the same final pattern, in particular the recognizable plateau between 50° and 55° . XRD measurement performed after 1 day in air displays both the $\text{Ce}(\text{OH})_3$ phase and its “aged form” (Figure 5C): there are two distinct phases (stressed by blue arrows). In the final product, the phase which is not CeO_2 looks like a shifted pattern of $\text{Ce}(\text{OH})_3$ (Figure 6A-B). The shift occurring toward the high angles, it would correspond to a contraction of the crystal structure.

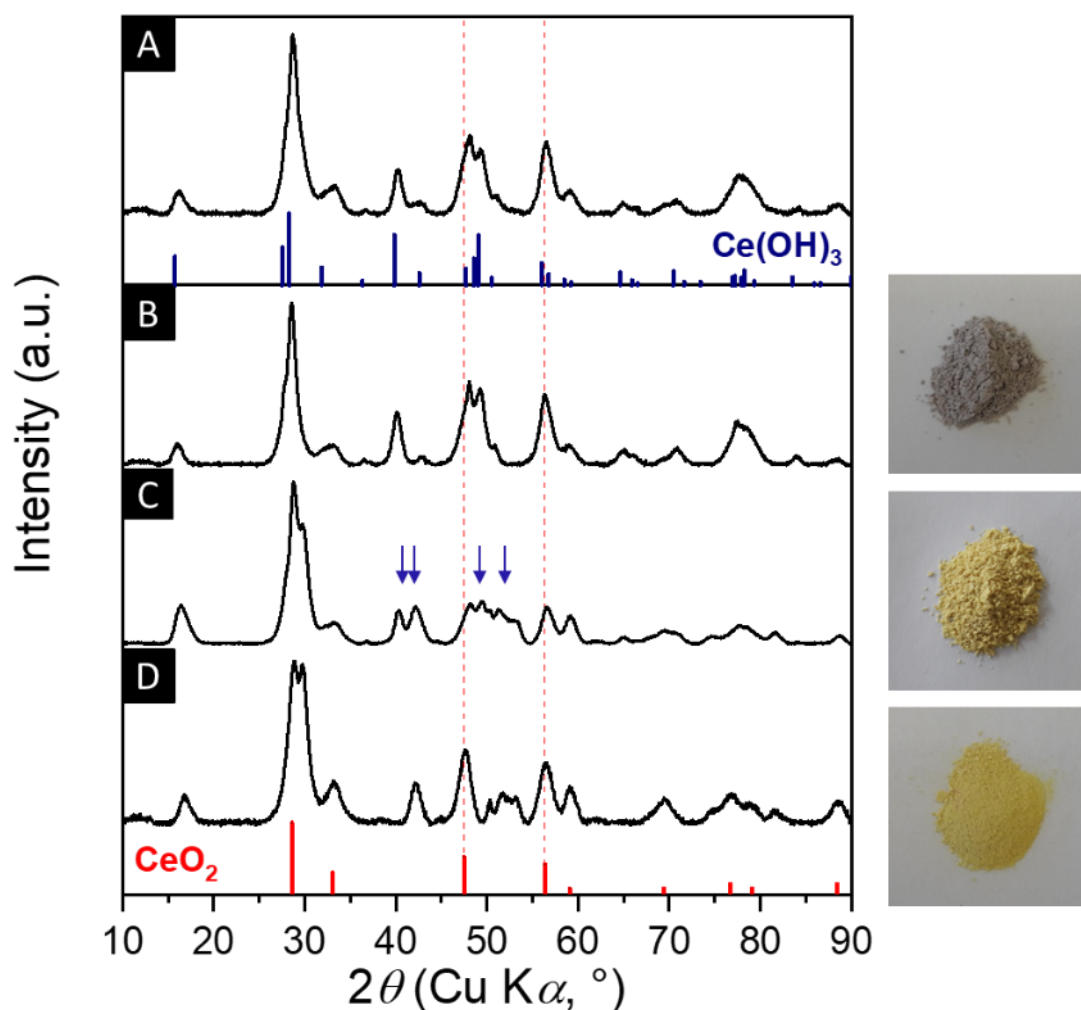


Figure 5. Left: XRD patterns of the aging of cerium trihydroxide from Synthesis IV.2. (A) Fresh sample, (B) after 4 days in Ar, (C) after 1 day in air, (D) after 4 days in air. Blue arrows stress the simultaneous presence of two crystallographic phases. Right: pictures of the corresponding samples. As a guide to the eye, the red dotted lines stress the peak positions of CeO_2 not superimposed with the “aged $\text{Ce}(\text{OH})_3$ phase”.

Three points should be stressed at this stage:

- (1) The XRD of our material termed “aged $\text{Ce}(\text{OH})_3$ ” matches perfectly with the “non porous precursor with a mixed phase $\text{Ce}(\text{OH})_3/\text{CeO}_2$ ” reported by Qu *et al.* (Figure 3) but there seems to be a discrepancy between the attribution they suggest (mix of CeO_2 and $\text{Ce}(\text{OH})_3$) and the diffractogram. There is no mention of aging or evolution of the precursor in their article.
- (2) Intriguingly, no phase could match the diffractogram of aged $\text{Ce}(\text{OH})_3$ in the JCPDS database. The current section will therefore be devoted to its analysis.
- (3) To the best of our knowledge, there is no mention in the literature of an evolution of $\text{Ce}(\text{OH})_3$ in a crystalline material different from CeO_2 .⁵ This point will be further discussed later.

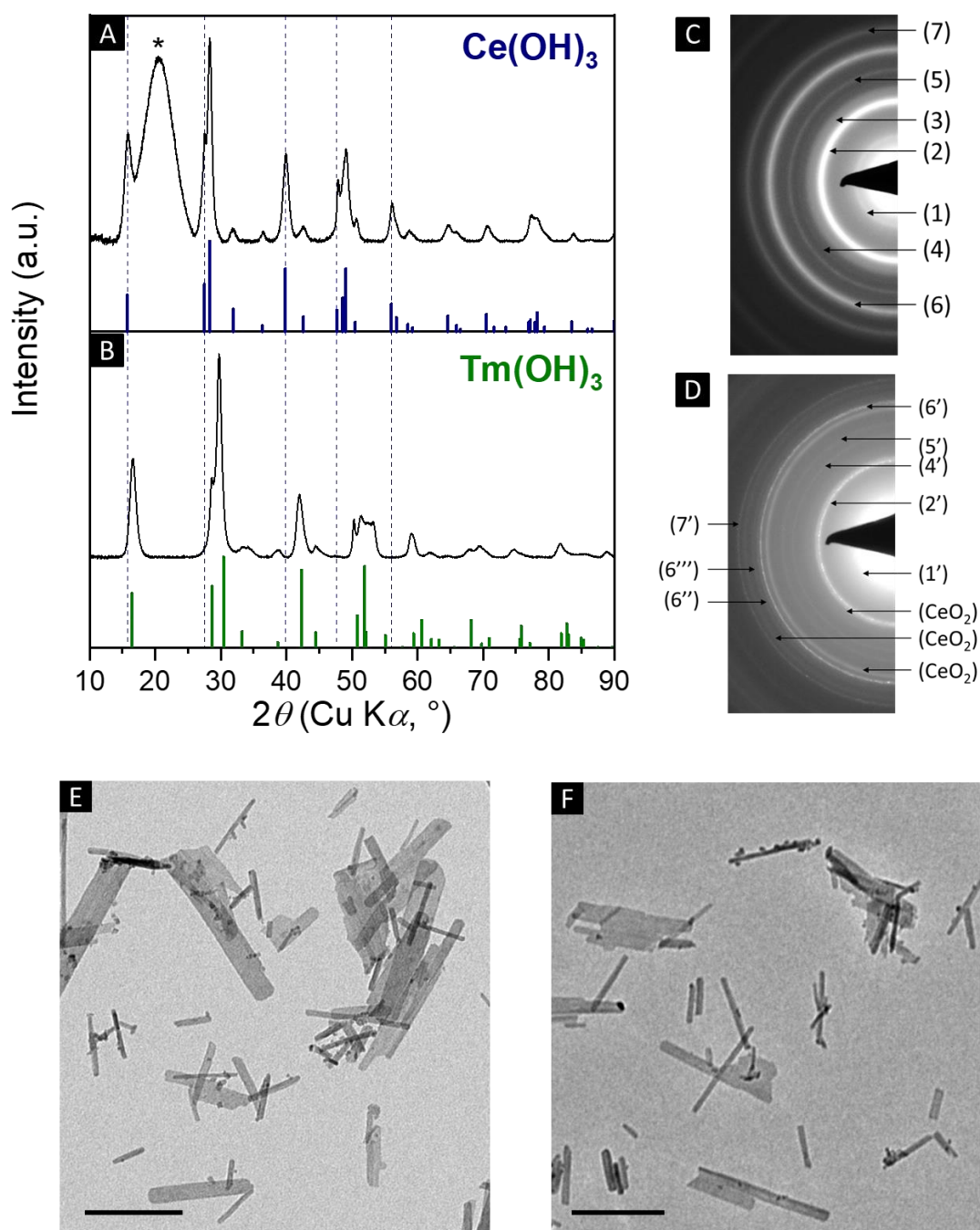


Figure 6. Aging phenomenon of Ce(OH)_3 . XRD patterns of (A) the fresh Ce(OH)_3 (the asterisk denotes the big hump due to the presence of a protection dome) and (B) the aged Ce(OH)_3 (the comparison with Tm(OH)_3 is discussed in section IV.3.2.). As a guide to the eye, blue dotted lines were plotted for a few peaks of Ce(OH)_3 . (C-D) Corresponding electron diffraction patterns. TEM images of the sample (E) before aging and (F) after one week aging (scale bars represent 100 nm on both images).

Electron microscopy. Cerium trihydroxide from Synthesis IV.2. crystallized in polydisperse nanorods very similar to the ones obtained with CeO_2 in Synthesis IV.1: the average length was 100 nm for a mean width of 10 nm (Figure 6E). We noticed the

presence of large plates which look like the sintering of several rods. Very few cubes were also produced. Upon aging in air, we did not observe any modification of the morphology of the nanoparticles (Figure 6F). When zooming on the aged sample, we nonetheless observed a beam damage of the material: black zones appeared and moved along the nanorods until stabilization after a few minutes (Figure 7A,B). This damage may be due to the reduction of the sample with electrons or, more probably, to the heat produced by the beam. The global morphology was preserved but numerous defects appeared, with characteristic size below 5 nm (Figure 7C). Such a behavior was not observed on the fresh $\text{Ce}(\text{OH})_3$ nor on CeO_2 .

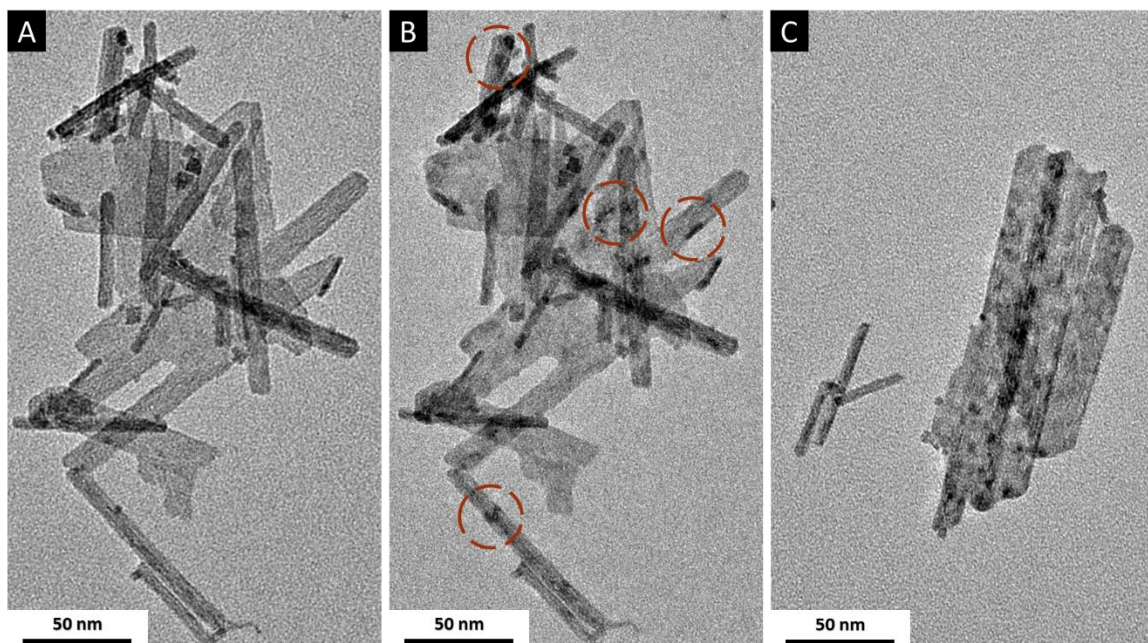


Figure 7. (A-C) TEM images of the electron beam damages to aged $\text{Ce}(\text{OH})_3$ (A and B were taken a few second apart, red circles stress the beam damages).

Electron diffraction. As a second structural method to characterize distances, we performed SAED on fresh $\text{Ce}(\text{OH})_3$ and aged $\text{Ce}(\text{OH})_3$ (Figure 6C-D). We used the shifts between the diffraction distances measured on a CeO_2 sample from a previous synthesis and the theoretical distances to estimate the error bar. For CeO_2 , the measured distances were 3.22 Å, 2.78 Å, 1.98 Å and 1.69 Å and the theoretical ones are 3.12 Å, 2.71 Å, 1.91 Å and 1.63 Å for respectively the (111), (200), (220) and (311) planes (peaks at 29°, 33°, 47° and 56°, *cf.* Figure 1 for (hkl) attribution). The error bar for SAED is therefore *ca.* 0.1 Å. To facilitate the cross-interpretation of the data from XRD and electron diffraction, we reported together the distances obtained by electron diffraction and the distances estimated using XRD peaks (Table 2). For fresh $\text{Ce}(\text{OH})_3$, all diffraction rings could reasonably be attributed to a diffraction peak in XRD (Table

2, left and Figure 6A,C): we noted that all the measured distances by electron diffraction are slightly larger than the expected ones, as for the aforementioned CeO_2 sample. However, we could not detect any ring that would correspond to the XRD peak at 42.6° , probably due to its low intensity. The selection rules for diffraction are different for X-rays and electrons and this may explain why intense peaks in XRD such as the one at 39.8° have a much lower relative intensity in electron diffraction (ring (5)). The sample of aged $\text{Ce}(\text{OH})_3$ contained traces of CeO_2 : we attributed three rings at 3.12 \AA , 1.97 \AA and 1.70 \AA , slightly larger than the other ones, to this last phase (Table 2, right and Figure 6B,D). All the other rings could reasonably be attributed to XRD diffraction peaks and we suggest the rings 1, 2, 4, 5, 6 and 7 in fresh $\text{Ce}(\text{OH})_3$ became respectively the rings 1', 2', 4', 5', {6', 6'', 6'''} and 7' in aged $\text{Ce}(\text{OH})_3$.

Fresh $\text{Ce}(\text{OH})_3$					Aged $\text{Ce}(\text{OH})_3$			
	Electron diffraction	X – ray diffraction		(hkl)		Electron diffraction	X – ray diffraction	
		2θ	Distance				2θ	Distance
1	5.65 \AA	15.7°	5.62 \AA	(100)	1'	5.51 \AA	16.6°	5.36 \AA
2	3.21 \AA (I)	$27.4 - 28.3^\circ$	$3.24 \text{ \AA} - 3.15 \text{ \AA}$	(110) – (101)	2'	3.22 \AA (I)	$28.6 - 29.7^\circ$	3.12 \AA
3	2.82 \AA	31.8°	2.81 \AA	(200)				
4	2.52 \AA	36.4°	2.47 \AA	(111)	4'	2.45 \AA	38.7°	2.33 \AA
5	2.31 \AA	39.8°	2.26 \AA	(201)	5'	2.20 \AA	42.0°	2.15 \AA
	-	42.6°	2.12 \AA	(210)		-	44.0°	2.05 \AA
6	1.94 \AA (I)	$47.7 - 50.6^\circ$	$1.90 \text{ \AA} - 1.80 \text{ \AA}$	(002) – (300) – (211)	6'	1.88 \AA (I)	50.3°	1.81 \AA
					6''	1.84 \AA	51.3°	1.78 \AA
					6'''	1.79 \AA	53.3°	1.72 \AA
7	1.68 \AA	$55.9 - 56.7^\circ$	$1.64 \text{ \AA} - 1.62 \text{ \AA}$	(112) – (220)	7'	1.62 \AA	59.1°	1.56 \AA

Table 2. Diffraction distances obtained by electron diffraction (I denotes the strongest rings) and the estimated corresponding peak in PXRD (angle and distance) for a fresh $\text{Ce}(\text{OH})_3$ sample and an aged one.

Infrared spectroscopy. Attenuated Total Reflectance-Fourier Transform InfraRed (ATR-FTIR) analysis was performed on fresh and aged $\text{Ce}(\text{OH})_3$ (Figure 8A). In fresh $\text{Ce}(\text{OH})_3$, an O–H stretching band of the hydroxide is detected at 3606 cm^{-1} (Figure 8B). This band splits in two at 3597 cm^{-1} and 3586 cm^{-1} and loses intensity upon aging. The splitting may be the mark of a loss of symmetry in the crystal structure or of the presence of different sites. Another Ce–OH stretching band, specific of the hydroxide, is present at 650 cm^{-1} (Figure 8C).¹⁸ The band is shifted and splits in two

at 741 cm^{-1} and 713 cm^{-1} upon aging. As no IR spectrum could be found in literature for $\text{Ce}(\text{OH})_3$, this attribution was done on the basis of that of $\text{La}(\text{OH})_3$ IR spectrum, expected to be very similar: bands at 3610 cm^{-1} , 645 cm^{-1} and 510 cm^{-1} were respectively attributed to O–H, La–OH and La–O vibrations.¹⁹ The broad band at 3350 cm^{-1} and the thin one at 1640 cm^{-1} are attributed to respectively O–H stretching and O–H scissor bending of adsorbed water molecules. We suggest the bands between 1600 cm^{-1} and 1300 cm^{-1} are attributed to C=O stretching and those at 1097 cm^{-1} and 1047 cm^{-1} , on fresh $\text{Ce}(\text{OH})_3$, to C–O stretching of surface carbonate CO_3^{2-} species as carbon dioxide from atmosphere is known for being easily adsorbed on metal oxides and hydroxides.^{20,21} We could not attribute the intense and broad band at 1000 cm^{-1} observed in both samples and whose origin is still under investigation. We excluded the nitrate ions at the surface of ceria as more intense peaks would have also be observed at *ca.* 1200 cm^{-1} and 1500 cm^{-1} .²² The presence of sharp peaks in the characteristic hydroxide region confirms that bulk hydroxyl groups are still present in aged $\text{Ce}(\text{OH})_3$ and not only surface hydroxyls.

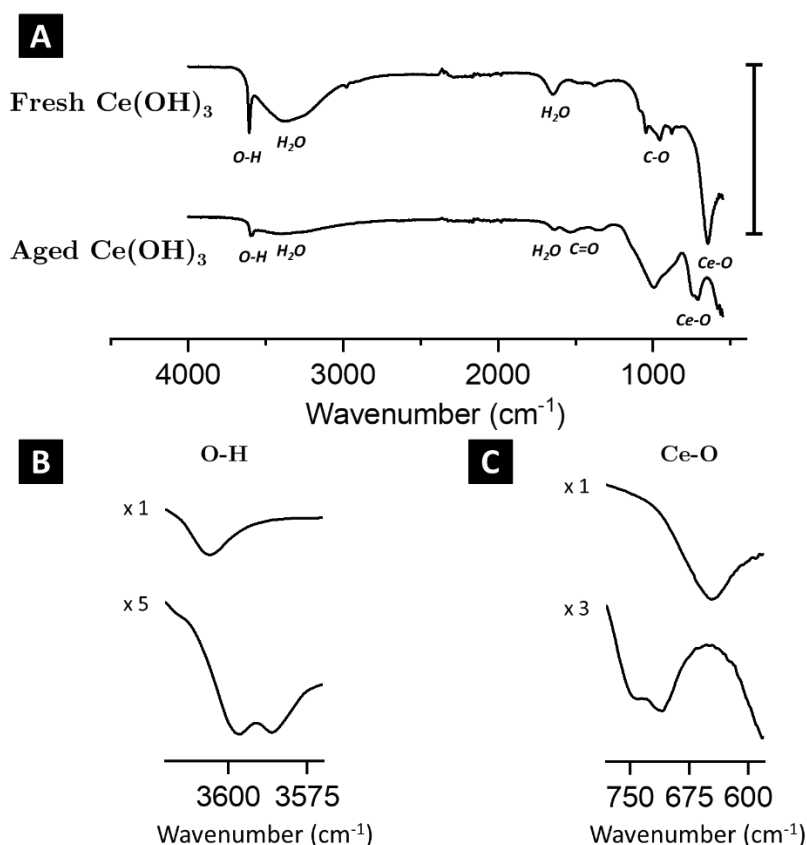


Figure 8. (A) ATR-FTIR spectra of fresh and aged $\text{Ce}(\text{OH})_3$. Zooms on the (B) O–H and (C) Ce–O regions (top: fresh $\text{Ce}(\text{OH})_3$, bottom: aged $\text{Ce}(\text{OH})_3$). The vertical bar denotes a 50 % absorption.

X-Ray Photoelectron Spectroscopy. The oxidation state of surface cerium and oxygen atoms in fresh $\text{Ce}(\text{OH})_3$, aged $\text{Ce}(\text{OH})_3$ and CeO_2 nanorods were studied by means of XPS and results are displayed on Figure 9. $\text{Ce}(\text{NO}_3)_3 \cdot 6\text{H}_2\text{O}$ was used as a $\text{Ce}^{(\text{III})}$ reference as this salt is stable under air and commercial CeO_2 was used as a cerium dioxide reference. The peak fitting procedure is developed in the experimental section and was based on already published works.^{10,23–27} The Ce 3d high-resolution X-ray photoelectron spectra are typically composed of five doublets, two characteristic of $\text{Ce}^{(\text{III})}$ (in pink and violet) and three of $\text{Ce}^{(\text{IV})}$ species (in yellow, orange and red). The multiple peaks arise from the different occupancies of the Ce 4f level in the final state. For $\text{Ce}^{(\text{IV})}$, the peaks V''' and U''' (orange component) result from the $\text{Ce } 3\text{d}^9 \text{O } 2\text{p}^6 \text{Ce } 4\text{f}^0$ final state, the peaks U, V, U'' and V'' (red and yellow components) from a mixture of the $\text{Ce } 3\text{d}^9 \text{O } 2\text{p}^5 \text{Ce } 4\text{f}^1$ and $\text{Ce } 3\text{d}^9 \text{O } 2\text{p}^4 \text{Ce } 4\text{f}^2$ final states. For $\text{Ce}^{(\text{III})}$, the four peaks U_0 , V_0 , U' and V' (pink and violet components) result from a mixture of the $\text{Ce } 3\text{d}^9 \text{O } 2\text{p}^6 \text{Ce } 4\text{f}^1$ and $\text{Ce } 3\text{d}^9 \text{O } 2\text{p}^5 \text{Ce } 4\text{f}^2$ final states. We chose a linear background even though the Shirley algorithm is usually chosen for heavy atoms because the Shirley background is not well defined on zones with multiple peaks with no absolute maxima, which is our case. The spin-orbit coupling values for the five doublets were estimated on the reference spectra and were in agreement with literature: 18.35 eV for $\text{Ce}^{(\text{III})}$ components and 18.5 eV for $\text{Ce}^{(\text{IV})}$ ones. The peak positions were constrained on a range of approximately 0.8 eV around the expected position. The integration of the peak areas allows an estimation of the $\text{Ce}^{(\text{III})}$ and $\text{Ce}^{(\text{IV})}$ fractions, the error bar for this procedure being estimated at *ca.* 10 %.¹⁰

According to our fit, cerium nitrate salt $\text{Ce}(\text{NO}_3)_3 \cdot 6\text{H}_2\text{O}$ is composed of 91 % $\text{Ce}^{(\text{III})}$ which is compatible with a fully reduced state if we consider an error bar of *ca.* 10 %. Fresh $\text{Ce}(\text{OH})_3$ is composed of 77 % of $\text{Ce}^{(\text{III})}$, whereas aged $\text{Ce}(\text{OH})_3$ and CeO_2 nanorods display a lower $\text{Ce}^{(\text{III})}$ fraction (respectively 28 % and 26 %), similar to commercial CeO_2 (29 %). The surface $\text{Ce}^{(\text{IV})}$ species in the fresh $\text{Ce}(\text{OH})_3$ are either inherent of the synthesis or correspond to a slow surface oxidation during the washing steps of the material or during the sample preparation for XPS. The difference with aged $\text{Ce}(\text{OH})_3$ is however large enough to conclude that aging in air is the dominant process leading to $\text{Ce}^{(\text{IV})}$.

As largely developed in the literature, cerium dioxide presents both $\text{Ce}^{(\text{III})}$ and $\text{Ce}^{(\text{IV})}$ atoms at the surface, with a $\text{Ce}^{(\text{III})}$ fraction typically up to 30 %. This $\text{Ce}^{(\text{III})}$ is however mostly present at the surface: by changing the incident angle of the beam in XPS, Freund *et al.* proved the cerium oxide they studied comported 17 % of $\text{Ce}^{(\text{III})}$ within the topmost 1.7 nm but only 6 % within the topmost 3.5 nm.¹⁰

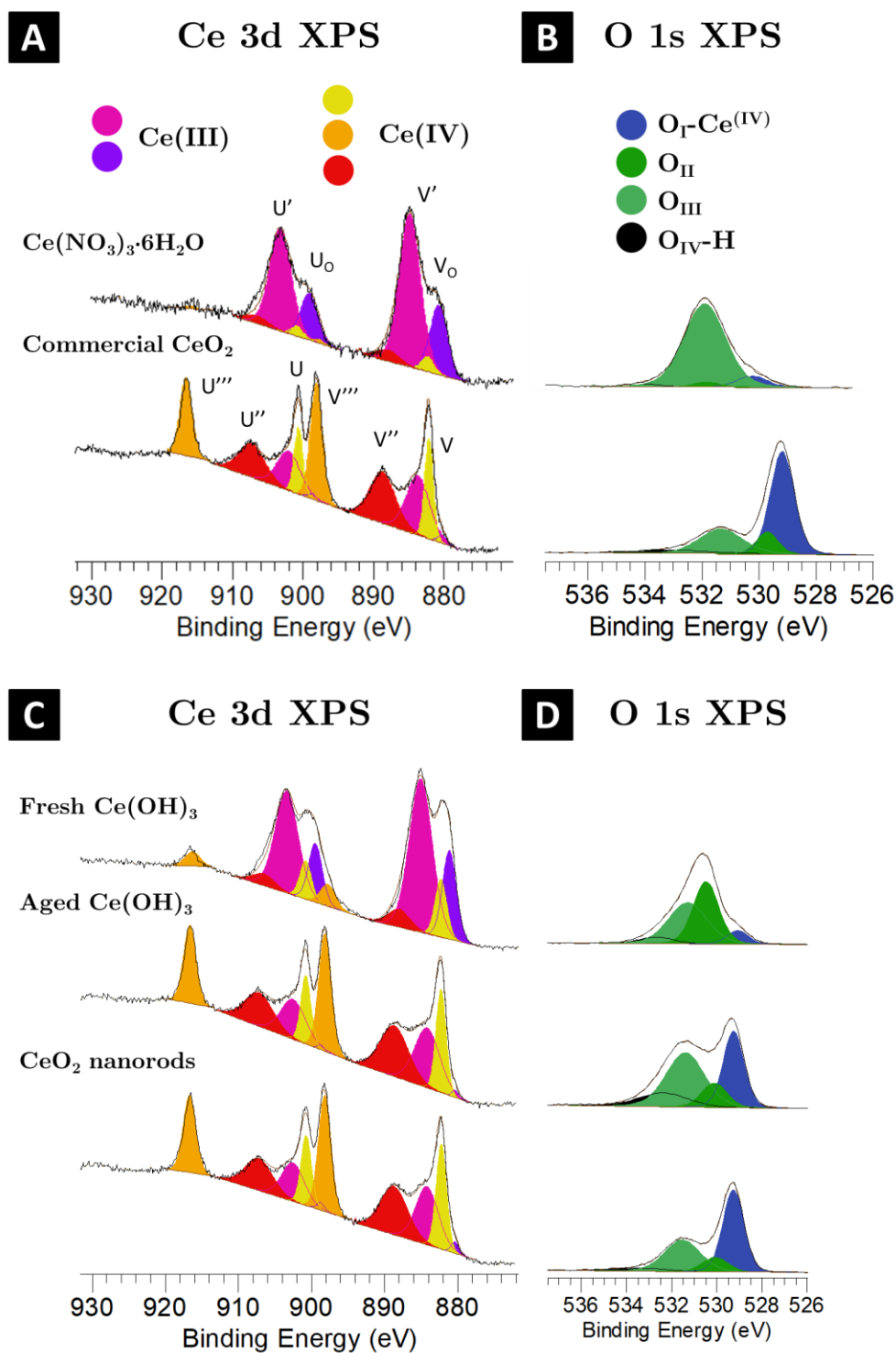


Figure 9. XPS spectra: (A) Ce 3d region and (B) O 1s region of $\text{Ce}(\text{NO}_3)_3 \cdot 6\text{H}_2\text{O}$ and commercial cerium oxide with deconvolution of Ce(III) and Ce(IV) peaks and of different oxygen peaks. (C) Ce 3d region and (D) O 1s region of fresh $\text{Ce}(\text{OH})_3$, aged $\text{Ce}(\text{OH})_3$ (Synthesis IV.2.) and CeO_2 nanorods (Synthesis IV.1.)

XPS spectra of O 1s core level are displayed in Figure 9B and D for all samples. The oxygen signal for cerium nitrate essentially originates from water molecules and nitrate ions. The oxygen spectra of the other samples can be deconvoluted in four components: a blue component denoted O_I at a binding energy of *ca.* 529.2 eV, attributed to lattice oxygens linked to $Ce^{(IV)}$ atoms, two green components, denoted O_{II} and O_{III} , at *ca.* 530.1 eV and 531.4 eV and a broad black component O_{IV} , merely not visible in these spectra, at *ca.* 532.5 eV, generally ascribed to surface hydroxyl OH or adsorbed water H_2O . The deconvolution with only three components (O_I , O_{II} and O_{IV}) which may be found in different works gave here a fit of low quality.¹⁰ There is consensus in literature on the attribution of O_I to lattice oxygens linked to oxidized cerium atoms. There is however no consensus on the attribution of O_{II} and O_{III} . Among the different possibilities, they are either associated to oxygens linked to $Ce^{(III)}$ atoms or to “adsorbed” oxygens, *i.e.* surface hydroxyls or carbonates.²⁸ The energy split of 2.2 eV between O_I and O_{III} is in line with literature: Palmqvist *et al.* reported an energy split of 1.9 eV between the contributions of what they reported as O- $Ce^{(III)}$ and O- $Ce^{(IV)}$ while Pfau *et al.* reported 2.4 eV.^{29,30} During the reduction of CeO_2 films, Reichling *et al.* modelled the O 1s with four peaks just as us and attributed the two ones of medium energies (O_{II} and O_{III}) to oxygens linked to $Ce^{(III)}$.²⁶ In this context, the presence of $Ce^{(III)}$ was explained by surface defects consisting in oxygen vacancies. Considering the difficulty in ascribing accurately chemical species to components O_{II} and O_{III} , our analysis below only relies on the area evolution of the O_I component associated to O- $Ce^{(IV)}$ and is qualitative.

Similar spectra are obtained for commercial CeO_2 and CeO_2 nanorods from Synthesis IV.1. with a relatively important and sharp O_I peak, in agreement with the Ce 3d spectra (high ratio of $Ce^{(IV)}$). Aged $Ce(OH)_3$ also displays a non negligible O_I peak but a much higher contribution of O_{III} , probably accounting for a more defective structure. As to fresh $Ce(OH)_3$, the main contribution is clearly O_{III} and the O_I peak is small, thereby denoting the limited number of $Ce^{(IV)}$ atoms.

X-ray Absorption Spectroscopy (XAS). XAS spectroscopy at the Ce L_{III} -edge was used to characterize the oxidation degree of the cerium atoms in the core of the material and not only on surface. The experiments were performed by Benedikt Lassalle-Kaiser, beamline scientist on the LUCIA beamline at the SOLEIL synchrotron. Details on the protocols are given in Appendix I (ES.9). Figure 10 displays the XAS spectra of pellets of commercial $Ce(NO_3)_3 \cdot 6H_2O$, commercial CeO_2 , CeO_2 from Synthesis IV.1. and aged $Ce(OH)_3$ from Synthesis IV.2. The positions of the edges indicate aged $Ce(OH)_3$ (5725.8 eV) possesses an average oxidation degree for Ce identical to that of commercial CeO_2 (5725 eV) and CeO_2 from Synthesis IV.1. (5725.4 eV), *i.e.* mostly $Ce^{(IV)}$. Cerium nitrate, an air-stable $Ce^{(III)}$ salt, has an edge-shift situated at lower energy (5723.3 eV), in coherence with a more reduced state.

Although the XRD patterns of CeO_2 from Synthesis IV.1. and aged $\text{Ce}(\text{OH})_3$ are different (Figure 1 and Figure 6B), their XAS spectra are very similar.

Schuman *et al.* reported a complete Ce L_{III} -edge investigation of cerium oxides.³¹ They decomposed the signal in four peaks (Figure 10, inset): two main ones, A and B, at high energies assigned to a mixture of final configurations $4f^05d^1$ and $4f^15d^1$, a low energy shoulder C originating from the splitting of the $5d$ orbitals in the cubic crystal field of O^{2-} and a pre-edge peak D resulting from a forbidden $2p_{3/2} \rightarrow 4f$ transition. They assigned the signal at 5723 eV to $\text{Ce}^{(\text{III})}$ atoms and that at 5725 eV to $\text{Ce}^{(\text{IV})}$ atoms. The doublet feature at 5741.5 eV in commercial CeO_2 sample spectrum could not be explained and was not present in the spectra displayed by Schuman *et al.* Otherwise, our spectra are coherent with their data. We interpreted the similarity between CeO_2 and aged $\text{Ce}(\text{OH})_3$ spectra as similar environment and oxidation degree for Ce in these materials and concluded the aging of $\text{Ce}(\text{OH})_3$ in air leads to its total oxidation.

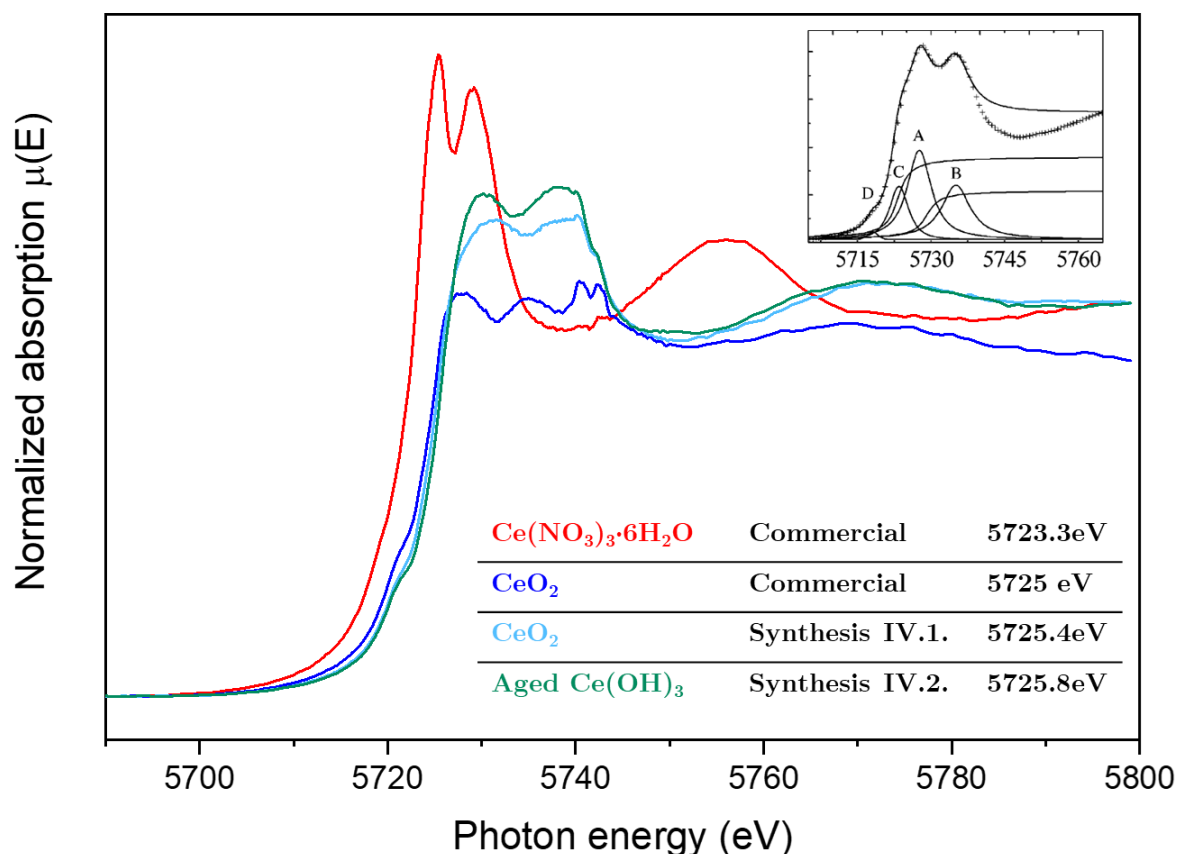


Figure 10. Ce L_{III} -edge XAS spectra at 5725 eV of commercial $\text{Ce}(\text{NO}_3)_3 \cdot 6\text{H}_2\text{O}$, commercial CeO_2 , CeO_2 from Synthesis IV.1. and aged $\text{Ce}(\text{OH})_3$ from Synthesis IV.2., measured as pellets in graphite. Edge values are indicated for each. Inset is a reproduction of a typical spectrum of CeO_2 from reference [31].

IV.2.2 Structural comparison with lanthanide hydroxides

The XRD patterns obtained with fresh and aged $\text{Ce}(\text{OH})_3$ were compared with the ones of other lanthanide hydroxides $\text{Ln}(\text{OH})_3$, studied by Milligan *et al.* in the 1970s.³²⁻³⁵ Lanthanide hydroxides are generally synthesized under similar conditions than the ones described in Synthesis IV.2. of $\text{Ce}(\text{OH})_3$, *i.e.* by addition of a base (NaOH , NH_4OH or KOH) in an aqueous solution of $\text{Ln}(\text{NO}_3)_3$. When heated, these hydroxides usually form the metal oxyhydroxide LnOOH at *ca.* 300-350 °C and then the metal sesquioxide Ln_2O_3 at *ca.* 450-500 °C.³⁶ Cerium is an exception as there is no mention of a metal oxyhydroxide CeOOH and as the most stable oxide is CeO_2 and not Ce_2O_3 . The exception of cerium may be explained by the high stability of $\text{Ce}^{(\text{IV})}$ in comparison with other $\text{Ln}^{(\text{IV})}$ and the capacity of CeO_2 to accommodate a large number of oxygen deficiencies. To the exception of cubic $\text{Lu}(\text{OH})_3$, all $\text{Ln}(\text{OH})_3$ crystallize in a hexagonal structure ($\text{P6}_3/\text{m}$, space group N°176) where the lanthanide cation $\text{Ln}^{(\text{III})}$ is at the center of a triaugmented trigonal prism whose 9 vertexes are occupied by oxygen atoms. The triaugmented trigonal prism is one of the two typical AX_9 VSEPR structures: it consists in a trigonal prism composed of two equilateral triangles and three equatorial faces onto which were attached rectangular base pyramids (Figure 11A). There are therefore 6 equivalent positions P_A corresponding to the vertexes of the initial trigonal prism (apical position) and 3 equivalent ones P_B corresponding to the tops of the three pyramids (equatorial position). In this crystallographic structure, the c-axis of the 6_3 -screw rotation is the generatrix of the trigonal prism and the mirror m is the plane containing the central cation and the three positions P_B .

CeO_2 adopts a different structure, the fluorite face-centered one, in which the cerium cations are linked to 8 oxygens O^{2-} forming the corners of a cube. The oxygens are in tetrahedral environment. All Ce–O bonds are equivalent.

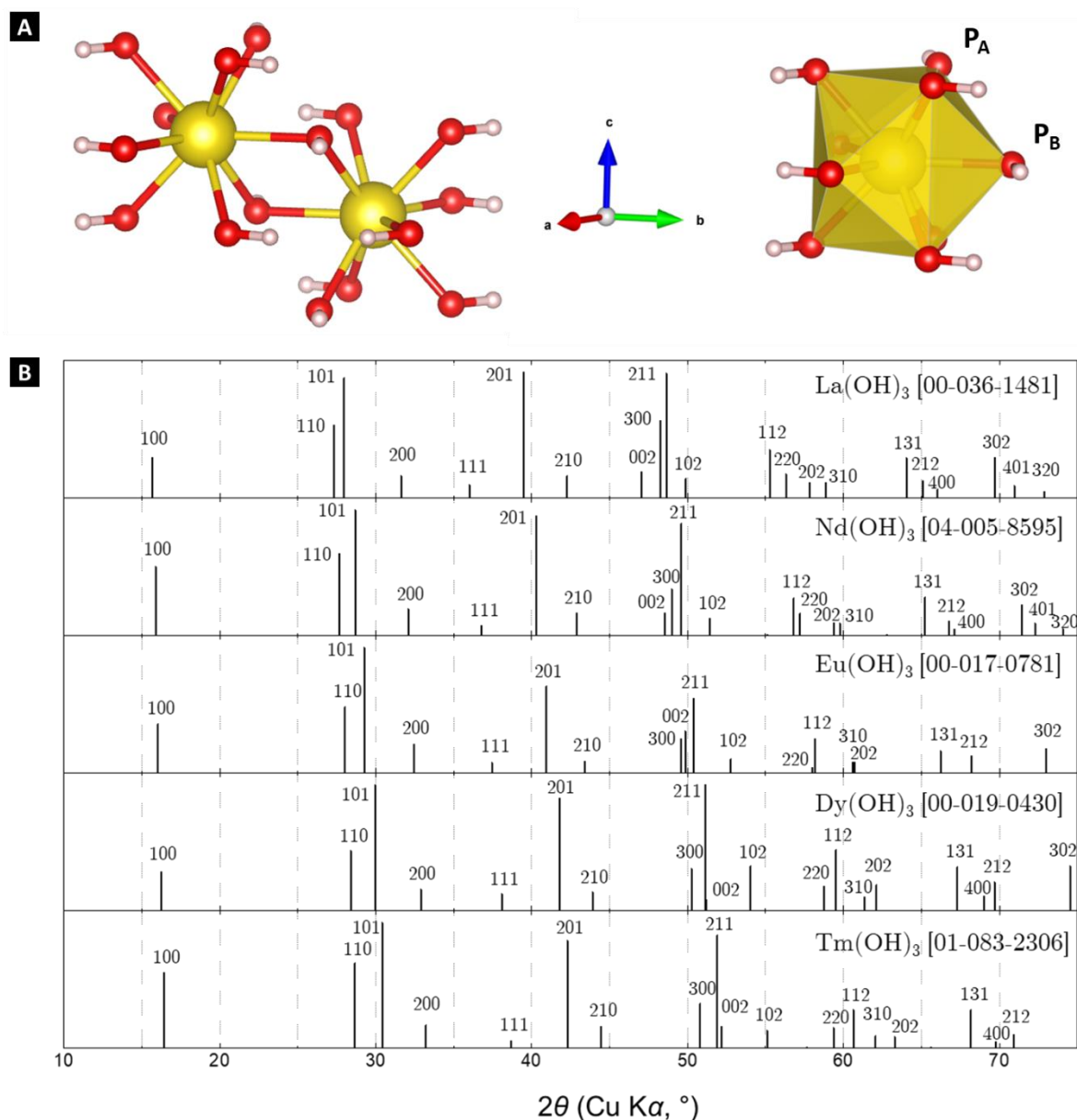


Figure 11. (A) Local environment of Ln atoms in lanthanide trihydroxides (yellow = Ln, red = O, white = H). Yellow polyhedron delineates the triaugmented trigonal prism. Positions P_A and P_B are respectively the apical and the equatorial positions. Pictures created with VESTA.³⁷ (B) XRD patterns of Ln(OH)_3 with hkl attributions, from top to bottom: La(OH)_3 , Nd(OH)_3 , Eu(OH)_3 , Dy(OH)_3 and Tm(OH)_3 .

We reported in Table 3 the distances $\text{M-O}_{\text{apical}}$ and $\text{M-O}_{\text{equatorial}}$ as well as their ratio for all the lanthanide trihydroxides. We notice a decrease of both $\text{M-O}_{\text{apical}}$ and $\text{M-O}_{\text{equatorial}}$ from respectively 2.588 Å and 2.551 Å for La to 2.371 Å and 2.430 Å for Yb. The distance ratio $d(\text{M-O}_{\text{apical}})/d(\text{M-O}_{\text{equatorial}})$ also decreased from 1.014 to 0.976. Through the lanthanide series, there are therefore both a contraction of the distances (of 8.4% for $\text{M-O}_{\text{apical}}$ and 4.8% for $\text{M-O}_{\text{equatorial}}$) and a deformation of the structure (distance ratio from 1.014 to 0.976). As to XRD, this structural evolution results in a

shift of the peaks toward the high angles (contraction of the crystal lattice) but not of the same amount for all peaks. Consequently, the global aspect of the diffractogram changes from La to Yb with peaks which swap their respective positions (Figure 11B). This is notably the case for $\{(002), (300), (211)\}$ diffraction peaks *ca.* 50° and $\{(112), (220), (202), (310)\}$ diffraction peaks *ca.* 62° . This evolution is related to the “lanthanide contraction” *i.e.* the ionic radius of Ln^{3+} which decreases from 121.6 ppm for La^{3+} to 104.2 ppm for Yb^{3+} when in the coordination IX (Table 3).

Structure	M–O bond length (Å)		Distance ratio	Ionic radius of Ln^{3+} (pm)
	O in P_A (apical)	O in P_B (equatorial)		
$\text{La}(\text{OH})_3$	2.588	2.551	1.014	121.6
$\text{Ce}(\text{OH})_3$	2.567	2.529	1.015	119.6
$\text{Pr}(\text{OH})_3$	2.538	2.516	1.009	117.9
$\text{Nd}(\text{OH})_3$	2.522	2.492	1.012	116.3
$\text{Sm}(\text{OH})_3$	2.487	2.478	1.004	113.2
$\text{Eu}(\text{OH})_3$	2.473	2.466	1.003	112
$\text{Gd}(\text{OH})_3$	2.462	2.465	0.999	110.7
$\text{Tb}(\text{OH})_3$	2.444	2.458	0.994	109.5
$\text{Dy}(\text{OH})_3$	2.429	2.452	0.991	108.3
$\text{Ho}(\text{OH})_3$	2.416	2.444	0.989	107.2
$\text{Er}(\text{OH})_3$	2.403	2.439	0.985	106.2
$\text{Tm}(\text{OH})_3$	2.396	2.429	0.986	105.2
$\text{Yb}(\text{OH})_3$	2.371	2.430	0.976	104.2

Table 3. Crystallographic characteristics of some lanthanide trihydroxides: M–O distances for oxygen in apical and equatorial positions and their ratio $d(\text{M}-\text{O}_{\text{apical}})/d(\text{M}-\text{O}_{\text{equatorial}})$. Data are reproduced from references.^{32–35} Ionic radii are those given by Shannon for coordination IX.³⁸

The final state of $\text{Ce}(\text{OH})_3$ exposed to air matches relatively well with hexagonal $\text{Ln}(\text{OH})_3$ for metals of the end of the lanthanide series such as $\text{Tm}(\text{OH})_3$ (Figure 6B). Our intermediate conclusion is therefore that $\text{Ce}(\text{OH})_3$ evolves in a structurally close structure with an ionic radius of the lanthanide of *ca.* 105.2 pm, to be compared to 119.6 pm for $\text{Ce}^{(\text{III})}$. A natural reasoning would be that the central ion is $\text{Ce}^{(\text{IV})}$, resulting from the oxidation of $\text{Ce}^{(\text{III})}$ in air, in agreement with the XPS and XAS data and with literature.¹¹ No ionic radius is reported for $\text{Ce}^{(\text{IV})}$ in coordination IX but values for coordination VIII and X are respectively 97 and 107 pm which would be coherent with the expected value of 105.2 pm.³⁸

IV.2.3 Phase proposal

If the $\text{Ce}^{\text{(III)}}$ atoms of fresh $\text{Ce}(\text{OH})_3$ did actually oxidize in $\text{Ce}^{\text{(IV)}}$ upon aging while conserving a similar crystallographic structure ($\text{P6}_3/\text{m}$, coordination IX), the charge neutrality would not be respected in “ $\text{Ce}^{\text{(IV)}}(\text{OH})_3^+$ ”. Indeed, cerium presents this particularity that the only crystalline reported hydroxide is not at the same degree of oxidation that the cerium atoms in the most common oxide, CeO_2 . In order to respect the charge neutrality of the material, rearrangements have to operate, they can consist in:

- (1) Defects of $\text{Ce}^{\text{(IV)}}$ atoms,
- (2) Abstraction of H^+ from the hydroxide,
- (3) Additional interstitial anions such as O^{2-} or HO^-

In case (1), $\text{Ce}_{0.75}(\text{OH})_3$, a lower occupancy state of the Ce positions would result in different peak intensities but not in different peak positions compared to a hypothetical hexagonal “ $\text{Ce}(\text{OH})_3^+$ ” phase. Case (2) would correspond to a cerium oxyhydroxide $\text{CeO}(\text{OH})_2$. Due to the small ionic radii difference between HO^- and O^{2-} (respectively 134 pm and 138 pm) and to the low contribution of H in the XRD diffraction, moderate variations are expected from a hypothetical “ $\text{Ce}(\text{OH})_3^+$ ” phase. Finally, case (3) would formally correspond to $\text{Ce}(\text{OH})_4$ or $\text{CeO}_{0.5}(\text{OH})_3$ with potentially larger structural modifications. Considering the phase modification occurs even in presence of negligible water quantities, which would be the source of HO^- , we favor the hypotheses (2) and (3) which only necessitate O_2 .

Three distinct relevant materials “oxide/hydroxide of cerium” are reported in the scientific community:

- (1) Cerium(III) trihydroxide, $\text{Ce}(\text{OH})_3$, [N° CAS 15785-09-8], an air sensitive grey solid.
- (2) Cerium(IV) dioxide (also termed ceric oxide or ceria), CeO_2 , [N° CAS 1306-38-3], a light yellow solid.
- (3) Cerium(IV) tetrahydroxide (also termed hydrous cerium oxide), $\text{Ce}(\text{OH})_4$, [N° CAS 12014-56-1], a bright yellow solid.

The name of this last material (3) presents ambiguities as researchers and manufacturers mention it either as a hydroxide $\text{Ce}(\text{OH})_4$ or as a hydrous cerium oxide $\text{CeO}_2 \cdot 2\text{H}_2\text{O}$, of same elemental composition. A work led by Balasubramanian *et al.* showed that this material has a local structure comparable with CeO_2 (similar XRD patterns and EXAFS oscillations at the Ce L_{III}-edge) but is disordered at long ranges, typically distances $> 4 \text{ \AA}$.³⁹ This disorder results in an XRD pattern close to CeO_2 but with broader peaks. As there is no sharp OH signal in Raman spectroscopy, typical of true hydroxides,⁴⁰ the authors suggested the term cerium tetrahydroxide $\text{Ce}(\text{OH})_4$ is not adequate, and proposed “disordered hydrous cerium oxide” whose formula would

be $\text{CeO}_2 \cdot 2\text{H}_2\text{O}$. Hydrous metal oxides correspond to poorly crystalline or amorphous materials containing hydration water molecules and whose elemental composition is not precisely known: they are generally formed by sol-gel chemistry and may be calcined to form crystalline metal oxides. There is no entry in the JCPDS X-ray diffraction database for $\text{Ce}(\text{OH})_4$ and most of the literature works mentioning this phase do not report any XRD measurements or structural characterization: either the authors indicate the material was used as received or it originated from the oxidation of $\text{Ce}(\text{OH})_3$ in air.^{2,5,11,41} The only occurrences of X-ray diffractograms of $\text{Ce}(\text{OH})_4$ correspond to broad CeO_2 and the material we bought from Strem Chemicals displayed this feature too (XRD in Figure 12C).^{39,42–44} As no crystalline structure exists for $\text{Ce}(\text{OH})_4/\text{CeO}_2 \cdot 2\text{H}_2\text{O}$ other than that of CeO_2 , we will prefer the writing $\text{CeO}_2 \cdot x\text{H}_2\text{O}$ (with x close to 2) rather than $\text{Ce}(\text{OH})_4$.^{45,46} Furthermore, the elemental composition cannot be formally established and the writing $\text{CeO}_2 \cdot x\text{H}_2\text{O}$ gives flexibility as to the hydration water molecule number, contrarily to $\text{Ce}(\text{OH})_4$.

The material we synthesized is clearly different from what is termed cerium tetrahydroxide $\text{Ce}(\text{OH})_4$, in the literature, based on the XRD pattern. The modifications of the XRD and of the IR spectra between fresh and aged $\text{Ce}(\text{OH})_3$ attest of atoms movements in the crystal structure. We could not decide whether the material we termed “aged $\text{Ce}(\text{OH})_3$ ” is a non-reported cerium oxide/hydroxide phase or a metastable state along the transformation of $\text{Ce}(\text{OH})_3$ in $\text{CeO}_2 \cdot x\text{H}_2\text{O}$. To elucidate its crystallographic structure, a Rietveld refinement on the diffractograms of the fresh and aged samples is ongoing.

We already stressed that, to the best of our knowledge, all articles mentioning the synthesis and the aging of $\text{Ce}(\text{OH})_3$ report a CeO_2 or $\text{CeO}_2 \cdot 2\text{H}_2\text{O}$ final phase with a fluorite-like structure. For instance, Golberg *et al.* synthesized $\text{Ce}(\text{OH})_3$ nanotubes by hydrothermal treatment of CeCl_3 with a 12 M NaOH solution in an autoclave between 100 °C and 150 °C.⁵ The obtained tubes, of several hundreds of nanometers in length were exposed to air for several days under ambient conditions and, to the contrary of our results, the $\text{Ce}(\text{OH})_3$ phase directly evolved toward a cubic phase CeO_2 with broad peaks. The authors attributed the broadness of the peaks to a certain level of disorder associated with the presence of water molecules and called their material “ $\text{CeO}_2 \cdot 2\text{H}_2\text{O}$ ”, in agreement with Balasubramanian’s work. The material, initially purple, gradually turned yellow. The spontaneous oxidation of $\text{Ce}(\text{OH})_3$ in CeO_2 in air led to broken and irregular particles. So far, we could not find explanation on why the $\text{Ce}(\text{OH})_3$ phase we produced evolved in a different way than in Golberg’s work but this result is reproducible and is similar to Qu’s work.

IV.3. Post-synthesis treatments

IV.3.1 Hydrothermal dehydration

As the targeted non porous CeO_2 precursor was successfully synthesized, we applied the second step described by Qu *et al.* as a hydrothermal treatment of the powder in an autoclave at 160 °C.³

Thermal treatment IV.1. Hydrothermal dehydration. In a 25 mL Teflon autoclave, 80 mg of 7-days aged $\text{Ce}(\text{OH})_3$ powder obtained from Synthesis IV.2. were dispersed by sonication in 17 mL of deoxygenated water to yield a yellow suspension. The autoclave was closed under air and let to react in a preheated oven at 160 °C for 20 h. After reaction, the solution was let to cool down naturally to r.t. The solution was centrifugated under air (9,000 rpm, 10 min, 20 °C) and the powder was washed once with 30 mL of EtOH. The obtained powder was then dried on the bench under air.

The material obtained from Synthesis IV.2. followed by Thermal treatment IV.1. is an off-white powder and is isostructural with cerium dioxide CeO_2 according to XRD (Figure 12A), with a crystallite size close to 10 nm, in agreement with Qu's work.

IV.3.2 Dry calcination in inert and reductive atmosphere

Considering the off-white color of the CeO_2 catalyst after Thermal treatment IV.1., the surface $\text{Ce}^{(\text{III})}$ ratio is certainly low. We therefore also attempted at creating surface defects in the cerium oxide *via* another thermal treatment under stronger conditions. We applied a “dry” treatment, *i.e.* a calcination at high temperature (Thermal treatment IV.2.), to the different cerium-containing materials we synthesized (CeO_2 nanorods, fresh $\text{Ce}(\text{OH})_3$ and aged $\text{Ce}(\text{OH})_3$) and to commercial $\text{Ce}(\text{OH})_4$. Fresh $\text{Ce}(\text{OH})_3$ is understood as $\text{Ce}(\text{OH})_3$ from Synthesis IV.2. which has not been exposed to air and was stored in Ar while aged $\text{Ce}(\text{OH})_3$ is understood as $\text{Ce}(\text{OH})_3$ from Synthesis IV.2. which has been exposed at least 7 days to air and which does not present any signal of $\text{Ce}(\text{OH})_3$ in XRD.

Thermal treatment IV.2. Dry calcination under Ar or pure H_2 . In an Ar-filled glovebox, 100 mg of powder (CeO_2 from Synthesis IV.1. or fresh or 7-days aged $\text{Ce}(\text{OH})_3$ powder from Synthesis IV.2.) were introduced in a 25 mL glass autoclave. The Ar atmosphere was eventually changed for pure H_2 (7 bar) after two cycles vacuum/ H_2 . The autoclave was introduced in an oil bath which was then heated to 60 °C, 100 °C or 200 °C for 2 h. A pressure of 8 bar was attained at 200 °C. After reaction, the solution was let to cool down naturally to r.t. and the autoclave pressure was released in the glovebox.

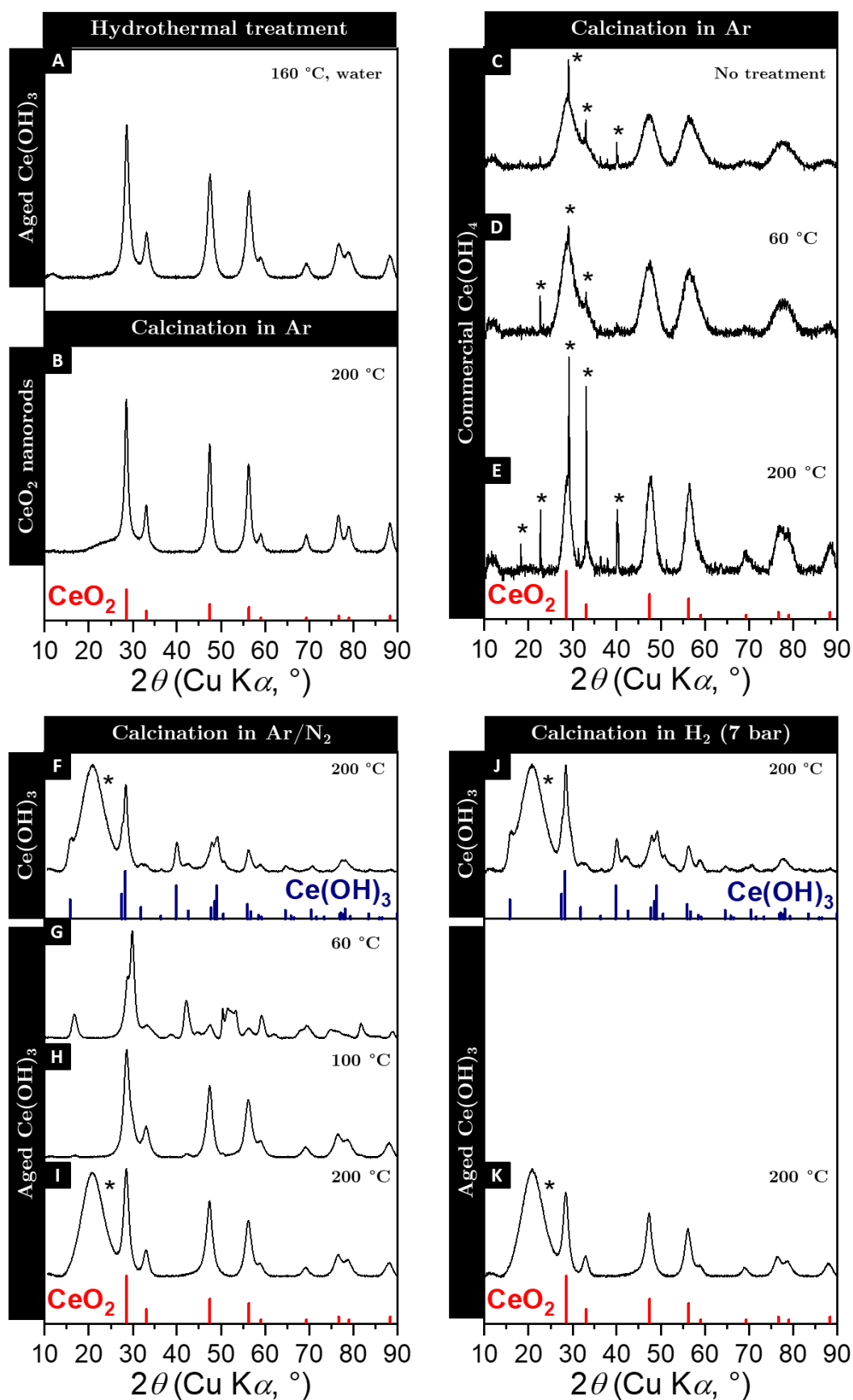


Figure 12. XRD patterns cerium oxide samples after treatments. (A) Cerium oxide from hydrothermal treatment IV.1. applied to aged $\text{Ce}(\text{OH})_3$. (B) Calcinated CeO₂ in Ar at 200 °C

(Thermal treatment IV.2.). (C) commercial $\text{Ce}(\text{OH})_4$ as received and after calcination under Ar (D) at 60 °C and (E) at 200 °C (asterisks denote impurities). (F) fresh $\text{Ce}(\text{OH})_3$ after calcination at 200 °C and (G-I) aged $\text{Ce}(\text{OH})_3$ after calcination at 60 °C, 100 °C and 200 °C under Ar (Thermal treatment IV.2.). (J) fresh $\text{Ce}(\text{OH})_3$ and (K) aged $\text{Ce}(\text{OH})_3$ after calcination at 200 °C under H_2 (asterisks indicate the signal due to the protective plastic dome).

Cerium oxide. The cerium dioxide powder from Synthesis IV.1, *i.e.* the CeO_2 nanorods, initially beige-yellow, was let to react in an autoclave during 2 h at 200 °C in inert (Ar) or reductive atmosphere (H_2 , 7 bar) according to Thermal treatment IV.2. The observations, X-ray diffractograms and IR spectra were similar whatever was the gas phase during the calcination (Ar or H_2). The CeO_2 powder first turned grey at *ca.* 150 °C and then violet after a few minutes at 200 °C. As long as the powder was kept under argon after the calcination, there was no change of color over weeks. It however instantaneously turned back to yellow when exposed to air, because of the reoxidation of surface cerium atoms. An XRD measurement of the powder right after its exposure to air was performed and no phase change was observed: the sample was composed of cubic CeO_2 with similar peak widths (Figure 12B). It is noteworthy that a treatment at only 100 °C for 2 h does not affect the color of the powder: the formation of oxygen vacancies and the reduction of $\text{Ce}^{(\text{IV})}$ in $\text{Ce}^{(\text{III})}$ is then expected to occur mainly above 100 °C. The same treatment applied to commercial cerium oxide CeO_2 , initially light grey, did not lead to any visual change.

Commercial $\text{Ce}(\text{OH})_4$. $\text{Ce}(\text{OH})_4$ from a commercial provider was calcinated under Ar at 60 °C and 200 °C to establish a comparison point with aged $\text{Ce}(\text{OH})_3$. According to XRD, the initial state corresponds to a broad CeO_2 pattern, in line with aforementioned literature,³⁹ with the presence of an unidentified species (Figure 12C-E). When calcinated at 60 °C, the CeO_2 was not modified whereas a calcination at 200 °C led to thinner peaks, associated to a larger crystallite size. We hypothesized the calcination at 200 °C dehydrated the material and consequently increased its crystallinity. We assumed the difference in intensity of the different impurity peaks in spectra C-E is not related to their growth during calcination but rather to the inhomogeneity of the commercial powder.

Fresh and aged $\text{Ce}(\text{OH})_3$. The same Thermal treatment IV.2. was applied to fresh and 7-days aged $\text{Ce}(\text{OH})_3$ from Synthesis IV.2. The experiments were run under inert gas (Ar for fresh $\text{Ce}(\text{OH})_3$ and N_2 for aged $\text{Ce}(\text{OH})_3$) and under 7 bar of H_2 with similar observations for both gases (Figure 12F-K). Fresh $\text{Ce}(\text{OH})_3$, initially grey, turned lilac whereas aged $\text{Ce}(\text{OH})_3$, initially yellow, turned off white. The four calcinated samples at 200 °C were analyzed by XRD with a sample holder equipped with an air-tight plastic dome. XRD measurements reveal that fresh $\text{Ce}(\text{OH})_3$ was not

structurally modified (Figure 12F,J) whereas aged $\text{Ce}(\text{OH})_3$ was transformed in cerium oxide (Figure 12I,K). The CeO_2 phase has small crystallite size *ca.* 10 nm in all cases according to Scherrer analysis. The formation of CeO_2 is not total at 100 °C, even though well advanced (Figure 12H). At a lower temperature of 60 °C, there is merely no transformation of the aged $\text{Ce}(\text{OH})_3$ in CeO_2 (Figure 12G). This difference of evolution between fresh and aged $\text{Ce}(\text{OH})_3$ is coherent with the aforementioned beam damage we observed: the heat produced by the electron beam was enough to trigger the CeO_2 formation. We concluded a calcination step of aged $\text{Ce}(\text{OH})_3$ produces a highly defective cerium oxide, suitable for catalysis.

Considering that most of the CeO_2 synthesis protocols in literature include a drying final step in an oven at 60 °C overnight, the material may be transformed before the diffractograms are recorded, explaining the lack of characterization of aged $\text{Ce}(\text{OH})_3$ in literature. Although $\text{Ce}(\text{OH})_3$ is known to form CeO_2 by calcination in air, no data could be found in the literature regarding the dehydration of $\text{Ce}(\text{OH})_3$ under an inert or reductive atmosphere at only 200 °C. The formation of CeO_2 from $\text{Ce}(\text{OH})_3$ in an ammonia atmosphere was nonetheless reported by Golberg *et al.* at 450 °C.⁵

Infrared spectroscopy. We previously showed that two sharp peaks at *ca.* 3600 cm^{-1} and 700 cm^{-1} are characteristic of a hydroxide material, respectively of the O–H and Ce–OH stretching vibrations. If a dehydration occurs, a modification of the peaks is expected. We therefore studied by ATR-FTIR the calcinated samples at 200 °C in Ar of fresh $\text{Ce}(\text{OH})_3$, aged $\text{Ce}(\text{OH})_3$ (both from Synthesis IV.2.) and CeO_2 (Synthesis IV.1.) (Figure 13). For fresh $\text{Ce}(\text{OH})_3$, the two hydroxide peaks in FTIR were not modified in position nor intensity after the calcination step, indicating the hydroxide is still present, in agreement with XRD. We noticed a decrease in intensity of the peaks linked to adsorbed water (broad bands at 3400 cm^{-1} and 1600 cm^{-1}), which was expected due to the high temperatures. On the contrary, for aged $\text{Ce}(\text{OH})_3$, the peaks at 3590 cm^{-1} and 730 cm^{-1} were not present any more after the calcination and a new peak appeared at 550 cm^{-1} , identical to the FTIR spectra of pristine and calcined CeO_2 nanorods. The unidentified band at 1000 cm^{-1} was preserved by the calcination for both fresh and aged $\text{Ce}(\text{OH})_3$. No particular modification of the spectrum of calcined CeO_2 was detected. FTIR measurements comfort the formation of CeO_2 from aged $\text{Ce}(\text{OH})_3$ and the disappearance of any hydroxide phase.

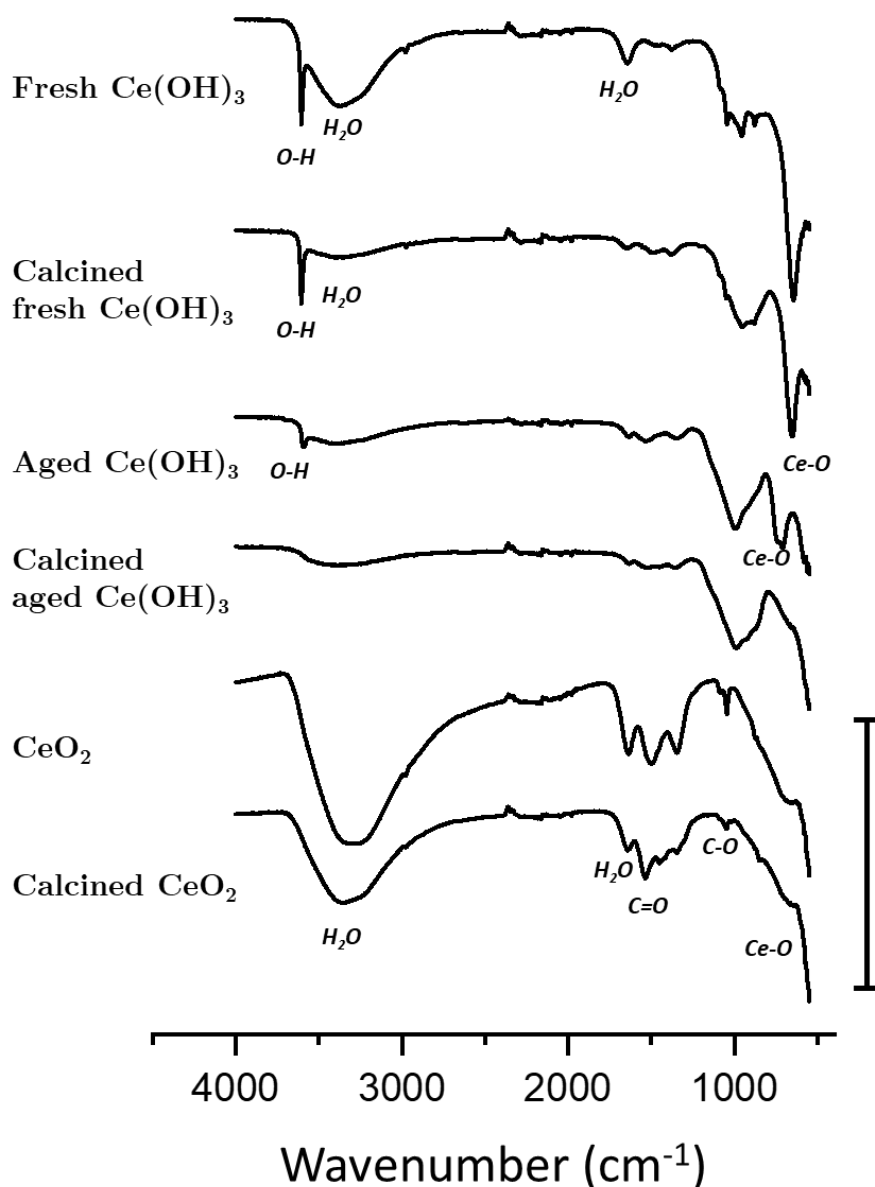


Figure 13. ATR-FTIR spectra of fresh $\text{Ce}(\text{OH})_3$, calcined fresh $\text{Ce}(\text{OH})_3$, aged $\text{Ce}(\text{OH})_3$, calcined aged $\text{Ce}(\text{OH})_3$, CeO_2 nanorods and calcined CeO_2 nanorods (the vertical bar indicates 50 % absorption).

IV.3.3 NAP-XPS: *in situ* measurements of thermal annealing

Considering the difference in the products and the striking color changes occurring during the dry thermal treatments, we chose to study the evolution of the oxidation state of Ce and O at the surface of the cerium oxide nanorods and of the cerium hydroxide $\text{Ce}(\text{OH})_3$ by Near-Ambient Pressure X-Ray Photoelectron Spectroscopy (NAP-XPS). The experiments were performed on the TEMPO B beamline at the SOLEIL synchrotron. The protocol is described in the Appendix I ES.8. There is technically no gas pressure in the experiments commented in Section

IV.3.3. but we retained the term of NAP-XPS experiments for two reasons: first, the samples were subjected to thermal treatments (calcination at 500 °C) that generate a background pressure of gas, usually delicate to achieve in laboratory instruments, and then the samples at the end of the experiments described in Figure 14 were directly used for actual NAP-XPS experiments which will be the object of section IV.4.1. The setup allows the *in situ* study of the calcination step *in vacuo* and then the impact of the exposition of the reduced material to a few mbar of H₂. The sample preparation for NAP-XPS requires a deposition of the powder by drop casting from a suspension in ethanol on a gold-coated silicon wafer, to the contrary of the lab XPS measurements where the powders are pressed as pellets: we therefore indicated the fresh Ce(OH)₃ from Synthesis IV.2. as “air-exposed”. The powder was already yellow by the time it was introduced in the inert measurement chamber of the NAP-XPS. The two samples, air exposed Ce(OH)₃ from Synthesis IV.2. and CeO₂ nanorods from Synthesis IV.1., were disposed on the same sample holder and were subjected to the same conditions: the thermal treatment consisted in heating ramps of 10 °C/min and 1 h plateaus during which the XPS measurements were performed. The fitting of the Ce 3d region on noisy data is delicate as there is superimposition of 5 doublets with close positions and close splitting values for four of them (violet and yellow components on one side and pink and red ones on the other) (Figure 14). The peak positions were therefore slightly more constrained than for lab-measurements previously discussed.

In normal configuration (electron beam perpendicular to the probed surface), the probed depth for a laboratory instrument operating at 1486.6 eV is estimated to be 3.5 nm in the Ce 3d region.¹⁰ The initial state of Ce(OH)₃ comports a Ce^(III) fraction of 33 %, in line with the oxidation of the extreme surface during the sample preparation in air (Figure 14A). The initial state is therefore very similar to that of cerium oxide nanorods regarding the cerium oxidation state (Ce^(III) fraction of 34 %). An important increase in the Ce^(III) fraction occurred upon temperature increase, from 33 % at r.t. to 67 % at 500 °C for Ce(OH)₃ and from 34 % to 73 % for CeO₂. This evolution is in perfect agreement with the color changes: from grey to lilac in the case of Ce(OH)₃ and from yellow to grey-violet in the case of CeO₂. We can note the reduction of cerium atoms occurs in the full range from room temperature to 400 °C and then seems to get stabilized. Calcination at 200 °C can be performed in the laboratory and would correspond to a Ce^(III) fraction of *ca.* 55 % which is satisfactory for us (Figure 14C). Finally, the oxidation state was not deeply modified upon cooling to 100 °C (final state), indicating the stability of the so-formed highly oxygen-defective cerium oxide.

The increase in Ce^(III) concentration with calcination is in agreement with Freund’s work on cerium oxide microparticles although the extent of the modification of the oxidation state of cerium is higher in our case: from 34 % to 73 % for cerium oxide nanorods *versus* 6 % to 9.2 % for microparticles, for a similar treatment (30 min at 500 °C under vacuum).¹⁰ We attribute this difference to the characteristic size of the

particles: as oxygen vacancies are more easily formed near surface, high surface/volume ratio favors the formation of defective materials.

A similar behavior was observed for the O 1s spectra (Figure 14B). In comparison with the previously displayed spectra, a proper fit required the introduction of a fourth large component attributed to water or hydroxyl group (black component).¹⁰ The initial states of both air exposed $\text{Ce}(\text{OH})_3$ and CeO_2 nanorods display particularly broad features in comparison to the measurements performed with a lab-instrument. The differences may be caused by the difference in X-Ray beam energy (1100 eV for synchrotron, 1486.6 eV for laboratory), the nature of the samples (deposition *versus* powder) or the drop casting method. Besides, CeO_2 is known for presenting electron charge issues at temperatures below 100 °C. In the case of fresh $\text{Ce}(\text{OH})_3$, the $\text{O}_I\text{-Ce}^{(\text{IV})}$ peak got sharpened upon calcination at 100 °C, probably due to a CeO_2 formation, in line with our previous calcination experiments (Figure 12I). Then, the contribution of O_I gradually decreased in favor of those of O_{II} and O_{III} , accounting for the defects and the reduction of $\text{Ce}^{(\text{IV})}$ in $\text{Ce}^{(\text{III})}$ as observed with the Ce 3d spectra. The final state contains a more important contribution of surface hydroxyl/water, it may be due to the cooling of the material from 500 °C down to 100 °C: as the temperature goes down, hydroxyls may form on surface from the adsorption of background water molecules. The observations are in agreement with those for CeO_2 nanorods calcination which contain merely no $\text{Ce}^{(\text{IV})}$ in the end.

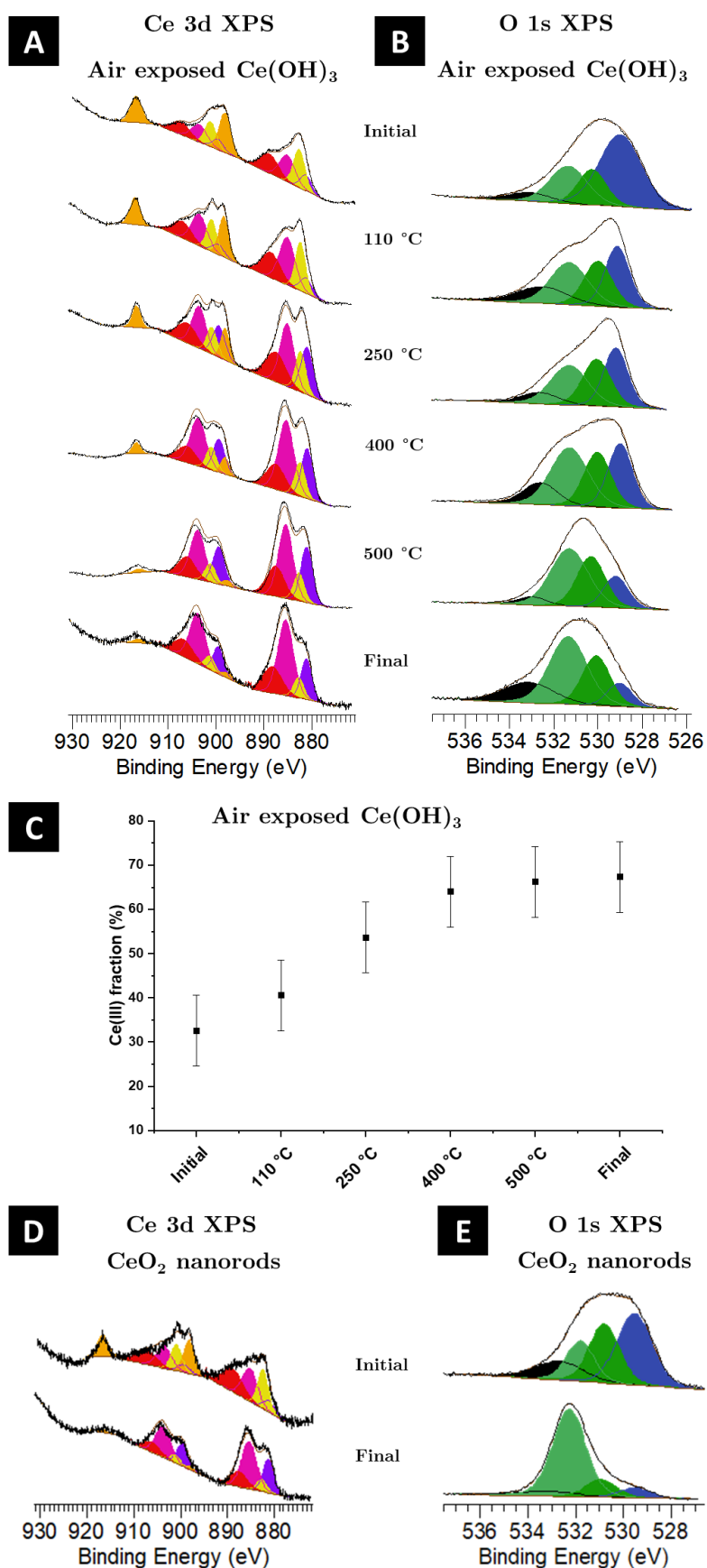


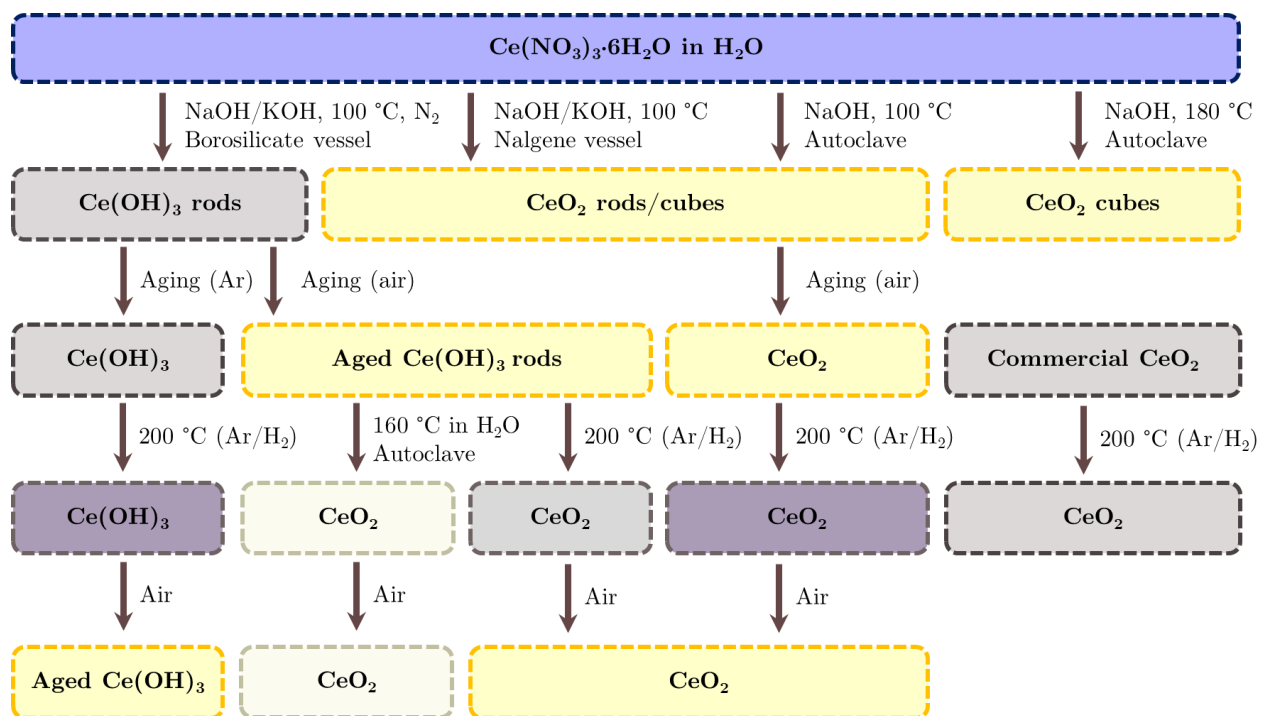
Figure 14. (A) NAP-XPS Ce 3d spectra of air exposed $\text{Ce}(\text{OH})_3$ along calcination in vacuum and of (D) CeO_2 nanorods before and after calcination at 500 °C in vacuum. Color code is

identical to Figure 9. Figure 8: violet and pink for $\text{Ce}^{(\text{III})}$, yellow, orange and red for $\text{Ce}^{(\text{IV})}$. (B) NAP-XPS O 1s spectra of air exposed $\text{Ce}(\text{OH})_3$ along calcination in vacuum. (C) Evolution of the $\text{Ce}^{(\text{III})}$ fraction as a function of the temperature for the air exposed $\text{Ce}(\text{OH})_3$ sample determined with Ce 3d (black) and O 1s (red).

IV.3.4 Summary of the syntheses and treatments of cerium-containing phases

We synthesized cerium oxide CeO_2 and cerium hydroxide $\text{Ce}(\text{OH})_3$ by hydrothermal treatment of $\text{Ce}(\text{NO}_3)_3 \cdot 6\text{H}_2\text{O}$ precursor with an alkali solution of NaOH and KOH and demonstrated the crucial importance of the nature of the reaction vessel, and to a lower extent of the gas phase, to obtain $\text{Ce}(\text{OH})_3$ (Scheme 2). The hydroxide phase evolved in ambient conditions to a new one with an unknown XRD pattern. We fully characterized this unexpected material by means of XRD, TEM, SAED, FTIR, XPS and XAS and suggested it results from the oxidation of some $\text{Ce}^{(\text{III})}$ sites in $\text{Ce}^{(\text{IV})}$ while preserving the global crystallographic structure. This is in contradiction with literature works reporting the evolution in crystalline CeO_2 under ambient conditions. Work is currently ongoing for a better crystallographic description of the unknown phase by means of Rietveld refinement on XRD data.

In order to obtain catalytic materials, different thermal treatments were applied to the materials to increase the $\text{Ce}^{(\text{III})}$ fraction at the surface of the material: $\text{Ce}^{(\text{III})}$ fraction up to 55 % could be obtained in conditions reproducible in the laboratory, *i.e.* a 2 h calcination at 200 °C in absence of air under Ar or H_2 .



Scheme 2. Recapitulative scheme of the different hydrothermal reaction conditions and treatments. The colors of the cases correspond to those of the powders. Materials indicated are those identified by XRD and the morphology, determined by TEM, is preserved along the post-synthesis treatments.

IV.4. Hydrogenation reactions by reduced cerium oxide

IV.4.1 NAP-XPS of hydrogen activation by reduced cerium oxide in the gas phase

As developed in introduction, we believe the presence of oxygen vacancies at the surface of the cerium oxide is essential to its use as a Lewis acid for an FLP-like catalysis. We therefore investigated the presence of these oxygen vacancies and the ability of $\text{Ce}^{(\text{III})}$ atoms to react with H_2 by NAP-XPS. Freund *et al.* showed the addition of H_2 on a reduced cerium oxide increases the surface $\text{Ce}^{(\text{IV})}$ ratio through the formation of Ce-H hydride species.¹⁰ This hydride, and consequently the H_2 activation, may thus be indirectly probed by a growth of the $\text{Ce}^{(\text{IV})}$ components in Ce 3d XPS spectra and of the $\text{O}_\text{I}-\text{Ce}^{(\text{IV})}$ component in O 1s XPS spectra. As no phenylacetylene could be introduced in the NAP-XPS chamber, we chose to inject acetylene as a model substrate at the end of the H_2 activation experiment to detect a potential hydrogenation reaction. We chose a final temperature of 250 °C and an H_2 :acetylene ratio of *ca.* 5 to be as close as possible to the conditions of semi-hydrogenation with cerium oxide developed by Pérez-Jamírez *et al.*¹⁶ The two cerium oxide catalysts were disposed on the same sample holder and were therefore subjected to the same conditions: one catalyst originated from air exposed $\text{Ce}(\text{OH})_3$ dehydration (Synthesis IV.2.) and the other was the CeO_2 nanorods from Synthesis IV.1.

The catalysts contained high concentration of oxygen defects after the calcination step at 500 °C in the NAP-XPS chamber (*cf.* section IV.3.3., 30 min at 500 °C under ultra high vacuum). As cerium oxide charges under the X-ray beam at low temperatures, we measured the initial state at 100 °C, then added a low pressure of H_2 (0.14 mbar then 0.52 mbar), then increased the temperature up to 250 °C, then introduced the acetylene (0.1 mbar of acetylene) and finally measured the final state when all gases were removed (Figure 15A).

Both the samples displayed initial $\text{Ce}^{(\text{III})}$ ratio *ca.* 70 % (Figure 15, state 1). Upon exposure to 0.14 mbar of H_2 at 100 °C, we observed the growth of the $\text{Ce}^{(\text{IV})}$ orange component at 917 eV (state 2) on the Ce 3d XPS spectra indicating the cerium atoms got oxidized in $\text{Ce}^{(\text{IV})}$. Increasing the H_2 pressure further decreased the $\text{Ce}^{(\text{III})}$ concentration down to respectively 58 % and 48 % (state 3). However, heating to 250 °C induced the reduction of the cerium atoms to the initial levels, or close (state 4). In the O 1s spectra, the main feature is the growth of the O_I blue component from state 1 to state 3. As this component is associated to oxygen in oxidized environment, *i.e.* linked to $\text{Ce}^{(\text{IV})}$ atoms, we concluded the surface $\text{Ce}^{(\text{III})}$ atoms in reduced cerium oxide get oxidized by H_2 even at low pressures. This oxidation is however reversible upon heating as shown by state 4. The addition of acetylene did not significantly modify the spectra envelope of neither the Ce 3d nor O 1s regions.

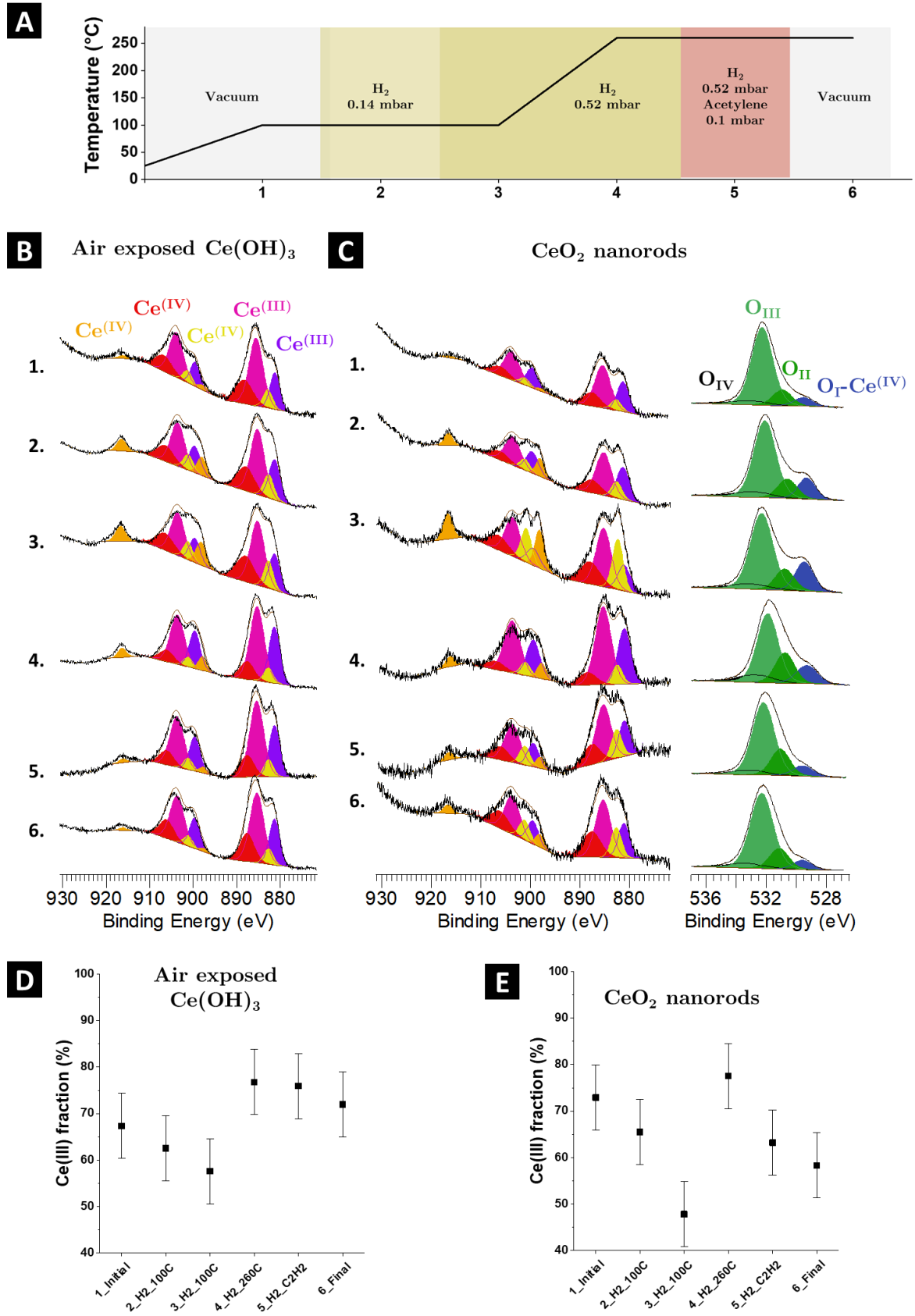
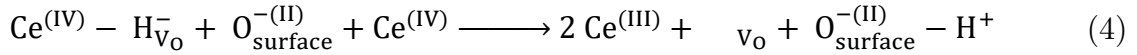
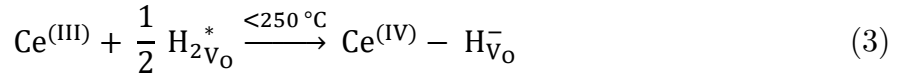
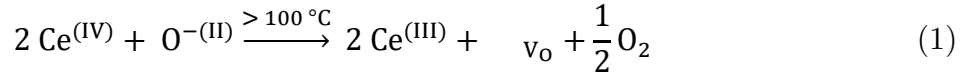


Figure 15. (A) *In situ* treatment of the samples in the NAP-XPS device: (1) vacuum/100 °C, (2) H₂ 0.14 mbar/100 °C, (3) H₂ 0.52 mbar/100 °C, (4) H₂ 0.52 mbar/260 °C, (5) H₂ 0.52 mbar + acetylene 0.1 mbar/260 °C and (6) vacuum/260 °C. NAP-XPS Ce 3d and O 1s

spectra of (A) air exposed $\text{Ce}(\text{OH})_3$ and of (B) CeO_2 nanorods. Color code is identical to Figure 9: pink and violet for $\text{Ce}^{(\text{III})}$, yellow, orange and red for $\text{Ce}^{(\text{IV})}$. Evolution of the $\text{Ce}^{(\text{III})}$ fraction based on Ce 3d spectra for (D) the air exposed $\text{Ce}(\text{OH})_3$ sample and (E) the CeO_2 nanorods sample.

We showed the reduction of cerium dioxide under vacuum led to the formation of surface $\text{Ce}^{(\text{III})}$ atoms, presumably due to defect formation (according to Eq. (1)). Furthermore, these oxygen vacancies may adsorb H_2 (according to Eq. (2)) and then activate it by forming Ce–H hydride species (according to Eq. (3)). The H linked to the cerium atom is thought to be situated in an oxygen vacancy and to be negatively charged considering the increase in the oxidation state of the cerium, hence the hydride terminology.¹⁰ Upon heating, typically above 200 °C, the hydride species recombine as H_2 and desorb from the cerium oxide (according to reverse Eq. (3) and (2)).



Our observations therefore agree with the hydrogen adsorption-induced oxidation of reduced cerium oxide reported by Freund *et al.*¹⁰ but, like for the calcination step previously studied, the extent of the phenomenon is much higher in our case, presumably due to the high surface/volume ratio of the objects. DFT studies for oxygen defective $\text{CeO}_2(111)$ indicated the recombination of two $\text{Ce}^{(\text{IV})}\text{--H}^-$ species in H_2 is more kinetically favored than the formation of the homolytic dissociation product according to Eq. (4), *i.e.* the migration of the proton from the metal site to a surface oxygen site accompanied with a reduction of two $\text{Ce}^{(\text{IV})}$ in $\text{Ce}^{(\text{III})}$.¹⁰ This indicates the $\text{Ce}^{(\text{IV})}\text{--H}^-$ species are relatively stable at moderate temperatures, and potentially active for hydrogenation reactions, and that there is a limited formation of hydroxyls. Although the samples used in this experiment were calcinated at 500 °C prior to H_2 exposure, which is not reproducible in laboratory, we hypothesized the calcination at 200 °C already formed a significant number of surface $\text{Ce}^{(\text{III})}$ atoms (surface fraction of 55 % at 250 °C *vs.* 32 % and 68 % for respectively the initial and final state at 500 °C, *cf.* Figure 9), and thus of active sites for H_2 activation. We therefore chose to heat the pre-catalyst samples used for liquid catalysis at 200 °C during 2 h in presence of H_2 .

IV.4.2 Liquid phase hydrogenation of styrene and phenylacetylene

Inspired by the recent literature on acetylene hydrogenation by CeO_2 in the gas phase^{16,47} and the results obtained in the liquid phase for alkene and alkyne hydrogenation,⁸ we chose styrene and phenylacetylene (PhCCH) as model substrates. The set of reaction conditions was chosen close to that of Qu's work, *i.e.* the reaction was conducted in toluene at 100 °C under 7 bar H_2 during 16 h, in autoclave, with 40 mg of material for 2 mmol of substrate.⁸

Catalysis IV.1. Olefin hydrogenation in toluene. In air, 40 mg of pre-catalyst powder (0.24 mmol, 0.12 equiv. of $[\text{Ce}]$) were introduced in a 25 mL glass autoclave. The atmosphere was changed for H_2 (7 bar) after 2 cycles vacuum/ H_2 . The autoclave was introduced in a preheated oil bath at 200 °C for 2 h. The pre-catalyst powder, initially yellow, turned grey. After reaction, the autoclave was let to cool down naturally to r.t. and introduced in an Ar-filled glovebox where it was reopened. To the autoclave were added 2 mmol of alkene or alkyne (210 μL of styrene or 220 μL of phenylacetylene, 1 equiv.), anhydrous toluene (1 mL) and eventually a phosphine (0.1 mmol, 0.05 equiv.). The autoclave was closed and the atmosphere was changed for H_2 (7 bar) after 2 cycles vacuum/ H_2 . The autoclave was then introduced in a preheated oil bath at 100 °C for 16 h. The powder was suspended in solution with stirring. After reaction, it was let to cool down naturally to r.t. before opening. An aliquot of the liquid phase was studied by ^1H NMR in CDCl_3 .

Styrene hydrogenation. No hydrogenation of styrene occurs with CeO_2 nanorods from Synthesis IV.1. whatever was the pre-treatment: raw (no pre-treatment), reduced during 2 h at 100 °C or at 200 °C. Instead, a small fraction of styrene polymerized, as attested by a broad signal at *ca.* 6.60 ppm in ^1H NMR. The same results were observed when 5 mol% of tricyclohexylphosphine (PCy_3) were added.

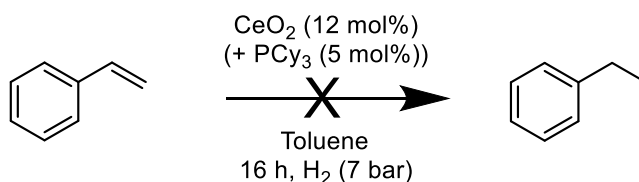
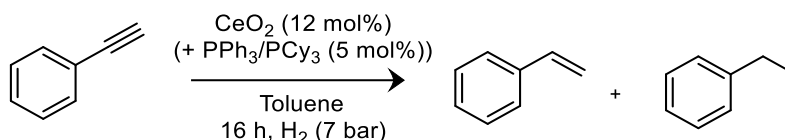


Figure 16. Hydrogenation of styrene with cerium oxide.

Phenylacetylene semi-hydrogenation. First studies on phenylacetylene with a pre-catalyst batch initially containing a mix of aged $\text{Ce}(\text{OH})_3$ and CeO_2 , led to a 12 % conversion yield of phenylacetylene without phosphine, and to higher yields (35 % and 75 %) in presence of PPh_3 or PCy_3 (5 mol%), with even a small proportion of ethylbenzene (Table 4, entries 1-3). The good catalytic activity of this batch supports the results displayed by Qu *et al.* Unfortunately, these interesting results could not be reproduced on another batch, although we explored more than ten different batches of pre-catalyst leading to XRD-pure aged $\text{Ce}(\text{OH})_3$, mix of aged $\text{Ce}(\text{OH})_3$ and CeO_2 or XRD-pure CeO_2 , as well as different post-synthesis treatments (no calcination, calcination at 200 °C, hydrothermal treatment at 160 °C in autoclave). The difficulties in obtaining as high catalytic activities as those obtained with the first batch underline the sensitivity of the catalyst synthesis, as already stressed by Qu *et al.* in their articles.^{3,17} When following the hydrothermal treatment at 160 °C during 16 h in autoclave proposed by Qu *et al.*, no reactivity at all was observed (Table 4, entries 4-5). When using raw materials without calcination, no reactivity was observed at 100 °C (Table 4, entries 6 and 8) although a consequent one was obtained at 200 °C (Table 4, entries 7 and 9): respectively 40 % and 77 % conversion of phenylacetylene for aged $\text{Ce}(\text{OH})_3$ and CeO_2 nanorods. Finally, if the first batch was excluded, no significant difference in phenylacetylene hydrogenation was detected between reduced pure aged $\text{Ce}(\text{OH})_3$ and reduced mix of aged $\text{Ce}(\text{OH})_3$ and CeO_2 , both of them displaying a conversion *ca.* 1-2 % (Table 4, entries 10 and 12 and Figure 17, entries 1 and 3). Reduced CeO_2 nanorods from Synthesis IV.1 led to slightly higher styrene yields, *ca.* 8 % (Table 4, entry 14 and Figure 17, entry 5).



Entry	Catalyst	Phosphine (5 mol%)	Temp.	Styrene yield	Ethylbenzene yield
Highly active batch ^a					
1	Mix aged Ce(OH) ₃ /CeO ₂	-	100 °C	12 %	0 %
2		PPh ₃		30 %	5 %
3		PCy ₃		65 %	10 %
Hydrothermal treatment ^b					
4	Aged Ce(OH) ₃	-	100 °C	0 %	0 %
5		PPh ₃		1 %	0 %
Non calcinated catalysts ^c					
6	Aged Ce(OH) ₃	-	100 °C	0 %	0 %
7		-	200 °C	40 %	0 %
8	CeO ₂	-	100 °C	0 %	0 %
9		-	200 °C	61 %	16 %
	Calcinated catalysts ^d				
10	Aged Ce(OH) ₃	-	100 °C	1 %	0 %
11		PPh ₃		5 %	0 %
12	Mix aged Ce(OH) ₃ /CeO ₂	-		1 %	0 %
13		PPh ₃		4 %	0 %
14	CeO ₂	-		8 %	0 %
15		PPh ₃		7 %	0 %

Table 4. Hydrogenation of phenylacetylene with different cerium oxide samples according to Catalysis IV.1. For entries 1-3 and 10-15, the samples were reduced by calcination at 200 °C during 2 h under H₂ (7 bar). Yields were determined by NMR. ^aData corresponding to a single batch of catalyst. ^bHydrothermal treatment at 160 °C for 16 h in water autoclave, two experiments per condition with identical results. ^cNo calcination performed before catalysis. Unidentified products with aromatic protons at 200 °C. ^dAverage results, correspond to data on Figure 3.

Although we could not obtain a consequent hydrogenation of phenylacetylene in similar conditions than the targeted ones,⁸ our results are in line with Pérez-Ramírez *et al.* on alkyne hydrogenation with CeO₂/TiO₂: at 100 °C in toluene, they report a reasonable conversion (above 50 %) of 1-hexyne in 1-hexene when H₂ pressure was higher than 50 bar, and only residual conversion below 10 bar of H₂.⁴⁷ Moreover, our results clearly indicate the hydrogenation catalytic activity of a cerium oxide stand-

alone catalyst exists at 100 °C, even though with moderate efficiency, at the condition of reducing it at high temperature, hence the importance of oxygen vacancies.

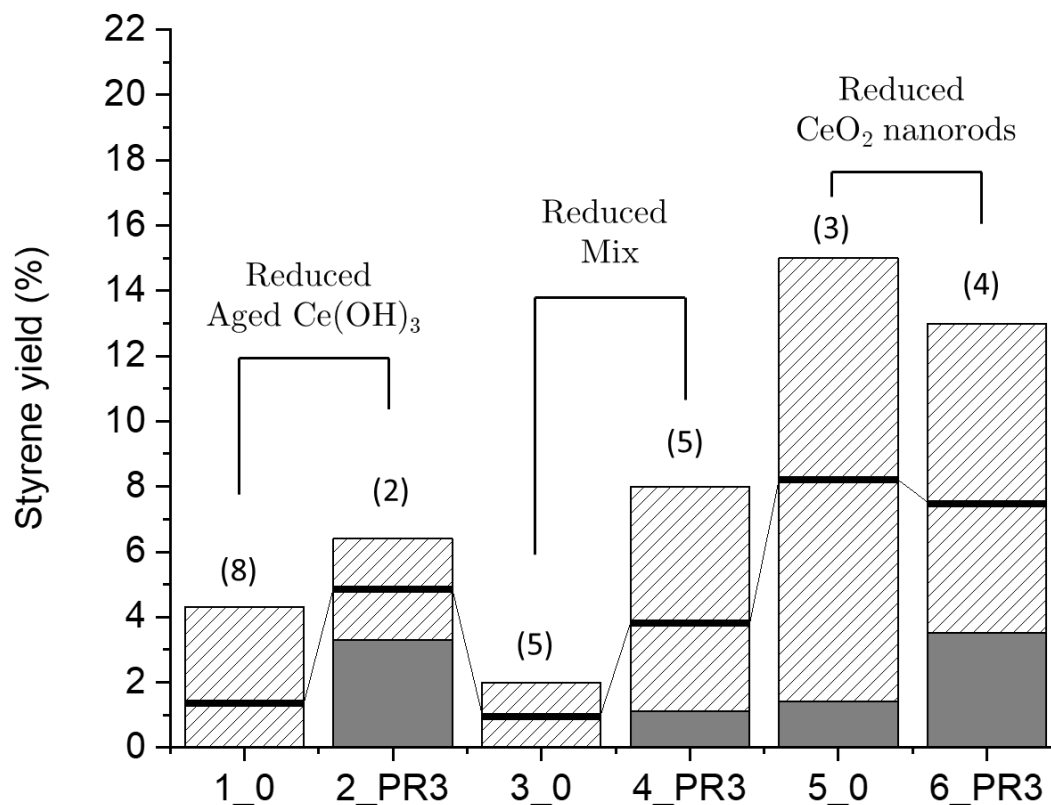


Figure 17. Styrene yield obtained during phenylacetylene semi-hydrogenation by reduced cerium oxide samples, from (1-2) aged $\text{Ce}(\text{OH})_3$, (3-4) an aged mix of $\text{Ce}(\text{OH})_3$ and CeO_2 and (5-6) CeO_2 nanorods. Triphenylphosphine (PPh_3) at 5 mol% was added in experiments 2, 4 and 6. The dashed sectors indicate the ranges of obtained yields, the black line denoting the average. The figures in brackets indicate the number of experiments per bar. Conversion yields were determined by NMR.

Phosphine addition. An increase in phenylacetylene hydrogenation rate was observed upon addition of PPh_3 or PCy_3 when aged $\text{Ce}(\text{OH})_3$ or a mix aged $\text{Ce}(\text{OH})_3/\text{CeO}_2$ was used (*ca.* 5 % conversion in presence of phosphine vs. 1 % without) (Figure 17, entries 1-4). No meaningful difference is observed between the styrene yield for reduced CeO_2 nanorods with and without addition of a phosphine (Figure 17, entries 5-6). Although the results with aged $\text{Ce}(\text{OH})_3$ seem encouraging, the very large variability in the obtained yields and the poor reproducibility of the results impend us from formally asserting there is an impact of the phosphine.

IV.4.3 Conclusion on the catalytic activity of cerium oxide

In summary, we proved with NAP-XPS the capacity of defective cerium oxide obtained by calcination at 500 °C to activate H₂ in the gas phase *via* the Ce^(III) atoms. We then used the catalyst for the liquid phase semi-hydrogenation of phenylacetylene under mild conditions (100 °C, 7 bar H₂, toluene). Limited conversion yields were obtained and the results obtained by Qu *et al.* could not be fully reproduced. We stressed the large variability of the catalytic activity depending on the cerium oxide pre-catalyst batch and treatment.

As the conversion yields are too low for assessing the impact of the phosphine on the hydrogenation, we suggest as perspective to use stronger conditions (150 °C or higher H₂ pressures). Indeed, when the reaction was conducted at 200 °C, high conversions were attained as well as conversion to ethylbenzene. In this regime, we will certainly be able to study the impact of the addition of PPh₃ or PCy₃. We suggest to use reduced cerium oxide from Synthesis IV.1. as the synthesis of this material is more straightforward and common in literature, and already displays higher catalytic activities. Even though the proposed conditions would be limiting for practical applications, we estimate the interest resides in the possibility of boosting the reactivity of a metal oxide with a phosphine, a concept still relatively unexplored.

IV.5. Bibliography

1. Montini, T., Melchionna, M., Monai, M. & Fornasiero, P. Fundamentals and Catalytic Applications of CeO₂-Based Materials. *Chem. Rev.* **116**, 5987–6041 (2016).
2. Wang, R. & Dangerfield, R. Seed-mediated synthesis of shape-controlled CeO₂ nanocrystals. *RSC Adv.* **4**, 3615–3620 (2014).
3. Li, J. *et al.* Low pressure induced porous nanorods of ceria with high reducibility and large oxygen storage capacity: synthesis and catalytic applications. *J. Mater. Chem. A* **2**, 16459–16466 (2014).
4. Chen, J. *et al.* Surface Engineering Protocol To Obtain an Atomically Dispersed Pt/CeO₂ Catalyst with High Activity and Stability for CO Oxidation. *ACS Sustain. Chem. Eng.* **6**, 14054–14062 (2018).
5. Tang, C. C., Bando, Y., Liu, B. D. & Golberg, D. Cerium Oxide Nanotubes Prepared from Cerium Hydroxide Nanotubes. *Adv. Mater.* **17**, 3005–3009 (2005).
6. Mai, H.-X. *et al.* Shape-Selective Synthesis and Oxygen Storage Behavior of Ceria Nanopolyhedra, Nanorods, and Nanocubes. *J. Phys. Chem. B* **109**, 24380–24385 (2005).
7. Garcia, X. *et al.* Ceria-Based Catalysts Studied by Near Ambient Pressure X-ray Photoelectron Spectroscopy: A Review. *Catalysts* **10**, 286 (2020).
8. Zhang, S. *et al.* Solid frustrated-Lewis-pair catalysts constructed by regulations on surface defects of porous nanorods of CeO₂. *Nat. Commun.* **8**, 1–11 (2017).
9. Riley, C. *et al.* Design of Effective Catalysts for Selective Alkyne Hydrogenation by Doping of Ceria with a Single-Atom Promotor. *J. Am. Chem. Soc.* **140**, 12964–12973 (2018).
10. Li, Z. *et al.* Oxidation of Reduced Ceria by Incorporation of Hydrogen. *Angew. Chemie Int. Ed.* **58**, 14686–14693 (2019).
11. Abi-aad, E., Bechara, R., Grimblot, J. & Aboukais, A. Preparation and characterization of ceria under an oxidizing atmosphere. Thermal analysis, XPS, and EPR study. *Chem. Mater.* **5**, 793–797 (1993).
12. Wang, L. *et al.* Room-Temperature Activation of H₂ by a Surface Frustrated Lewis Pair. 9501–9505 (2019).
13. Fiorio, J. L., López, N. & Rossi, L. M. Gold–Ligand-Catalyzed Selective Hydrogenation of Alkynes into cis-Alkenes via H₂ Heterolytic Activation by

- Frustrated Lewis Pairs. *ACS Catal.* **7**, 2973–2980 (2017).
14. Fiorio, J. L. *et al.* Accessing Frustrated Lewis Pair Chemistry through Robust Gold@N-Doped Carbon for Selective Hydrogenation of Alkynes. *ACS Catal.* **8**, 3516–3524 (2018).
 15. Silva, R. J. M., Fiorio, J. L., Vidinha, P. & Rossi, L. M. Gold Catalysis for Selective Hydrogenation of Aldehydes and Valorization of Bio-Based Chemical Building Blocks. **30**, 2162–2169 (2019).
 16. Albani, D. *et al.* Semihydrogenation of Acetylene on Indium Oxide: Proposed Single-Ensemble Catalysis. *Angew. Chemie Int. Ed.* **56**, 10755–10760 (2017).
 17. Li, J. *et al.* Pressure Regulations on the Surface Properties of CeO₂ Nanorods and Their Catalytic Activity for CO Oxidation and Nitrile Hydrolysis Reactions. *ACS Appl. Mater. Interfaces* **8**, 22988–22996 (2016).
 18. Weltner, W. & DeKock, R. L. Spectroscopy of rare earth oxide molecules in inert matrices at 4 K. *J. Phys. Chem.* **75**, 514–525 (1971).
 19. Ajmal, M. *et al.* Structural and optical properties of La₂O₃:Ho³⁺ and La(OH)₃:Ho³⁺ crystalline particles. *Mater. Today Proc.* **4**, 4900–4905 (2017).
 20. Bozon-Verduraz, F. & Bensalem, A. IR studies of cerium dioxide: influence of impurities and defects. *J. Chem. Soc. Faraday Trans.* **90**, 653 (1994).
 21. Vayssilov, G. N., Mihaylov, M., Petkov, P. St., Hadjiivanov, K. I. & Neyman, K. M. Reassignment of the Vibrational Spectra of Carbonates, Formates, and Related Surface Species on Ceria: A Combined Density Functional and Infrared Spectroscopy Investigation. *J. Phys. Chem. C* **115**, 23435–23454 (2011).
 22. Mihaylov, M. Y. *et al.* Infrared spectra of surface nitrates: Revision of the current opinions based on the case study of ceria. *J. Catal.* **394**, 245–258 (2021).
 23. Bêche, E., Charvin, P., Perarnau, D., Abanades, S. & Flamant, G. Ce 3d XPS investigation of cerium oxides and mixed cerium oxide (Ce_xTi_yO_z). *Surf. Interface Anal.* **40**, 264–267 (2008).
 24. Matolín, V. *et al.* A resonant photoelectron spectroscopy study of Sn(O_x) doped CeO₂ catalysts. *Surf. Interface Anal.* **40**, 225–230 (2008).
 25. Larquet, C. *et al.* Synthesis of Ce₂O₂S and Gd_{2(1-y)}Ce_{2y}O₂S Nanoparticles and Reactivity from in Situ X-ray Absorption Spectroscopy and X-ray Photoelectron Spectroscopy. *Inorg. Chem.* **56**, 14227–14236 (2017).
 26. Barth, C. *et al.* A perfectly stoichiometric and flat CeO₂(111) surface on a bulk-like ceria film. *Sci. Rep.* **6**, 21165 (2016).

27. Mullins, D. ., Overbury, S. . & Huntley, D. . Electron spectroscopy of single crystal and polycrystalline cerium oxide surfaces. *Surf. Sci.* **409**, 307–319 (1998).
28. Kumar, A., Babu, S., Karakoti, A. S., Schulte, A. & Seal, S. Luminescence Properties of Europium-Doped Cerium Oxide Nanoparticles: Role of Vacancy and Oxidation States. *Langmuir* **25**, 10998–11007 (2009).
29. Pfau, A. & Schierbaum, K. D. The electronic structure of stoichiometric and reduced CeO₂ surfaces: an XPS, UPS and HREELS study. *Surf. Sci.* **321**, 71–80 (1994).
30. Palmqvist, A. E. ., Wirde, M., Gelius, U. & Muhammed, M. Surfaces of doped nanophase cerium oxide catalysts. *Nanostructured Mater.* **11**, 995–1007 (1999).
31. Shahin, A. M., Grandjean, F., Long, G. J. & Schuman, T. P. Cerium L_{III}-Edge XAS Investigation of the Structure of Crystalline and Amorphous Cerium Oxides. *Chem. Mater.* **17**, 315–321 (2005).
32. Beall, G. W., Milligan, W. O. & Wolcott, H. A. Structural trends in the lanthanide trihydroxides. *J. Inorg. Nucl. Chem.* **39**, 65–70 (1977).
33. Milligan, W. O., Mullica, D. F. & Oliver, J. D. Rare-earth trihydroxide parameters. *J. Appl. Crystallogr.* **12**, 411–412 (1979).
34. Mullica, D. F., Oliver, J. D. & Milllgan, W. O. Cerium trihydroxide. *Acta Crystallogr. Sect. B Struct. Crystallogr. Cryst. Chem.* **35**, 2668–2670 (1979).
35. Milligan, W. O., Mullica, D. F., Grossie, D. A. & Lok, C. K. C. Crystal structure of Yb(OH)₃. *J. Solid State Chem.* **50**, 129–132 (1983).
36. Neumann, A. & Walter, D. The thermal transformation from lanthanum hydroxide to lanthanum hydroxide oxide. *Thermochim. Acta* **445**, 200–204 (2006).
37. Momma, K. & Izumi, F. VESTA: a three-dimensional visualization system for electronic and structural analysis. *J. Appl. Crystallogr.* **41**, 653–658 (2008).
38. Shannon, R. D. Revised effective ionic radii and systematic studies of interatomic distances in halides and chalcogenides. *Acta Crystallogr. Sect. A* **32**, 751–767 (1976).
39. Balasubramanian, M., Melendres, C. & Mansour, A. An X-ray absorption study of the local structure of cerium in electrochemically deposited thin films. *Thin Solid Films* **347**, 178–183 (1999).
40. Balasubramanian, M., Melendres, C. A. & Mansour, A. N. X-Ray Absorption Spectroscopy Study of the Local Structure of Heavy Metal Ions Incorporated into Electrodeposited Nickel Oxide Films. *J. Electrochem. Soc.* **146**, 607–614 (1999).

41. Abellan, P. *et al.* The formation of cerium(III) hydroxide nanoparticles by a radiation mediated increase in local pH. *RSC Adv.* **7**, 3831–3837 (2017).
42. Ansari, A. A. & Kaushik, A. Synthesis and optical properties of nanostructured $\text{Ce}(\text{OH})_4$. *J. Semicond.* **31**, 033001 (2010).
43. Tang, K. *et al.* Construction of $\text{Ce}(\text{OH})_4$ nanostructures from 1D to 3D by a mechanical force-driven method. *CrystEngComm* **17**, 2690–2697 (2015).
44. Zhang, X., Xia, C., Li, K. & Lin, Y. Surface nucleation and independent growth of $\text{Ce}(\text{OH})_4$ within confinement space on modified carbon black surface to prepare nano- CeO_2 without agglomeration. *Front. Mater. Sci.* **12**, 168–175 (2018).
45. Nilchi, A., Yaftian, M., Aboulhasanlo, G. & Rasouli Garmarodi, S. Adsorption of selected ions on hydrous cerium oxide. *J. Radioanal. Nucl. Chem.* **279**, 65–74 (2009).
46. Guo, H. *et al.* A study of phosphate adsorption by different temperature treated hydrous cerium oxides. *Rare Met.* **30**, 58–62 (2011).
47. Vilé, G. *et al.* Stereo- and Chemoselective Character of Supported CeO_2 Catalysts for Continuous-Flow Three-Phase Alkyne Hydrogenation. *ChemCatChem* **6**, 1928–1934 (2014).

Chapter V

Indium oxide catalysts for phenylacetylene hydrogenation

Indium oxide In_2O_3 recently raised interest as a stand-alone catalyst for gas phase hydrogenation of CO_2 and acetylene.^{1,2} In 2014, Ozin *et al.* reported the possibility to use hydroxylated indium oxide nanoparticles $\text{In}_2\text{O}_{3-x}(\text{OH})_y$ as a photocatalyst for CO_2 reduction in CO and H_2O according to the Reverse Water Gas Shift (RWGS) reaction.^{3,4} The H_2 molecule was thought to be heterolytically cleaved on two close sites, [In] and [In-O], the indium site playing the role of a Lewis acid and the oxygen one that of a Lewis base. The authors thus revisited the H_2 activation on transition metal oxides surfaces with a mechanism related to Frustrated Lewis Pair (FLP) catalysis.⁵ They also proved the substitution of 1 % of the indium atoms by bismuth ones increased the photocatalytic activity due to a better light absorption and to the stronger Lewis acidity of $\text{Bi}^{(\text{III})}$.^{6,7} They finally achieved the hydrogenation of CO_2 in methanol at 270 °C with rhombohedral In_2O_3 .² As to acetylene, Pérez-Ramírez *et al.* reported its selective hydrogenation in ethylene (> 85 % selectivity) in the presence of cubic In_2O_3 .¹ The reaction was conducted in flux at atmospheric pressure with a $\text{H}_2:\text{C}_2\text{H}_2$ feed ratio of 30. A sharp increase in activity occurred between 250 °C (< 5 % conversion) and 350 °C (> 95 % conversion). There is however, to the best of our knowledge, no published work reporting the use of indium oxide as a stand-alone catalyst for hydrogenation reaction in solvent.

One of the targets of this thesis is the construction of an FLP-like catalytic system at the surface of NPs between a molecular base and a metal cation. In Chapter IV, we focused on the use of ceria with cerium atoms as the Lewis acidic centers. In this Chapter, we suggest to test in solvent the catalytic activity of In_2O_3 which already proved its ability to activate H_2 in the gas phase following a solid FLP mechanism. We envision a boost in catalytic activity by addition of a Lewis base such as a phosphine. The objective of Chapter V is not to obtain a performant catalyst but rather to investigate whether a system “metal oxide (Lewis base)/phosphine (Lewis base)” is in capacity to activate H_2 in solvent. We targeted the hydrogenation of phenylacetylene as a model substrate with catalysts similar to the ones used by Ozin, Pérez-Ramírez and coworkers. We are potentially interested in both the cubic and rhombohedral indium oxide phases as they both displayed a catalytic activity in CO_2 hydrogenation. We chose to target both the pristine and a bismuth doped phases, even though no photocatalytic activity was investigated here, because $\text{Bi}^{(\text{III})}$ atom sites are stronger Lewis acids than $\text{In}^{(\text{III})}$ ones in $\text{Bi}_x\text{In}_{2-x}\text{O}_3$ phases.⁷

V.1. Syntheses of indium oxide catalysts

There are two main stable phases for $\text{In}^{(\text{III})}$ oxide: the cubic one (bixbyite type), $\text{c-In}_2\text{O}_3$, and the rhombohedral one (corundum type), $\text{rh-In}_2\text{O}_3$. To maximize the surface/volume ratio, essential for colloidal catalysis, we focused on the synthesis of In_2O_3 nanoparticles smaller than 100 nm. $\text{c-In}_2\text{O}_3$ NPs can be obtained from an aqueous solution of InCl_3 or $\text{In}(\text{NO}_3)_3$ heated at 100-200 °C.⁸ Fu *et al.* in particular studied the case of $\text{In}(\text{NO}_3)_3 \cdot 5\text{H}_2\text{O}$ in a binary mixture DMF/ H_2O at 150 °C: the product phase was determined by the amount of water. They obtained 4-8 nm large $\text{c-In}_2\text{O}_3$ NPs in absence of water and 20 nm large InOOH NPs in presence of 8.8 % of water.⁸ Ozin *et al.* reported similar syntheses. No comparable hydrothermal synthesis directly leading to $\text{rh-In}_2\text{O}_3$ could be found: a dry calcination of indium oxyhydroxide InOOH is the usual pathway.⁹ To keep a high specific area hardly achievable with purely solid state syntheses, we propose the calcination of InOOH NPs obtained *via* the hydrothermal treatment in $\text{rh-In}_2\text{O}_3$ NPs, in line with Ozin's work.²

V.1.1 Bismuth doped cubic indium oxide

We reproduced in Synthesis V.1. the synthesis in one step of bismuth doped cubic indium oxide $\text{c-Bi}_{0.02}\text{In}_2\text{O}_3$ reported by Ozin *et al.*⁷ and Fu *et al.*⁸

Synthesis V.1. Cubic $\text{Bi}_{0.02}\text{In}_2\text{O}_3$. In a borosilicate vessel in air, 1.2 g of $\text{In}(\text{NO}_3)_3 \cdot 5\text{H}_2\text{O}$ (3.1 mmol, 1 equiv.) and 11 mg of $\text{Bi}(\text{NO}_3)_3 \cdot 5\text{H}_2\text{O}$ (0.031 mmol, 0.01 equiv.) were dissolved in 68 mL of anhydrous DMF (0.87 mol, 285 equiv.). Once the salts were dissolved after 30 min stirring (slightly turbid solution), the solution was transferred in three Teflon autoclaves of 25 mL. The autoclaves were sealed and put in an oven at 150 °C for 24 h. After reaction, the solution was let to cool down naturally to r.t. A grey-brown powder sedimented at the bottom of the autoclave. The whole solutions were brought together and centrifugated (9,000 rpm, 10 min, 20 °C). The powder was washed once with 30 mL of H_2O and once with 30 mL of EtOH, without change of aspect. The obtained grey-brown powder (471 mg, 110 % yield) was then dried under flux of N_2 and stored under air. The excess of mass may be either attributed to residual solvents or to nitrate ions which would not have been washed away.

The material obtained in Synthesis V.1. is isostructural with cubic In_2O_3 [PDF card N°04-004-3575] according to XRD with a crystallite size *ca.* 8 nm, calculated with the Scherrer formula applied to the peaks at 22°, 31° and 36° (Figure 1A). TEM images reveal the material consists in crystalline and relatively monodisperse 6 nm large nanoparticles, partially aggregated when dispersed in EtOH (Figure 1B-C). Selected area electron diffraction comforts the XRD attribution to $\text{c-In}_2\text{O}_3$ (Figure 1D). If compared to $\text{c-In}_2\text{O}_3$ which is a white powder, the brown color obtained here supports the insertion of bismuth atom. Indeed, Ozin *et al.* reported a darkening of

the powder color with an increasing Bi content: they attributed it to a change in the bandgap energy (1.212 eV for pristine In_2O_3 *versus* 0.818 eV in $\text{Bi}_{0.02}\text{In}_2\text{O}_3$).⁷ The absence of any peak but those of $\text{c-In}_2\text{O}_3$ in XRD, the presence of only one type of particle in TEM and the difference of powder color led us to consider the bismuth atoms were inserted in the indium oxide structure with little distortion, as previously reported. The material will be later referred to as $\text{c-Bi}_{0.02}\text{In}_2\text{O}_3$.

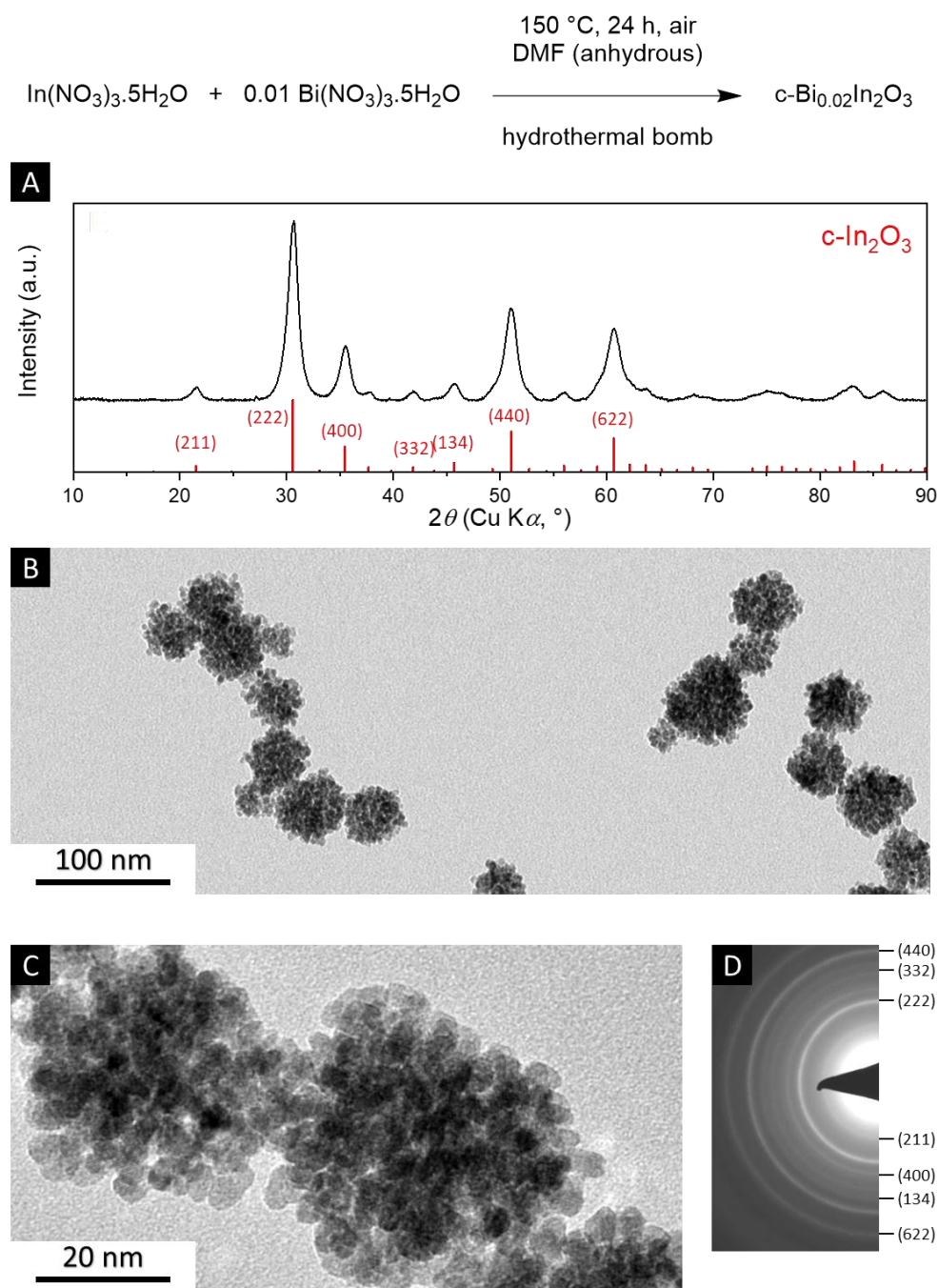


Figure 1. Synthesis and characterization of $\text{c-Bi}_{0.02}\text{In}_2\text{O}_3$ from Synthesis V.1. with (A) powder XRD with (hkl) attributions, (B-C) TEM images and (D) selected area electron diffraction pattern.

V.1.2 Pristine and bismuth doped rhombohedral indium oxide

The rhombohedral rh-In₂O₃ phase, without bismuth doping, was obtained by formation of InOOH in DMF,⁸ followed by a calcination step (Synthesis V.2.).²

Synthesis V.2. Rhombohedral In₂O₃. In a borosilicate vessel, 240 mg of In(NO₃)₃ · 5H₂O (0.614 mmol, 1 equiv.) were dissolved in 0.64 mL of water (35.5 mmol, 58 equiv.) and 13.6 mL of anhydrous DMF (0.175 mol, 285 equiv.) were added. After 30 min stirring, once the solution was limpid, the solution was transferred in a Teflon autoclave of 25 mL. The autoclave was sealed and put in a preheated oven at 150 °C for 24 h. After reaction, the solution was let to cool down naturally to r.t. on the bench. A white powder sedimented at the bottom of the autoclave. The whole solution was centrifugated (9,000 rpm, 10 min, 20 °C) and the powder was washed once with 10 mL of H₂O, once with 10 mL of EtOH and then dried under flux of N₂ without change of aspect. The white powder was placed in a ceramic crucible which was transferred to a muffle furnace. The material was heated during 3 h at 350 °C (heating ramp of 10 °C/min) under air before being cooled down to r.t. The powder turned yellow (70 mg, 78 % yield) and was finally stored under air.

The intermediate product (before calcination at 350 °C) consists in XRD-pure indium oxyhydroxide InOOH [PDF card N°04-009-3421] with a crystallite size *ca.* 10 nm, calculated with the Scherrer formula applied to the peaks at 26° and 49° (Figure 2A). TEM images reveal the product consisted in crystalline 10 nm large nanoparticles (Figure 2B), and electron diffraction comforts the XRD attribution to InOOH (Figure 2C). The final product consists in XRD-pure rhombohedral In₂O₃ [PDF card N°00-022-0336] with a crystallite size *ca.* 10 nm, calculated with the Scherrer formula applied to the peaks at 22.5°, 46° and 50.5° (Figure 2D). The morphology is not affected by the calcination step according to TEM images (Figure 2E). The material will later be referred to as rh-In₂O₃.

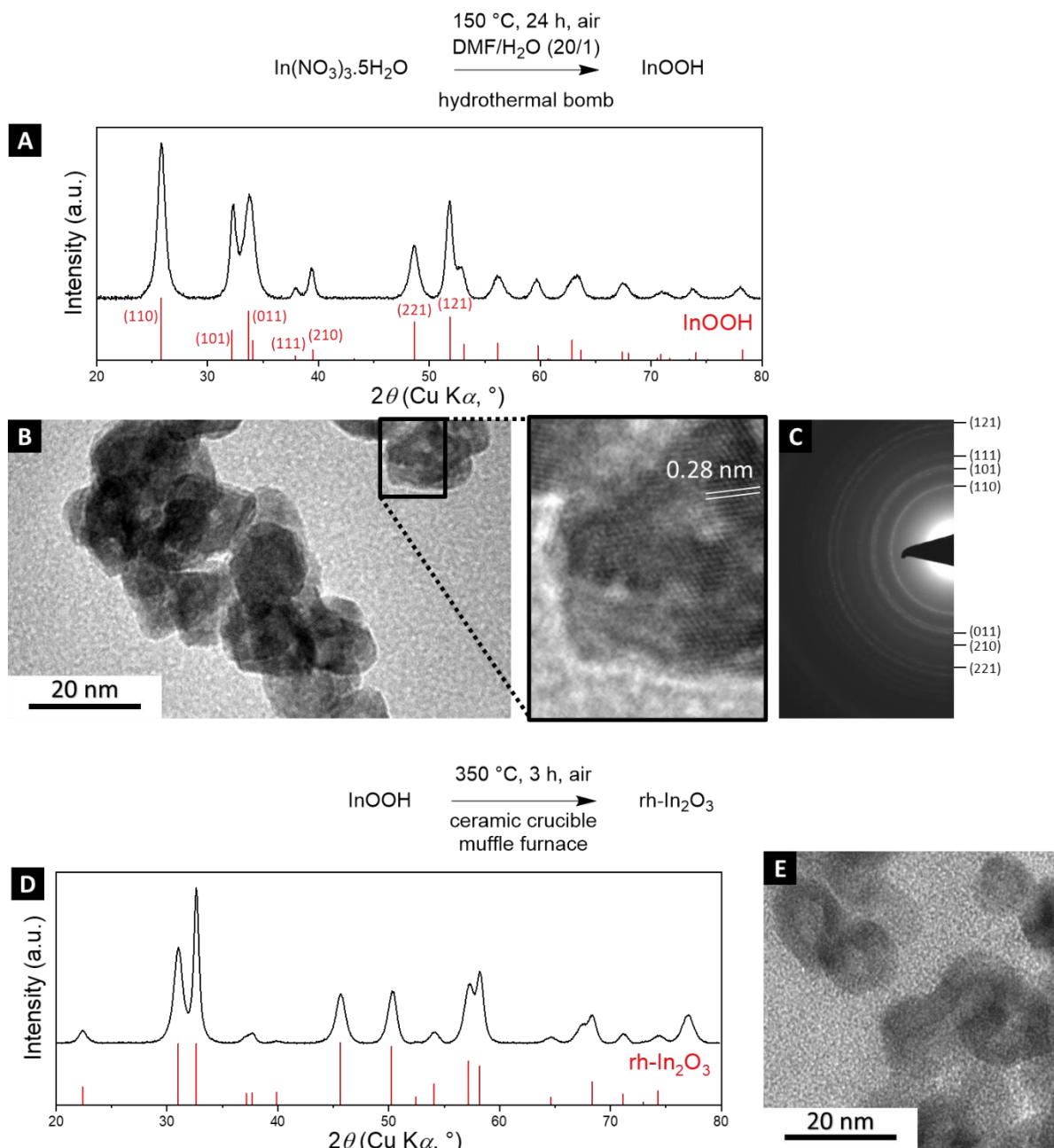


Figure 2. Synthesis and characterization of InOOH and rh-In₂O₃ from Synthesis V.2. (A) powder XRD, (B) TEM images and (C) electron diffraction of the intermediate material. (D) powder XRD and (E) TEM image of the final material.

In order to introduce acidic Bi^(III) atoms in rh-In₂O₃, the synthesis of a bismuth doped rhombohedral indium oxide rh-Bi_{0.02}In₂O₃ phase was attempted *via* a bismuth doped indium oxyhydroxide Bi_{0.01}InOOH phase. The protocol was similar to the one used for non-doped rh-In₂O₃ (Synthesis V.2.) with the substitution of 1 % of the indium nitrate precursor by the bismuth nitrate one (Bi(NO₃)₃ · 5H₂O). The material after the hydrothermal step was a grey powder (372 mg, 82 %). According to XRD, it was composed of InOOH as the major species and of Bi(0) [PDF card N°00-005-0519] as a minor species (Figure 3A): the Bi_{0.01}InOOH was not formed. After the calcination step, the powder turned ochre, a part of the InOOH was converted into rh-In₂O₃ and the Bi(0) phase disappeared in favor of the tetragonal bismuth oxide β-Bi₂O₃ [PDF card N°04-007-1443] (Figure 3B). As the synthesis of a bismuth doped rhombohedral indium oxide rh-Bi_{0.02}In₂O₃ phase failed following this route, no further work was conducted in this direction.

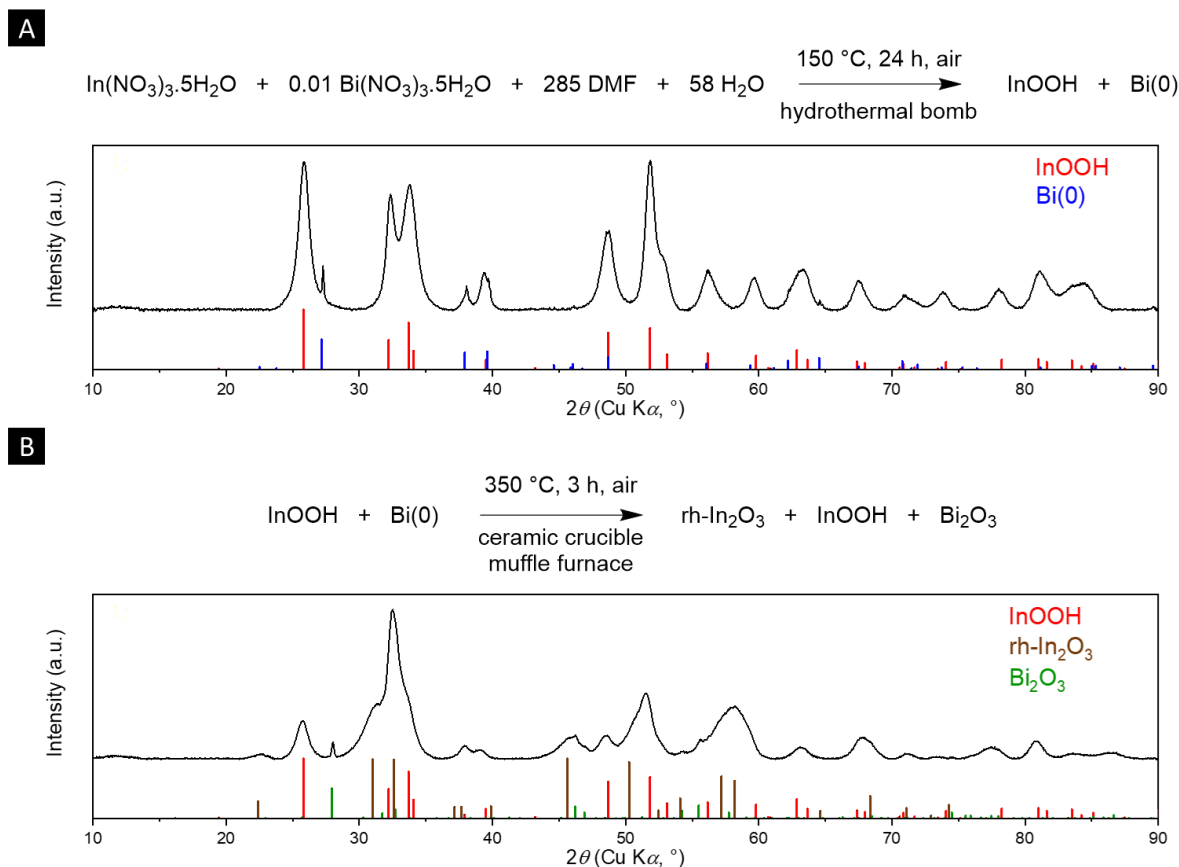


Figure 3. Attempt at the synthesis of rh-Bi_{0.02}In₂O₃. Powder XRD (A) of the intermediate product and (B) of the final product.

V.2. Hydrogenation reactions

To test the catalytic activity of indium oxide catalysts for hydrogenation reactions, a protocol similar to that used for ceria catalysts was followed (Catalysis IV.1.): the reaction was conducted overnight in toluene with an H_2 pressure of 7 bar (Table 1). The catalyst loading was of 5.3 mol% based on the number of In atoms. The crude reaction was directly analyzed using 1H NMR (Figure 4). At 100 °C, no reproducible conversion of phenylacetylene in styrene was recorded both in absence and presence of PPh_3 (entries 1-6). Instead, low amounts of acetophenone were detected at 2.63 ppm and 7.99 ppm, the oxidation reaction being presumably catalyzed by the metal oxide. Increasing the reaction temperature to 150 °C led to a higher oxidation yield in acetophenone (6 % vs 2 % on average at 100 °C) and to the hydrogenation of $PhCCH$ in styrene with a modest yield between 2 % and 10 % (entries 7-9). Though low, this conversion attested the catalytic activity of $c-Bi_{0.02}In_2O_3$ as no hydrogenation occurred without catalyst. At 200 °C, 25 % of the initial phenylacetylene were recovered at the end of the reaction while the combined yields of styrene and acetophenone accounted for only 12 to 20 % (entries 10-11). Ill-defined signals appeared in the aromatic region in 1H NMR, we therefore hypothesized side reactions occurred either on phenylacetylene or on the formed styrene, for instance oligomerization reactions. The possible effect of the addition of a phosphine at 150 °C or 200 °C is in the error bar of the conversion yield and we cannot conclude at this stage on the possible synergy between the NPs and the molecular base on H_2 activation.

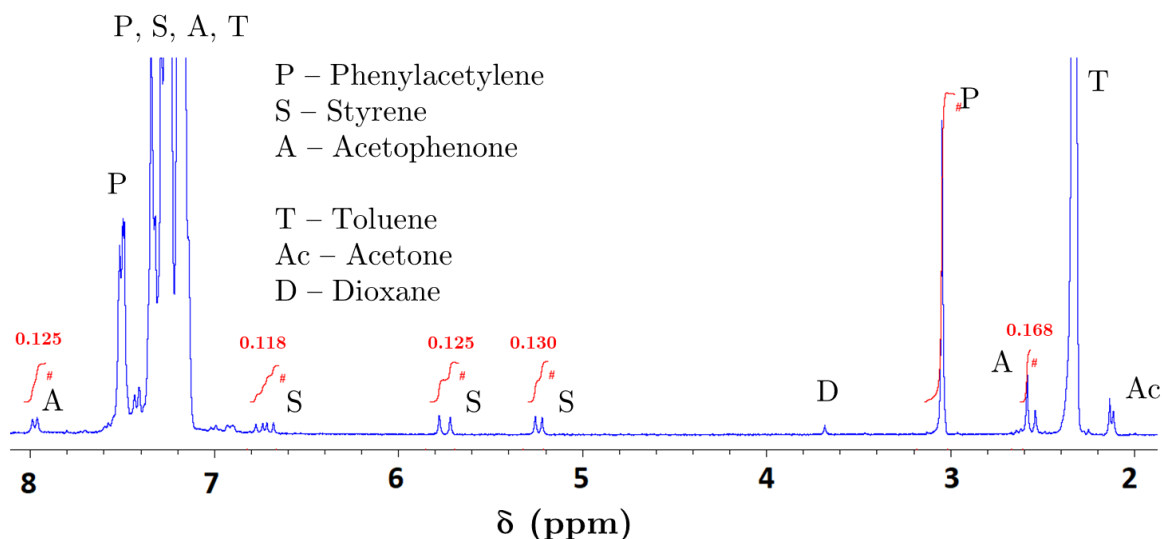


Figure 4. 1H NMR spectrum of crude reaction phenylacetylene in toluene at 150 °C in presence of $Bi_{0.02}In_2O_3$. Traces of acetone and dioxane do not originate from the synthesis.



	Catalyst (5.3 mol%)	Phosphine (10 mol%)	Temp.	PhCCH conversion	Styrene yield	Acetophenone yield
1	c-Bi _{0.02} In ₂ O ₃	-	100 °C	< 10 %	0 %	3 %
2				< 10 %	0 %	2 %
3				< 10 %	0 %	2 %
4		PPh ₃		< 10 %	2 %	1 %
5				< 10 %	0 %	2 %
6				< 10 %	0 %	1 %
7		-	150 °C	10 %	2 %	6 %
8				17 %	10 %	6 %
9		PPh ₃		10 %	3 %	6 %
10		-	200 °C	75 %	4 %	8 %
11		PPh ₃		75 %	8 %	12 %

Table 1. Hydrogenation of phenylacetylene with indium oxide catalysts. Reaction conditions: 220 μ L of phenylacetylene (2 mmol), 30 mg of catalyst (0.106 mmol, [In] 5.3 mol%), 1 mL of toluene (9.4 mmol), H₂ (7 bar, 7 mmol), 16 h in autoclave (25 mL). Conversion and yield determined by NMR.

V.3. Conclusion

In conclusion, two types of indium oxide nanoparticles were synthesized following protocols from literature (c-Bi_{0.02}In₂O₃, rh-In₂O₃) and the bismuth doped one was tested for phenylacetylene hydrogenation in toluene. At 100 °C, no hydrogenation was observed but a low conversion in acetophenone, an oxidation product, occurred. At higher temperatures, 150 °C and 200 °C, styrene was detected as a minor species, in addition to acetophenone. There did not seem to be a strong influence of the presence of PPh₃. The low activity of the catalyst at these temperatures could have been expected as high hydrogenation rates of acetylene and CO₂ in gas phase were obtained only for temperatures between 230 °C and 300 °C.^{1,2}

We suggest complementary experiments could be performed to study the hydrogenation activity of rh-In₂O₃ as Ozin *et al.* reported a higher activity for this polymorph than for c-In₂O₃,^{2,10} or to use a model substrate having a chemistry closer to that of CO₂ such as benzaldehyde. Furthermore, we showed in Chapter I that the H₂ pressure has a crucial importance on the gas solubility and therefore on the reaction yields, we estimate catalytic trials at moderate temperatures, *i.e.* 150 °C, but higher H₂ pressures, typically 30 bar, would be worthwhile to conclude on the impact of the phosphine.

V.4. Bibliography

1. Albani, D. *et al.* Semihydrogenation of Acetylene on Indium Oxide: Proposed Single-Ensemble Catalysis. *Angew. Chemie Int. Ed.* **56**, 10755–10760 (2017).
2. Yan, T. *et al.* Polymorph selection towards photocatalytic gaseous CO₂ hydrogenation. *Nat. Commun.* **10**, 2521 (2019).
3. Hoch, L. B. *et al.* The Rational Design of a Single-Component Photocatalyst for Gas-Phase CO₂ Reduction Using Both UV and Visible Light. *Adv. Sci.* **1**, 1400013 (2014).
4. Ozin, G. A. & Veer, C. Illuminating CO₂ reduction on frustrated Lewis pair surfaces: investigating the role of surface hydroxides and oxygen vacancies on. 14623–14635 (2015).
5. Ghuman, K. K. *et al.* Surface Analogues of Molecular Frustrated Lewis Pairs in Heterogeneous CO₂ Hydrogenation Catalysis. *ACS Catal.* **6**, 5764–5770 (2016).
6. Dong, Y. *et al.* Tailoring Surface Frustrated Lewis Pairs of In₂O_{3-x}(OH)_y for Gas-Phase Heterogeneous Photocatalytic Reduction of CO₂ by Isomorphous Substitution of In³⁺ with Bi³⁺. *Adv. Sci.* **6**, 1700732 (2018).
7. Yan, T. *et al.* Bismuth atom tailoring of indium oxide surface frustrated Lewis pairs boosts heterogeneous CO₂ photocatalytic hydrogenation. *Nat. Commun.* **11**, 6095 (2020).
8. Yan, T. *et al.* Controlled preparation of In₂O₃, InOOH and In(OH)₃ via a one-pot aqueous solvothermal route. *New J. Chem.* **32**, 1843 (2008).
9. Nielsen, I. G., Sommer, S. & Iversen, B. B. Phase control for indium oxide nanoparticles. *Nanoscale* **13**, 4038–4050 (2021).
10. Dang, S. *et al.* Rationally designed indium oxide catalysts for CO₂ hydrogenation to methanol with high activity and selectivity. *Sci. Adv.* **6**, eaaz2060 (2020).

Part 3

Solvothermal syntheses

Chapter VI

Non-aqueous syntheses of molybdenum and tungsten oxides for hydrogenation reactions

In this chapter, we target the use of early transition metal oxides as hydrogenation catalysts in colloidal solutions. There are rare occurrences in literature of the use of these compounds for H_2 activation in solvent. As developed in Chapter I, numerous works on the use of metal oxides for H_2 activation stressed the role of the oxygen defects to create active sites.³⁻⁵ Seebauer *et al.* studied in 2014 the relation between the Fermi level position of a series of metal oxides and their catalytic activity for reactions implying their Lewis acidity.² They concluded WO_3 and MoO_3 were the more susceptible to present a strong Lewis acidity on the metallic center. We therefore chose MoO_{3-x} and WO_{3-x} as potential FLP-like catalysts. A work by Wang *et al.* reported in 2015 the reduction of linear and cyclic olefins as well as of nitroarenes by oxygen deficient tungsten oxide $WO_{2.72}$.¹ They proved the catalytic activity of the material was linked to the presence of defects, the reaction rate was indeed directly proportional to the surface oxygen vacancies density. A DFT study supported this conclusion: the H_2 splitting was found to be more favorable on $WO_{2.72}$ than on WO_3 on both the thermodynamical and kinetical aspects. To the best of our knowledge, there is no mention of molybdenum oxide as a stand-alone hydrogenation catalyst in solvent.

To minimize the surface hydroxyl group density which would occupy the oxygen vacancy sites and potentially protonate the molecular co-catalyst, we performed the syntheses in non-aqueous conditions. Furthermore, this synthetic pathway also leads to organophilic surface ligands that will improve the colloidal stability of the metal oxides during catalysis.

Different goals were pursued in this chapter:

- (1) Synthesizing molybdenum and tungsten oxides following non aqueous pathways and characterizing their surface state (surface ligands, active sites) for catalytic applications
- (2) Reproducing the results obtained by Wang *et al.* on the use of $W_{18}O_{49}$ for hydrogenation reactions and extending them to the use of MoO_x particles
- (3) Studying the impact of the addition of a cocatalyst, such as a tertiary phosphine, as mentioned for cerium oxide and indium oxide catalysts in Chapters IV and VI

We developed in the first section (VI.1.) the study of the non-aqueous syntheses of tungsten oxide ($\text{W}_{18}\text{O}_{49}$) and molybdenum oxide (MoO_x , $2 < x < 3$) nanoparticles. For this last material, a more in-depth study of the synthesis was required than for $\text{W}_{18}\text{O}_{49}$ due to the difficulty to characterize it by XRD. The materials were then tested in section VI.2. for hydrogenation reactions of nitrobenzene and phenylacetylene. This last section only reports preliminary data.

VI.1. Non-aqueous metal oxide syntheses in high boiling point solvents

In a solvothermal nanoparticle synthesis, the solvent molecule may have different roles beyond the sole one of reaction medium: it may be the reducing agent if the degree of oxidation of the metal center diminishes,⁶ it may provide light elements by decomposition for non-purely metallic particles syntheses (oxide^{7,8} carbide,⁹ phosphide¹⁰) and it may ensure the stability of the colloidal suspension by playing the role of ligand. This versatility allows simple reactions to be run with only one metal precursor, typically a metal chloride, alkoxide, acetate or acetylacetonate complex, and one liquid reagent, typically oleylamine or benzyl alcohol.^{11,12} But this versatility also complicates the understanding of the reaction mechanisms as the organic and inorganic processes are intertwined. Correlating the two aspects requires the use of multiple characterization techniques: NMR (Nuclear Magnetic Resonance), GC-MS (Gas Chromatography – Mass Spectrometry) and FTIR (Fourier Transform Infrared) to monitor the molecular species transformations and XRD (X-Ray Diffraction), XAS (X-Ray Absorption), XPS (X-Ray Photoelectron Spectroscopy), SAXS (Small Angle X-Ray Scattering) and electron microscopy for the inorganic counterpart (crystal phase, local environment of the atoms, degree of oxidation, morphology).^{6,12–15}

Our approach focuses here on the understanding of the mechanism leading to the NPs formation. Indeed, we target a fine understanding of the surface state: what are the surface ligands, what is the environment of the surface metal atoms. These points are crucial for the catalytic reactions envisioned and will be addressed through a use of a combination of organic (NMR) and inorganic (XRD, XAS, electron microscopy) characterization techniques. To simplify the system and therefore its rationalization, we used solvents which are classical reaction media for non-aqueous NPs syntheses and basic precursors (WCl_6 and $\text{MoO}_2(\text{acac})_2$). We present here a study of the syntheses of tungsten and molybdenum oxides in high boiling point solvents (oleylamine, oleic acid and oleyl alcohol) and in mixtures thereof.

VI.1.1 Tungsten oxide $W_{18}O_{49}$ nanowires

We first reproduced the synthesis reported by Leite *et al.* for the synthesis of tungsten oxide nanowires ($W_{18}O_{49}$) in a mixture oleyl alcohol/oleylamine (8/0.5) (v/v) (Synthesis VI.1.).¹⁶

Synthesis VI.1. Tungsten oxide nanowires. In a 25 mL three-necked round-bottom flask, 8 mL of oleyl alcohol (OAl) (25.2 mmol, 66 equiv.) and 0.5 mL of oleylamine (OAm) (1.51 mmol, 4 equiv.) were degassed under vacuum at r.t. during 20 min and the flask was purged with N_2 three times. Under N_2 , 150 mg of WCl_6 (0.38 mmol, 1 equiv.) were added to the solution. The resulting yellow solution was heated up to 220 °C under stirring. It turned violet-blue at approximately 80 °C and white fumes appeared at 120 °C. The solution became dark blue at 170 °C and was let to react 2 h 30 at 220 °C. After cooling to r.t. under N_2 , acetone (10 mL) was added to the crude solution and a dark blue solid was isolated by centrifugation (9,000 rpm, 10 min, 20 °C). The blue supernatant was removed and the particles were redispersed in toluene (2 mL), precipitated by adding acetone (4 mL) and centrifugated. This operation was repeated another time. The obtained blue-violet powder (78 mg, 91 % yield) was then dried under N_2 and stored under inert atmosphere.

The XRD of the obtained powder, displayed on Figure 1A, is attributed to an oxygen-deficient tungsten oxide $W_{18}O_{49}$ [PDF card N°00-064-0773]. No calculations of the Scherrer size of the crystallites can be performed considering the large width of the peaks: the characteristic size is below 5 nm for the peaks (200), (202) and (240) at respectively 28.2°, 37.0° and 56.7°. The diffraction peaks corresponding to the lattice planes (020) and (040) at 23.5° and 48.1° are thinner than the (200), (202) and (240) ones, indicating the objects are anisotropic with the **b** axis as the preferential direction (Figure 1E). Transmission Electron Microscopy reveals the objects are nanowires, 100-500 nm long and 1-2 nm wide (Figure 1B-C). The highly anisotropic morphology is coherent with the XRD peaks of different width depending on the crystallographic direction: the nanowires have grown along the **b** direction. The electron diffraction pattern is in line with the XRD with two intense rings corresponding to the (020) and (040) diffraction planes (Figure 1D).

Depending on the batch, the powder color varied from royal blue to petrol blue. As comparison, tungsten trioxide (WO_3) is yellow-green. The blue color in oxygen-deficient tungsten oxides is due to a cation-to-cation charge transfer between $W^{(VI)}$ and a reduced tungsten atom, $W^{(V)}$ or $W^{(IV)}$.¹⁷ These two lower oxidation states are allowed by the loss of oxygen atoms in $W_{20}O_{58}$ ($WO_{2.9}$) and $W_{18}O_{49}$ ($WO_{2.72}$) but are absent of WO_3 .

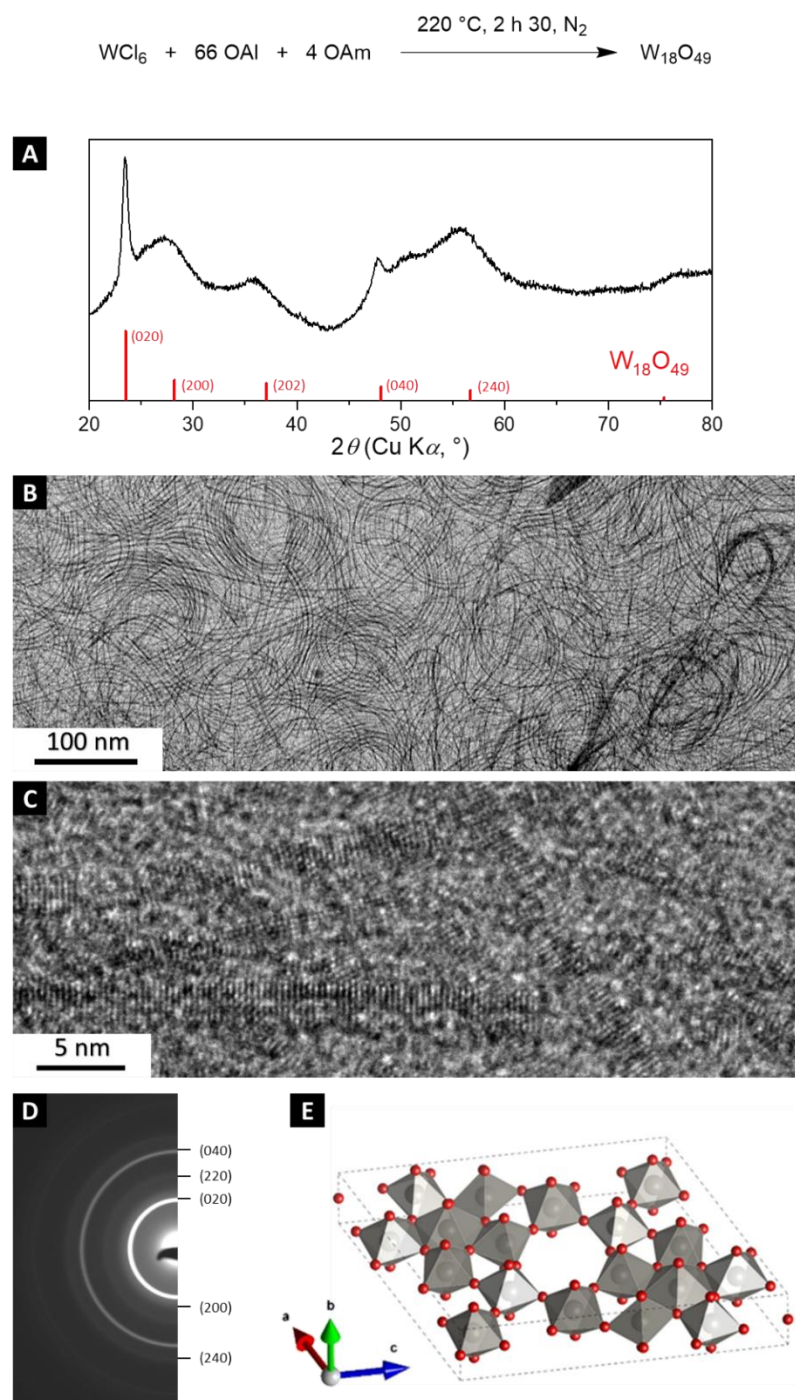


Figure 1. Synthesis and characterization of $\text{W}_{18}\text{O}_{49}$ nanowires with (A) powder XRD with (hkl) attributions, (B-C) TEM images and (D) electron diffraction pattern. (E) Crystal structure of $\text{W}_{18}\text{O}_{49}$ (red: oxygen, grey; tungsten). Picture created with Vesta software.¹⁸

On the first attempts at synthesizing $\text{W}_{18}\text{O}_{49}$ nanowires, W(0) was systematically detected in XRD (peaks at 40° , 58° and 73° , Figure 2). These peaks, corresponding to an minor species, were only detected because the XRD signal of the main product ($\text{W}_{18}\text{O}_{49}$) was particularly broad. We first hypothesized the metallic tungsten may originate from a reduction by oleylamine as this last molecule is known for being a

reducing agent when nanoparticles are formed from $M(\text{acac})_2$.¹¹ We therefore explored sets of conditions in order to limit this reduction reaction, playing on the OAl/OAm/OAc ratio and on the reaction temperature (Table 1). For OAl/OAm ratios of 8/3, 8/1 and 8/0.5 at 220 °C, the W(0) peaks were always present (Figure 2, entries 1-3). The absence of oleylamine or its substitution by oleic acid also led to a material identified as $W_{18}O_{49}$ by XRD but the syntheses were much more explosive and had to be stopped before their ends (Figure 2, entries 4-5). Moreover, TEM images revealed ill-formed agglomerated particles rather than well dispersed nanowires. We concluded the presence of oleylamine was essential to the formation of the tungsten oxide nanowires, probably as a ligand molecule. When reaction temperature was set to 260 °C, hexagonal tungsten trioxide (WO_3) 100 nm large cube-like nanoparticles were obtained in addition of the $W_{18}O_{49}$ nanowires (Figure 2, entry 6).

	Oleyl alcohol (OAl)	Oleylamine (OAm)	Oleic acid (OAc)	Temperature	XRD phase attribution	Morphology
1	8 mL	3 mL	-	220 °C	$W_{18}O_{49} + W(0)$	Nanowires
2	8 mL	1 mL	-	220 °C	$W_{18}O_{49} + W(0)$	Nanowires
3	8 mL	0.5 mL	-	220 °C	$W_{18}O_{49} + W(0)$	Nanowires
4	8 mL	-	-	220 °C	$W_{18}O_{49} + W(0)$	Ill-shaped
5	8 mL	-	0.5 mL	220 °C	$W_{18}O_{49} + W(0)$	Ill-shaped
6	8 mL	1 mL	-	260 °C	WO_3	Cubes
7	8 mL	0.5 mL	-	240 °C	$W_{18}O_{49} + W(0)$	Nanowires
8 ^a	8 mL	0.5 mL	-	240 °C	$W_{18}O_{49} + W(0)$	Nanowires
9 ^b	8 mL	0.5 mL	-	220 °C	$W_{18}O_{49}$	Nanowires

Table 1. Sets of conditions for $W_{18}O_{49}$ nanowires syntheses from Synthesis VI.3. ^aWCl₆ from Strem Chemicals. ^bWCl₆ from Sigma Aldrich, purified by sublimation.

Finally, considering as unlikely that tungsten was reduced to its metallic state from $W^{(VI)}$, we investigated whether the W(0) was already present in the metal hexachloride precursor (WCl₆). PXRD of the commercial WCl₆ powder from Sigma-Aldrich was recorded and revealed traces of W(0) in addition of α -WCl₆ at 73.3° (Figure 3). We therefore used WCl₆ from two different providers (Sigma Aldrich and Strem Chemicals) but the same W(0) residual signal was observed in both cases (Figure 2, entries 7-8). These traces were certainly a leftover of the chlorination of W(0) by Cl₂ for the WCl₆ production. The commercial precursor was purified by sublimation (experimental procedure for sublimation described in Appendix I ES.1.) and no W(0) signal was recorded anymore on the final diffractograms of the $W_{18}O_{49}$ nanowires

(Figure 2, entries 9). For the rest of the work and the catalysis section, we only used purified WCl_6 . This $\text{W}(0)$ signal was also present, although not commented, in the work of Leite¹⁶ but not in the one of Niederberger.⁷

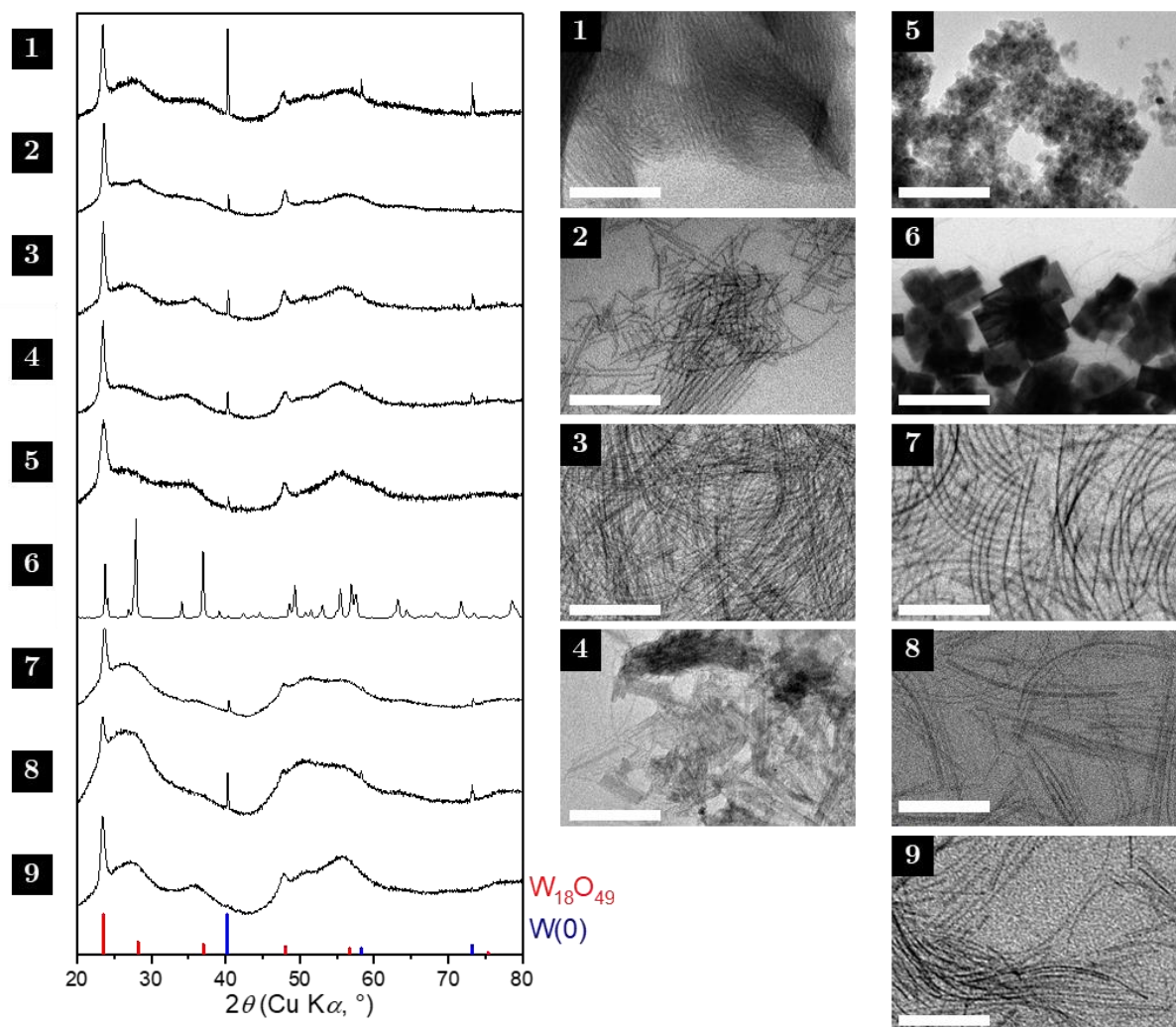


Figure 2. Powder X-ray diffractograms and TEM images of tungsten oxides for different sets of experimental conditions (numbers refer to Table 1). Dispersion solvent was THF for (1) and hexane for (2-9). The scale bar represents 50 nm, except for (6) where it represents 200 nm.

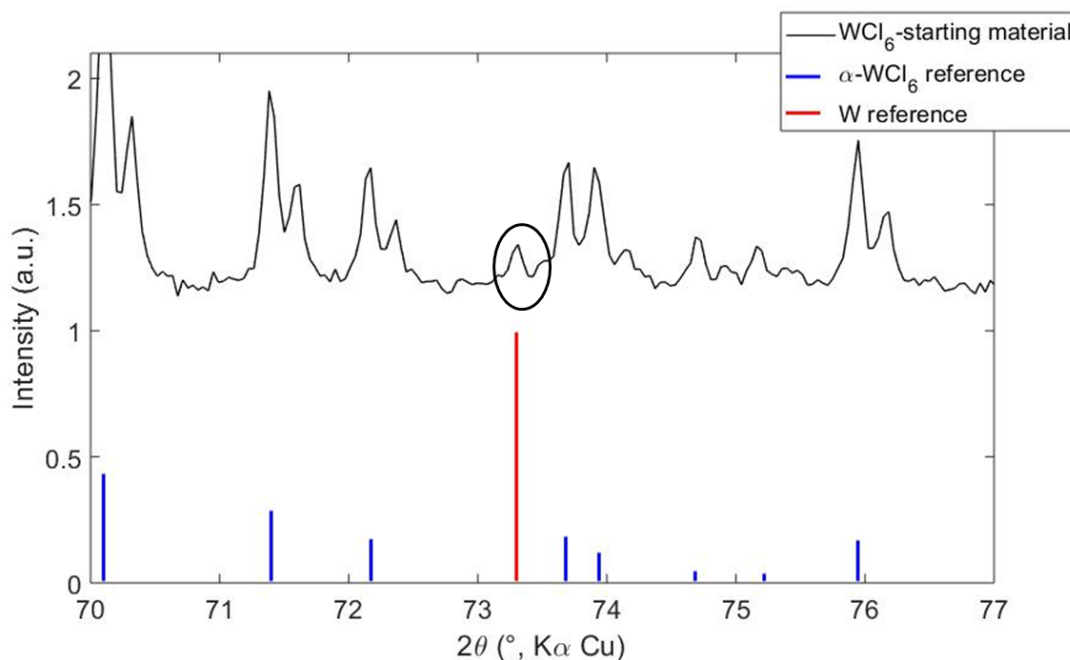


Figure 3. Zoom on the XRD pattern of the WCl_6 precursor from Sigma-Aldrich. All diffraction peaks are doublet as the X-ray beam from the copper anode is not perfectly monochromatic but comports two contributions, $\text{K}\alpha_1$ and $\text{K}\alpha_2$.

VI.1.2 Molybdenum oxide nanoparticles

We then attempted a synthesis of MoO_x ($2 < x < 3$) nanoparticles by thermal decomposition of $\text{MoO}_2(\text{acac})_2$ in pure oleylamine (OAm) (Synthesis VI.2.) or oleic acid (OAc) (Synthesis VI.3.). This synthetic pathway is at the intersection of a work by Tatsuma *et al.* synthesizing oxygen deficient molybdenum oxides in fatty acids from $\text{MoO}_2(\text{acac})_2$,¹⁹ and of Niederberger *et al.* using MoO_2Cl_2 as precursor in a mixture benzyl alcohol/acetophenone to synthesize MoO_2 nanoparticles.¹³ In this last work, the authors described a complete study of the synthesis mechanism with *in situ* XAS measurements.

Synthesis VI.2. Molybdenum oxide nanoparticles in OAm. In a round-bottom flask, 10 mL of oleylamine (OAm) (30.4 mmol, 66 equiv.) were degassed under vacuum at r.t. during 20 min and the flask was purged with N₂ three times. Under N₂, 150 mg of MoO₂(acac)₂ (0.46 mmol, 1 equiv.) were added to the solution. The resulting pale-yellow solution was heated up to 220 °C under agitation and turned gradually from pale yellow to dark brown between 85 °C and 125 °C. Condensation of a colorless liquid was observed at 115 °C. The solution was let to react 2 h at 220 °C. After cooling to r.t. under N₂, methanol (10 mL) was added to the crude solution and a brown solid was isolated by centrifugation (9,000 rpm, 10 min, 20 °C). The supernatant was removed and the particles were redispersed in toluene (5 mL), precipitated by adding methanol (10 mL) and centrifugated. This operation was repeated another time. The obtained brown powder (63 mg) was then dried under a flux of N₂ and stored in air.

[*Caution*] OAm and OAc are degraded upon heating if exposed to air, emitting acrid smokes and irritating white fumes. Their respective smoke points are situated *ca.* 150 °C and 120 °C respectively.

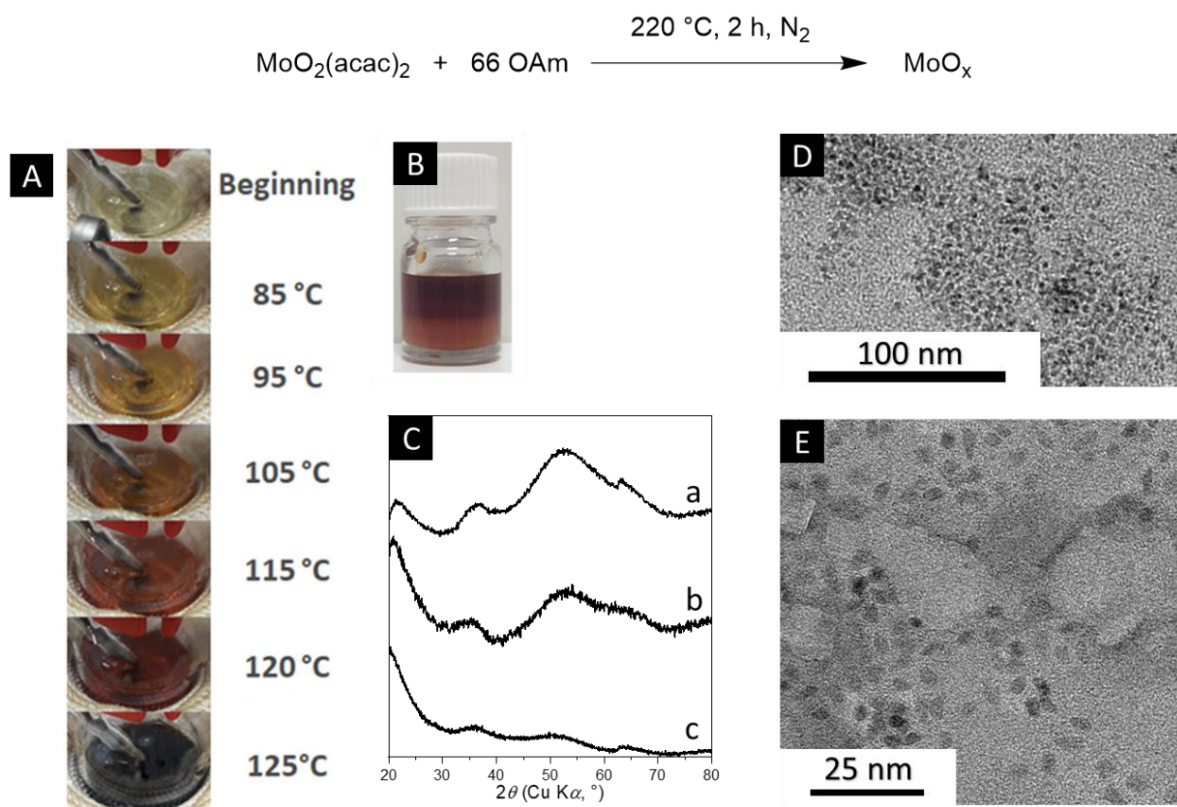


Figure 4. Molybdenum oxide synthesis from MoO₂(acac)₂ in OAm according to Synthesis VI.2. (A) Color evolution and (B) final state of the solution. (C) XRD of the powders when solvent was decylamine (DAm) (a) ($T_{\text{reaction}} = 217\text{ }^\circ\text{C}$) and OAm (b-c). (D-E) TEM images of nanoparticles synthesized in OAm.

Synthesis VI.3. Molybdenum oxide nanoparticles in OAc. In a round-bottom flask, 10 mL of oleic acid (OAc) (32 mmol, 69 equiv.) were degassed under vacuum at r.t. during 20 min and the flask was purged with N₂ three times. Under N₂, 150 mg of MoO₂(acac)₂ (0.46 mmol, 1 equiv.) were added to the solution. The resulting yellow suspension (solid not dissolved) was heated up to 220 °C under agitation. At approximately 50 °C, the solid dissolved and the solution turned dark blue within a few minutes *via* green and turquoise. The solution turned gradually from blue to dark brown between 100 °C and 140 °C. The solution was let to react 2 h at 220 °C and then let to cool down to r.t. under N₂. The nanoparticles could not be isolated by addition of a counter-solvent (acetone, EtOH, MeOH). They were stored as a stable suspension in OAc under N₂. The solution turned green-grey after a few hours if exposed to air.

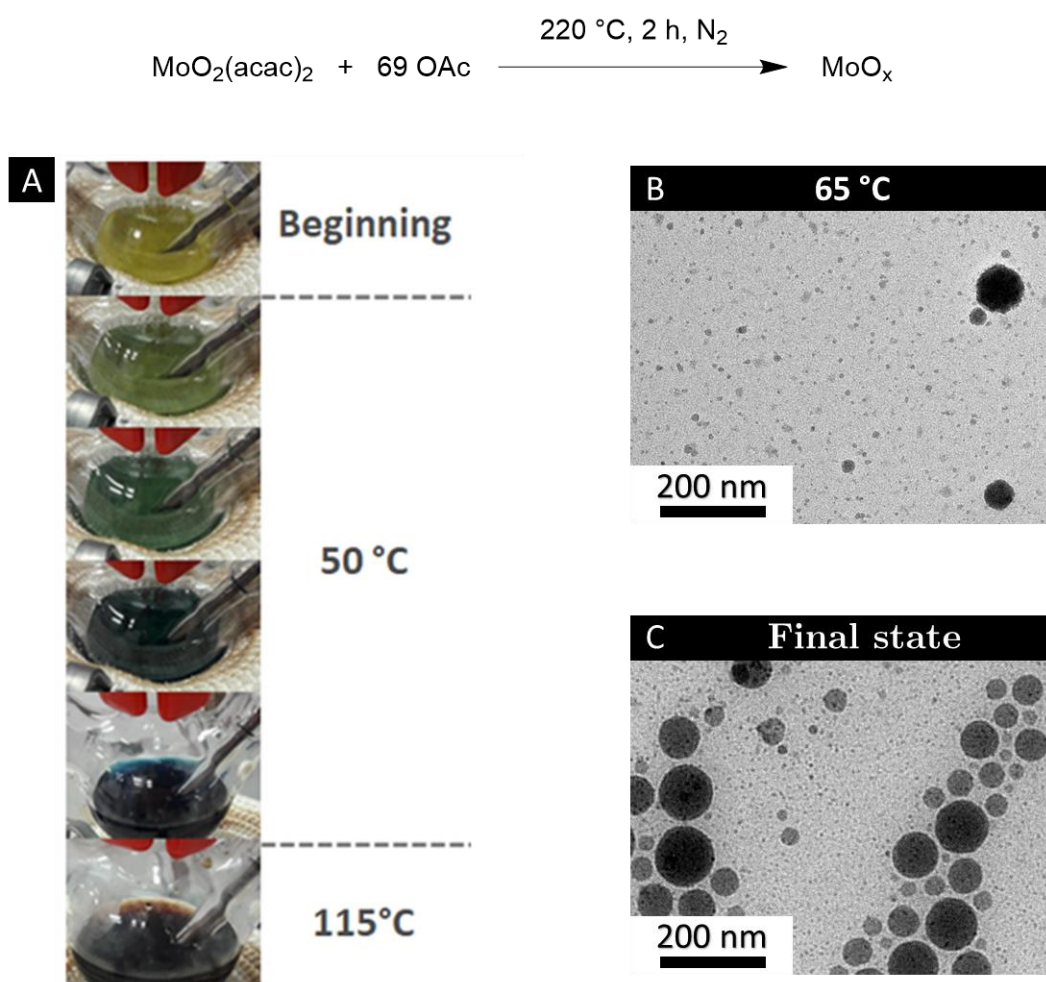


Figure 5. Molybdenum oxide synthesis from MoO₂(acac)₂ in OAm according to Synthesis VI.3. (A) Color evolution of the solution. TEM images of (B) an aliquot collected at 65 °C and (C) of the final state.

Non aqueous synthesis in OAm. Synthesis VI.2. reports the synthesis with oleylamine as solvent. The precursor was first dissolved at room temperature and formed a pale-yellow solution, suggesting the formation of a complex between oleylamine and $\text{MoO}_2(\text{acac})_2$. Upon heating, the solution gradually turned brown (Figure 4A). This color was attributed to plasmonic transitions in MoO_x nanoparticles.¹⁹ The absorbed frequencies depend on the size of the particles and on the density of charge carriers, *i.e.* oxygen defects here.²⁰ A kinetic study by UV-visible spectroscopy would therefore be of interest to determine whether the apparent colour change from yellow to brown was only due to the nanoparticles concentration or if the characteristic energies of the plasmonic transitions themselves were modified during the reaction. Just after synthesis, the colloidal suspension was stable but a light brown material sedimented along the following hours/days (Figure 4B). The XRD of the collected powder is not informative on the chemical composition of the material because of the broadness of the measured diffractograms (Figure 4C). However, the pattern was reproducible from batch to batch, even when substituting the OAm solvent by the similar one decylamine (DAm) (all other parameters kept identical, including solvent volume). TEM of the material dispersed in THF reveals the presence of elongated nanoparticles (Figure 4D-E). Their typical size is close to 2 nm, in line with the broad diffractogram features. Based on close works of reduction of $\text{MoO}_2(\text{acac})_2$ in fatty acids,¹⁹ we can suggest the obtained material was an amorphous molybdenum oxide and will be referred to as $\text{MoO}_x\text{-OAm}$ in the following.

Non aqueous synthesis in OAc. In Synthesis VI.3 in oleic acid and contrarily to Synthesis VI.2., the precursor $\text{MoO}_2(\text{acac})_2$ did not dissolve as a pale-yellow solution but rather stayed suspended as yellow aggregates (Figure 5A). Upon heating to 50 °C, the yellow solid disappeared to form a deep blue solution. Aliquots were collected at different times of the reaction to perform UV-vis measurements but the color of the solution changed to dark green in a few seconds once removed from the N_2 protected round bottom flask. This color change was probably due to the oxidation of molybdenum species when exposed to air. We observed the transition from the yellow ill-dissolved $\text{MoO}_2(\text{acac})_2$ precursor to the blue solution also occurred at room temperature on longer timescales, typically a few days.

We could not determine whether the blue color displayed between 50 °C and 100 °C correspond to plasmonic transitions in the molybdenum oxide nanoparticles already formed or from the color of a molybdenum dioxo complex. One could imagine a neutral complex $[\text{MoO}_2(\text{OAc})_2]$ between a $[\text{MoO}_2]^{2+}$ moiety and oleate ions. The complex geometry would be either a tetrahedron, a distorted octahedron with the carboxylate ligands coordinating the metal in a $\kappa^2(\text{O},\text{O-bidentate})$ mode,²¹ or even a polynuclear species. We could not find any mention in the literature of a $[\text{MoO}_2]$ -oleate complex but oleate complexes of a large range of metals (Zn^{22} , Cd^{22} , $\text{Fe}^{23,24}$, Mn^{25}) leading to NPs by thermal decomposition are reported. These oleate complexes generally have

ill-defined stoichiometries with dynamic structures, making them difficult to describe.²⁴ Resolving the structure of this hypothetical molybdenum complex was beyond the scope of this work.

When the temperature was increased above 120 °C, the suspension turned brown, just as with pure OAm (Figure 5A). We interpreted this last evolution as the formation of molybdenum oxide nanoparticles and the quasi-total consumption of the blue coloured complex if it existed. No XRD study was performed on MoO_x-OAc as the powder could not be isolated by addition of a counter-solvent. The suspensions were stable for at least 6 months under ambient conditions in air. TEM of the final solution reveals the presence of spherical nanoparticles (Figure 5C). The particles are polydisperse with diameters ranging from 10 to 200 nm. TEM of an aliquot collected at 65 °C already displays the presence of spherical nanoparticles: they seem smaller (up to 60 nm in diameter) than at the end of the reaction but the large polydispersity in size renders size measurement by TEM delicate. We envision a kinetic study of the morphology by collecting aliquots at different moments of the reaction course. Electron microscopy is by essence a technique which is not representative of the whole sample, we therefore used other techniques sensitive to the average signal, such as XAS mentioned later.

Non aqueous synthesis in OAm/OAc mixture. Finally, the reaction was run in a mixture of both solvents OAm/OAc (90:10) (v:v). The color evolution of the reaction medium was similar to the one with pure OAm and the XAS spectrum of the liquid crude at the end of the reaction was very close to that of pelletized MoO_x-OAm from Synthesis VI.2. (*cf.* below Figure 8). The suspension was as stable as the reaction in pure OAc. These observations suggest the dominant synthesis mechanism was the one associated with OAm as solvent but that the OAc molecules helped at the nanoparticles suspension stability and prevented the sedimentation. We conclude oleate ions are excellent ligands for these metal oxides in organic solvents. Considering the hydrophobic moieties of OAc and OAm are the same, we interpret the sedimentation with OAm as the absence of tight bond between the nanoparticle and the amine ligand. Although the stability of the suspension is limited, the loose coordination of the OAm molecules compared to the oleate ions at the nanoparticle surface favors the approach of substrate molecules in the context of catalysis.

NMR study. ¹H solution NMR was performed on reaction crudes to enlighten the molecular reactions at stake during the nanoparticle syntheses. The ¹H NMR spectrum of MoO₂(acac)₂ in CDCl₃ was first recorded under ambient conditions (Figure 6C). Signals measured at 5.80 ppm (H⁸), 2.16 ppm (H^{7,9}) and 2.14 ppm (H^{7,9}), all singlets, correspond to respectively the ethylenic and the methyl protons of the bound acac⁻ ligands in MoO₂(acac)₂.²⁶ Free acetylacetone (acacH) was also detected as an equilibrium between the dione, at 3.60 ppm (H¹, CH₂ singlet) and 2.24 ppm (H²,

two CH₃ singlet), and the enol tautomer, at 15.46 ppm (H⁶, OH singlet), 5.50 ppm (H⁴, CH singlet) and 2.05 ppm (H^{3,5}, two CH₃ singlet). Although the two methyl groups of the enol tautomer are chemically different, their chemical shifts are close enough to appear as a singlet. Free acetylacetone was detected in a solution of MoO₂(acac)₂ in CDCl₃ even when using dried aprotic solvents and freshly sublimed MoO₂(acac)₂.²⁶

We prepared a highly concentrated suspension of MoO₂(acac)₂ in oleic acid to be in capacity to detect organic products of the nanoparticle synthesis. The solution **A** (5 OAc molecules per MoO₂(acac)₂) was heated to 50 °C and produced a blue solution. The NMR spectrum of this solution **A** displays signals of MoO₂(acac)₂, acetylacetone and oleic acid but no other product (data not shown). We cannot consider the presence of acacH in the ¹H NMR spectrum at 50 °C as a proof of the protonation of acac⁻ by oleic acid as free acetylacetone signals were already present in the NMR spectrum of MoO₂(acac)₂. The concentrated solution **A** was then heated in a close reaction tube at 200 °C during two hours: it turned brown, as observed in Synthesis VI.3. After reaction, no MoO₂(acac)₂ was detected anymore by ¹H NMR and the signal of acetylacetone was more intense (Figure 6A). An integration of the peaks gave a final ratio 5:1 for OAc:acacH, to be compared with the ratio 5:2.2 for OAc:acac⁻ at 50 °C: not all the acetylacetonate ligands produced free acetylacetone. We do not have hypothesis on the molecular reactions at stake. At the end of the reaction, two intense peaks appeared at 2.09 ppm and 2.17 ppm (stressed by black arrows on Figure 6A) and modest ones at 1.83 ppm and *ca.* 2.5-2.6 ppm. The peak at 2.17 ppm could correspond to acetone but the other ones were not identified. Similar results were obtained with the crude of the regular reaction Synthesis VI.3. conducted in round bottom flask with diluted conditions (69 OAc molecules per MoO₂(acac)₂). The new features were less obvious considering the lower initial concentration of MoO₂(acac)₂ and the evaporation of volatile compounds (*T*_{boiling}(acacH) = 140 °C). We concluded the molybdenum precursor MoO₂(acac)₂ was entirely consumed to produce inorganic molybdenum species, presumably molybdenum oxides, and that there was a limited transformation of the solvent OAc (Figure 6A-B).

Xia *et al.* recently published a mechanistic study of the formation of Pt nanoparticles from Pt(acac)₂ while using oleic acid as solvent.²⁷ The authors reported the formation of Pt^(III)-oleate complex at 80 °C which were then decomposed in nanoparticles at 120 °C. The reduction of the metal center was associated to the decarbonylation/decarboxylation of OAc in CO/CO₂ and an alkyl chain. Hyeon *et al.* proposed a similar mechanism for the decomposition of Fe^(III)-oleate in Fe₃O₄ nanoparticles: they suggested the decomposition of metal carboxylates produced thermal free radicals R·, RCOO· and RC·O.²⁸ Similar mechanisms could be considered here for the decomposition in MoO_x (Scheme 1).

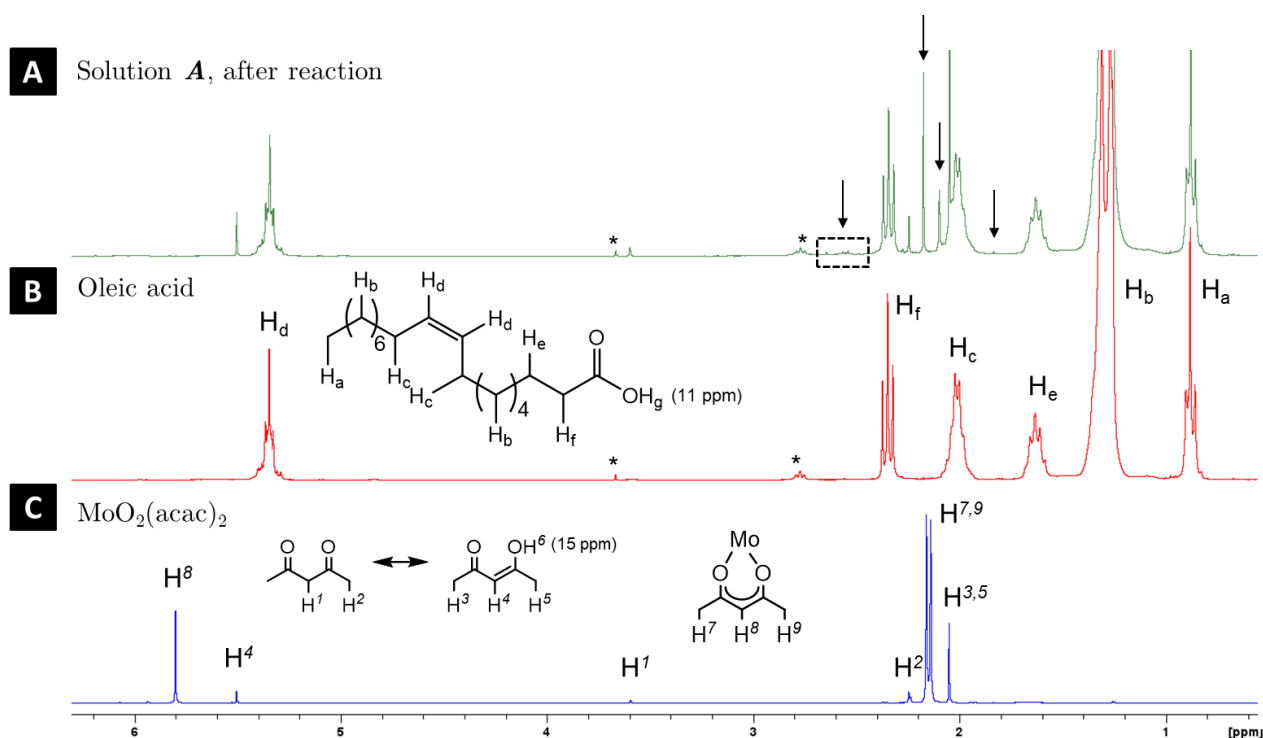
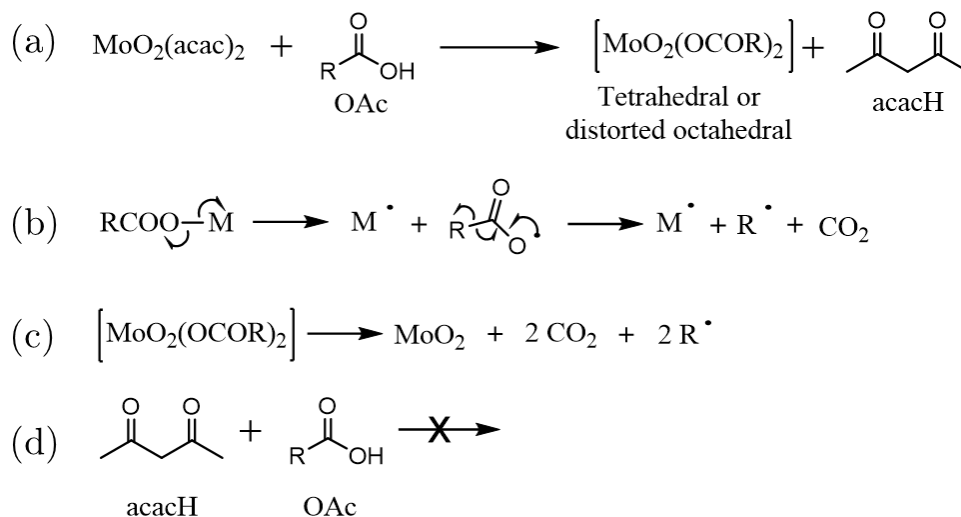


Figure 6. ^1H NMR spectra of (A) solution **A** after reaction, (B) oleic acid and (C) $\text{MoO}_2(\text{acac})_2$ in CDCl_3 . Asterisks indicate impurities in OAc and the black arrows the main new features corresponding to neither OAc nor acetylacetone.



Scheme 1. Proposed reaction mechanism with OAc. (a) Ligand exchange with OAc, (b) reductive decarboxylation, (c) decarboxylation of the intermediate complex, (d) no reaction between oleic acid and acetylacetone. R designates the oleyl group.

The same NMR experiments were conducted with OAm as solvent, both in a concentrated solution **A'** (5 OAm molecules per $\text{MoO}_2(\text{acac})_2$) in a close reaction tube at 200 °C and in a diluted one **B'** in round-bottom flask (Synthesis VI.2.) (Figure 7).

For both reactions **A'** and **B'**, no acetylacetone nor $\text{MoO}_2(\text{acac})_2$ were detected at the end but new peaks were observed. At the end of reaction **A'**, we noticed the absence of the signal H_f at 2.67 ppm of the $-\text{CH}_2-$ moiety linked to the amino group, denoting the oleylamine solvent has entirely reacted to form new species (Figure 7A). A precedent study on $\text{Ni}(\text{acac})_2$ reduction by oleylamine reported the condensation of oleylamine on acetylacetone to form a keto-ene-amine (Scheme 1).⁶ The presence of this last molecule was confirmed in our work by a singlet at 10.9 ppm (secondary amine hydrogen atom), one at 4.94 ppm (ethylenic proton of the keto-ene function) and a triplet at 3.30 ppm (proton in α of the NH group) (Figure 7A, stressed by blue arrows). As for reactions in OAc, the new features observed in ^1H NMR were less intense for the regular reaction in diluted conditions but were still present (Figure 7B). The oleylamine peaks did not significantly decreased in intensity in **B'** indicating the oleylamine reactivity in the concentrated conditions was linked to a stoichiometric reaction with the precursor and not to a catalytic one with the final nanoparticles.

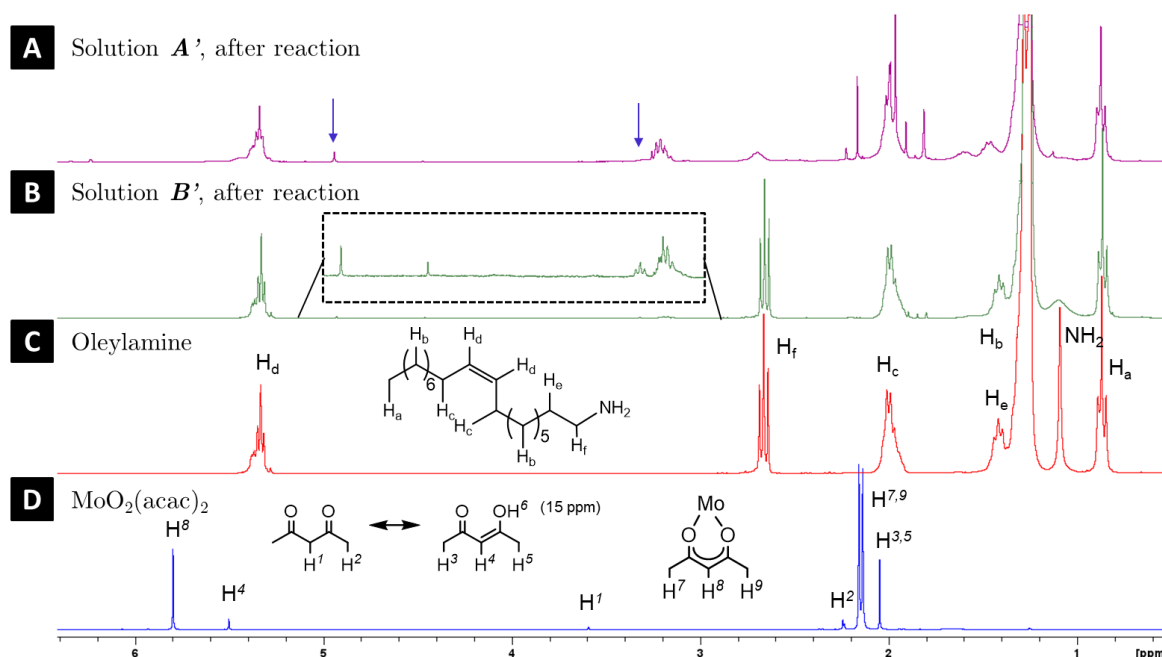
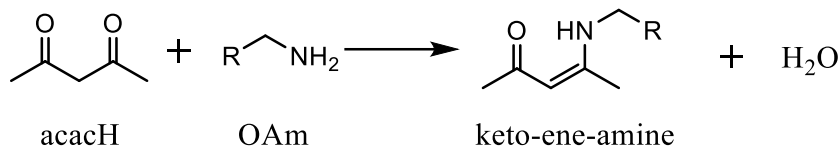


Figure 7. ^1H NMR spectra of (A) solution **A'** after reaction, (B) solution **B'** after reaction (Synthesis VI.1.), (C) oleylamine and (D) $\text{MoO}_2(\text{acac})_2$ in CDCl_3 . Blue arrows indicate the position of the keto-ene-amine peaks.

The molecular mechanisms at stake in the OAc/OAm syntheses are still under investigation but these NMR spectra clearly demonstrate different pathways were followed in OAc and in OAm. This presumably led to different final oxidation degrees for Mo, surface state and nanoparticle ligands. The difference between the two solvents

is still to be rationalized as only a small number of works in literature focused on the reaction mechanisms with pure OAc.²⁷



Scheme 2. Condensation reaction between acetylacetone and oleylamine to form a keto-ene-amine. R designates the oleyl group.

X-ray absorption spectroscopy. Characterization of the inorganic part was impossible or poorly informative by XRD, we therefore studied the samples by XAS at the Mo K-edge at 20 000 eV to get insight into the molybdenum oxidation states and local environments. The experiments were performed on the ROCK beamline at the SOLEIL synchrotron and details on the protocols are given in Appendix ES.8. Figure 8 displays the XAS spectra of pellets of the precursor $\text{MoO}_2(\text{acac})_2$, of two references, MoO_2 and $\alpha\text{-MoO}_3$, and of $\text{MoO}_x\text{-OAm}$ nanoparticles (fresh and 8 months old). In both MoO_2 and $\alpha\text{-MoO}_3$, the molybdenum atoms are in a distorted octahedral environment. The positions of the edges indicate the synthesized $\text{MoO}_x\text{-OAm}$ particles (20 018 eV) possess an average oxidation degree for Mo comprised between +IV (MoO_2 : 20 016 eV) and +VI (MoO_3 : 20 020 eV, $\text{MoO}_2(\text{acac})_2$: 20 019.5 eV), in line with a chemical composition MoO_x with $2 < x < 3$. Although the $\text{MoO}_x\text{-OAm}$ pattern looks closer to MoO_2 than to $\alpha\text{-MoO}_3$ (double peaks **a** and extremum **b**), the presence of a shoulder **c** in the pre-edge region and the shift of the extremum **d** towards lower energies impend its attribution to MoO_2 . A linear fit of MoO_2 and $\alpha\text{-MoO}_3$ gave poor results: the $\text{MoO}_x\text{-OAm}$ material is therefore probably a mixture of different molybdenum oxides of intermediate compositions. Upon aging in air, $\text{MoO}_x\text{-OAm}$ evolved and its XAS spectrum presents an edge shift at higher energy, *ca.* 20 019 eV, corresponding to a higher oxidation state. The intensification of the pre-edge **c**, the disappearance of **a** in favor of a maximum **e** are similar to features displayed by Mo_4O_{11} or h-MoO_3 .²⁹ Besides, the absence of the maximum **f** in old $\text{MoO}_x\text{-OAm}$ comforts our hypothesis old $\text{MoO}_x\text{-OAm}$ is not $\alpha\text{-MoO}_3$. We also measured in a liquid cell a reference of molybdate MoO_4^{2-} in an aqueous solution, the supernatant of the crude of the $\text{MoO}_x\text{-OAm}_{(\text{liq})}$ synthesis and the $\text{MoO}_x\text{-OAc}$ solution. The spectrum of the $\text{MoO}_x\text{-OAm}_{(\text{liq})}$ supernatant presents strong similarities with that of MoO_4^{2-} , in particular the important pre-edge at 20 010 eV, the inflexion point *ca.* 20 025 eV and the very flat oscillations in the EXAFS region. The pre-edges are attributed to a forbidden transition $1s \rightarrow 4d$, generally relaxed in tetrahedral environment, and to a lesser extent in distorted octahedral geometries. The flat oscillations in the EXAFS region suggest a high disorder, *i.e.*

molecular species or a poorly crystalline object. We concluded not all the molybdenum atoms were consumed for the nanoparticles synthesis in Synthesis VI.2. with OAm and that molecular species, probably with tetrahedral geometry, are still present in the liquid crude. As the edge shift in the supernatant $\text{MoO}_x\text{-OAm}_{(\text{liq})}$ (20 020.4 eV) is close to the $\alpha\text{-MoO}_3$ one (20 020 eV), the molybdenum atoms should be at a high oxidation degree, *i.e.* +V or +VI. The absence in the supernatant $\text{MoO}_x\text{-OAm}_{(\text{liq})}$ of the characteristic features observed in the pelletized sample $\text{MoO}_x\text{-OAm}$ indicates most of the particles have precipitated out of solution after synthesis.

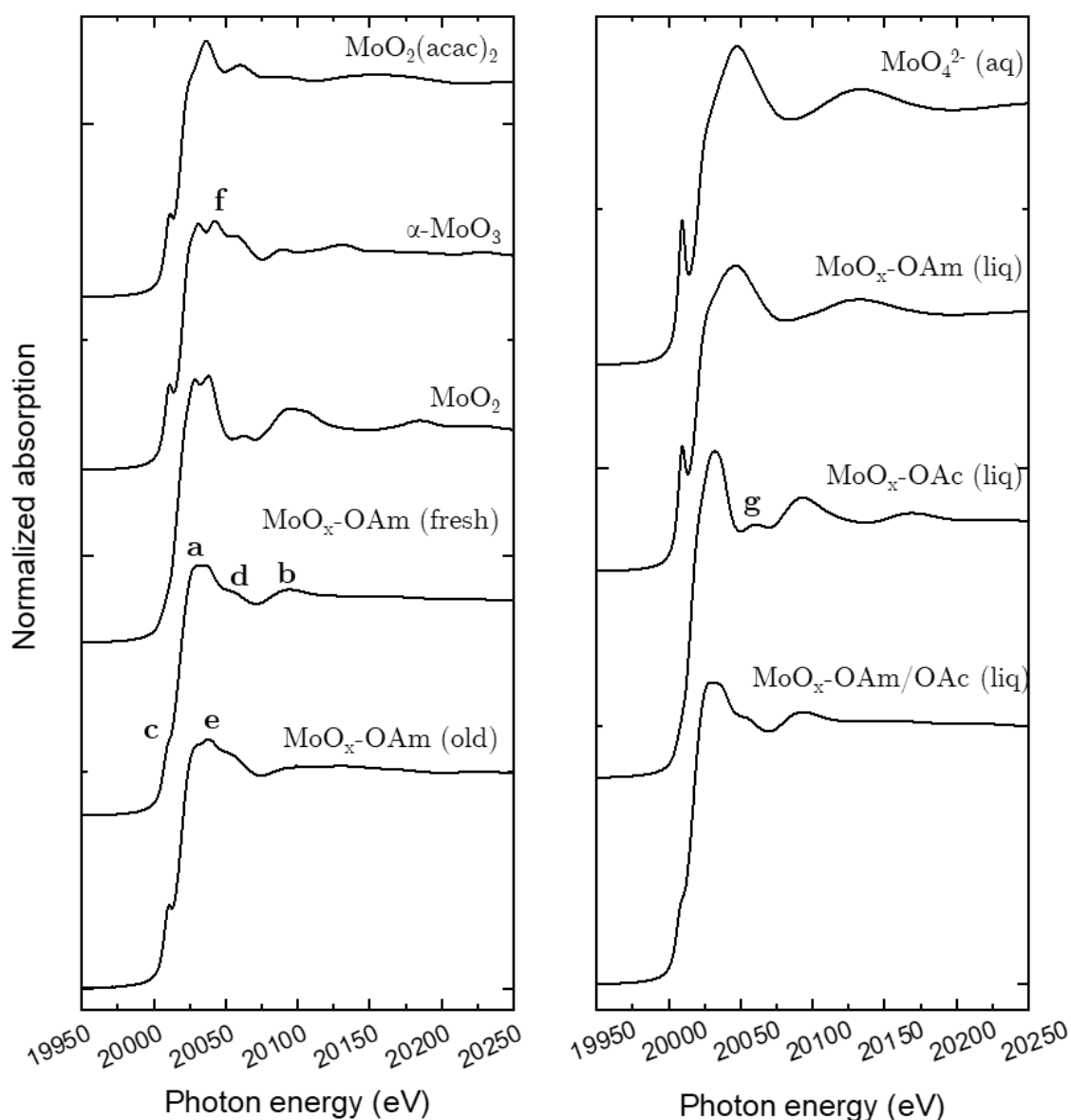


Figure 8. Mo K-edge XAS spectra at 20 000 eV of references MoO_2 , $\alpha\text{-MoO}_3$, $\text{MoO}_2(\text{acac})_2$ and of sample $\text{MoO}_x\text{-OAm}$ (fresh and 8 months old), measured as pellets in graphite, and of reference $\text{MoO}_4^{2-}(\text{aq})$ and of samples $\text{MoO}_x\text{-OAm}$ (crude supernatant), $\text{MoO}_x\text{-OAc}$ and $\text{MoO}_x\text{-OAm-OAc}$, measured in a liquid cell.

The XAS spectrum of $\text{MoO}_x\text{-OAc}$ corresponds to a species in a reduced environment (edge at 20 015.3 eV) with no pre-edge at all. The XAS fingerprint is close to that of MoO_2 but with broader features. The maximum μ is at the same energy that for MoO_2 , contrarily to the maximum in $\text{MoO}_x\text{-OAm}$. We therefore concluded small molybdenum dioxide nanoparticles were formed in Synthesis VI.3., and stayed suspended in solution thanks to the oleic acid capping agent. Moreover, considering the absence of pre-edge, we suggest that limited amount of molecular species are still present in the solution at the end of the reaction, at least none presenting a tetrahedral or strongly distorted octahedral environment.

XAS study clearly demonstrated that the chemical natures of the final objects were different whether OAc or OAm was used as solvent. With oleylamine, intermediate oxides MoO_x ($2 < x < 3$) were synthesized whereas poorly crystalline or small MoO_2 particles were obtained with OAc. The XAS spectrum of the supernatant of the Synthesis VI.2. in OAm strengthened the hypothesis of the formation of a molecular complex between $[\text{MoO}_2]^{2+}$ and the solvent molecule, OAm in this case. In both Syntheses VI.2. and VI.3., the oxidation state of Mo decreased from +VI in the precursor ($\text{MoO}_2(\text{acac})_2$) to +IV/+V in the product: a modification of the solvent or ligand molecules should therefore be expected as redox reactions were implied.

XAS *in situ* study. The reaction progress of Syntheses VI.2. and VI.3. was monitored by *in situ* XAS. The reaction cell used on the beamline was not perfectly air-tight and the solvents burnt and decomposed when heated at temperatures higher than their fume points (respectively 150 °C and 120 °C for OAm and OAc), we therefore limited the reaction temperatures to 140 °C for synthesis in OAm and 120 °C for reaction in OAc (Figure 9A-C). We also added a plateau at 60 °C of 30 min before the ramp toward the highest temperatures. All the XAS spectra were normalized in order to obtain an edge jump of 1. However, studying the actual edge jump value (plotted in red in Figure 9) is an efficient way to determine the evolution of Mo atom concentration in the X-ray beam path. The edge jump thus reflects the dissolution/consumption of the precursor and the stability of the objects in the suspension. The initial precursor concentration was adjusted to target an edge jump of 1 for a total dissolution. A first experiment was conducted without preliminary mixing of the precursor $\text{MoO}_2(\text{acac})_2$ in OAm (Figure 9A), a second one with preliminary mixing (Figure 9B) and a third one in OAc with preliminary mixing (Figure 9C). XAS spectra at different moments of the reaction are displayed on the right panels of Figure 9. The limited stirring capacity of the device could not permit a total suspension of the precursor grains from beginning. The stirring was intermittent because it was coupled with the heating power, hence the initial edge jumps lower than 1.

In the non-homogenized reaction in OAm, the Mo concentration in solution increased with temperature until a maximum right after the beginning of the plateau

at 140 °C (Figure 9A,D). As the edge jump was close to 1 at the maximum, we estimated all the Mo atoms were put in solution from $\text{MoO}_2(\text{acac})_2$. XAS spectrum D1 corresponding to the initial state presents strong similarities with the MoO_4^{2-} solution (Figure 8) which strengthens the hypothesis of the complex formation at the early stage of the reaction. The XAS signature evolved between room temperature and 60 °C (spectrum D2) and became close to that of the supernatant of the crude at the end of the reaction (Figure 8, $\text{MoO}_x\text{-OAm}_{(\text{liq})}$). The important pre-edge in D2 suggests a tetrahedral or a distorted octahedral environment while the flat oscillations indicate the Mo atoms are still in molecular species. We concluded there was a modification of the complex upon heating to 60 °C, for instance ligand exchange, rearrangement or dimerization. Upon heating to 140 °C, the spectrum evolved with a decrease of the pre-edge and sharper oscillations (spectrum D3). After 2 h at 140 °C, the tendency was confirmed with a final pattern D4 close to that measured for pelletized $\text{MoO}_x\text{-OAm}$ (Figure 8, $\text{MoO}_x\text{-OAm}$ (fresh)). As the XAS signature changed during the plateau at 140 °C, we deduced the thermal decomposition reaction was not immediate at 140 °C. The edge jump diminution from 0.95 to 0.65 during the first hour of the plateau was attributed to the sedimentation of formed particles. The slow increase of the molybdenum concentration after 2 h of reaction might be explained by the gradual degradation of the solvent. Indeed, at this temperature, OAm burns when in contact with O_2 : the solvent volume diminishes and the Mo concentration increases.

The reaction initially homogenized displayed similar evolution, confirming the repeatability of the observations (Figure 9B,E). The initial edge jump was of 0.5, indicating the XAS spectrum of the initial state was representative of the greatest part of the Mo atoms in the medium. The absence of the $\text{MoO}_2(\text{acac})_2$ signature at the initial stage confirmed the decomposition of $\text{MoO}_2(\text{acac})_2$ in another compound, presumably a complex with OAm molecules. We can stress once again the difference between room temperature and 60 °C, much clearer in this case due to the higher signal/noise ratio. From the plateau at 60 °C, *i.e.* when the whole amount of precursor was mixed with the solvent, to the end of reaction, identical spectra and edge jumps were recorded than the reaction with no preliminary mixing.

Contrarily to the reactions in OAm, the initial state of the reaction in OAc has a XAS signature corresponding to $\text{MoO}_2(\text{acac})_2$ (Figure 8 and Figure 9-F1, similarity stressed by an arrow), denoting the absence of new complex formation at room temperature at short timescales. Although the initial state was homogenized, the edge jump was low, *ca.* 0.2, because the metal precursor sedimented in spite of the stirring. Upon reaction course, the edge jump constantly increased from 0 to nearly 1 with a characteristic reaction time *ca.* 2 h, denoting the absence of sedimentation. The intermediate state (F2) during the plateau at 60 °C could not be clearly identified but was different from the molecular species observed with OAm. As there are similarities between F2 and spectra D3/E3, we suggest a mix between molecular species and

molybdenum oxide particles. The presence of nanoparticles at this temperature would be coherent with the TEM observations of the aliquot collected at 65 °C. The XAS signature of the final state F4 was close to the *ex situ* measurements of the reaction performed at 220 °C (Figure 8, $\text{MoO}_x\text{-OAc}_{(\text{liq})}$), but with a non negligible shoulder in the pre-edge region. This pre-edge may be the sign of an incomplete consumption of a molecular precursor $\text{MoO}_2\text{-oleate}$ at 120 °C.

We have qualitatively commented the evolution of the XAS spectra, with all the limitations of such an approach, but a quantitative study using the MCR-ALS approach (Multivariate Curve Resolution-Alternating Least Square) is ongoing. This approach is a statistical technique relying on a high number of spectra (typically hundreds or thousands) acquired during the reaction. It allows the extraction of the different XAS components constituting of the system: molecular species, intermediate states, inorganic materials. We will thus first interpret chemically the extracted spectra, and then determine the proportions of the different chemical components at all times of the reaction.^{13,15}

In summary, we synthesized molybdenum oxide nanoparticles by thermal decomposition of $\text{MoO}_2(\text{acac})_2$ in oleylamine, $\text{MoO}_x\text{-OAm}$, or in oleic acid, $\text{MoO}_x\text{-OAc}$. The NMR and XAS studies performed on both reaction conditions indicated different reaction pathways were followed, resulting in different objects. As aforementioned, the mechanism of the decomposition of $\text{M}(\text{acac})_2/\text{M}(\text{acac})_3$ precursor in oleylamine solvent to form $\text{M}(0)$ nanoparticles has already been extensively studied,¹¹ to the contrary of reactions in oleic acid. The particularity of the syntheses reported here is that the product was not a purely metallic particle but a molybdenum oxide, among a large variety of intermediate oxides between MoO_2 and MoO_3 . We therefore suggest as a perspective to exploit these different possible outcomes as a way to probe the difference in the synthesis mechanisms with OAm and OAc. We could also compare the results with a $\text{M}(0)$ synthesis, for instance from $\text{Ni}(\text{acac})_2$ or $\text{Pd}(\text{acac})_2$. This comparative study on both the solvent and the metal would be of interest in a field where the mechanisms at stake with OAc are not fully understood yet.

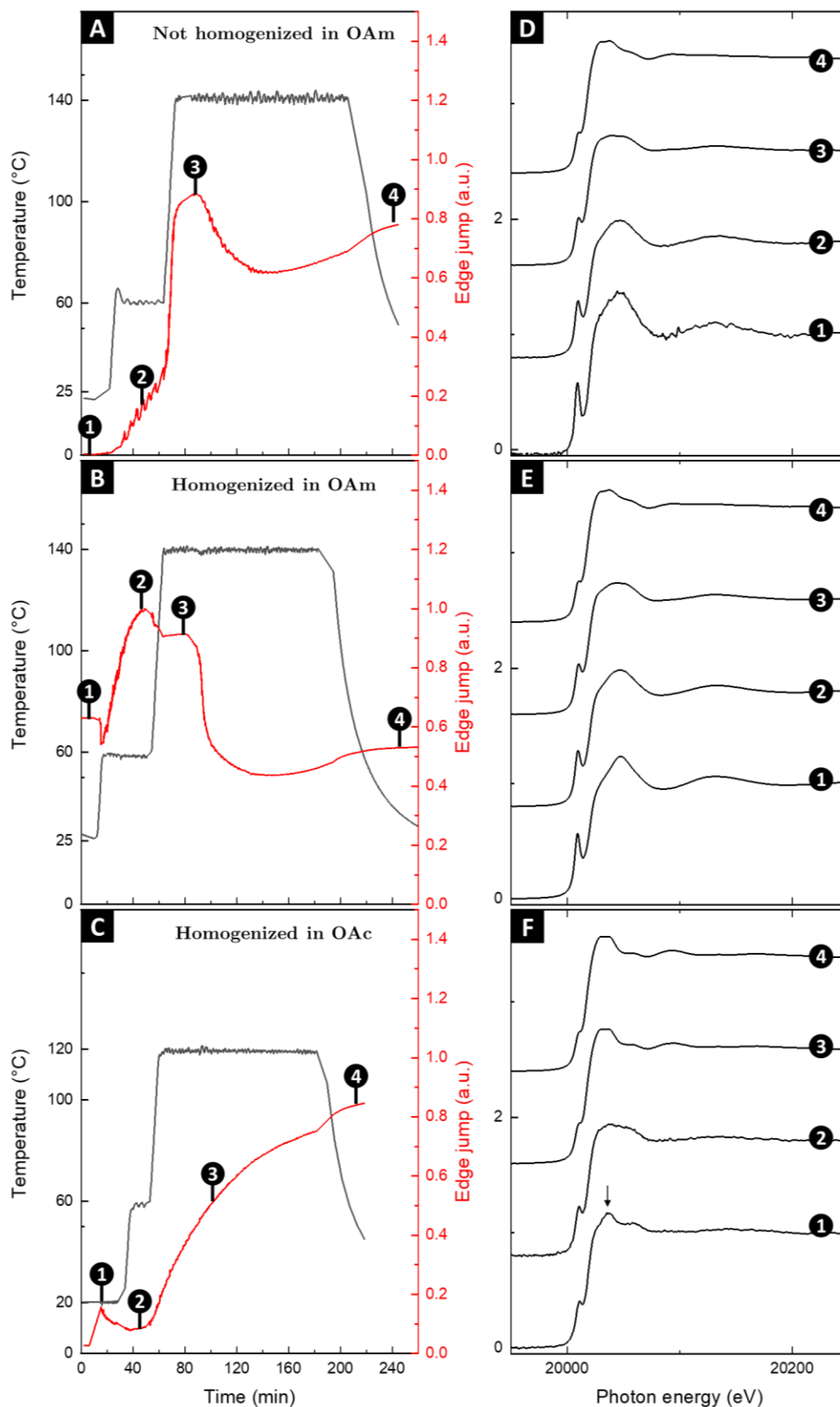


Figure 9. Temperature and edge jump of the *in situ* experiments (A) in OAm, with the precursor initially at the bottom of the liquid reaction cell, (B) in OAm and (C) in OAc, with the precursor initially dispersed. (D-F) Corresponding Mo K-edge X – ray absorption spectra for indicated times (arrow on F1 stresses the similarity with $\text{MoO}_2(\text{acac})_2$ spectrum).

VI.1.3 Conclusion on metal oxides syntheses

We could successfully reproduce a synthesis of XRD-pure $W_{18}O_{49}$ nanowires from WCl_6 in oleyl alcohol and oleylamine. The nanowire morphology is favorable for catalytic applications considering the high number of exposed tungsten atoms. The presence of oxygen vacancies associated to $W^{(IV)}$ and $W^{(V)}$ cations is also expected to help at the activation of H_2 as hydride species, made possible by the oxidation of the [W] sites. As to molybdenum oxides, the obtained crystal phase was not well determined but XAS measurements revealed an intermediate degree of oxidation for Mo, between +IV and +VI. This intermediate oxidation degree is probably associated to oxygen vacancies and therefore to active sites for H_2 activation. A powder could be isolated when synthesis was run in oleylamine, making possible the use of the catalyst for the next section. This was not the case for the synthesis in oleic acid which was therefore excluded for catalytic trials. Work is still ongoing to better understand the nature of the ligands at the surface of the nanoparticles, originating from thermal decomposition of $MoO_2(acac)_2$: so far, we only could identify OAm leftover and a condensation product with acetylacetone for thermal decomposition of $MoO_2(acac)_2$ in OAm.

Although there are still elements to be enlightened on the synthesis mechanism, the reaction is reproducible and the obtained materials present the expected characteristics: high surface/volume ratios, good suspension stability in organic solvents and presence of oxygen defects and of metallic centers with versatile oxidation degrees. We therefore used the $W_{18}O_{49}$ and MoO_x -OAm materials for preliminary catalytic experiments.

VI.2. Hydrogenation reactions

As aforementioned, oxygen deficient tungsten oxide $\text{WO}_{2.72}$, obtained from WCl_6 and ethanol, was recently reported for its catalytic activity for nitroarenes and alkynes hydrogenation (30 bar H_2 , 150 °C, 15 h).¹ The tungsten oxide synthesized in this PhD thesis has a similar chemical composition but the synthetic pathway was different as we used a mixture of oleylamine and oleyl alcohol. Hydrogenation of phenylacetylene and nitrobenzene were attempted with $\text{W}_{18}\text{O}_{49}$ and $\text{MoO}_x\text{-OAm}$ following Catalysis VI.1. Considering the expected low catalytic activity of the materials compared to conventional catalysts, we first used relatively hard conditions, *i.e.* an H_2 pressure of 30 bar and a reaction temperature of 150 °C. We chose toluene and EtOH as solvents for reactions with $\text{W}_{18}\text{O}_{49}$ to match with the conditions reported by Wang *et al.*,¹ and THF for reactions with $\text{MoO}_x\text{-OAm}$ in order to have stable suspensions. Results are given in Table 2.

Catalysis VI.1. Hydrogenation with metal oxides. In air, 0.2 mmol of catalyst powder (25.6 mg of $\text{MoO}_x\text{-OAm}$ or 45.5 mg of $\text{W}_{18}\text{O}_{49}$, 0.1 equiv. of [M]) were introduced in a 25 mL steel autoclave (Teflon reaction cuve). To the autoclave was added 2 mmol of substrate (220 μL of phenylacetylene or 210 μL of nitrobenzene, 1 equiv.) and 1 mL of solvent. The autoclave was closed and the atmosphere was changed for H_2 (30 bar) after 2 cycles vacuum/ H_2 (1 bar). The autoclave was then introduced in a preheated oil bath at 150 °C for 16 h. The pressure increased to *ca.* 40 bar. After reaction, the autoclave was let to cool down naturally to r.t. before opening. An aliquot of the liquid phase was studied by ^1H NMR in CDCl_3 .

Phenylacetylene was hydrogenated in styrene with yields of respectively 22 % and 13 % and partially over-hydrogenated in ethylbenzene (entries 1-2 and Figure 10). These preliminary data proved the two synthesized metal oxides were active catalysts for alkyne/alkene hydrogenation though not chemoselective as total hydrogenation in ethylbenzene occurred at moderate styrene yields. On the contrary, nitrobenzene was not hydrogenated in aniline by any of the two catalysts (entries 3-4). The catalytic activity toward $\text{C}=\text{C}$ and $\text{C}\equiv\text{C}$ hydrogenation and not toward NO_2 reduction is sufficiently unusual to be noticed.

In summary, we proved the possible use of Group VI metal oxides (Mo, W) synthesized *via* a non-aqueous pathway for hydrogenation reactions in solvent. The organic ligands did not completely impend the catalytic reactions to occur. However, the experimental conditions used in this preliminary study (30 bar H_2 , 150 °C, 16 h, [M] 10 mol%) were already strong for liquid phase catalysis with limited conversion yields in hydrogenation of phenylacetylene. We therefore suggest to directly evaluate the impact of the addition of a co-catalyst, such as a phosphine or an amine, on the reaction yield and selectivity.

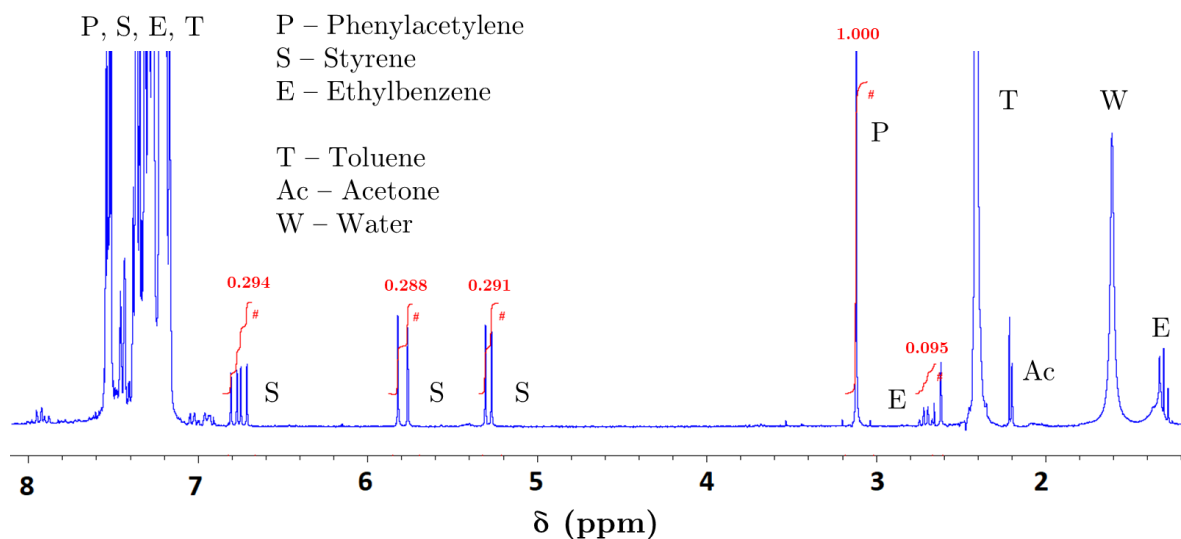
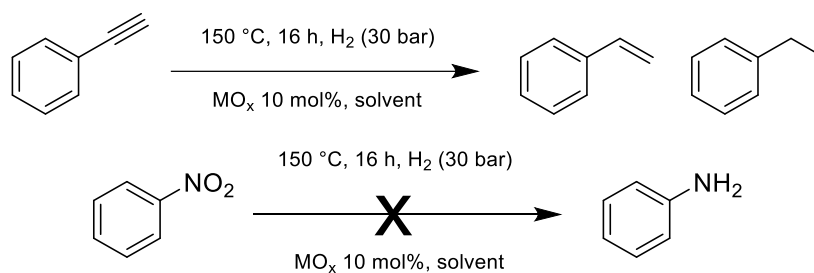


Figure 10. ^1H NMR spectrum of crude reaction of hydrogenation of phenylacetylene in toluene at 150 °C in presence of $\text{W}_{18}\text{O}_{49}$. Traces of acetone do not originate from the synthesis.



	Catalyst (mol%)	Substrate	Solvent	Temp.	Substrate conversion	Products
1	$\text{W}_{18}\text{O}_{49}$	Phenylacetylene	Toluene	150 °C	26 %	Styrene: 22 % Ethylbenzene: 4 %
2	$\text{MoO}_x\text{-OAm}$	Phenylacetylene	THF	150 °C	13 %	Styrene: 13 % Ethylbenzene: < 1 %
3	$\text{W}_{18}\text{O}_{49}$	Nitrobenzene	EtOH	150 °C	0 %	-
4	$\text{MoO}_x\text{-OAm}$	Nitrobenzene	THF	150 °C	0 %	-

Table 2. Hydrogenation of styrene phenylacetylene (PhCCH) and nitrobenzene (PhNO_2) with metal oxide catalysts. Reaction conditions: 220 μL of PhCCH /210 μL of PhNO_2 (2 mmol), 25.6 mg of MoO_x /45.5 mg of $\text{W}_{18}\text{O}_{49}$ (0.2 mmol, $[\text{M}]$ 10 mol%), 1 mL of solvent, H_2 (30 bar, 30 mmol), 16 h in autoclave (25 mL) at 150 °C. Conversion and yield determined by NMR.

VI.3. Bibliography

1. Song, J. *et al.* Oxygen-Deficient Tungsten Oxide as Versatile and Efficient Hydrogenation Catalyst. *ACS Catal.* **5**, 6594–6599 (2015).
2. Nandakumar, N. K. & Seebauer, E. G. Relating Catalytic Activity of d 0 Semiconducting Metal Oxides to the Fermi Level Position. *J. Phys. Chem. C* **118**, 6873–6881 (2014).
3. Zhang, Y.-C. *et al.* Unraveling the facet-dependent and oxygen vacancy role for ethylene hydrogenation on Co₃O₄ (110) surface: A DFT+U study. *Appl. Surf. Sci.* **401**, 241–247 (2017).
4. Zhang, S. *et al.* Solid frustrated-Lewis-pair catalysts constructed by regulations on surface defects of porous nanorods of CeO₂. *Nat. Commun.* **8**, 1–11 (2017).
5. Dong, Y. *et al.* Tailoring Surface Frustrated Lewis Pairs of In₂O_{3-x}(OH)_y for Gas-Phase Heterogeneous Photocatalytic Reduction of CO₂ by Isomorphous Substitution of In³⁺ with Bi³⁺. *Adv. Sci.* **6**, 1700732 (2018).
6. Carencio, S. *et al.* Revisiting the Molecular Roots of a Ubiquitously Successful Synthesis: Nickel(0) Nanoparticles by Reduction of [Ni(acetylacetonate)₂]. *Chem. - A Eur. J.* **18**, 14165–14173 (2012).
7. Cheng, W. *et al.* Large-area alignment of Tungsten oxide nanowires over flat and patterned substrates for room-temperature gas sensing. *Angew. Chemie - Int. Ed.* **54**, 340–344 (2015).
8. Niederberger, M., Bartl, M. H. & Stucky, G. D. Benzyl alcohol and transition metal chlorides as a versatile reaction system for the nonaqueous and low-temperature synthesis of crystalline nano-objects with controlled dimensionality. *J. Am. Chem. Soc.* **124**, 13642–13643 (2002).
9. Sarac, M. F., Wu, W. & Tracy, J. B. Control of Branching in Ni₃C_{1-x} Nanoparticles and Their Conversion into Ni₁₂P₅ Nanoparticles. *Chem. Mater.* **26**, 3057–3064 (2014).
10. Himstedt, R. *et al.* Halide ion influence on the formation of nickel nanoparticles and their conversion into hollow nickel phosphide and sulphide nanocrystals. *Nanoscale* **11**, 15104–15111 (2019).
11. Mourdikoudis, S. & Liz-Marzán, L. M. Oleylamine in Nanoparticle Synthesis. *Chem. Mater.* **25**, 1465–1476 (2013).
12. Deshmukh, R. & Niederberger, M. Mechanistic Aspects in the Formation,

- Growth and Surface Functionalization of Metal Oxide Nanoparticles in Organic Solvents. *Chem. - A Eur. J.* **23**, 8542–8570 (2017).
13. Ludi, B. *et al.* Interplay Between Size and Crystal Structure of Molybdenum Dioxide Nanoparticles-Synthesis, Growth Mechanism, and Electrochemical Performance. *Small* **7**, 377–387 (2010).
 14. Olliges-Stadler, I. *et al.* Study of the chemical mechanism involved in the formation of tungstite in benzyl alcohol by the advanced QEXAFS technique. *Chem. - A Eur. J.* **18**, 2305–2312 (2012).
 15. Staniuk, M. *et al.* Matching the organic and inorganic counterparts during nucleation and growth of copper-based nanoparticles – in situ spectroscopic studies. *CrystEngComm* **17**, 6962–6971 (2015).
 16. Gonçalves, R. H., Leite, L. D. T. & Leite, E. R. Colloidal WO₃ nanowires as a versatile route to prepare a photoanode for solar water splitting. *ChemSusChem* **5**, 2341–2347 (2012).
 17. Tilley, R. *Colour and the Optical Properties of Materials*. (John Wiley & Sons, Ltd, England, 2019).
 18. Momma, K. & Izumi, F. VESTA: a three-dimensional visualization system for electronic and structural analysis. *J. Appl. Crystallogr.* **41**, 653–658 (2008).
 19. Lee, S. H., Nishi, H. & Tatsuma, T. Tunable plasmon resonance of molybdenum oxide nanoparticles synthesized in non-aqueous media. *Chem. Commun.* **53**, 12680–12683 (2017).
 20. Li, Y. *et al.* Manipulation of Surface Plasmon Resonance in Sub-Stoichiometry Molybdenum Oxide Nanodots through Charge Carrier Control Technique. *J. Phys. Chem. C* **121**, 5208–5214 (2017).
 21. Toyos-Rodríguez, C. *et al.* A Simple and Reliable Synthesis of Superparamagnetic Magnetite Nanoparticles by Thermal Decomposition of Fe(acac)₃. *J. Nanomater.* **2019**, 1–10 (2019).
 22. Oh, N. & Shim, M. Metal Oleate Induced Etching and Growth of Semiconductor Nanocrystals, Nanorods, and Their Heterostructures. *J. Am. Chem. Soc.* **138**, 10444–10451 (2016).
 23. Bronstein, L. M. *et al.* Influence of Iron Oleate Complex Structure on Iron Oxide Nanoparticle Formation. *Chem. Mater.* **19**, 3624–3632 (2007).
 24. Chang, H. *et al.* Molecular-Level Understanding of Continuous Growth from Iron-Oxo Clusters to Iron Oxide Nanoparticles. *J. Am. Chem. Soc.* **141**, 7037–7045 (2019).

25. Ullrich, A., Rahman, M. M., Longo, P. & Horn, S. Synthesis and high-resolution structural and chemical analysis of iron-manganese-oxide core-shell nanocubes. *Sci. Rep.* **9**, 19264 (2019).
26. Conte, M. & Hippler, M. Dynamic NMR and Quantum-Chemical Study of the Stereochemistry and Stability of the Chiral $\text{MoO}_2(\text{acac})_2$ Complex in Solution. *J. Phys. Chem. A* **120**, 6677–6687 (2016).
27. Xie, M., Lyu, Z., Chen, R. & Xia, Y. A Mechanistic Study of the Multiple Roles of Oleic Acid in the Oil-Phase Synthesis of Pt Nanocrystals. *Chem. – A Eur. J.* **26**, 15636–15642 (2020).
28. Kwon, S. G. *et al.* Kinetics of Monodisperse Iron Oxide Nanocrystal Formation by “Heating-Up” Process. *J. Am. Chem. Soc.* **129**, 12571–12584 (2007).
29. Ressler, T., Jentoft, R. E., Wienold, J., Günter, M. M. & Timpe, O. In Situ XAS and XRD Studies on the Formation of Mo Suboxides during Reduction of MoO_3 . *J. Phys. Chem. B* **104**, 6360–6370 (2000).

Chapter VII

Nickel-containing nanoparticles for hydrogenation in solvent

Note: this chapter partially consists in the work of Léna Meyniel, intern for 6 months under my supervision. Her work covers a part of the synthesis section (literature review, syntheses, characterizations and data interpretation).

Nickel is a widely used catalyst for hydrogenation reactions in liquid phase with for instance the well-known Raney[®] nickel, a finely divided nickel mixed with aluminum, patented by Murray Raney in 1926.¹ Different nickel-based catalysts have since been developed for the hydrogenation of unsaturated compounds in the context of fine chemistry.² As already mentioned, different limitations exist for this metal: low resistance to poisonous elements (N, P, S), pyrophoricity, poor chemoselectivity. As a consequence, in the past years a series of work targeted the use of nickel compounds for colloidal hydrogenation: borides,^{3,4} nitrides,⁵ silicides,⁶ phosphides,^{4,7} and sulfides.⁸ The insertion of light elements such as carbon or phosphorus in the metal lattice modifies the *d*-band electronic structure of the material, although the extent and the sense of the modification are challenging to predict.^{9–11} Such a modification may give a noble metal-like catalytic behavior and favors the H₂ activation, as was shown on WC for instance.¹² Nickel carbide was reported as an active catalyst for vegetal oil hydrotreatment at 400 °C and under 30 bar of H₂, and similar conversions were obtained with nickel sulfides and phosphides.¹³ However, to the best of our knowledge, there is no mention of Ni₃C catalyst in colloidal hydrogenation of olefin or nitro compounds. Furthermore, although phosphine assisted heterolytic splitting of H₂ at the surface of noble metal was reported by Rossi *et al.*¹⁴, the influence of phosphine additives have rarely been explored for catalyst nanoparticles that are not purely metallic.

In the context of this thesis, nickel carbides and phosphides were thought to be interesting catalysts as they display an intermediate metallic/covalent character, although at different degree: the electronegativity of phosphorus ($\chi(\text{P}) = 2.19$) indeed differs from that of the carbon ($\chi(\text{C}) = 2.55$). So far in our study, the covalent character was only present in the carbides studied in chapter II/III and the corresponding catalysts had a limited activity. In this chapter, we considered the use of nickel carbide (Ni₃C) and nickel phosphides (Ni₂P and Ni₁₂P₅) nanoparticles for colloidal hydrogenation of model substrates such as phenylacetylene or nitrobenzene.

Three main goals are pursued:

- (1) Investigating whether Ni_3C displays a catalytic activity for hydrogenation, and eventually comparing the catalytic activity of Ni_3C with Ni_2P and Ni_{12}P_5 nanoparticles of similar size and surface state
- (2) Studying the catalytic activity of a catalyst (Ni_3C , Ni_{12}P_5 or Ni_2P) over a variety of substrates (alkyne, nitroarene, furanic aldehyde) under similar conditions in order to establish a bridge between the works from fine chemistry and hydroprocessing communities
- (3) Investigating the influence of an additional phosphine ligand on the conversion and selectivity

Nickel-containing nanoparticles are synthesized in organic solvents with temperatures in the 200-300 °C range. Their surface is therefore expected to be covered with organic ligands (amines, phosphines) to the contrary of most of the materials presented so far. Different experimental issues or concerns are commented, in particular on the influence of the reaction temperature on the product phase. In the first section, we report the synthesis of Ni_3C nanoparticles, which are subsequently phosphidized in either Ni_2P or Ni_{12}P_5 . The catalysts are characterized by XRD, TEM and XAS. In the second section, the reactivity of Ni_3C is studied for the hydrogenation of nitrobenzene (PhNO_2) and phenylacetylene (PhCCH).

VII.1. Nickel carbide and phosphide syntheses

VII.1.1 One-step nickel phosphide synthesis

A direct solvothermal synthesis of Ni_2P nanoparticles was first attempted following the work of Robinson *et al.*¹⁵ The Synthesis VII.1. was conducted in an oleylamine (OAm)/dioctyl ether (Oct_2O)/trioctylphosphine (TOP) (2/1/1) (v/v/v) mixture. Nickel nanoparticles were first formed by thermal decomposition of $\text{Ni}(\text{acac})_2$ and the trioctylphosphine introduced in excess, 5.6 equiv. per atom of Ni, constituted the phosphorus source.

Synthesis VII.1. One-step synthesis of NiP_x nanoparticles. In a 50 mL three-necked round-bottom flask, 10 mL of oleylamine (8.1 g, 30.4 mmol, 13.3 equiv.) and 5 mL of dioctyl ether (4 g, 16.6 mmol, 7.3 equiv.) were degassed under vacuum at r.t. during 20 min and the flask was purged with N_2 three times. Under N_2 , $\text{Ni}(\text{acac})_2$ (586 mg, 2.28 mmol, 1 equiv.) and TOP (5 mL, 11.2 mmol, 4.9 equiv.) were added to the solution. The resulting blue gelatinous solution was heated to 230 °C: it became limpid at 55 °C, emerald green at 80 °C and a black suspension at 140 °C. Explosions occurred *ca.* 215 °C and the temperature increase slowed down in this temperature range. The solution was let to react for 1 h 30 at 230 °C and target temperature was then set to 300 °C for 3 h (the actual reaction temperatures were between 270 °C and

300 °C). After cooling to r.t. under N₂, ethanol (20 mL) was added to the crude solution and a black solid was isolated by centrifugation (9,000 rpm, 10 min, 20 °C). The yellowish biphasic supernatant was removed and the solid was redispersed in hexane (10 mL) and washed with ethanol (20 mL) and centrifugated. This operation was repeated another time. The obtained black powder (190 mg, 112 % yield) was then dried under N₂ and stored in air.

The yields obtained in Syntheses VII.1. to VII.6. with high boiling point solvents are excellent and sometimes higher than 100 %. This is due to the presence of a non-negligible organic shell around the nanoparticles. We nonetheless considered they are indicative of quantitative reactions.

We first performed Synthesis VII.1. and stopped it at the end of the first plateau at 230 °C. The obtained powder consisted in a mixture of Ni₁₂P₅ [PDF card N°00-022-1190] and Ni₂P [PDF card N°04-003-1863] nanoparticles (equivalent to respectively NiP_{0.42} and NiP_{0.5}) (Figure 1Aa). The temperature setpoint of the heating device for the second plateau was always 300 °C but different maximal reaction temperatures were obtained for each batch, as low as 270 °C. An important reflux was observed at 260 °C, even though the measured temperature kept increasing. The reaction crude was a ternary mix of OAm, Oct₂O and TOP with boiling points of respectively 364 °C, 292 °C and 287 °C. Considering the evaporation temperatures were all above 270 °C, the mixture certainly presents a eutectic. The composition of the liquid fraction thus differed from that of the gas fraction which evaporated. As the vapors condensed along the air refrigerant, the total composition did not diverge with time. However, evaporation is an endothermic process and consumed part of the power delivered by the heating mantle. For some of our syntheses, 100 % of the nominal power of the heating mantle was delivered before the targeted temperature of 300 °C was reached. A combination of different experimental conditions either related to the delivered power (aging of the heating mantle) or to the heat losses (quality of the thermal insulation, contact between the heating mantle and the round-bottom flask) may explain the different temperatures obtained for the second plateau although the solvents mix was always the same. This point is not mentioned in the different works reporting the colloidal syntheses of nickel phosphides and carbides but we noticed the control of temperature is not performed the same way depending on the groups.^{15–17} Indeed, where Brock *et al.* directly put the thermocouple in contact with the heating mantle near the round-bottom flask, Carencio *et al.* placed it in a glass finger in the solution.^{18,19} Besides, some groups indicate a reaction temperature of 350 °C, well above the boiling points of the major part of the solvent: we believe they actually indicate the set point of the heating mantles. All these points prove the literature protocols for this NiP_x syntheses are not homogeneous and that a careful attention should be brought to the temperature control.

Even though not intentionally, we therefore performed a series of reactions with different temperatures for the second plateau. Considering the instability of the heating device mentioned earlier, the temperatures are indicative and may have fluctuated during the plateau. The phase speciation of the product between the different nickel phosphides was analyzed by XRD (Figure 1Ab-f for some of the relevant data). When the temperature of the plateau was increased from 270 °C to 290 °C, the proportion of Ni_{12}P_5 decreased in favor of Ni_2P , as can be observed with the diminution of the intensity of the peaks at 38° and 49°. For temperatures in the 280 °C-295 °C range, the product was nearly XRD-pure Ni_2P , plus three unattributed very broad peaks at 29°, 42° and 49°. The Ni_{12}P_5 phase was excluded due to the important peak at 29°, not referenced for this phase. Beyond 295 °C, a more phosphorus-rich nickel phosphide phase, Ni_5P_4 (equivalent to $\text{NiP}_{0.8}$) [PDF card N°04-014-7901] appeared, with in particular peaks at 46° and 56°. TEM images of the NPs produced at 270 °C and 300 °C revealed similar morphologies were obtained: monodisperse 8 nm large spherical nanoparticles (Figure 1B-G). Electron diffraction fringes appeared at high magnifications and SAED patterns confirmed the presence of the Ni_2P phase: the NPs are crystalline. We can stress the critical role of the washing steps as particles were severely aggregated for one batch (Figure 1B) and presented a thick organic shell (Figure 1C), probably composed of TOP ligands. The main result is that increasing the reaction temperature leads to more phosphorus-rich phases but that obtaining XRD-pure samples with this protocol is challenging. As this conclusion is shared by the authors of the initial work and as we are more interested in the catalytic applications in the synthesis development, we did not push further in this direction.¹⁵

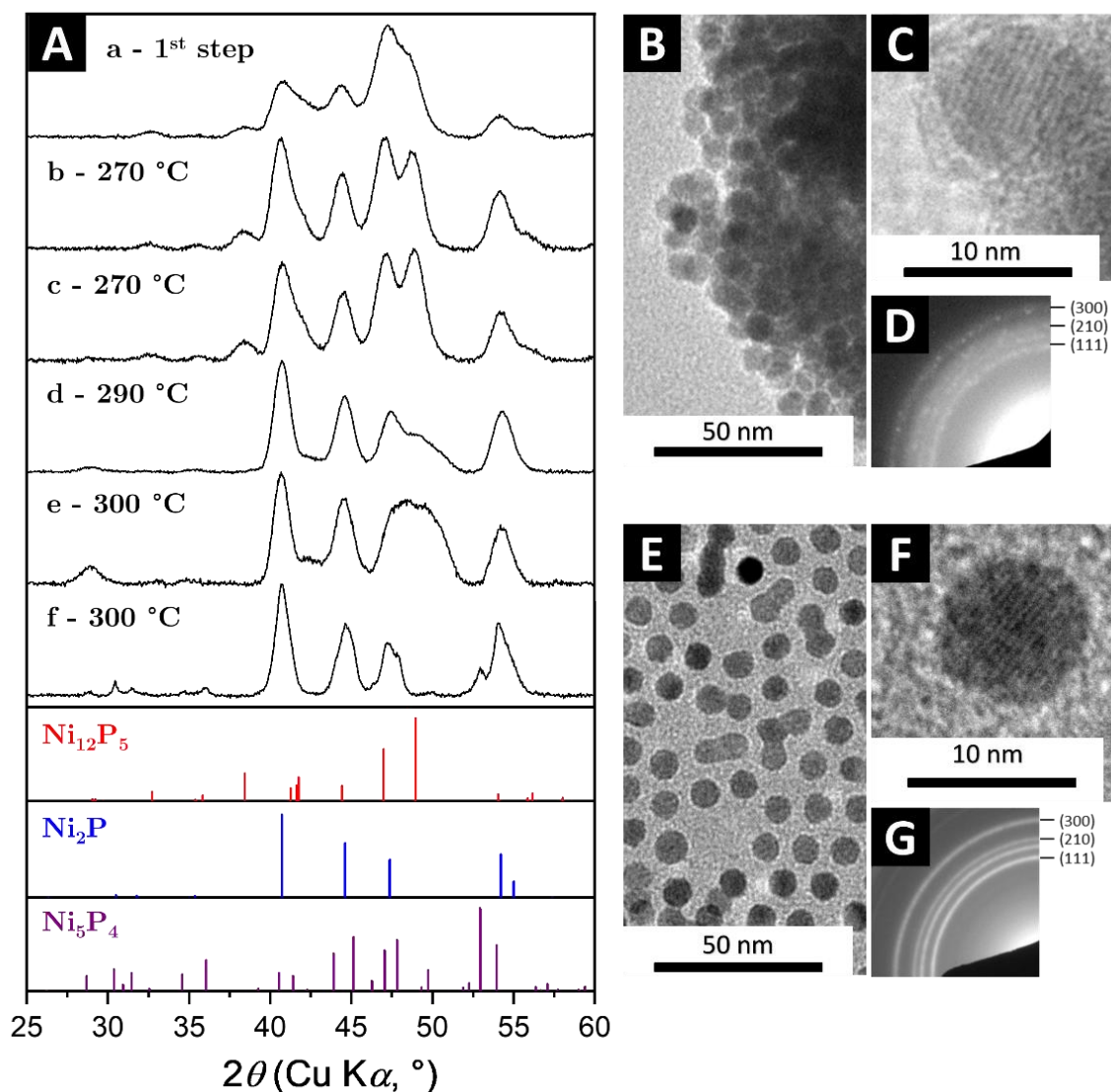


Figure 1. (A) PXRD patterns of powders obtained by Synthesis VII.1. after (a) the first plateau at 230 °C and (b-e) after the second plateau at respectively 270 °C, 270 °C, 290 °C, 300 °C and 300 °C. Transmission Electron Microscopy images and corresponding selected area electron diffraction (reference: Ni_2P) of (B-D) sample b (270 °C) and (E-G) sample f (300 °C).

VII.1.2 Synthesis of nickel carbide Ni_3C and subsequent phosphidization

The direct synthesis of XRD-pure nickel phosphides Ni_{12}P_5 and Ni_2P proved to be unsuccessful following Synthesis VII.1. We therefore chose to reproduce the two-step procedure for Ni_{12}P_5 NPs synthesis *via* Ni_3C reported by Tracy *et al.*¹⁷ In this synthetic pathway, the nickel phosphide nanoparticles are obtained by phosphidization of nickel carbide nanoparticles in a one-pot synthesis. The authors reported the Ni_{12}P_5 phase and we adapted the protocol to form Ni_2P nanoparticles as well. The nickel carbide and phosphide nanoparticles have similar dimensions which will permit the comparison of their catalytic activities in section VII.2.

Colloidal syntheses of transition metal carbides (Fe_3C , Co_2C , Co_3C , Ni_3C) require the use of a carbon source and a high enough temperature to decompose it.²⁰ One common and easily available carbon source is 1-octadecene (ODE), introduced in large excess in the reaction medium. It is most of the time used in combination with long-chain alkylamines, such as oleylamine (OAm) or hexadecylamine (HDA), or fatty acids, such as oleic acid (OAc). The use of ODE as carburizing agent in colloidal syntheses is justified by its low cost, its high boiling point (315 °C), convenient for NPs synthesis, and its relatively moderate decomposition temperature. It is important to note that no absolute decomposition temperature may be given for ODE, or any other carbon source, as the carburization process is thermodynamically possible at temperatures as low as 200 °C but is kinetically too slow to be observed.²¹ The first stage of the $\text{Ni}(0)$ carburization is challenging to observe with XRD and one can incorrectly assume pure metallic nickel was obtained.²¹ If solvents are compared as to their carburization capacity, both the reaction temperature and reaction time should be indicated. For instance, Kobayashi *et al.* studied the thermolysis of $\text{Ni}(\text{acac})_2$ in pure OAm at different temperatures: for a reaction time of 30 min, they obtained pure cubic $\text{Ni}(0)$ until a reaction temperature of 260 °C (Figure 2A) and observed Ni_3C at 280 °C and higher temperatures.²² When the reaction was conducted at 240 °C, a longer reaction time (180 min *versus* 30 min) was enough to form Ni_3C (Figure 2B). The phase indicated as hcp- $\text{Ni}(0)$ in Figure 2 was proven in an ulterior work of Schaak *et al.* to be a misattribution of the Ni_3C phase.²¹ The surface state of the $\text{Ni}(0)$ NPs may also infer on the carburization process. For instance, Tracy *et al.* reported the C uptake in an OAm/ODE (50/50) mixture at 230 °C in 30 min but the addition of minute amount of TOP ligands prevented the carburization of the $\text{Ni}(0)$ NPs under similar conditions.¹⁷ The authors hypothesized the TOP ligands are tightly bound at the surface of the nanoparticles and impend the approach of the ODE, responsible for the C uptake. The exact decomposition mechanism of ODE is rarely mentioned in the different works. As higher temperatures are required for carburization with OAm than with ODE, both

comporting a C=C bond, we suggest the higher reactivity of ODE is linked to the terminal position of the double bond.

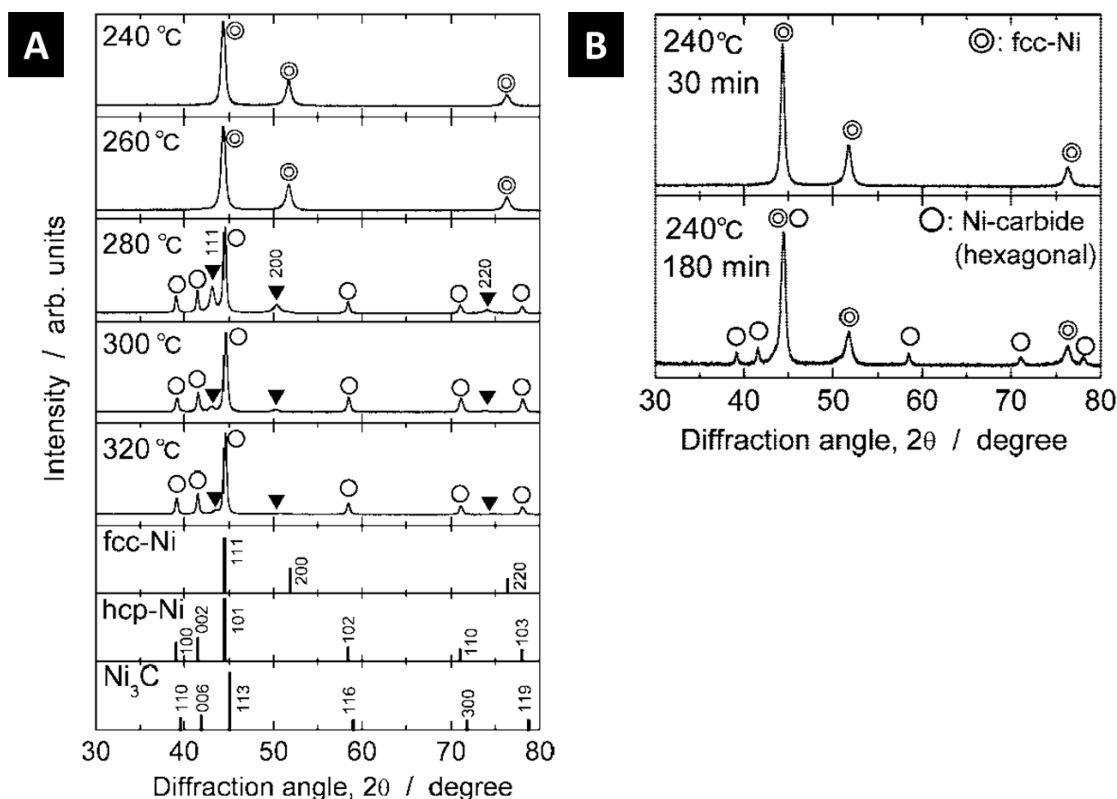


Figure 2. PXRD patterns of reaction product of thermolysis of $\text{Ni}(\text{acac})_2$ in pure OAm. (A) Reaction time of 30 min for all reactions. (B) 240 °C for both reactions. The figures are reproduced from reference [22].

Nickel carbide Ni_3C . We first reproduced in Synthesis VII.2. the first step of the protocol used by Tracy *et al.* for Ni_3C synthesis in an OAm/ODE (50/50) mixture.¹⁷ We did not add TOP in order to avoid any surface contamination by phosphorus or formation of nickel phosphide phases.

Synthesis VII.2. Nickel carbide nanoparticles. In a 100 mL three-necked round-bottom flask, 15 mL of oleylamine (12.2 g, 45.6 mmol, 8.9 equiv.) and 15 mL of 1-octadecene (11.8 g, 46.9 mmol, 9.15 equiv.) were degassed under vacuum at 60 °C during 20 min and the flask was purged with N_2 three times. Under N_2 , $\text{Ni}(\text{acac})_2$ (1.32 g, 5.14 mmol, 1 equiv.) was added to the solution. The resulting blue gelatinous solution was heated up to 250 °C under agitation. The solution was homogeneous and turned emerald green at 80 °C and darkened progressively with the heating ramp. A black suspension was obtained at 205 °C and explosions occurred at 236 °C. The increase in temperature stopped for a few minutes and then reached 250 °C. The

solution was let to react 2 h at 250 °C. After cooling to r.t. under N₂, ethanol (30 mL) was added to the crude solution and a solid was isolated by centrifugation (9,000 rpm, 10 min, 20 °C). The yellow biphasic supernatant was removed and the particles were redispersed in hexane (15 mL) before adding ethanol to precipitate them (15 mL). This operation was repeated another time. The obtained black powder (348 mg, 108 % yield) was then dried under N₂ and stored under air.

When performed several times at 230 °C during 30 min, the Synthesis VII.2. did not systematically provide XRD-pure Ni₃C [PDF card N°04-007-3753] as Ni(0) [PDF card N°03-065-2865] traces were also observed (Figure 3A). To avoid this metallic leftover, the reaction temperature was increased to 250 °C and the reaction time to 2 h: this strategy was successful as pure Ni₃C was then systematically obtained (Figure 3A). TEM images of the NPs formed in Synthesis VII.2. are displayed in Figure 3B-C: they have irregular shapes and are polydisperse in size with diameters ranging from 50 nm to 100 nm. This contrast in shape with the NPs formed in Synthesis VII.1. is explained by the absence of TOP which plays the role of ligand. Selected area electron diffraction performed on the sample confirmed the Ni₃C phase attribution by XRD (Figure 3D).

The observed temperature plateau at 236 °C and the explosions in the liquid were systematically observed for all batches. We suggest this temperature corresponds to a maximum rate of decomposition of 1-octadecene and of the carburization of the nanoparticles. The heat provided by the heating mantle was partially used for these chemical endothermic processes and the medium temperature stopped increasing as long as the carburization reaction was not complete. To examine this point and in order to catch reaction intermediates, Synthesis VII.2. was run and stopped during the heating ramp, right before (230 °C) or after (250 °C) the critical temperature of 236 °C. The reactions were treated as for the regular reactions and the obtained powders characterized by XRD (Figure 3A). When stopped at 230 °C, the reaction led to a mixture of Ni₃C (major phase) and Ni(0) (minor phase) and the two phases were associated to crystallites of similar size *ca.* 10 nm according to Scherrer analysis. When heated to 250 °C, merely all the product was Ni₃C and the Scherrer size of the crystallites increased to 22 nm. At this stage, we cannot decide whether the actual size of the crystallites increased during the heating ramp or if the size was preserved and the crystallinity, *i.e.* the quality of the crystalline order of the atoms, increased. As only traces of Ni(0) were still present for the reaction interrupted when the temperature reached 250 °C, increasing the reaction time to 2 h was probably not necessary.

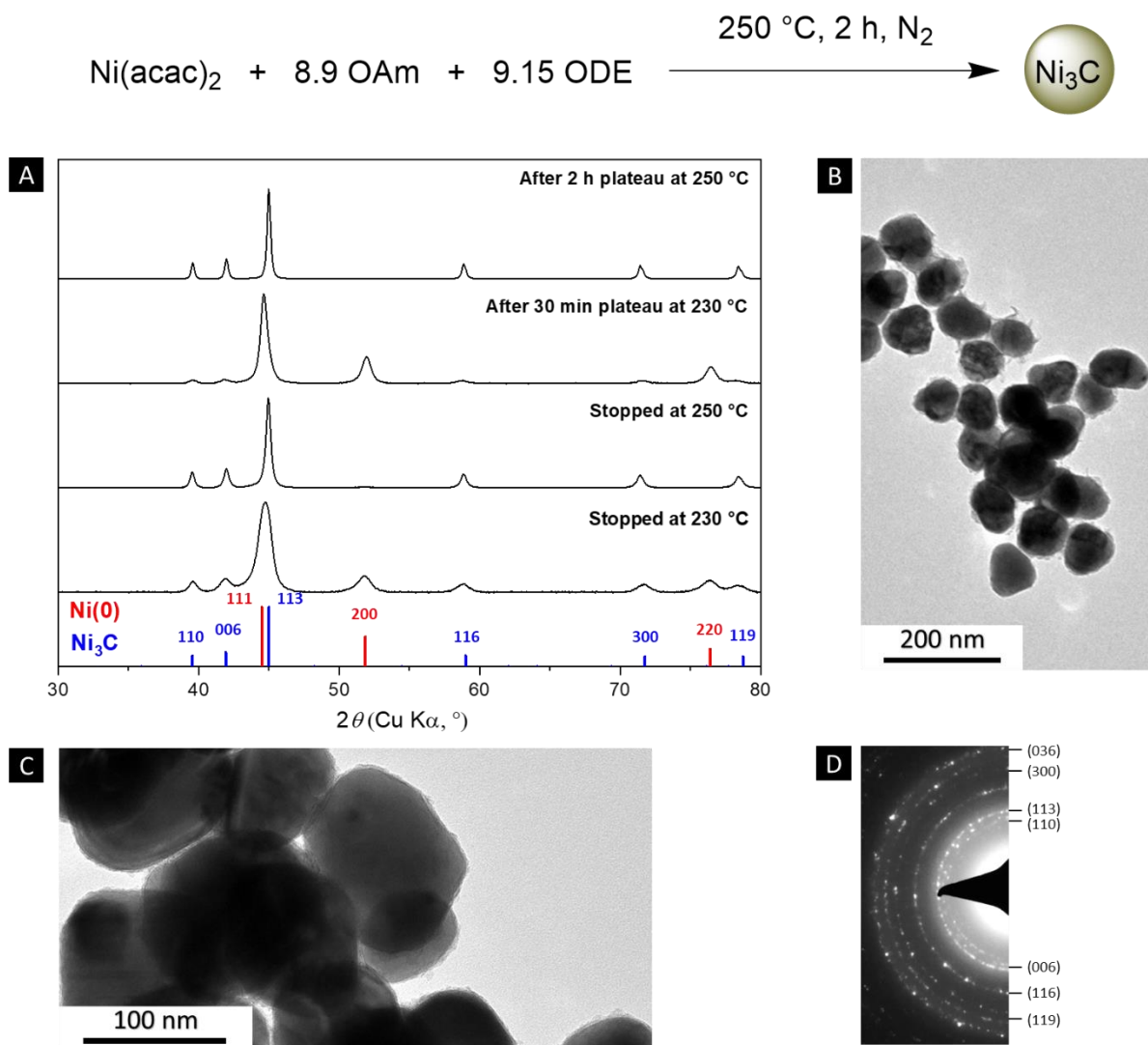


Figure 3. Structural and morphology characterizations of nickel carbide Ni_3C nanoparticles from Synthesis VII.2. (A) XRD of the powders with (hkl) attribution, (B-C) TEM images and (D) selected area electronic diffraction pattern.

Nickel carbide phosphidization. A synthesis of Ni_{12}P_5 nanoparticles was developed according to the protocol developed by Tracy *et al.*¹⁷ The protocol was similar to Synthesis VII.2. followed by an injection of trioctylphosphine (TOP) as phosphidizing agent. The amount of TOP and the temperature of the injection were varied in Syntheses VII.3., VII.4. and VII.5. in order to obtain different nickel phosphide phases.

Synthesis VII.3. Identical to Synthesis VII.2. until after the plateau of 2 h at 250 °C. The solution was then cooled down to r.t. 0.9 mL of TOP (2.02 mmol, 0.4 equiv.) were added by briefly opening one neck. The temperature was increased to 300 °C and the solution was let to react for 30 min at this temperature. After cooling to r.t.,

the crude was treated with an identical process than Synthesis VII.2. to yield a black powder (337 mg) which was dried under N₂ and stored under air.

In Synthesis VII.3., the TOP was injected after the reaction crude was cooled down to r.t. This low-temperature injection is safer than a hot-injection. The experiment was performed twice, one with 30 min of reaction at a targeted reaction temperature of 300 °C and one with 2 h of reaction at 350 °C, with similar results. The PXRD of the recovered powders are displayed on Figure 4 and are very similar to Ni₃C. A broad extra peak appeared at 47.7° and could not be attributed.

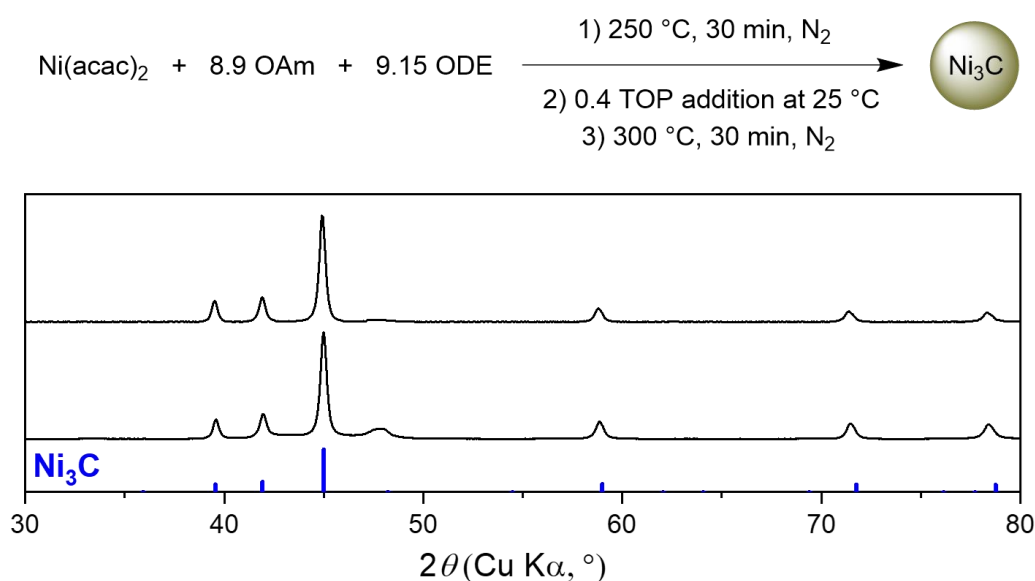


Figure 4. Attempt at phosphidization of nickel carbide nanoparticles according to Synthesis VII.3.: XRD of the powders (top: 30 min at 300 °C, bottom: 2 h at 350 °C).

Synthesis VII.4. Two-step nickel phosphide Ni₁₂P₅. Identical to Synthesis VII.2. until after the plateau of 2 h at 250 °C. The solution was then heated toward 300 °C. When 285 °C were reached, 0.9 mL of TOP (2.02 mmol, 0.4 equiv.) were injected with a syringe by briefly opening one neck. The temperature slightly decreased and then reached 300 °C. The solution was let to react for 30 min at this temperature. After cooling to r.t., the crude was treated with an identical process than Synthesis VII.2. to yield a black powder (375 mg, 102 % yield) which was then dried under a flux of N₂ and stored under air.

Synthesis VII.4. led to Ni₁₂P₅ XRD-pure NPs and was successfully reproduced several times in our lab with similar results, denoting the robustness of the protocol (Figure 5A). The crystalline NPs are 100 nm large irregular spheres with a core-shell morphology (Figure 5B-C). In TEM, the core of the particles is lighter than the shell: the contrast is interpreted as a higher electron density in the shell. We suggest the

dark shell is the phosphide phase which was obtained upon decomposition of the TOP ligands at the surface of the nickel carbide NPs. The phosphorus atoms diffuse at the surface while the nickel atoms are pulled toward the exterior of the nanoparticles. This Ni atom migration results in a modification of the core of the nanoparticle. The phenomenon is often referred to as “nanoscale Kirkendall effect” in literature.^{16,23} The chemical nature of the core was not investigated, it may consist in a void or in amorphous carbon originating from the carbide phase, hence the lower electron density. The solubility of carbon in nickel is good and it would be surprising that the phosphide formation would be responsible for the whole exsolution of carbon from the nickel phase. One possibility is the synthesized NPs are isostructural with Ni_{12}P_5 but consist in a ternary mixture of nickel, carbon and phosphorus. To the best of our knowledge, the characterization of mixed Ni–P–C systems, “nickel phosphocarbide”, has not been reported in literature.

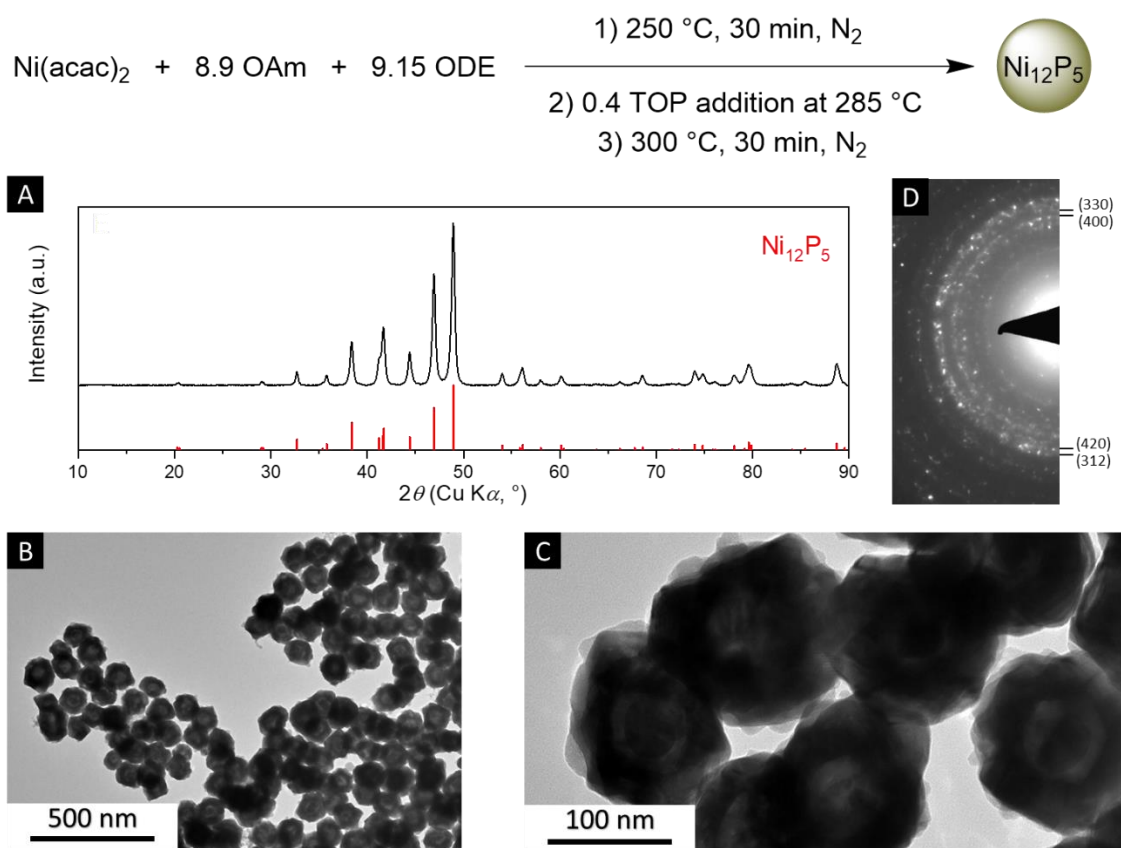


Figure 5. Synthesis of nickel phosphide Ni_{12}P_5 nanoparticles according to Synthesis VII.4. with structural and morphology characterizations. (A) XRD of the powder, (B-C) TEM images and (D) electronic diffraction pattern.

Synthesis VII.5. Two-step nickel phosphide Ni_2P . Identical to Synthesis VII.2. until after the plateau of 2 h at 250 °C. 1.8 mL of TOP (4.04 mmol, 0.8 equiv.) were added by briefly opening one neck. The solution was then heated to 300 °C. Explosions occurred *ca.* 290 °C. The temperature slightly decreased and then reached 300 °C. The solution was let to react for 30 min at this temperature. After cooling to r.t., the crude was treated with an identical process than Synthesis VII.2. to yield a black powder (370 mg, 98 % yield), was dried under N_2 and stored under air.

The quantity of TOP was doubled in Synthesis VII.5. compared to Synthesis VII.4. in order to obtain a more phosphorus-rich phosphide phase. Synthesis VII.5. was performed once and led to Ni_2P XRD-pure NPs (Figure 6A). The increase in TOP proportion was therefore a successful strategy. As for Ni_{12}P_5 NPs in Synthesis VII.4., the irregular spheres have a core-shell morphology with a light core and a dark shell. A similar synthesis mechanism is therefore expected. So far, we could not explain why changing the injection temperature and the TOP:Ni ratio has such a dramatic impact on the final phase, especially considering its high purity (no traces of Ni_{12}P_5). We believe performing several times the experiment to check its reproducibility is essential before commenting the difference between Synthesis VII.4. and VII.5.

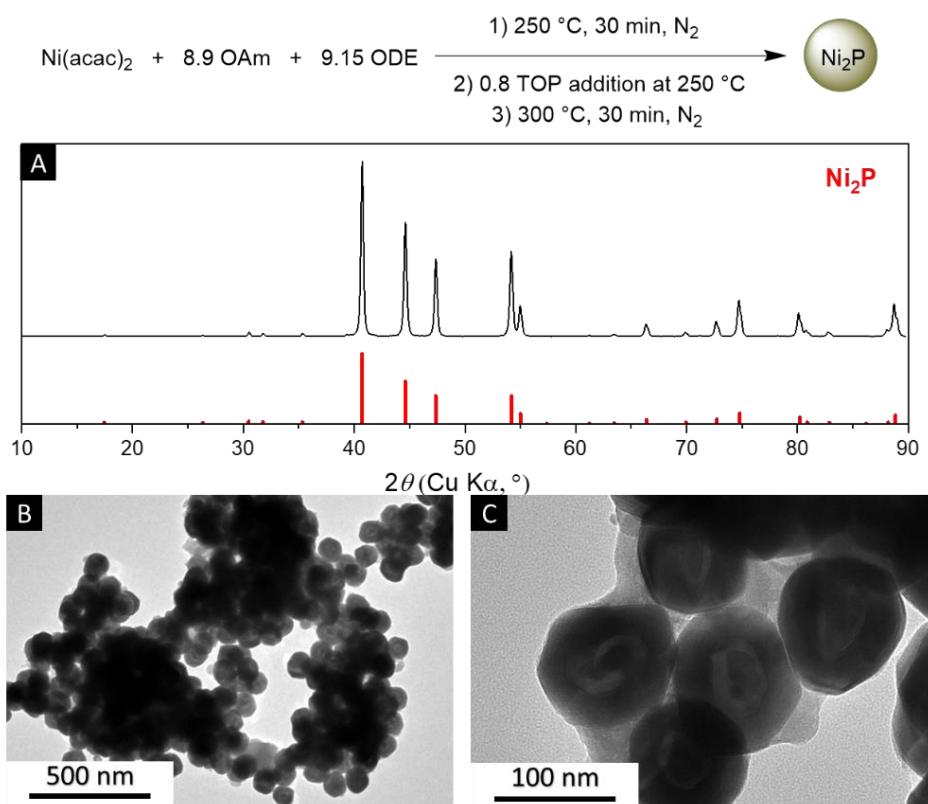


Figure 6. Synthesis of nickel phosphide Ni_2P nanoparticles according to Synthesis VII.5. with structural and morphology characterizations. (A) XRD of the powder, (B-C) TEM images.

X-ray absorption spectroscopy. To further explore the structural features of the crystalline samples, characterization of the nickel-containing nanoparticles was performed by XAS at the Ni K-edge at 8333 eV. The experiments were performed on the ROCK beamline at the SOLEIL synchrotron and details on the protocols are given in Appendix I ES.9.

Figure 7 displays the XAS spectra and the Fourier transforms spectra in the R-space of Ni_2P , Ni_{12}P_5 and Ni_3C phases reported in literature.^{24–27} For Ni_2P , two main peaks are observed at 1.78 Å and 2.24 Å, corresponding to respectively the first shell Ni–P and Ni–Ni distances.²⁵ For Ni_{12}P_5 , the position and the low intensity of the white line support the metallic character of the material and indicate the Ni atoms have a low oxidation state.²⁶ Two coordination shells at 1.80 Å and 2.15 Å were observed in the EXAFS spectrum, corresponding to respectively the Ni–P and Ni–Ni distances. If compared with pure Ni(0) reference, the Ni–Ni bond peak intensity is largely decreased which is interpreted as a lower number of direct Ni–Ni bonds, in accordance with the theoretical crystal structure. For Ni_3C , the EXAFS region differs totally with these of the Ni(0) reference.²⁷ The characteristic distances observed with the Fourier transform of the spectra revealed the first Ni and C shells for Ni_3C (at respectively 1.41 Å and 2.38 Å) and the first Ni shell for Ni(0) (2.19 Å). All the values are in line with the crystallographic data with literature: we can note in particular an increase of Ni–Ni distance upon carburization.

Figure 8 displays the XAS spectra of the Ni(0) foil (used as a reference) and of pellets of Ni_3C , Ni_{12}P_5 and Ni_2P from respectively Syntheses VII.2., VII.4. and VII.5. We can first note the XAS spectra and the Fourier transforms spectra are similar to the ones reported in literature for the corresponding phases (see Table 1 for distances), indicating that most of the material is actually composed of the phase attributed by XRD. Nonetheless, considering the close positions of the Ni–P and Ni–Ni distances in the EXAFS spectra, we cannot exclude at this stage the presence of traces of carbide (Ni_3C) or that of a phosphocarbide phase in the phosphidized samples. On Figure 8B are plotted zooms of the edge regions for all samples. Considering the flatness of the curves, determining an inflexion point is challenging and the edge position can be hardly defined. This is a consequence of the metallic character of the materials with complex electronic structures around the Fermi level.²⁸ Even though ill-defined, the positions of the edges are close to that of Ni(0), indicating the materials are mostly reduced.

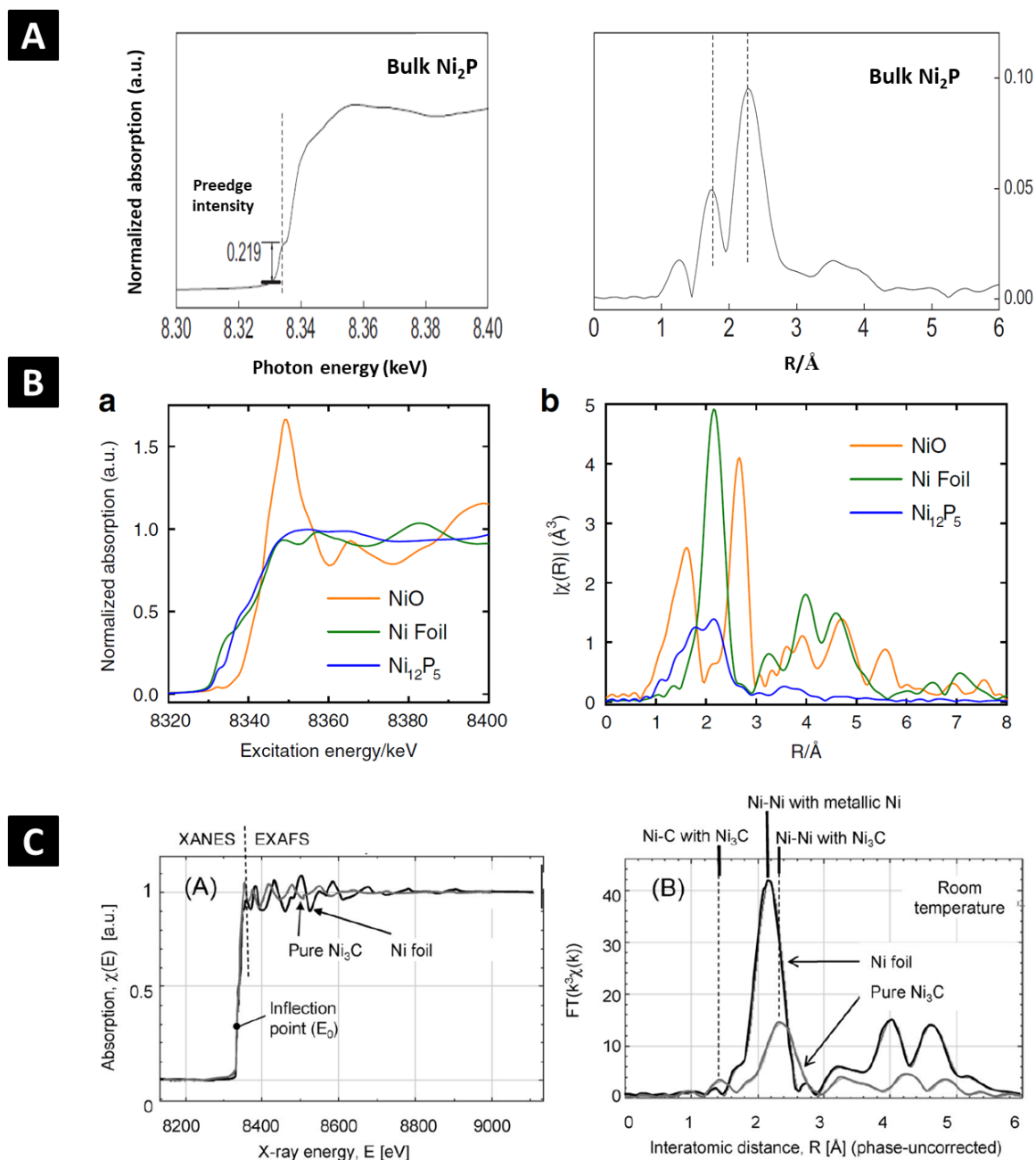


Figure 7. X-ray absorption spectra (left) and k^3 -weighted Fourier transform spectra in the R-space (right) of (A) Ni_2P , (B) Ni_{12}P_5 and (C) Ni_3C . Adapted from respectively references [25], [26] and [27].

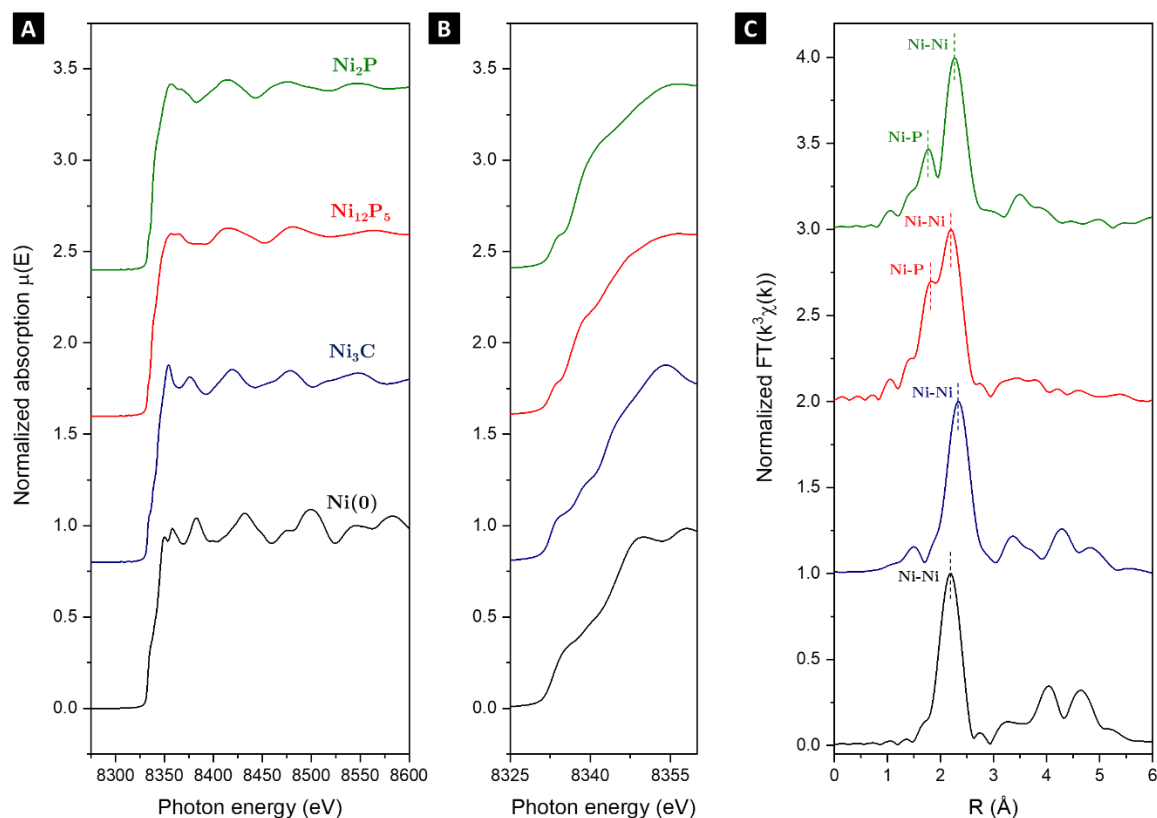


Figure 8. (A) Ni K-edge XANES spectra with (B) zoom on the edge region. (C) k^3 -weighted Fourier transforms in the R-space of a reference Ni(0) foil, Ni₃C nanoparticles (Synthesis VII.2.) and the subsequent phosphidized samples of Ni₁₂P₅ (Synthesis VII.4.) and Ni₂P (Synthesis VII.5.), measured as pellets in graphite.

	Ni–Ni / Å	Ni–C / Å	Ni–P / Å
Ni(0) foil	2.20 (2.19)	-	-
Ni ₂ P	2.27 (2.24)	-	1.77 (1.78)
Ni ₁₂ P ₅	2.21 (2.15)	-	1.83 (1.80)
Ni ₃ C	2.35 (2.38)	1.50 (1.41)	-

Table 1. Characteristic distances (peak positions) extracted from EXAFS spectra in Figure 8C, data in brackets correspond to the ones from literature (Figure 7).

Materials stability. The stability of the catalysts from Syntheses VII.2. (Ni_3C), VII.4. (Ni_{12}P_5) and VII.5. (Ni_2P) under oxidizing conditions was studied. The materials were subjected to dry calcination treatment in air at 200 °C according to Thermal treatment VII.1.

Thermal treatment VII.1. Dry calcination in air. The isolated powders from Syntheses VII.2. (Ni_3C), VII.4. (Ni_{12}P_5) and VII.5. (Ni_2P) were placed in open glass cups and introduced in a muffle furnace. A heating ramp to 200 °C (10 °C/min) was launched and the powders were let at this temperature for 2 h. The furnace was then let to naturally cool down to room temperature. The powders did not undergo any change concerning their visual aspect.

After Thermal treatment VII.1., the Ni_3C sample and the two nickel phosphides originating from the two-step protocols were characterized by XRD and XAS (Figure 9). The spectra and diffractograms before calcination (solid lines) and after calcination (dotted lines) are perfectly identical. This denotes the structural stability of the NPs toward oxidation in spite of the high surface/volume ratio. The stability of the materials in bulk as probed with XAS and XRD is nonetheless not enough to conclude on the stability of their surfaces which are the relevant part of the objects for catalysis. XPS studies of the samples before and after Thermal treatment VII.1. are envisioned to elucidate this question.

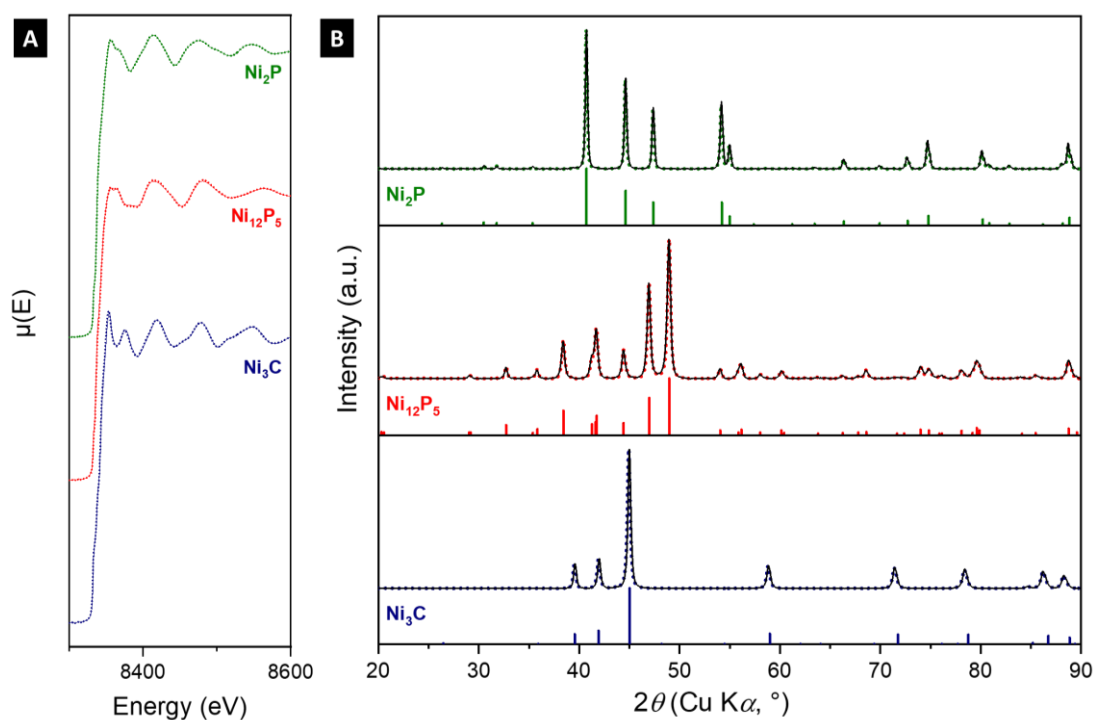


Figure 9. (A) Ni K-edge XANES spectra and (B) XRD spectra of materials from Syntheses VII.2. (Ni_3C), VII.4. (Ni_{12}P_5) and VII.5. (Ni_2P), before (solid lines) and after (dotted lines) Thermal treatment VII.1.

VII.1.3 Carbide-free nickel(0) nanoparticle synthesis

As just developed in the above section, Ni(0) nanoparticles may be easily carburized in Ni₃C in presence of a carburizing agent such as 1-octadecene (ODE). Even in the absence of ODE, works report the synthesis of Ni₃C from Ni(acac)₂ in oleylamine at temperatures as low as 240 °C, provided the reaction time is long enough.²² The temperature triggering the carbide formation from the metal being just above the usual synthesis temperature of the Ni(0) nanoparticles (*ca.* 210 °C), there is a risk the carbide phase got formed, even in small quantities, during an overshoot of the heating ramp or due to an ill-calibrated thermocouple. We propose here a synthesis of Ni(0) performed in decylamine rather than in oleylamine. With this new procedure, the temperature cannot exceed the boiling point of decylamine (DAm) at 217 °C, much lower than that of oleylamine at 364 °C. Previous works already proved the reducing character of oleylamine, required for Ni(0) formation, was not linked to the C=C double bond but rather to the amino group, there is therefore no problem in using DAm for the thermal decomposition of Ni(acac)₂ in Ni(0).²⁹ The synthesis was conducted with and without TOP as ligand for nanoparticle size control (Synthesis VII.6.).

Synthesis VII.6. Carbide-free Ni(0) nanoparticles in DAm. In a 25 mL three-necked round-bottom flask, 9 mL of decylamine (7.1 g, 45 mmol, 37.2 equiv.) were degassed under vacuum at r.t. during 20 min and the flask was purged with N₂ three times. Under N₂, Ni(acac)₂ (310 mg, 1.21 mmol, 1 equiv.) and eventually TOP (0.43 mL, 0.96 mmol, 0.8 equiv.) were added to the solution. The solution was heated to 217 °C with a heating mantle. The resulting solution became emerald green then turquoise and finally a black suspension *ca.* 190 °C. The solution was let to react 2 h at reflux and was then cooled to r.t. under N₂. A black solid was aggregated on the stirring bar and the supernatant was yellowish. The black solid was washed three times with 10 mL. The obtained black powder (69 mg, 97 % yield) was then dried under N₂ and stored in air.

XRD patterns of the particles formed in Synthesis VII.6. are displayed in Figure 10A: Ni(0) NPs are obtained both with and without TOP with respective Scherrer sizes of 8 nm and 25 nm. TEM images of the samples reveal the NPs are spherical in presence of TOP and irregular in absence of TOP (Figure 10B-C) with dimensions coherent with the Scherrer analysis. The TOP acts as a ligand in the synthesis and regulates the growth of the NPs, leading to smaller and more spherical objects. The NPs obtained with Synthesis VII.6. are similar to the ones obtained following a similar synthesis in OAm.¹⁸ The use of DAm solvent instead of OAm in order to obtain a reproducible reaction temperature of 217 °C is therefore validated.

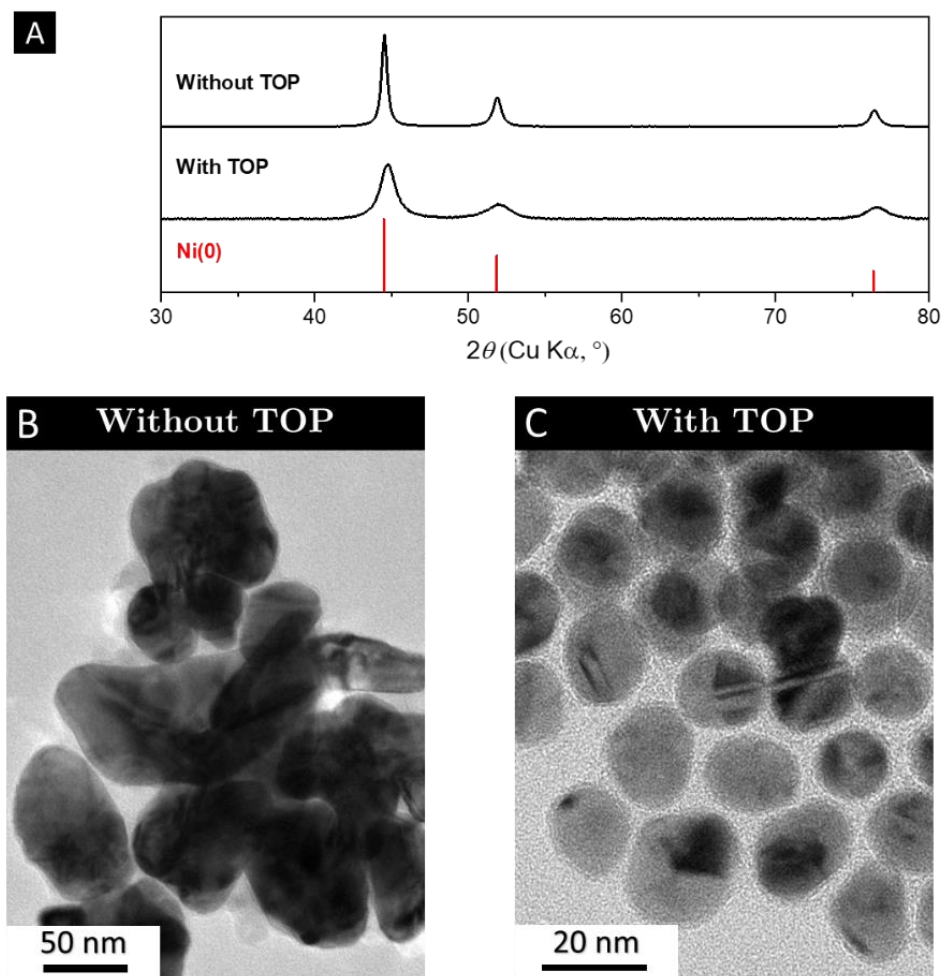


Figure 10. (A) XRD spectra of Ni(0) nanoparticles obtained from Synthesis VII.6. without (top) and with TOP (bottom). Corresponding TEM images of the samples (B) without and (C) with TOP.

VII.2. Hydrogenation reactions

The use of different nickel-containing nanoparticles for hydrogenation reactions in the liquid phase was reviewed in Chapter I. Hydrogenation reactions of nitrobenzene (PhNO_2) and phenylacetylene (PhCCH) under soft conditions were reported with respectively Ni_2P or Ni_{12}P_5 ($100\text{ }^\circ\text{C}$, 10 bar H_2 , EtOH)³⁰ and Ni_2P ($85\text{ }^\circ\text{C}$, 6 bar H_2 , dioxane)⁷. There is however no mention of the use of nickel carbide (Ni_3C) for hydrogenation reaction in solvents. We explored whether this phase, easier to obtain than nickel phosphide as nanoparticles and more resistant to poisoning than $\text{Ni}(0)$, is also active for the reduction of the model compounds PhNO_2 and PhCCH .

A series of experiments was also performed to study the hydrogenation of furfural in furfuryl alcohol by Ni_2P nanoparticles from Synthesis VII.1. and by Ni_3C nanoparticles from Synthesis VII.2. under mild conditions ($90\text{ }^\circ\text{C}$, 7 bar, iPrOH). The catalysis were successful with a conversion in furfuryl alcohol of *ca.* 50 % for Ni_2P and *ca.* 4 % for Ni_3C . We nonetheless chose not to display the results as these experiments were purely exploratory, the protocols for the catalysis not yet fully operational at that time and because the Ni_2P synthesis was not reproducible.

VII.2.1 Nitrobenzene hydrogenation

Catalysis VII.1. Nitrobenzene hydrogenation. In air, 12.5 mg of Ni_3C from Synthesis VII.2. (0.2 mmol, 0.1 equiv. of $[\text{Ni}]$), 1 mL of solvent and 210 μL of nitrobenzene (2 mmol, 1 equiv.) were introduced in a 25 mL glass autoclave. The nanoparticles were suspended by sonication during *ca.* 1 min. The autoclave was closed and the atmosphere was changed for H_2 (7 bar) after 2 cycles vacuum/ H_2 . The autoclave was then introduced in a preheated oil bath at $60\text{ }^\circ\text{C}$ or $100\text{ }^\circ\text{C}$ for 16 h. The pressure initially increased to *ca.* 8 bar and then decreased to *ca.* 5 bar (the characteristic time of decrease depended on the solvent). After reaction, the autoclave was let to cool down naturally to r.t. before opening. An aliquot of the liquid phase was studied by ^1H NMR in CDCl_3 .

Hydrogenation of nitrobenzene in aniline was attempted at $100\text{ }^\circ\text{C}$ in a variety of solvents (EtOH , iPrOH , 1-butanol, dioxane, toluene) with nickel carbide Ni_3C (10 mol%) as catalyst (Catalysis VII.1.). Black suspensions were recovered for all solvents, indicating the colloidal stability of the Ni_3C NPs was good during catalysis. After 2 h, the pressure had dropped by 2.5 bar, 1.5 bar, 1 bar, 0.5 bar and 0.5 bar for respectively EtOH , iPrOH , toluene, dioxane and 1-butanol. The pressure after 2 h being close to the final one for EtOH (5 bar) we suggest the reaction was over much before the end of the 16 h duration. Complete conversions were obtained for all solvents with a 100 % selectivity to aniline at $100\text{ }^\circ\text{C}$ (Figure 11A). Upon decrease of reaction temperature, the conversion dropped below 20 % for all solvents except EtOH for which a complete conversion was still obtained. We concluded the H_2

activation for nitro group hydrogenation on Ni_3C NPs was more favorable in protic and polar solvents than in apolar ones and that there is still a margin of progression as to the temperature and H_2 pressure for the reaction run in EtOH.

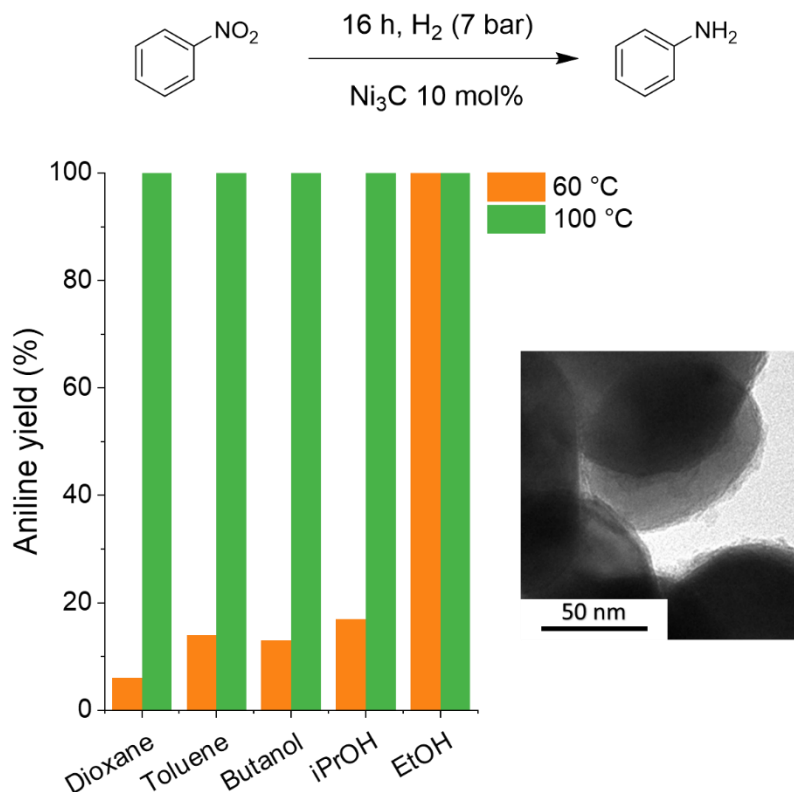


Figure 11. Hydrogenation of nitrobenzene with Ni_3C according to Catalysis VII.1. Yields determined by NMR.

The protocol for Catalysis VII.1. was chosen after optimization. In the original one, a simple stirring but no sonication was performed to disperse the NPs. It appeared *a posteriori* the sonication step was essential to well disperse the NPs and obtain optimal and well reproducible results. The results obtained without sonication with Ni_3C from Synthesis VII.2. and Ni_{12}P_5 from Synthesis VII.4. are displayed in Figure 12. We believe they should be treated as a proof of concept and not directly compared with those obtained with Catalysis VII.1. It appears Ni_{12}P_5 NPs indeed have a catalytic activity for PhNO_2 hydrogenation, and apparently lower than Ni_3C NPs. The reactions with Ni_{12}P_5 and Ni_2P NPs following Catalysis VII.1. are currently under investigation to be compared with those with Ni_3C .

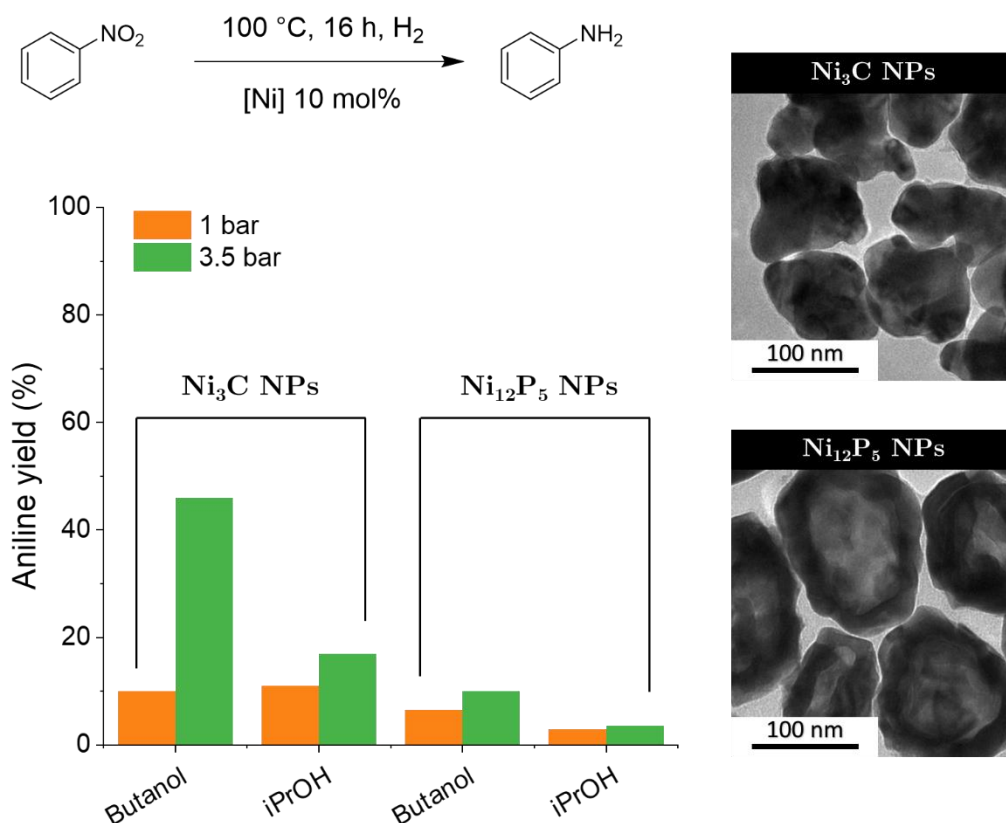


Figure 12. Hydrogenation of nitrobenzene with Ni_3C and Ni_{12}P_5 according to modified Catalysis VII.1. (no sonication, 330 μL PhNO_2 , 1.67 mL of solvent, with lower H_2 pressures). Yields determined by NMR.

VII.2.2 Phenylacetylene hydrogenation

Catalysis VII.2. Phenylacetylene hydrogenation. In air, 12.5 mg of Ni_3C from Synthesis VII.2. (0.2 mmol, 0.1 equiv. of $[\text{Ni}]$), 1 mL of solvent and 220 μL of phenylacetylene (2 mmol, 1 equiv.) were introduced in a 25 mL glass autoclave. The nanoparticles were suspended by sonication during *ca.* 1 min. The autoclave was closed and the atmosphere was changed for H_2 (7 bar) after 2 cycles vacuum/ H_2 . The autoclave was then introduced in a preheated oil bath at 100 $^{\circ}\text{C}$ for 16 h. The pressure initially increased to *ca.* 8 bar and then decreased to *ca.* 5 bar (the characteristic time of decrease depended on the solvent). After reaction, the autoclave was let to cool down naturally to r.t. before opening. An aliquot of the liquid phase was studied by ^1H NMR in CDCl_3 .

Hydrogenation of phenylacetylene in styrene and ethylbenzene was attempted at 100 $^{\circ}\text{C}$ in a variety of solvents (EtOH, iPrOH, 1-butanol, dioxane, toluene) with nickel carbide Ni_3C (10 mol%) as catalyst (Catalysis VII.2.). All the phenylacetylene was hydrogenated in the different studied solvents and a more important over-hydrogenation was observed for the protic and polar solvents (alcohols) (Figure 13A).

Reactions at lower temperatures and with Ni_{12}P_5 and Ni_2P NPs following are currently under investigation to be compared with those with Ni_3C .

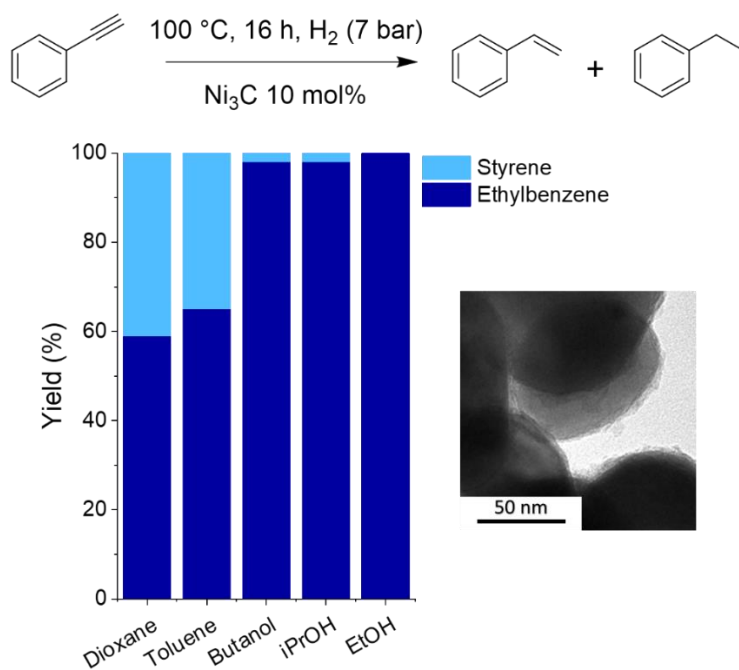


Figure 13. Hydrogenation of phenylacetylene with Ni_3C according to Catalysis VII.2. Yields determined by NMR.

VII.3. Conclusion

We attempted the solvothermal synthesis of < 10 nm large NPs of nickel phosphide (Ni_2P , Ni_{12}P_5) but the materials were not XRD-pure which would have complicated the catalytic results interpretations. We nonetheless provided a few clues on the influence of temperature on phase speciation and stressed the critical importance of the heating setup on the reaction temperature. By following and adapting a previously published two-step protocol, we successfully synthesized a family of comparable 100 nm large nickel-containing NPs (Ni_3C , Ni_2P and Ni_{12}P_5). The phosphide NPs were obtained by hot-injection of TOP in a Ni_3C NPs suspension and displayed a core-shell morphology. For these optimized syntheses, the catalysts appeared XRD-pure and the XAS signatures were coherent with the ones reported in literature. The absence of modification of the XAS spectra upon oxidizing conditions denoted the core stability of the NPs.

Nickel carbide proved to be an efficient catalyst for nitrobenzene reduction in aniline and for phenylacetylene hydrogenation in ethylbenzene, with a total conversion in EtOH at respectively 60 °C and 100 °C. An important influence of the solvent was observed with the highest activities obtained in alcohols (1-butanol, 2-propanol, ethanol) compared to dioxane and toluene. The same solvent trend was followed for both nitro and alkyne hydrogenation. Preliminary data on furfural hydrogenation indicated Ni_3C has a catalytic activity for $\text{C}=\text{O}$ hydrogenation under soft conditions (90 °C, 7 bar H_2). Catalytic hydrogenation of furfural in furfuryl alcohol with < 10 nm large Ni_{12}P_5 - Ni_2P NPs was obtained with a higher conversion than with Ni_3C .

Different perspectives based on these results are envisioned:

- (1) The use of softer conditions and shorter reaction times for nitrobenzene and phenylacetylene hydrogenation with Ni_3C as complete conversions were obtained in both cases, and the extension to other substrates such as benzaldehyde or benzonitrile.
- (2) Reproducible syntheses of comparable Ni_{12}P_5 , Ni_2P and $\text{Ni}(0)$ NPs have been established. We suggest using all these NPs for similar reactions (with the $\text{Ni}(0)$ NPs as a benchmark catalyst) to compare the catalytic activities (conversions and chemoselectivities)
- (3) Studying the impact of the addition of a phosphine on the hydrogenation reactions

VII.4. Bibliography

1. Raney, M. Method of producing finely-divided nickel - US1628190A. 2 (1927).
2. Delgado, J. A., Benkirane, O., Claver, C., Curulla-Ferré, D. & Godard, C. Advances in the preparation of highly selective nanocatalysts for the semi-hydrogenation of alkynes using colloidal approaches. *Dalt. Trans.* **46**, 12381–12403 (2017).
3. Kalyon, N. *et al.* Catalytic activity of nanoscale borides: Co₂B and Ni₇B₃ in the liquid-phase hydrogenation of citral. *J. Catal.* **352**, 436–441 (2017).
4. Carenco, S., Portehault, D., Boissière, C., Mézailles, N. & Sanchez, C. Nanoscaled metal borides and phosphides: Recent developments and perspectives. *Chem. Rev.* **113**, 7981–8065 (2013).
5. Gage, S. H., Trewyn, B. G., Ciobanu, C. V., Pylypenko, S. & Richards, R. M. Synthetic advancements and catalytic applications of nickel nitride. *Catal. Sci. Technol.* **6**, 4059–4076 (2016).
6. Yang, K., Chen, X., Guan, J. & Liang, C. Nickel silicides prepared from organometallic polymer as efficient catalyst towards hydrogenation of phenylacetylene. *Catal. Today* **246**, 176–183 (2015).
7. Carenco, S. *et al.* Nickel phosphide nanocatalysts for the chemoselective hydrogenation of alkynes. *Nano Today* **7**, 21–28 (2012).
8. Cao, F. *et al.* One-pot synthesis of flowerlike Ni₇S₆ and its application in selective hydrogenation of chloronitrobenzene. *J. Mater. Chem.* **20**, 1078–1085 (2010).
9. Quesne, M. G., Roldan, A., de Leeuw, N. H. & Catlow, C. R. A. Bulk and surface properties of metal carbides: implications for catalysis. *Phys. Chem. Chem. Phys.* **20**, 6905–6916 (2018).
10. Sautet, P. & Cinquini, F. Surface of Metallic Catalysts under a Pressure of Hydrocarbon Molecules: Metal or Carbide? *ChemCatChem* **2**, 636–639 (2010).
11. Alexander, A. M. & Hargreaves, J. S. J. Alternative catalytic materials: carbides, nitrides, phosphides and amorphous boron alloys. *Chem. Soc. Rev.* **39**, 4388–4401 (2010).
12. Levy, R. B. & Boudart, M. Platinum-Like Behavior of Tungsten Carbide in Surface Catalysis. *Science* **181**, 547–549 (1973).
13. Phimsen, S. *et al.* Nickel sulfide, nickel phosphide and nickel carbide catalysts

- for bio-hydrotreated fuel production. *Energy Convers. Manag.* **151**, 324–333 (2017).
14. Fiorio, J. L., López, N. & Rossi, L. M. Gold–Ligand-Catalyzed Selective Hydrogenation of Alkynes into cis-Alkenes via H₂ Heterolytic Activation by Frustrated Lewis Pairs. *ACS Catal.* **7**, 2973–2980 (2017).
 15. Moreau, L. M. *et al.* Defining Crystalline/Amorphous Phases of Nanoparticles through X-ray Absorption Spectroscopy and X-ray Diffraction: The Case of Nickel Phosphide. *Chem. Mater.* **25**, 2394–2403 (2013).
 16. Muthuswamy, E. & Brock, S. L. Solid-state phase transformations in solution: templated conversion of nanoscale nickel phosphides. *Chem. Commun.* **47**, 12334 (2011).
 17. Sarac, M. F., Wu, W. & Tracy, J. B. Control of Branching in Ni₃C_{1-x} Nanoparticles and Their Conversion into Ni₁₂P₅ Nanoparticles. *Chem. Mater.* **26**, 3057–3064 (2014).
 18. Carenco, S. *et al.* Controlled Design of Size-Tunable Monodisperse Nickel Nanoparticles. *Chem. Mater.* **22**, 1340–1349 (2010).
 19. Muthuswamy, E., Savithra, G. H. L. & Brock, S. L. Synthetic Levers Enabling Independent Control of Phase, Size, and Morphology in Nickel Phosphide Nanoparticles. *ACS Nano* **5**, 2402–2411 (2011).
 20. Yang, W., Rehman, S., Chu, X., Hou, Y. & Gao, S. Transition Metal (Fe, Co and Ni) Carbide and Nitride Nanomaterials: Structure, Chemical Synthesis and Applications. *ChemNanoMat* **1**, 376–398 (2015).
 21. Schaefer, Z. L., Weeber, K. M., Misra, R., Schiffer, P. & Schaak, R. E. Bridging hcp-Ni and Ni₃C via a Ni₃C_{1-x} Solid Solution: Tunable Composition and Magnetism in Colloidal Nickel Carbide Nanoparticles. *Chem. Mater.* **23**, 2475–2480 (2011).
 22. Goto, Y. *et al.* Formation of Ni₃C Nanocrystals by Thermolysis of Nickel Acetylacetonate in Oleylamine: Characterization Using Hard X-ray Photoelectron Spectroscopy. *Chem. Mater.* **20**, 4156–4160 (2008).
 23. Chiang, R.-K. & Chiang, R.-T. Formation of Hollow Ni₂P Nanoparticles Based on the Nanoscale Kirkendall Effect. *Inorg. Chem.* **46**, 369–371 (2007).
 24. Chen, Y. *et al.* Metal Phosphides Derived from Hydrotalcite Precursors toward the Selective Hydrogenation of Phenylacetylene. *ACS Catal.* **5**, 5756–5765 (2015).
 25. Seo, H.-R., Cho, K.-S. & Lee, Y.-K. Formation mechanisms of Ni₂P

- nanocrystals using XANES and EXAFS spectroscopy. *Mater. Sci. Eng. B* **176**, 132–140 (2011).
26. Xu, Y.-F. *et al.* High-performance light-driven heterogeneous CO₂ catalysis with near-unity selectivity on metal phosphides. *Nat. Commun.* **11**, 5149 (2020).
 27. Struis, R. P. W. J., Bachelin, D., Ludwig, C. & Wokaun, A. Studying the Formation of Ni₃C from CO and Metallic Ni at T = 265 °C in Situ Using Ni K-Edge X-ray Absorption Spectroscopy. *J. Phys. Chem. C* **113**, 2443–2451 (2009).
 28. Bekaert, E. *et al.* Direct Correlation between the ³¹P MAS NMR Response and the Electronic Structure of Some Transition Metal Phosphides. *J. Phys. Chem. C* **112**, 20481–20490 (2008).
 29. Carenco, S. *et al.* Revisiting the Molecular Roots of a Ubiquitously Successful Synthesis: Nickel(0) Nanoparticles by Reduction of [Ni(acetylacetonate)₂]. *Chem. - A Eur. J.* **18**, 14165–14173 (2012).
 30. Liu, P., Zhang, Z.-X., Jun, S. W., Zhu, Y.-L. & Li, Y.-X. Controlled synthesis of nickel phosphide nanoparticles with pure-phase Ni₂P and Ni₁₂P₅ for hydrogenation of nitrobenzene. *React. Kinet. Mech. Catal.* **126**, 453–461 (2019).

General conclusion and Perspectives

The objective of this PhD work was to develop the syntheses of metal-containing nanoparticles for H_2 activation in solvent. To do so, we targeted three main categories of syntheses: solvent-free, in water and in organic solvent. As the H_2 splitting on non-purely metallic catalyst surfaces is largely guided by the presence of defects and singularities leading to coordinatively unsaturated sites (CUS), we favored the syntheses susceptible to create such active sites. We therefore devoted a particular attention to the mechanisms of nanoparticles formation.

From nanoparticles syntheses...

Part 1 – Solid-state metathesis. The solid-state metathesis of several early transition metal nanocarbides and nanohydrides was deeply investigated in this PhD work, essentially through XRD and TEM. Using the results obtained with the different metals (Zr, Nb, Mo, Hf, Ta and W), we could propose a mechanism for their formation: reduction, carburization, hydrogenation and finally oxidation. A rational understanding of the reactivity was established with thermodynamic considerations: the temperature of combustion was indeed estimated with the enthalpy of reaction and the heat capacity of the reactive mixture. We evidenced the influence of several parameters on the phase speciation in the product, such as the nature of the carbon support, the presence of a gas phase or the scale of the reaction. The thermodynamic considerations previously mentioned seemed to exclude the extension of this SSM reaction to late transition metals and rare-earth metals, as well as the substitution of the metal chloride precursors by metal oxides. The nanoparticles of the initially targeted phases (Mo_2C , W_2C) could be easily obtained in gram scale quantities. Besides, they are already disposed on a conductive carbon support, very well suited for electrocatalysis and colloidal catalysis.

Part 2 – Hydrothermal syntheses. Cerium hydroxide and oxide nanorods were synthesized following a hydrothermal route: a solution of $Ce(NO_3)_3$ was mixed with a solution of NaOH or KOH, the precipitating agent, and then heated at 100 °C. We demonstrated the crucial importance of the reaction container (Teflon autoclave, Nalgene vessel or Borosilicate vessel) on the obtained phase: either a cerium oxide, CeO_2 , for the Teflon autoclave and the Nalgene vessel or a cerium trihydroxide, $Ce(OH)_3$, for the Borosilicate vessel. During the development of a catalytically active cerium oxide phase, we reported an unusual evolution of the $Ce(OH)_3$ phase in an unknown crystalline compound. By comparison with other lanthanide hydroxides, we suggested this compound may correspond to a cerium(IV) hydroxide or oxyhydroxide

rather than a cerium oxide. In addition of the crystallographic characterization (XRD, SAED), different techniques were used to establish the degree of oxidation of cerium (XPS, XAS), the presence of hydroxyl groups (IR) and of multiple defects upon heating (TEM). There is an ongoing study to elucidate the crystal structure of the aged $\text{Ce}(\text{OH})_3$. The synthesis of indium oxide nanoparticles was then successfully achieved according to literature protocols, and yields to similar results than the published ones.

Part 3 – Solvothermal syntheses. The synthesis of tungsten oxide nanowires was achieved from WCl_6 in an oleyl alcohol/oleylamine mixture. As this structure presents tungsten atoms at various degrees of oxidation and oxygen defects, we estimated the materials would be of interest for H_2 activation. We also conducted the synthesis of molybdenum oxides nanoparticles in oleylamine and oleic acid. The characterization of the nanoparticles was quite challenging considering the amorphous structure in the first case and the failure to isolate the nanoparticles in the second case. We therefore used XAS to determine what were the oxidation degrees of the metallic center (Mo) in each case. To our surprise, the two materials were different: an intermediate metal oxide MoO_x ($2 < x < 3$) for the synthesis in OAm and a phase close to MoO_2 for the synthesis in OAc. The study by ^1H NMR of the crudes of reaction revealed the organic byproducts were substantially different. The study of the mechanism of formation of these metal oxides would be of interest in order to compare OAm and OAc as solvents for nanoparticles syntheses. Up to now, most of the mechanistic studies with OAm focused on reduced metals (Pd, Ni, Cu) and the study of MoO_x nanoparticles would enlarge the scope. *In situ* XAS data on the formation of molybdenum oxides in OAm and OAc are currently under investigation using the MCR-ALS approach. Finally, the syntheses of two nickel phosphide (Ni_2P and Ni_{12}P_5) and one nickel carbide (Ni_3C) nanoparticles were achieved in an oleylamine/1-octadecene/trioctylphosphine mixture. The one-pot two-step procedure (carburization followed by phosphidization) was first developed by Tracy *et al.* to obtain the Ni_{12}P_5 phase but we adapted it to form Ni_2P nanoparticles (higher amount of injected TOP and lower temperature of injection).

...to colloidal catalysis...

Hydrogenation with metal carbides. Hydrogenation of styrene and phenylacetylene was attempted with Mo_2C and W_2C nanoparticles supported on carbon. No catalytic activity for hydrogenation of styrene was obtained for W_2C . Preliminary data indicated the Mo_2C sample possessed a catalytic activity in gas phase hydrogenation of butadiene but a very poor one at 100 °C for phenylacetylene reduction in solvent. As the reduction of an oxidized shell around the nanoparticles at temperatures higher than 120 °C seemed necessary, we suggest for the future the use of temperatures in the range 150-200 °C for the hydrogenation reaction. In addition of

their use in hydrogenation catalysis, Mo₂C/C samples are currently under study, through collaborations, for Reverse Water Gas Shift reaction (RWGS) and electrocatalysis, respectively at the LSFC by the group of Helena Kaper and at the FHI by the group of Beatriz Roldan. Besides, the quite unique formation of nanoparticles of supported metal hydrides would be the occasion to investigate their catalytic activity, for the Haber Bosch process for instance as the catalysis by isolated tantalum hydride species was previously reported.

Hydrogenation with metal oxides. Hydrogenation of phenylacetylene was studied in presence of CeO₂ and Bi_{0.02}In₂O₃. The results presented in this PhD work confirmed and extended first the H₂ adsorption on reduced CeO₂ already presented by different published works on close materials and then the alkyne hydrogenation in solvent. The preliminary data for phenylacetylene and nitrobenzene hydrogenations with W₁₈O₄₉ and MoO_x nanoparticles showed very poor yields even at elevated temperature (150 °C) and under high H₂ pressures (30 bar). We could eventually suggest the study of the addition of a phosphine or amine to boost the reactivity but we think it would be more pertinent to focus on the cerium and indium oxide catalysts.

Colloidal hydrogenation with nickel-containing nanoparticles. The catalytic activity for colloidal hydrogenation with nickel carbide (Ni₃C) nanoparticles was reported for the first time in this PhD work. Although Ni–C catalysts have already been mentioned in gas phase hydrogenation or for hydrotreatment, there was no published work on its use for nitro compounds or olefins reduction in solvent. Experiments are planned to first reach the mildest conditions as possible (temperature, pressure, metal loading) and then extend the scope of the studied substrates (nitrile, ketone, aldehyde). We envision then the comparative study of the catalytic activity of the phosphide phases (Ni₂P, Ni₁₂P₅) and the carbide one.

Multiple categories of materials were synthesized in this work, we therefore concentrated our effort on the ones leading to the most interesting results with our current setup, *i.e.* the cerium containing phases and the nickel containing phases. Up to recently, the laboratory was equipped with a gas system allowing pressures up to only 7 bar, but has now been upgraded to 100 bar. Different catalysts (metal oxides, early transition metal carbides), for which lower activities are expected according to preliminary results, will therefore be the object of a postdoctoral work in the laboratory with higher H₂ pressures.

...to reach a “Nano” Frustrated Lewis Pair

H₂ activation. The most promising results as to the construction of a NanoFLP system, *i.e.* a colloidal activation of H₂ in solvent between a molecular base and an inorganic nanoparticle, were obtained with the cerium oxide nanoparticles. We indeed demonstrated the stability of surface hydride species on reduced cerium oxide. Now we

developed reproducible syntheses for defective CeO_2 and nickel-containing nanoparticles, we suggest as a perspective to study the influence of the presence of phosphines (PCy_3 , P^tBu_3 , PPh_3) or amines (tmp, lutidine) on the hydrogenation reactions, eventually after increasing the reaction temperature to have higher yields.

CO_2 activation. The CO_2 molecule is known for its affinity with metal oxide surfaces. A perspective we envision is the activation of the $\text{C}=\text{O}$ bond of carbon dioxide, on the different metal oxides we synthesized, with the eventual addition of a molecular base. Activation of CO_2 *via* an FLP mechanism is indeed currently under investigation in the laboratory by Cyprien Poucin (PhD 2019-2022) and Anthony Ropp (PhD 2021-2024).

To conclude, it is time to look back at the initial question of this PhD: “Can we develop tailored syntheses of new metal-containing catalysts for colloidal hydrogenation, resistant to poisoning and without rare elements?” Our contribution to the answer can be decomposed in several points:

- We first developed a synthetic method of early transition carbides nanoparticles, easily performed in laboratory, with common precursors and on the scale of several grams. The metals present in these materials (Ti, V, Zr, Nb, Mo, W) are abundant enough not to present tensions as to their supply for catalytic applications. Some of the corresponding materials (Mo_2C , WC) are currently the object of intense research by the heterogeneous catalysis community.
- Cerium oxide is already used on large scales for catalytic applications and we exposed an unreported evolution of a hydroxide precursor for the CeO_2 nanoparticles synthesis. We also confirmed there is a potential for selective hydrogenation reactions in solvent in addition of that of acetylene in gas phase. Although cerium is a rare-earth element, its natural abundance, 66 ppm in the Earth crust, is between those of Cu (60 ppm) and Ni (84 ppm): its supply is therefore not problematic.
- We paved the way for a simple solvothermal synthesis of small and defective molybdenum oxide nanoparticles.
- We demonstrated the catalytic activity of Ni_3C for hydrogenation of nitro compounds and olefins, unheard of so far. Nickel carbide is expected to be more tolerant to deactivation by light element insertion than $\text{Ni}(0)$ and the synthesis of XRD-phase pure nanoparticles *via* solvothermal pathway is more straightforward than those of the nickel phosphide counterparts.

Appendix I

Experimental section

ES.1. Chemicals

Unless otherwise stated, all chemicals were used as received and without purification. NbCl_5 (99.9 %), WCl_6 (99.9 %), K (99.5 %), phenylacetylene (98 %), styrene (99 %), toluene (99.8 %), tetrahydrofuran (99 %), hexane (98 %), 1-butanol (97 %), butylamine (99.5 %), PPh_3 (98 %), NaOH (98 %), KOH (98 %), oleylamine (OAm) (98 %), oleic acid (85 %), oleyl alcohol (85 %), 1-octadecene (ODE) (90 %), octyl ether (99 %), furfural (99 %), dioxane (99.5 %), DMF (99.8 %), DMSO (95 %), acetone (97 %), $\text{Bi}(\text{NO}_3)_3 \cdot 5\text{H}_2\text{O}$ (98 %), MoO_3 (99 %) and CeO_2 (99.9 %) were purchased from Sigma-Aldrich. Ethanol (96 %), methanol (95 %) and isopropanol (95 %) were purchased from VWR. ZrCl_4 (99.5 %), MoCl_3 (99.5 %), PCy_3 (97 %), TOP (97 %), $\text{MoO}_2(\text{acac})_2$ (95 %), $\text{Ni}(\text{acac})_2$ (95 %) and $\text{Ce}(\text{OH})_4$ were purchased from Strem Chemicals. HfCl_4 (99.9 %), MoCl_5 (99.6 %), TaCl_5 (99.8 %), carbon black acetylene (99.9 %, 50 % compressed), natural graphite powder (99.9 %, Ultra F purity), $\text{Ce}(\text{NO}_3)_3 \cdot 6\text{H}_2\text{O}$ (99.5 %) and $\text{In}(\text{NO}_3)_3 \cdot 6\text{H}_2\text{O}$ (99.9 %), were purchased from Alfa Aesar.

Commercial WCl_6 from Sigma Aldrich and Strem Chemicals was contaminated with traces of metallic W(0). It was purified by recrystallization in a Schlenk tube under static vacuum at 210 °C during 2 h. The solid at the bottom of the Schlenk gradually sublimates (red gas phase) and recrystallizes as big violet crystals on the glass walls in the cold part of the Schlenk

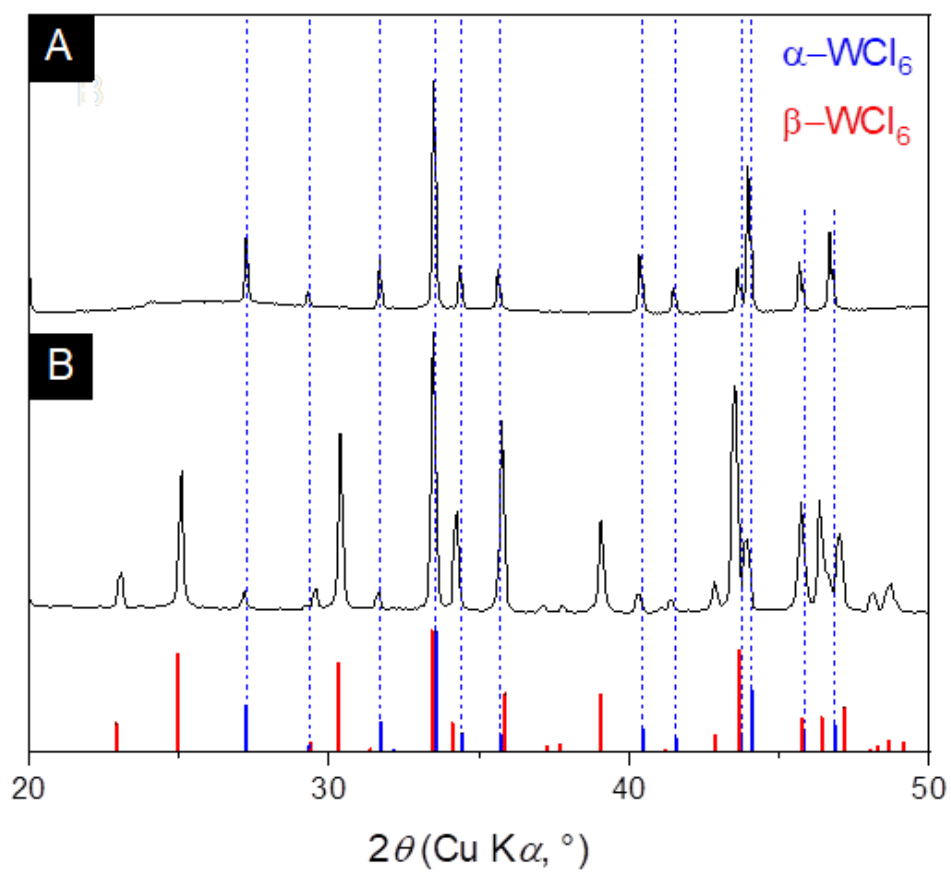


Figure 1: PXRD pattern of (A) commercial WCl_6 and (B) recrystallized sample (210 °C under vacuum).

ES.2. Nanoparticle syntheses and catalysis

The different synthetic protocols and catalysis protocols were given along the PhD thesis. The hydrothermal syntheses in Chapters IV and V were performed in borosilicate vessels, Nalgene vessels or hydrothermal bombs as shown in Figure 2.

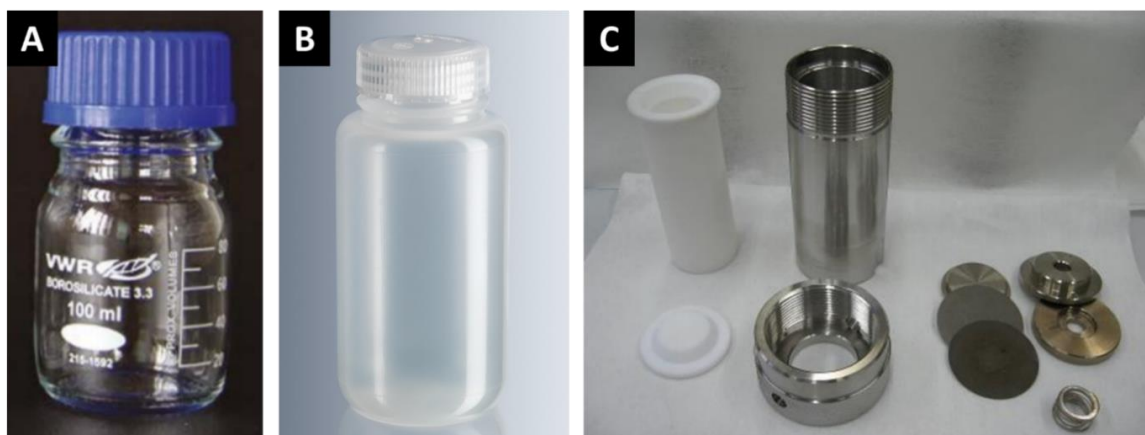


Figure 2. Typical glassware used for hydrothermal syntheses of CeO_2 and In_2O_3 catalysts. (A) Borosilicate vessel (reproduced from www.vwr.com), (B) Nalgene vessel, (C) Teflon autoclave/hydrothermal bomb.

The solvothermal syntheses in Chapters VI and VII were performed in regular glassware under N_2 with the use of a Schlenk ramp. The round-bottom flask was disposed in a heating mantle and the temperature was regulated with the aid of a thermocouple inserted in a glass finger directly in contact with the solution (Figure 3). After reactions, the glassware was thoroughly washed with aqua regia to remove any trace of metals.

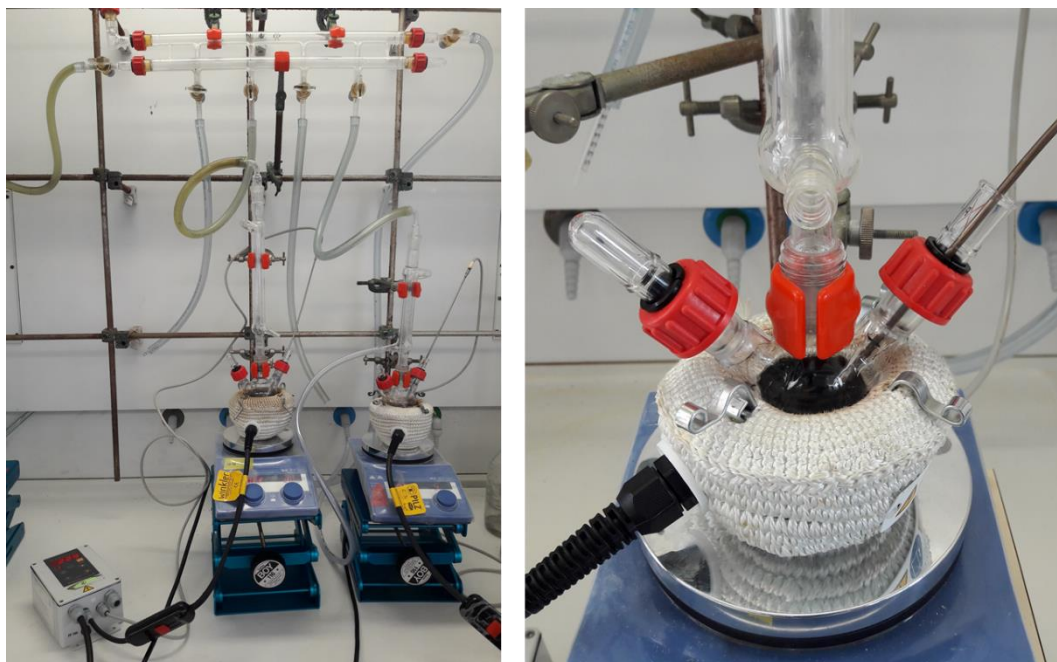


Figure 3. Typical setup used for solvothermal syntheses of MoO_x , $\text{W}_{18}\text{O}_{49}$ and nickel containing NPs.

Liquid phase catalysis under a pressure of H_2 were performed in a Büchi autoclave composed of a head and a container, in glass for pressures below 7 bar and in Teflon + steel for pressures below 100 bar (Figure 4). The autoclaves were then directly disposed in an oil bath for heating.



Figure 4. Typical Büchi autoclave used for catalytic experiments under pressure. Left: Teflon cuve. Right: glass cuve. Photo reproduced from the Büchi website (www.buchiglas.fr)

ES.3. Fourier Transform Infrared Spectroscopy (FTIR)

Infrared spectra were measured with a Spectrum 400 PerkinElmer spectrometer. The solids were pressed on the crystal in Attenuated Total Reflectance (ATR) mode and the transmittance was recorded on the 4000-550 cm^{-1} range with steps of 0.5 cm^{-1} .

ES.4. Nuclear Magnetic Resonance (NMR)

NMR experiments were performed on a Bruker AV^{III} 300 MHz. For catalysis and synthesis crudes analysis, an aliquot of the solution was collected and directly mixed with CDCl_3 . Spectra were acquired after locking to CDCl_3 signal and shimming. Typical ^1H NMR spectra are acquired in 5 min and treated with TopSpin software with calibration on the signal of CHCl_3 (7.26 ppm) if possible, otherwise on toluene methyl (2.36 ppm).

ES.5. Powder X-Ray Diffraction (XRD)

X-ray diffraction patterns of dry powders were measured on a Bruker D8 diffractometer using $\text{Cu K}\alpha$ radiation at 1.5406 Å. Measurements in capillary were performed on a Bruker D8 diffractometer using $\text{Mo K}\alpha$ radiation at 0.7093 Å. Typical diffractograms were collected with steps of 0.05 ° and a scanning speed of 3 s/point. Backgrounds of the patterns are subtracted and heights of the samples are corrected (KCl was used as an internal reference for solid-state metathesis reactions) using the DiffracEVA software. Debye-Sherrer analysis were conducted using DiffracEva software. Most of the PDF/JCPDS cards used in this work were listed in the body of the text.

Phase	PDF N°	Phase	PDF N°
$\alpha\text{-Zr(0)}$	[04-008-1477]	ZrH_2	[00-017-0314]
ZrC	[00-035-0784]	ZrO_2	[04-007-0952]
$\alpha\text{-Hf(0)}$	[00-038-1478]	$\text{HfH}_{1.74}$	[00-005-0641]
		HfO_2	[00-053-0560]
Nb(0)	[00-034-0370]	$\text{NbH}_{0.8}$	[01-081-6188]
Nb_6C_5	[04-007-6990]		
Ta(0)	[00-004-0788]	Ta_2H	[00-032-1281]
TaC	[00-035-0801]	TaO	
Mo(0)	[04-014-7435]	Mo_2C	[04-001-2996]
W(0)	[00-004-0806]	WC	[00-051-0939]
W_2C	[04-014-5679]		
KCl	[00-041-1476]		

Phase	PDF N°	Phase	PDF N°
CeO ₂	[00-034-0394]	Ce(OH) ₃	[00-055-0556]
La(OH) ₃	[00-036-1481]	Nd(OH) ₃	[04-005-8595]
Eu(OH) ₃	[00-017-0781]	Dy(OH) ₃	[00-019-0430]
Tm(OH) ₃	[01-083-2306]		
c-In ₂ O ₃	[04-004-3575]	rh-In ₂ O ₃	[00-022-0336]
InOOH	[04-009-3421]		
Bi(0)	[00-005-0519]	β-Bi ₂ O ₃	[04-007-1443]
W ₁₈ O ₄₉	[00-064-0773]		
Ni(0)	[03-065-2865]	Ni ₃ C	[04-007-3753]
Ni ₂ P	[04-003-1863]	Ni ₁₂ P ₅	[00-022-1190]
Ni ₅ P ₄	[04-014-7901]		

ES.6. Transmission Electron Microscopy (TEM)

For TEM analysis, a drop of a diluted solution of nanoparticles dispersed in ethanol (for hydrothermal syntheses) or hexanes (for solid-state and solvothermal syntheses) was allowed to dry on an amorphous carbon coated copper grid. TEM images were collected with a TWIN 120 (TECNAI SPIRIT) operating at 120 kV. STEM bright field (BF) and high angle annular dark field (HAADF) images were acquired using a probe corrector Cs JEOL 2100F microscope operating at 200 kV.

ES.7. Energy Dispersive X-Ray Spectroscopy (EDXS)

EDXS measurements were performed on a SEM Hitachi S-3400N operating at 10 keV. The samples were pressed on a carbon tape installed on a SEM sample holder. Measurements were performed in 3 zones to insure a better representativity of the analysis.

ES.8. X-Ray Photoelectron spectroscopy (XPS)

XPS spectra were acquired on an Omicron Argus X-ray photoelectron spectrometer, using a monochromated Al K α ($h\nu = 1486.6$ eV) radiation source having a 300 W electron beam power. The samples were analyzed under ultra-high-vacuum conditions (10^{-8} Pa). After recording a broad range spectrum (pass energy of 100 eV), high-resolution spectra were recorded for the C 1s, O 1s, Ce 3d core XPS levels (pass energy of 20 eV). The binding energies were calibrated with respect to the C 1s peak at 284.8 eV (adventitious carbon). Fitting of X-ray photoemission spectra has been performed using the CasaXPS software package.

All NAP-XPS spectra were collected on the TEMPO B beamline at SOLEIL synchrotron (electron energy of 2.7 GeV and average ring current of 450 mA). The samples were dispersed in ethanol by sonication during 10 min and then drop-casted on a gold coated silicon wafer. They were then disposed on a unique sample holder and introduced in the NAP-XPS setup (pressure of 10^{-9} mbar). The measurements were performed on different spots to minimize the impact of the beam damage. The incident photon energy was of 1100 eV for all experiments. Pass energy of 50 eV was used. Binding energies were calibrated using the Au $4f_{7/2}$ peak at 84 eV.

Ceria is known for charging at low temperatures: the spectra measured below 150 °C were calibrated on the satellite peak of Ce 3d at 916.6 eV. Spectra in the Ce 3d region were background-corrected by subtraction of three linear function defined in the ranges 919-913 eV, 913-894 eV and 894-878 eV and fitted with a linear combination of intensity envelopes from Ce^(IV) and Ce^(III) species. All peaks were fitted using the Gaussian-Lorentzian line shape GL(30) as an approximation of the Voigt curve. Constraints were imposed on signal intensity ratios (peak area ratio of 3:2 for $3d_{5/2}$: $3d_{3/2}$), separation between spin-orbit split peaks (18.35 eV for Ce^(III) doublets and 18.5 eV for Ce^(IV) doublets, determined on the reference compounds) and peak width (similar values of Full Width Half Maximum (FWHM) for both peaks of any spin-orbit split doublet). As the signals are broad and the data quite noisy for experiments performed on the Synchrotron beamline, more strict peak positions and peak widths were imposed than for laboratory instrument, as summarized in Table ES.1. and ES.2.

Species		Binding energy (eV)	Doublet splitting (eV)	FWHM (eV)	Color
Laboratory instrument (1486.6 eV)					
Ce ³⁺	Ce $3d_{5/2}$ U_0/V_0	881.3-878	18.35	1-3.5	Violet
	Ce $3d_{5/2}$ U'/V'	885.6-883.3	18.35	1-5	Pink
Ce ⁴⁺	Ce $3d_{5/2}$ U/V	882.8-881.9	18.5	1-2	Yellow
	Ce $3d_{5/2}$ U''/V''	888.9-887.6	18.5	1-5	Red
	Ce $3d_{5/2}$ U'''/V'''	898.4-897.7	18.5	1-3.5	Orange
Synchrotron beamline (1100 eV)					
Ce ³⁺	Ce $3d_{5/2}$ U_0/V_0	881.3-881.05	18.35	2.6-3.1	Violet
	Ce $3d_{5/2}$ U'/V'	885.6-885.2	18.35	3-3.8	Pink
Ce ⁴⁺	Ce $3d_{5/2}$ U/V	882.8-882.35	18.5	2.5-2.9	Yellow
	Ce $3d_{5/2}$ U''/V''	888.9-887.6	18.5	3-5	Red
	Ce $3d_{5/2}$ U'''/V'''	898.4-897.7	18.5	2-2.8	Orange

Table ES.1. Fitting parameters used in CasaXPS for Ce 3d region.

Species	Binding energy (eV)	FWHM (eV)	Color
Laboratory instrument (1486.6 eV)			
O _I	529.6-529	0.8-1.3	Blue
O _{II}	531.3-529	1-2	Dark green
O _{III}	531.6-531.3	0.2-1.5	Light green
O _{IV}	536-532	0.28-7	Black
Synchrotron beamline (1100 eV)			
O _I	529.6-529	0.8-2.5	Blue
O _{II}	531.3-529	1-2	Dark green
O _{III}	533-531.3	0.2-1.5	Light green
O _{IV}	536-532	0.28-7	Black

Table ES.2. Fitting parameters used in CasaXPS for O 1s region.

ES.9. X-Ray Absorption Spectroscopy (XAS)

All XAS data were collected on different beamlines at SOLEIL (electron energy of 2.7 GeV and average ring current of 450 mA). Spectrum processing was carried out using the Athena/Demeter software following literature procedures.¹ Normalization was performed using a linear fit of the pre-edge and post-edge regions and the edge height was normalized to unity with the post-edge values asymptotically approaching zero. The absorption threshold was determined by the first zero (not corresponding to a pre-edge peak) of the first derivative. For solid samples, a 6 mg portion of the powder was diluted in *ca.* 55 mg of graphite and compressed to form a 10 mm diameter pellet.

Mo K-edge and Ni K-edge XAS data were collected on the ROCK beamline. The incoming photons were selected with a Si (220) double-crystal monochromator. Ion chambers filled with a mixture of nitrogen and helium were installed in front of and behind the sample, which simultaneously detected the incident and transmitted X-ray intensities. Fourier transforms of the Ni-EXAFS spectra were carried out in a K-range from 3.0 to 13.9 Å⁻¹.

Ce L_{III}-edge XAS data were collected on the LUCIA beamline. The measurements were carried out under vacuum (10⁻² mbar) in fluorescence mode with an outgoing photon angle of 2°. The incoming photons were selected with a Si (111) double-crystal monochromator.

¹ Ravel, B. & Newville, M. ATHENA: data analysis for X-ray absorption spectroscopy using IFEFFIT. *J. Synchrotron Radiat.* **12**, 537–541 (2005)

Appendix II

Thermodynamic calculations

TC.1. Heat capacity models

Heat capacity of solid KCl as a function of reduced temperature t ($t=T(K)/1000$) in J/mol/K¹:

$$C_p(\text{KCl}) = 35.41 + 70.03 t - 91.38 t^2 + 52.52 t^3 + 0.1534 t^{-2}$$

KCl melts at 770 °C (1043 K) with a standard fusion enthalpy of 25.5 kJ/mol.

Liquid KCl heat capacity is estimated constant at 73.6 J/mol/K.

KCl boils at 1500 °C (1773 K) with a standard evaporation enthalpy of 162.4 kJ/mol.

Heat capacity of solid CaCl₂ as a function of reduced temperature t in J/mol/K:

$$C_p(\text{CaCl}_2) = 87.30 - 35.08 t + 44.13 t^2 - 9.85 t^3 - 0.6742 t^{-2}$$

CaCl₂ melts at 772 °C (1045 K) with a standard fusion enthalpy of 28.5 kJ/mol.

Liquid CaCl₂ heat capacity is estimated constant at 102.5 J/mol/K.

CaCl₂ boils at 1935 °C (2208 K).

Heat capacity of graphite as a function of reduced temperature t in J/mol/ K²:

$$C_p(\text{graphite}) = 27.02 + 0.0457 t - 4.528 t^{-1} - 2.179 t^{-2} + 0.7991 t^{-3} - 0.07207 t^{-4}$$

Heat capacity of metal (very close values for all the metals studied here, based on Tantalum) as a function of reduced temperature t in J/mol/K:

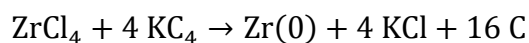
$$C_p(\text{metal}) = 20.69 + 17.29 t - 15.68 t^2 + 5.608 t^3 + 0.06158 t^{-2}$$

Pyrex glass has a heat capacity of 0.75 J/g/K which corresponds to a heat capacity of 7.5 J/K for the 10 g of the glass walls of the Schlenk tube near the powder. The auto-initiated reaction with WCl₆ released 300 J which would correspond to a final elevation of 45 °C of the part of the vessel in contact with the reaction. This order of magnitude is coherent with the feeling of heat with hand.

TC.2. Enthalpies of formation and of reaction

Unless otherwise stated, all the thermodynamical data are from the Thermodynamical tables of the NIST-JANAF.¹ The released energy by the reaction corresponds to the absolute value of the enthalpy of reaction, determined via Hess's law.

For instance, for the reaction with ZrCl_4 :



$$\Delta_{\text{reaction}}H^\circ = \Delta_f H^\circ(\text{Zr}) + 4 \Delta_f H^\circ(\text{KCl}) + 16 \Delta_f H^\circ(\text{C}) - (\Delta_f H^\circ(\text{ZrCl}_4) + 4 \Delta_f H^\circ(\text{KC}_4))$$

By definition, the enthalpy of formation of $\text{Zr}(0)$ and graphite is zero.

$$\Delta_{\text{reaction}}H^\circ (\text{kJ/mol}) = 4 (-436.7) - (-980.5 + 4 (-30.9)) = -642.7$$

Compounds	Enthalpy of formation (kJ/mol)	Compounds	Enthalpy of formation (kJ/mol)
Chlorides		Oxides	
ScCl ₃	-944.8		
YCl ₃	-982.4		
LaCl ₃	-1070.7		
TiCl ₃	-721.7		
ZrCl ₄	-980.5	ZrO ₂	-1097.5
HfCl ₄	-990	HfO ₂	<i>no data</i>
VCl ₃	-580.7		
NbCl ₅	-797.5	Nb ₂ O ₅	-1899.5
TaCl ₅	-859	Ta ₂ O ₅	-2046
CrCl ₂	-395.4		
CrCl ₃	-556.5		
MoCl ₃	-393	MoO ₂	-587.9
MoCl ₅	-527.2	MoO ₃	-745.2
WCl ₄	-443.1		
WCl ₆	-593.7	WO ₃	-842.9
MnCl ₂	-481.2		
FeCl ₂	-341.7		
FeCl ₃	-399.2		
CoCl ₂	-312.5		
NiCl ₂	-304		
Alkaline derivatives			
KC ₄	-30.9	KCl	-436.7
KC ₈	-33.4	K ₂ O	-363.2
CaC ₂	-62.8	CaCl ₂	-795.8
		CaO	-635.7
SrC ₂	-60	SrCl ₂	-828.8
		SrO	-592

Table TC.1. List of enthalpies of formation of the different relevant compounds.

Starting material	Enthalpy of reaction per atom of transition metal (kJ/mol)			
	Reduction by KC_4	Reduction by KC_8	Reduction by CaC_2	Reduction by SrC_2
Chlorides				
$TiCl_3$	-496	-488	-378	-432
$ZrCl_4$	-642	-632	-485	-557
$HfCl_4$	-633	-623	-476	-548
VCl_3	-637	-629	-519	-573
$NbCl_5$	-1231	-1219	-1035	-1125
$TaCl_5$	-1170	-1157	-974	-1063
$CrCl_2$	-416	-411	-338	-373
$CrCl_3$	-661	-653	-543	-597
$MoCl_3$	-824	-817	-707	-760
$MoCl_5$	-1502	-1489	-1305	-1395
WCl_4	-1180	-1170	-1023	-1095
WCl_6	-1841	-1826	-1605	-1713
$ScCl_3$		-272		
YCl_3		-235		
$LaCl_3$		-147		
$MnCl_2$		-330		
$FeCl_2$		-470		
$FeCl_3$		-818		
$CoCl_2$		-499		
$NiCl_2$		-507		
Oxides				
ZrO_2	495	505	-48	34
HfO_2	<i>n.d.</i>	<i>n.d.</i>	<i>n.d.</i>	<i>n.d.</i>
Nb_2O_5	197	197	-482	-380
Ta_2O_5	270	282	-409	-307
MoO_2	-15	-5	-558	-476
MoO_3	-160	-144	-974	-851
WO_3	-61	-46	-876	-753

Table TC.2. List of enthalpies of reaction for SSM and MSSM reactions.

Starting material	Adiabatic temperature T_{ad}		
	Reduction by KC_4	Reduction by KC_8	Reduction by CaC_2
$TiCl_3$	1000 °C	770 °C	1520 °C
$ZrCl_4$	990 °C	770 °C	1500 °C
$HfCl_4$	970 °C	770 °C	1470 °C
VCl_3	1270 °C	900 °C	> 1935 °C
$NbCl_5$	1490 °C	1040 °C	> 1935 °C
$TaCl_5$	1420 °C	1000 °C	> 1935 °C
$CrCl_2$	1210 °C	860 °C	1900 °C
$CrCl_3$	1310 °C	930 °C	> 1935 °C
$MoCl_3$	1500 °C	1130 °C	> 1935 °C
$MoCl_5$	1500 °C	1250 °C	> 1935 °C
WCl_4	1500 °C	1230 °C	> 1935 °C
WCl_6	1500 °C	1280 °C	> 1935 °C
$ScCl_3$		520 °C	
YCl_3		460 °C	
$LaCl_3$		320 °C	
$MnCl_2$		770 °C	
$FeCl_2$		980 °C	
$FeCl_3$		1140 °C	
$CoCl_2$		1040 °C	
$NiCl_2$		1050 °C	

Table TC.3. Adiabatic temperatures for SSM reactions with KC_4 and KC_8 . The determination of the adiabatic temperature is done graphically: T_{ad} is the temperature of the system when its enthalpy corresponds to the enthalpy of the reagents before reaction. KCl melts at 770 °C and boils at 1500 °C. $CaCl_2$ melts at 772 °C and boils at 1935 °C.

References

1. Chase, M. W. *NIST-JANAF Thermochemical Tables, 4th Edition*. (1998).
2. Butland, A. T. D. & Maddison, R. J. The specific heat of graphite: An evaluation of measurements. *J. Nucl. Mater.* **49**, 45–56 (1973).

Appendix III

Written and oral contributions

Articles

[1] F. D'Accriscio, E. Schrader, C. Sassoey, M. Selmane, R. F. André, S. Lamaison, D. Wakerley, M. Fontecave, V. Mougél, G. Le Corre, H. Grützmacher, C. Sanchez, S. Carenco. A single molecular stoichiometric P-source for phase-selective synthesis of crystalline and amorphous iron phosphide nanocatalysts. *ChemNanoMat* **6**, 1208-1219 (2020).

[2] A. P. Freitas, R. F. André, C. Poucin, T.K.-C. Le, J. Imbao, B. Lassalle-Kaiser, S. Carenco. Guidelines for Molybdenum oxidation state and geometry from X-ray absorption spectroscopy at the Mo L_{2,3}-edges. *The Journal of Physical Chemical C*, **in press** (2021).

[3] R. F. André, F. D'Accriscio, A. P. Freitas, G. Crochet, C. Ulhaq, M. Bahri, O. Ersen, C. Sanchez, S. Carenco. Early transition metal nano-carbides and nano-hydrides from solid-state metathesis initiated at room temperature. *Green Chemistry*, **in press** (2021).

Orals

International

[4] “Early transition metal nano-carbides and nano-hydrides from solid-state metathesis initiated at room temperature” by R. F. André, F. D'Accriscio, A. P. Freitas, G. Crochet, S. Carenco, at 5th EuChemS Conference on Green and Sustainable Chemistry (5th EuGSC), **2021**.

National

[5] “Insights into solid-state synthesis of finely dispersed early transition metal carbides and hydrides nanoparticles supported on carbon” by R. F. André, F. D'Accriscio, G. Crochet, S. Carenco, at GECat, **2021**.

Local

[6] “Solid-solid synthesis of early transition metal carbide nanoparticles” by R. F. André, S. Carenco, at Journée annuelle de l'Institut des Matériaux de Paris Centre (IMPC), **2019**.

Posters

National

[7] “Hydrogenation of model compounds with nickel carbide and phosphide in mild conditions” by R. F. André, L. Meyniel, S. Carenco, at SCF2021-Catalysis, **2021**.

Local

[8] “Energy efficient solid-state metathesis reactions for nanocarbides synthesis” by R. F. André, F. D’Accriscio, A. P. Freitas, G. Crochet, S. Carenco, at Journées de l’Ecole Doctorale 397 “Physique et Chimie des Matériaux”, **2020**.

Workshops

[9] “Non-hydrolytic syntheses of Lewis acidic metal oxide nanoparticles” by R. F. André, S. Carenco, at SchoolCat Summer School, **2019**.

[10] “Energy efficient solid-state metathesis reactions for nanocarbides synthesis” by R. F. André, F. D’Accriscio, A. P. Freitas, G. Crochet, S. Carenco, at Green Chemistry Online Postgraduate Summer School, **2020**.

Abstract

In this thesis work, the use of metal-containing nanoparticles such as carbides, oxides and phosphides is explored for colloidal catalysis. In an attempt to build a Frustrated Lewis Pair (FLP)-like catalytic system for H_2 activation, the synergy with a molecular Lewis base is assessed. In the bibliographic introduction, the stakes and the challenges of H_2 activation in solvent are presented, with an emphasis on the use of non-purely metallic catalysts for the hydrogenation of model compounds. In the first part, early transition metal carbides and hydrides are synthesized *via* solid-state metathesis. The influence of process parameters is explored to tune the phase speciation in the products. The most promising carbon-supported catalysts, Mo_2C/C and W_2C/C , are studied for gas phase and liquid phase hydrogenations of olefins. In the second part, cerium and indium oxides are obtained *via* hydrothermal pathways. The relevance of oxygen defects in CeO_{2-x} is established for H_2 gas phase activation and semi-hydrogenation of phenylacetylene in solvent. The last part is dedicated to the non-aqueous syntheses of molybdenum and tungsten oxides, and nickel carbide and phosphides. The syntheses mechanisms are studied by means of NMR for the organic species and XAS and XRD for the nature of the inorganic species. The catalytic activity of the unsupported nanoparticles is finally evaluated for the hydrogenation of nitrobenzene and phenylacetylene in various solvents.

Dans ces travaux de thèse, nous avons exploré différentes classes de nanoparticules métalliques telles que des carbures, des oxydes et des phosphures, pour des applications en catalyse colloïdale. Afin de construire un système catalytique de type « Paire de Lewis Frustrée », la synergie avec des bases de Lewis moléculaires a été étudiée. En introduction, les enjeux et les défis de l'activation de H_2 en solvant sont présentés, avec un focus sur les catalyseurs non purement métalliques pour l'hydrogénation de composés modèles. Dans la première partie, des carbures et des hydrides de métaux de début de transition ont été synthétisés par métathèse solide-solide. Nous avons exploré l'influence de différents paramètres de procédé sur la spéciation de phase des produits. Les catalyseurs supportés les plus prometteurs, Mo_2C/C et W_2C/C , ont été étudiées pour l'hydrogénation d'oléfines en phase gaz et en solvant. Dans la deuxième partie, des oxydes de cerium et d'indium ont été produits par voie hydrothermale. L'importance de défauts d'oxygène dans CeO_{2-x} pour l'activation de H_2 en phase gaz et pour la semi-hydrogénation du phénylacétylène a été établie. La dernière partie est dédiée à la synthèse solvothermale d'oxydes de molybdène et de tungstène, ainsi qu'à celle de carbure et de phosphures de nickel. Les mécanismes de synthèse ont été étudiés par RMN pour la partie organique et par XAS et DRX pour la partie inorganique. L'activité catalytique des nanoparticules non supportées a finalement été évaluée pour l'hydrogénation du nitrobenzène et du phénylacétylène dans plusieurs solvants.